Multidisciplinary design process applied to the next generation regional aircraft featuring low emission propulsion

Vincenzo Palladino

▶ **To cite this version:**

Vincenzo Palladino. Multidisciplinary design process applied to the next generation regional aircraft featuring low emission propulsion. Physics [physics]. ISAE - Institut Supérieur de l'Aéronautique et de l'Espace, 2023. English. NNT : . tel-04569326

HAL Id: tel-04569326
https://hal.science/tel-04569326

Submitted on 6 May 2024

HAL is a multi-disciplinary open access archive for the deposit and dissemination of scientific research documents, whether they are published or not. The documents may come from teaching and research institutions in France or abroad, or from public or private research centers.

L'archive ouverte pluridisciplinaire **HAL**, est destinée au dépôt et à la diffusion de documents scientifiques de niveau recherche, publiés ou non, émanant des établissements d'enseignement et de recherche français ou étrangers, des laboratoires publics ou privés.

Université Fédérale
Toulouse Midi-Pyrénées

THÈSE

En vue de l'obtention du

DOCTORAT DE L'UNIVERSITÉ DE TOULOUSE

Délivré par :

Institut Supérieur de l'Aéronautique et de l'Espace

Présentée et soutenue par :
Vincenzo PALLADINO

le jeudi 23 mars 2023

Titre :

Méthode de conception pluridisciplinaire appliquée à un avion régional à faibles émissions

---

École doctorale et discipline ou spécialité :
ED AA : Mathématiques et Applications

Unité de recherche :
Équipe d'accueil ISAE-ONERA ACDC

Directeur(s) de Thèse :

Mme Valérie POMMIER-BUDINGER (directrice de thèse)
Mme Nathalie BARTOLI (co-directrice de thèse)

Jury :
M. Stéphane BRISSET Professeur École Centrale de Lille - Président
M. Emmanuel BENARD Professeur ISAE-SUPAERO - Co-encadrant de thèse
Mme Nathalie BARTOLI Directrice de recherche ONERA - Co-directrice de thèse
M. Panos LASKARIDIS Full professor Cranfield University - Rapporteur
Mme Valérie POMMIER-BUDINGER Professeure ISAE-SUPAERO - Directrice de thèse
M. Peter SCHMOLLGRUBER Ingénieur ONERA, Toulouse - Co-encadrant de thèse
M. Frank THIELECKE Full professor Technische Universität Hamburg - Rapporteur

Contents

Abstract

With the rising pressure to reduce aviation environmental impact, coming both from public institutions and social movements (e.g. *flygskam*, Swedish word for "flight shame"), all the players in the aviation sector, from the universities to the industries, are looking for solutions to reduce greenhouse emissions generated by air transport drastically. Many aircraft concepts featuring disruptive technologies which could significantly reduce CO_2 and NO_x emissions are currently under study. Indeed, the aviation community is aware that the continuous improvement of the existing aircraft designs and technologies is not a viable approach to reach the emission reduction targets that have been agreed upon at the International Council on Clean Transportation to respond to the needs of society nowadays. Therefore, aircraft manufacturers as well as aerospace universities are exploring unconventional air-frame configurations and propulsion systems, which could offer significant efficiency gains for the long term future. This pursuit will most likely culminate in a new chapter of aviation history with the introduction of disruptive propulsion systems.

However, considering the needed time for the development and certification phases, no "low-emission" aircraft is expected to enter into service before 2035. Moreover, given the time needed to replace the "old generation" aircraft fleet, even more time is needed to actually see the effects of the exploitation of such aircraft on global air transport emissions. In order to close the technology gap between existing aircraft and next-generation zero-emission aircraft, this thesis explores the potential of several propulsion technologies suitable for the forward-fit design of an existing regional aircraft platform.

In particular, the present work focuses on the conceptual design of a 70-seat regional aircraft featuring hydrogen-based hybrid propulsion with the objective of providing the tools, methods and results to be used as a credible basis to drive hybrid aircraft design choices. After an initial survey of technology enablers, the most promising propulsive architectures with different power sources and layouts are identified. Then, a multidisciplinary aircraft design process suitable for designing a regional aircraft with disruptive propulsion technology is developed. To allow the evaluation of the performance of new propulsion systems at the aircraft level, an existing multidisciplinary design and optimization platform has been enhanced.

A down-selection approach consisting of three steps was set in place to analyze a total of eight propulsive architectures in a time-efficient manner. At each step, the number of architectures is reduced and the level of fidelity of the analyses is increased. The performances of each propulsive architecture are first assessed with high-level conceptual studies to identify its main drawbacks and benefits. Then the most promising architectures are evaluated more thoroughly with multidisciplinary design analysis and optimization techniques, where optimization algorithms are used to determine the optimal system design variables. Only the parameters introduced by the new propulsive systems were used as design variables for the Bayesian optimization in order to guarantee the best possible design for the given aircraft platform and operational scenario. Uncertainty management techniques are also used to identify uncertain parameters, which have a considerable impact on the quantity of interest, in order to determine the models that may need further development to improve the accuracy of the results.

The analyses conducted on the different propulsive systems under study indicate that hydrogen fuel cells, integrated into a parallel hybrid-electric propulsion system, are one of the most promising technologies to reduce aircraft emissions in the short term by more than 30%.

Acknowledgments

I would like to take this opportunity to express my heartfelt gratitude to all those who have allowed me to be here today to write the final words of this Ph.D. thesis. It has been a long journey, a true roller coaster of emotions. I have learned a lot about myself and discovered parts of me I had never known. At times it has been very, very hard. Doing this completely alone would have been simply impossible.

First and foremost, I am immensely grateful to all my supervisors. I would like to thank Valerie and Emmanuel, for your constant guidance and constructive feedback. I am truly grateful to you, Nathalie, for the constant support, and encouragement throughout my research journey. Your words have always been of great comfort and motivation in the most difficult times. Finally, thank you Peter, because although the change of role, you have always been there whenever I needed your guidance and precious advice.

I would also like to extend my sincere gratitude to all the colleagues at ATR, Krystel, Sophie, Ludo, Stefano, for all the good moments spent together. Thank you Giovanna, for believing in me and help me grow and learn. Heartfelt gratitude to you, Arnaud, because in the past four years you have been a lot to me, my tutor, my mentor, my colleague and my friend. I sincerely hope we will have another opportunity to work together in the future.

I also wish to express my gratitude to the group of students of ISAE-SUPAERO, and in particular Felix Pollet, because without your efforts and significant contribution this research would not have the same value.

I am genuinely thankful to my friends, Dimitris, Vaguelis, Dionisis, Paolo, for the emotional support and encouragement through all the ups and downs of these years. Thank you Marco, because sharing the burden with you has made it much easier to carry. I am sure that one day, looking back, we will be able to see more clearly plenty of good times and not only the tough and dark moments.

I am deeply grateful to my family for their unflinching love. Their unwavering belief in my abilities, since I was only a child, has been a constant source of strength for me. Every

success that I have achieved or that I will ever achieve in the future is dedicated to you. You deserve all the joy I will ever be able to give you.

The last lines are for you my Love. If I could put another name among the authors of this thesis it would be yours. I may have written alone all the words, done all the studies, but you have always been the constant source of my strength and motivation. In the darkest times, you took me under your arm and guided me when I could not see. Thank you for being at my side. Another chapter of our life is finished, a new exciting one has just started.

"Better things are coming." cit.

Publications

The following papers have been published by the author before the thesis submission and they include portions of the material in this thesis:

Journal Paper

Palladino, Vincenzo, et al. "Optimization of a hydrogen-based hybrid propulsion system under aircraft performance constraints." Chinese Journal of Aeronautics 36.5 (2023): 41-56. DOI: https://doi.org/10.1016.

Conference proceedings

Palladino, Vincenzo, et al. "A comparative study of different propulsion models for hybrid electric aircraft." 3AF Aerospace Europe Conference 2020. 2020.

Palladino, Vincenzo, et al. "Preliminary studies of a regional aircraft with hydrogen-based hybrid propulsion." AIAA AVIATION 2021 FORUM. 2021.

Nomenclature

λ	Relative air to fuel ratio
ρ_E	Energy density $[Wh/l]$
AFR	Air to fuel ratio
AFR_{st}	Air to fuel stoichiometric ratio
CNG	Compressed natural gas
CO_2	Carbon dioxide
E_{sp}	Specific energy $[Wh/kg]$
$FE\text{-}EB$	Full Electric Battery
$GHGs$	Green house gases
NM	Nautical mile
NOx	Nitrogen oxide
P_{sp}	Specific power $[W/kg]$
PH	Parallel Hybrid
$PH\text{-}EB$	Parallel Hybrid-Electric Battery
$PH\text{-}FC$	Parallel Hybrid Fuel Cell
SH	Series Hybrid
$SH\text{-}EB$	Series Hybrid-Electric Battery
$SH\text{-}FC$	Series Hybrid Fuel Cell
TE	Turbo-Electric
$TP\text{-}H2B$	Turboprop H_2 burn
AEO	All Engine Operative

BLI	Boundary layer ingestion
BoP	Balance of plant
C-H_2	Compressed hydrogen
Cc-H_2	Cryo-compressed hydrogen
CCS	CO_2 capture and storage
CFD	Computational fluid dynamics
DEP	Distributed electric propulsion
FEM	Finite element methods
GWP	Global warming potential
ICCT	International Council on Clean Transportation
ICE	Internal combustion engine
L-H_2	Liquid hydrogen
LCA	Life-cycle assessment
LHV	Low Heating Value
Li	Lithium
LiB	Lithium-based batteries
LOHC	Liquid organic hydrogen carrier
MCS	Monte Carlo simulations
MDA	Multidisciplinary analysis
MDAO	Multidisciplinary Design Analysis and Optimisation
MDO	Multidisciplinary optimization
OAD	Overall Aircraft Design
OEI	One Engine Inoperative
OWE	Operating Weight Empty
PCE	Polynomial chaos expansion
PDF	Probability distribution function

PEMFC	Proton exchange membrane fuel cell
Po	Polymer
PSFC	Power specific fuel consumption
RHEA	Regional Hybrid Electric Aircraft
RTO	Reserve Take Off
SAF	Sustainable Aviation Fuel
SOFC	Solid oxide fuel cell
TLAR	Top Level Aircraft Requirement
TOFL	Take Off Field Length
TTC	Time To Climb
TTW	Tank-to-Wake
UAV	Unmanned Aerial Vehicle
WTT	Well-to-Tank
WTW	Well-to-Wake

List of Figures

List of Tables

Introduction

Aviation currently accounts for around 13% of transport-related CO_2 emissions (see Fig. 1) and around 2.4% of global greenhouse gases [1]. Due to the increasing air transportation demand, according to the International Council on Clean Transportation (ICCT), global CO_2 emissions from commercial aviation increased approximately 30% in six years [2]. This number is expected to rise significantly considering that the demand for passenger and freight aviation will likely triple by 2070 as predicted by the International Energy Agency [3]. As shown in Fig. 2, aviation is indeed one of the fastest-rising sources of carbon emissions.

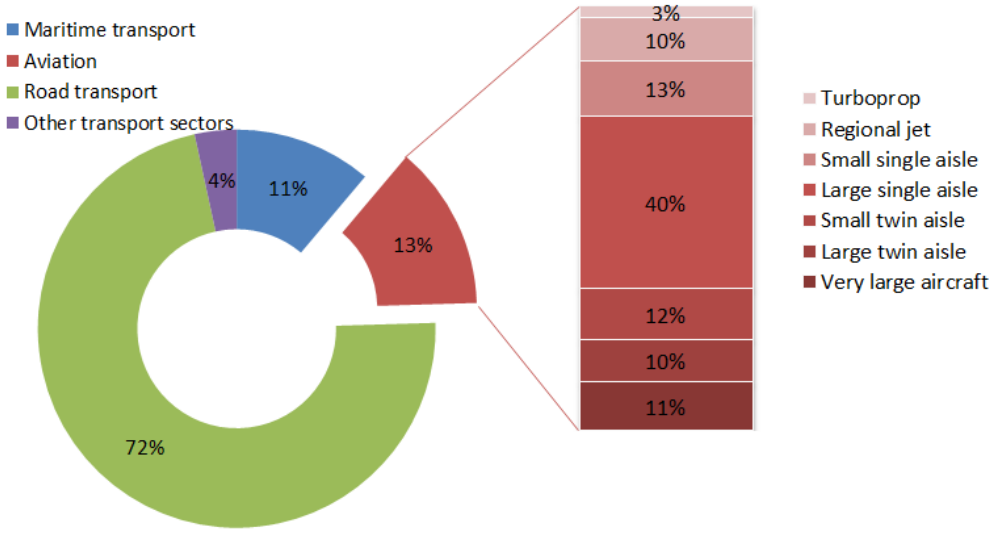

Figure 1: Direct $GHGs$ emissions of the transport sector. Data from [4, 5].

As of today, air travel together with maritime transport has an environmental impact that is comparable to that of a whole continent like Africa (see Fig. 3). Therefore aviation has an important role to play in reducing greenhouse gas emissions, regardless of traffic growth. As a consequence, the European Union (EU) Commission together with aviation industry players agreed on ambitious goals to reduce aircraft-related emissions in the long term as reported in "Flightpath 2050" [6]: 75% CO_2 reduction (in support to

the Air Transport Action Group - ATAG - target[1]), 90% NOx and 65% perceived noise reduction relative to a reference emission scenario in the year 2000.

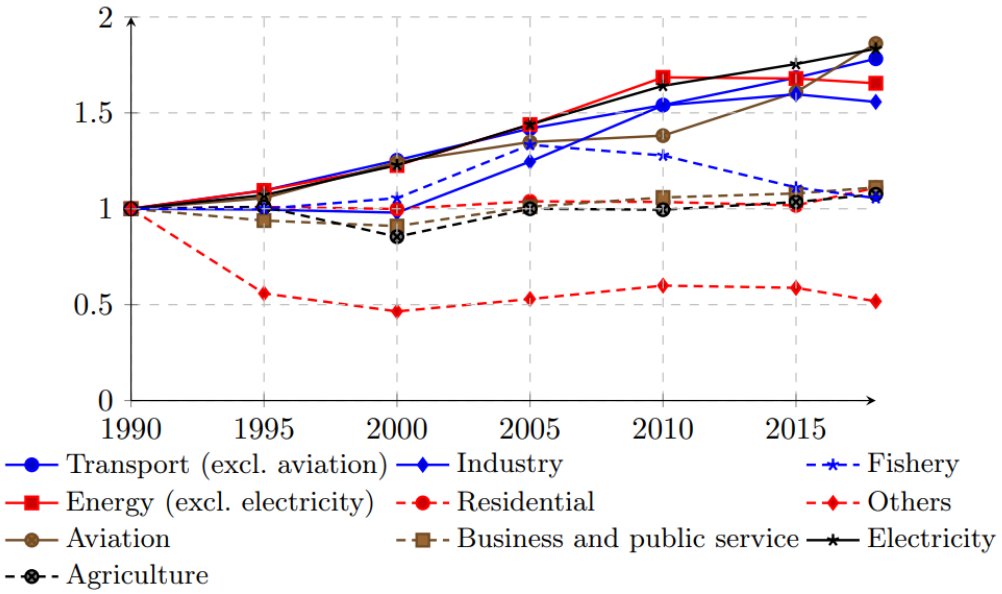

Figure 2: Change in CO_2 emissions according to their level in 1990 for different sectors. Figure from [1].

These goals are extremely challenging and unlikely to be achieved by the evolutionary improvement of existing aviation technology. The whole aviation sector, from the universities to the industries, is looking for solutions to drastically reduce greenhouse emissions generated by air transport. This pursuit will most likely culminate into a new chapter of aviation history with the introduction of disruptive propulsion systems and air-frame designs. Therefore, the design of air vehicles with low environmental impact is one of the most daunting endeavors of modern aviation. Nevertheless, the greatest benefits in terms of emission reduction are associated with technological solutions (e.g. unconventional air-frame designs and full electric propulsion) that will probably require major investments and long development time. Moreover, it will take several years until the existing aircraft fleet is replaced with new-generation vehicles. Therefore, an intermediate step in aircraft technology development is needed to reach the ambitious targets set by the EU Commission. As of today, in order to reduce aviation environmental impact in the short term, several alternatives are being investigated by the actors of the aviation sector. Sustainable aviation fuel (SAF), hydrogen fuel and hybrid-electric propulsion are the main technologies that may be suitable also for short-to-medium-term implementation.

The huge interest in alternative sustainable fuel is clear: it represents a drop-in solution with moderate to zero modifications to aircraft or engine design to reduce life-cycle CO_2

[1]Carbon-neutral growth starting 2020 and a 50% overall CO_2 emission reduction by 2050.

emissions. However, there are some significant drawbacks to the use of SAF, such as the adverse side-effects arising from the production of the feedstock for biofuel generation (for example, adverse impact on farming land, fresh-water supply, food prices, etc. [7]), the scarce availability of resources to satisfy today and future fuel demand as well as its poor cost-competitiveness. For all these reasons, while sustainable aviation fuel remains an interesting solution to reduce aviation-related CO_2 emissions, it is clear that other technologies must be developed and implemented, together with SAF, in order to meet the ambitious aviation emission targets.

Hydrogen fuel represents a non-drop-in alternative to kerosene which could lead to zero in-flight emissions of CO_2 and lower NOx emissions. The idea of burning hydrogen in a gas turbine has been around for many decades and although some studies and tests have already been performed, up to date the feasibility of such technology is still under investigation [8].

In recent years, there has been increased attention toward hybrid electric vehicles and alternative power sources. As of today, the automotive industry is addressing the same challenge with the introduction of battery and fuel cell-powered electric cars (e.g. Tesla[2], Toyota Mirai[3]), featuring zero-emission during operation. However, these propulsion systems show performance and weight deficits compared to conventional aircraft propulsive systems which represent a big challenge for the aviation industry.
Nevertheless, considering the ongoing investments in battery and electric motor development as well as fuel cell technology, the introduction of electric propulsion seems to be a viable option for regional transport aircraft, having moderate power and energy requirements. The adoption of alternative power sources, however, not only introduces challenges related to the performance of the technology itself but rises significant issues for aircraft design engineers. Conventionally, overall aircraft design (OAD) relies on well-established processes and equations that have been derived from the knowledge and experience coming from existing aircraft and previous designs. Therefore, the introduction of completely new technology raises challenges in the design of the aircraft inherent to the lack of data about existing similar aircraft. This lack of information that would otherwise be used to drive and verify the new aircraft design may lead to inaccurate assessments, resulting in significant schedule delays and cost overruns in the development phase.

To address this issue, the conceptual design of unconventional aircraft requires the development and integration into the design process of new evaluation methods and models, which are able to predict the performance and behavior of the technology we want to

[2] https://www.tesla.com/
[3] https://www.toyota.fr/vehicules-neufs/mirai

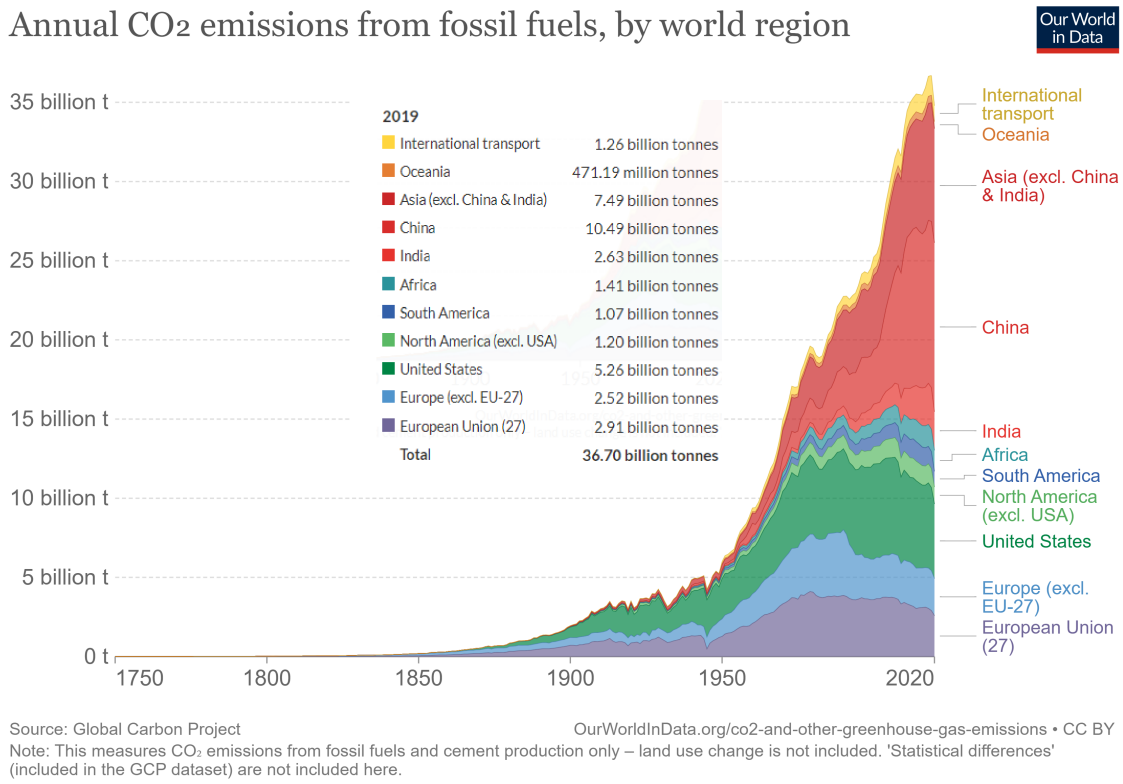

Figure 3: Annual CO_2 emissions by world region. International transport includes aviation and shipping. Emissions from domestic aviation and shipping are included in each country's total. Figure from ourworldindata.org.

investigate. Moreover, in order to handle all the possible interactions and dependencies between the disciplines, these models need to be integrated within a platform for aircraft sizing and performance evaluation, based on multidisciplinary design analysis and optimization techniques (MDAO). Some platforms have already been developed for the design and analysis of innovative aircraft architectures, which are able to handle the large number of interdisciplinary dependencies introduced by the adoption of alternative power sources. In [9], a conceptual level aircraft design environment developed at Stanford named SUAVE is presented, together with results obtained for a multi-mission regional aircraft, a family of UAVs and a tradeoff between noise and fuel burn on a large single-aisle aircraft. In [10], the platform developed by ONERA and ISAE-SUPAERO named FAST-OAD (Future Aircraft Sizing Tool - Overall Aircraft Design) is used for the preliminary sizing of a medium-range blended wing body. Other known tools suitable for unconventional aircraft design are MICADO [11], PrADO [12], XMDO [13] and Pacelab APD [14]. The overall working principle of these tools can be sometimes very similar, possibly they may also share the same models for main disciplines such as weights and aerodynamics. However, the codes are either proprietary, therefore not available for download, or not suited for the design of a regional twin-propeller aircraft and therefore need to be adapted.

In 2019, when this thesis started, research in this domain focused mainly on the use of batteries as the main electrical power source resulting in a lack of studies for hydrogen-based propulsive systems designed for regional aircraft. Therefore, this thesis focused on the development of a multidisciplinary aircraft design process suitable for the design of a 70-seat regional aircraft to be used in order to identify the most promising propulsive architectures with batteries or hydrogen, concerning its potential to reduce fuel consumption and CO_2 emissions.

Aims and Objectives

This thesis was financed by ATR aircraft[4] and the ANRT ("Association nationale de la recherche et de la technologie" in french) to provide the preliminary design team with tools, methods and results to be used as a credible basis to explore the potential of disruptive propulsion technologies on the regional transport aircraft class. A 70-seat twin-propeller aircraft with similar characteristics of the ATR72 (see Fig. 4) has been chosen as the baseline aircraft and starting point for all the work. This aircraft class is particularly interesting when exploring disruptive technologies such as hydrogen and electric propulsion because it has characteristics weights, speeds and mission ranges that imply low energy and power requirements. Therefore, the ease of those requirements may facilitate the integration of such propulsion systems even with short-term provisions for energy storage and motor power densities. Moreover, a 70-seat twin-propeller aircraft represents a valid benchmark to test the actual advantages in terms of emission reduction introduced by the new propulsion systems under study. As of today, the ATR72 has the lowest fuel consumption on the regional market, featuring 40% less CO_2 emissions than regional jets on an average route of 300 NM.

Figure 4: Main characteristic of a twin-propeller regional aircraft.

[4] https://www.atr-aircraft.com/

As shown in Fig. 1, the emissions share of the regional turboprop aircraft sector is only 3% of the total aviation emissions, therefore the impact of the development of highly efficient, low-emission regional aircraft on the global aviation environmental footprint may be considered negligible. Nevertheless, the application of this disruptive technology on small airplanes is an essential step to be performed before its introduction on larger aircraft in order to start creating certification standards and demonstrate the actual potential of new propulsive technologies. Therefore, this work aims at designing a 70-seat regional turboprop aircraft that is successively used as a baseline to explore the potential emissions reduction provided by the replacement of conventional gas turbines with several innovative propulsive systems based on hydrogen and/or electric propulsion. The design modifications to the baseline aircraft will consist of a forward-fit approach, meaning that the air-frame geometry and weight are kept unchanged and only the propulsive systems are changed. Such a design approach is considered key for rapid development and entry into service of a lower emissions aircraft, which should fill the gap between current technology and next-generation aircraft featuring unconventional airframe design and zero-emission propulsion.

At the time this thesis started, overall aircraft design platforms such as SUAVE[5] and FAST-OAD[6] were available open-source, however, the methods and design process used for the aircraft sizing and weight estimation were not suitable for the design of a turboprop regional aircraft, but rather suited for single-aisle medium-haul aircraft such as the Airbus A320 or the Boeing 737. Thus, the first contribution of this thesis consists of the development of a multidisciplinary aircraft design process with methods suitable for the design of a conventional 70-seat regional turboprop aircraft. The introduction of new propulsive technologies originates additional degrees of freedom to aircraft design and analysis, which leads to the need for modified multidisciplinary design analysis (MDA) processes integrating such degrees of freedom, making them suitable for the design of unconventional aircraft. As previously mentioned, the objective of this thesis is to explore and analyze the impact at the aircraft level of different technologies to reduce fuel consumption and CO_2 emissions. Only two technologies (hydrogen fuel cells and batteries) for power generation have been identified and studied in addition to the gas turbine. However, a large number of propulsive architectures can be generated by the different possible layouts and combinations of those technologies (e.g. full electric, hybrid-electric, etc.). Therefore, in order to manage the assessment of a large number of propulsive architectures to be performed in the time frame of a PhD thesis, a down-selection process consisting of three steps with increasing fidelity and modeling effort has been defined. This process also makes use of global sensitivity analyses as a tool to manage uncertainties by directing the modeling and development efforts toward the systems with the

[5] https://github.com/suavecode/SUAVE

[6] https://github.com/fast-aircraft-design/FAST-OAD

greatest impact on the quantities of interest. Such an approach, used here to explore the design space of innovative propulsion systems for regional aircraft, could be applied also in other domains, whenever there is a vast number of candidate options or architectures to be assessed.

To summarize, the main research contributions and key points that will be addressed are:

- The assessment of the potential emission reduction of new propulsion technologies applied to a regional 70-seat twin-propeller aircraft with a forward-fit approach rather than a clean-sheet design.
- The evolution of an OAD tool through the development of a multidisciplinary aircraft design process with methods to allow the design of a conventional 70-seat regional turboprop aircraft and suitable for the analysis of unconventional propulsion systems.
- Set-up of a down-selection process allowing for the exploration of a large design space in the time frame of a PhD with an overall approach based on uncertainty management.

The thesis structure is organized in three parts and each part is composed of several chapters. Part I, named "State of the art", shows the bibliographic studies that were carried out comprising a review of previous studies and state-of-the-art technologies for low-emission regional aircraft. A technological survey is also carried out to identify technology road-maps to forecast projected technology performance. Moreover, in Chapter 2 existing methods and tools for aircraft design are discussed, with a focus on the conceptual aircraft design framework, optimization and uncertainty management techniques.

Part II is dedicated to the developments within the conceptual aircraft design framework, which have been carried on to design the baseline aircraft and to perform the sizing of the innovative propulsive systems as well as the performance evaluation of the different aircraft configurations. Thus, Chapter 3 shows for each discipline the methods used for the baseline aircraft design, with a focus on the modifications and additions to the available methods in the conceptual design platform used. Then, Chapter 4 is dedicated to the presentation of the additional models developed for the new propulsion systems sizing and performance analysis. Finally, in Chapter 5, the multidisciplinary aircraft design process and the resulting design and performances of the baseline turboprop aircraft are shown. A comparison with existing turboprop aircraft of the same category is also provided to validate the design.

Part III deals with the analysis and the optimization of the different propulsive configurations under study. Chapter 6 presents the overall approach to the analysis of the design

space, consisting in a three-step down-selection process, where at each step, the number of configurations analyzed decreases, while the level of fidelity of the analyses increases. Then, the design process and algorithm used to forward-fit the baseline aircraft with the new propulsive systems are explained. Thereafter, each chapter is related to a single step of the down-selection process, where all the studies performed are presented. Finally, in the last section, final conclusions and future prospects are drawn.

Part I

State of the art

Chapter 1

Review of propulsion technologies for next generation low-emission regional aircraft

Contents

1.1 Previous studies

Although the aviation efforts in reducing aircraft emissions only started since the recognition of CO_2 as the dominant greenhouse gas responsible for global warming, the quest for increased efficiency has always been the utmost priority of aviation industries as well as the main research focus of universities and research centers in the aviation sector. The driver for those improvements was fuel costs rather than environmental emissions, but nonetheless, the average block fuel intensity (grams of fuel per tonne-kilometer) of new aircraft decreased more than 50% from 1960 to 2019 [15].

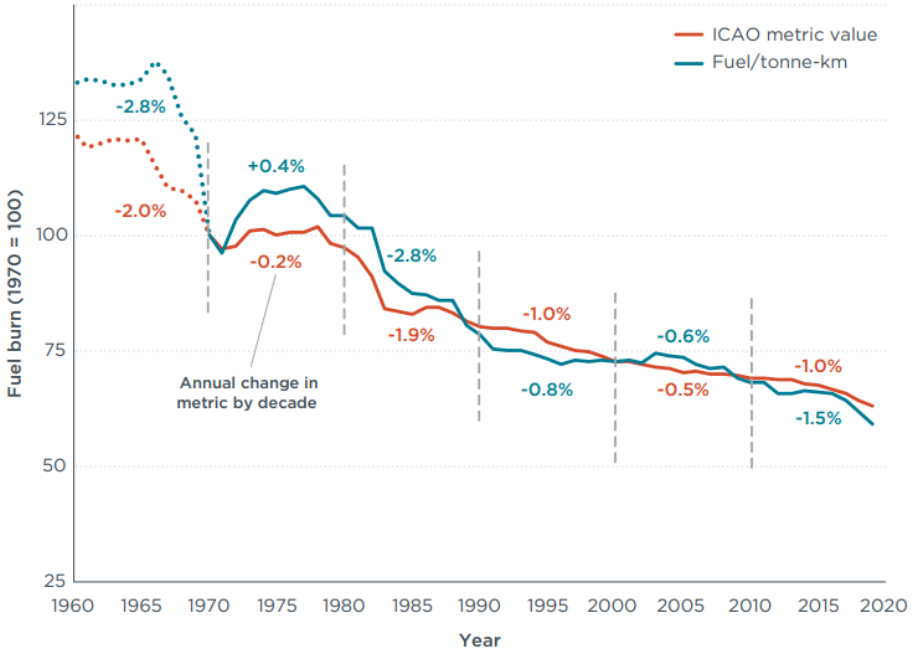

Figure 1.1: Average fuel burn of commercial jet aircraft from 1960 to 2019 [15].

As shown in Fig. 1.1, from a study that analyzed the fuel burn of new commercial jet aircraft from 1960 to 2019, the most drastic reductions in aircraft fuel burn were obtained during the 1980s, with the introduction of new single-aisle aircraft such as the Airbus A320 and the second generation of Boeing 737, featuring more efficient turbofan engines with higher bypass ratio. In the following two decades, only modest improvements were obtained until 2015, when the entry into the service of new engine technologies and clean-sheet aircraft designs led to an increase in the compound annual reduction rate between 2015 and 2019. Lower fuel consumption was mainly obtained due to the extensive implementation of advanced lightweight materials (up to 54% composite material for the Airbus A350) and the development of high bypass ratio engines (up to 12:1 compared to the 6:1 of the previous generation) that, alone, allowed a 20% reduction in specific fuel consumption [16]. Concerning the development of future aircraft in the upcoming decades, the aeronautical community is aware that the evolutionary development of conventional technologies alone would fall short of meeting the ambition to achieve the net

zero carbon goal by 2050. Therefore, many unconventional aircraft configurations (see Fig. 1.2), as well as propulsion technologies (e.g. distributed propulsion, open rotors, hydrogen propulsion, hybrid-electric and full electric propulsion), are under investigation, each at a different state of research or development level.

Figure 1.2: Unconventional aircraft configurations, clockwise from top left: box-wing configuration, strut-braced-wing configuration, lifting-fuselage configuration, and hybrid-wing-body configuration [17].

Examples of concept aircraft powered by hydrogen are the Airbus ZEROe aircraft, three hybrid-hydrogen concept aircraft shown in Fig. 1.3, powered by hydrogen combustion through modified gas turbine engines as well as hydrogen fuel cells.

Figure 1.3: Airbus ZEROe concepts: hybrid-hydrogen turbofan, turboprop and blended-wing-body. Figures from airbus.com

These concepts are expected to play a major role in reducing global aviation carbon emissions in the long-term future (2035 onwards). However, considering the upcoming decade

(from 2020 to 2030), the fuel burn reduction will slow down again if no breakthrough technologies are to enter into service in the short term. For that, a less radical approach in aircraft design, consisting of the integration of innovative yet mature technologies on board an existing aircraft platform may be the key to closing the gap between today's aircraft environmental performance and the disruptive configurations which could potentially allow net zero emissions. Such an approach, however, may not be applicable to all types and sizes of aircraft due to the high energy and power requirements that are not compatible with the aforementioned new propulsion technologies. Previous studies, however, have shown that there are significant benefits to be expected by the introduction of such technologies (in particular hydrogen and hybrid/electric propulsion) on regional transport aircraft such as the ATR72.

Whilst full-electric battery configurations have not proven yet to be a viable option for regional aircraft due to the huge weight of the batteries needed to provide the necessary energy for the typical flight mission, different studies [18, 19] have shown that hybrid electric configurations may be feasible with short-medium term predictions of technology levels. In [18], various propulsive architectures, shown in Fig. 1.4, have been compared on a regional aircraft similar to the ATR72. The study concludes that with current state-of-the-art electric components and battery technology levels (E_{sp}=200 Wh/kg for batteries) both turbo-electric and serial hybrid are responsible for a massive increase of weight and loss of total efficiency, which leads to increased fuel consumption, thus higher emissions. However, the parallel hybrid configuration shows the potential to reduce fuel consumption on a 300 NM mission.

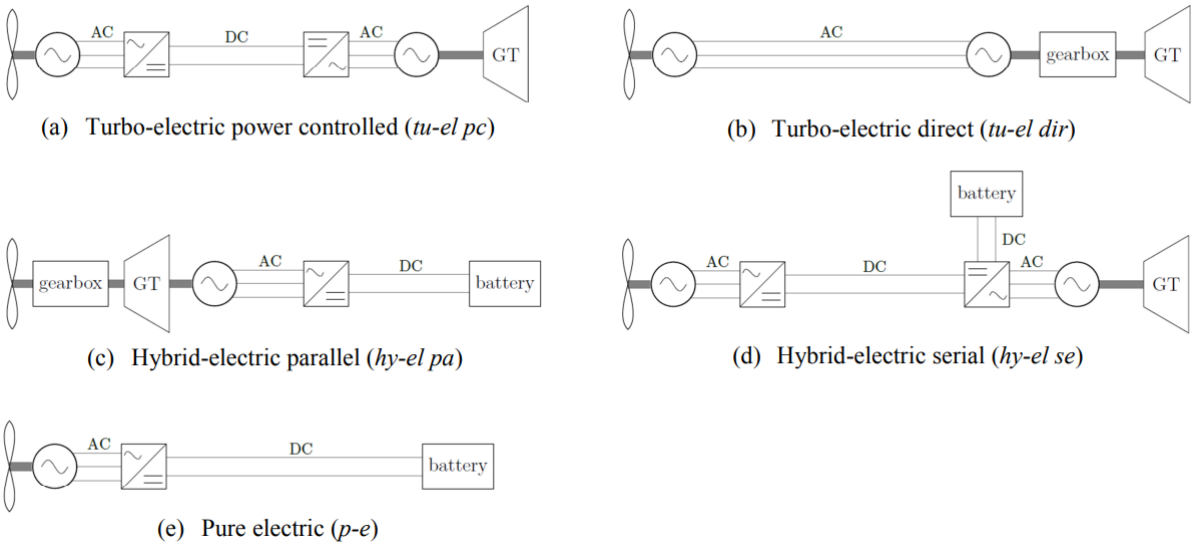

Figure 1.4: Turbo-electric and hybrid-electric propulsion architecture analyzed by [18] on a ATR72 aircraft.

In [19], the analysis of three case studies of a 2035 turboprop regional aircraft using parallel, series/parallel and distributed series configurations also show that the improvements

in terms of fuel consumption and emissions with respect to a reference ATR72 aircraft on an 800 NM mission are around 5% with a very optimistic value of battery specific energy of 500 Wh/kg at the cell level. The parallel hybrid configuration is identified as the most efficient among the three architectures considered, and it is outperformed by the series/parallel and distributed series configurations only in a really optimistic scenario where batteries reach 750 Wh/kg which ensures overall better performance despite their higher weight. In 2018 Jerome Thauvin [13] addressed the same research topic of this thesis by exploring the design space for a hybrid-electric regional aircraft. He evaluated the energy savings enabled by electric power generated by batteries in the case of a 70-seat regional aircraft, exploring not only different hybrid architectures of the propulsive system, but also different air-frame designs (varying the wing and tail geometries, the number of propellers, etc.) as shown in Fig. 1.5. The results of his research proved the parallel hybrid electric configuration to be the most promising in terms of reduction of fuel consumption, with expected fuel benefits between -5% and -14% according to the battery recharge strategy employed.

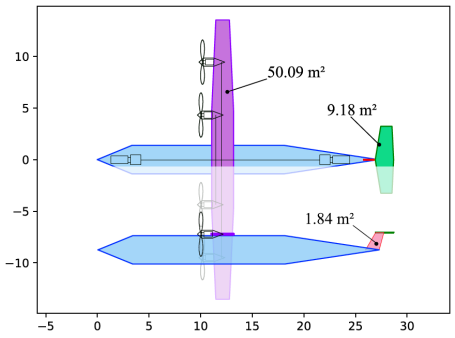

(a) Turbo-electric TE4: two turboshaft engines installed at each extremity of the fuselage powering 4 propellers.

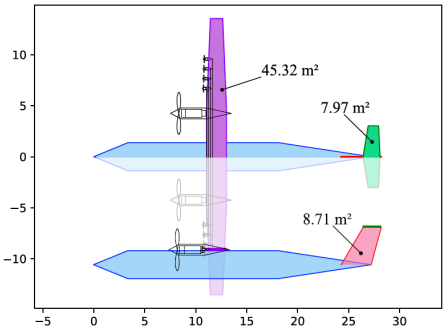

(b) Partial turbo-electric PT8: two wing-mounted turboprop units with generators to power 6 high lift propellers.

Figure 1.5: Two examples of the hybrid aircraft configurations designed by Thauvin [13] for a 70-seat regional aircraft.

Similar studies on a regional turboprop ATR-like aircraft have been conducted in the past years by [20, 21]. Although the assumptions regarding components technological levels as well as top-level aircraft requirements (TLARs) (e.g. mission range, speeds etc.) differ also significantly from one study to another leading to sometimes dissimilar results, a common agreement is about the conclusion that if battery technology does not improve dramatically, only small percentages of fuel reduction (less than 15%) may be achieved with the implementation of hybrid-electric propulsion. Nevertheless, such configuration will still be studied in this thesis in order to provide an assessment of its potential benefits with a forward-fit design approach. Indeed, except for [18], all the studies used a different design approach than the one proposed in this thesis, consisting in an overall optimiza-

tion or re-design of the existing ATR72 platform, which includes design variables such as wing surface and MTOW. Moreover, none of those studies explored the possibility of using hydrogen fuel cells instead of batteries as the main electrical power source in the parallel hybrid electric architecture. Therefore, an analysis of hydrogen-powered aircraft is still needed to provide a comprehensive assessment of the potential of hybrid electric regional aircraft.

Due to the hydrogen low heating value (LHV) being almost three times higher than jet fuel and efficiency which is roughly double that of gas turbines, fuel cells can be seen as key enablers for the next generation of hybrid electric regional aircraft to effectively reduce emissions. A comprehensive study about hydrogen-powered aviation, procured by Clean Sky 2 JU and FCH 2 JU and financially supported under the H2020 Framework Programme, was prepared by McKinsey & Company [22]. The aforementioned document addresses the technological, economic and environmental impacts of hydrogen propulsion providing a detailed assessment of its potential to reduce aviation's climate impact. By analyzing the different aircraft segments (from general aviation to long-range aircraft), projecting technological developments of hydrogen combustion as well as fuel-cell powered propulsion, and considering implications on aircraft design, airport infrastructure, and hydrogen supply chains, it gives insights into the main challenges and benefits of hydrogen-powered aircraft. The study concludes that H_2 propulsion could significantly reduce climate impact (-75% to -90% CO_2 emissions with fuel-cell propulsion compared to about -30% to -60% with synthetic fuels) and that the technological advancements needed to overcome the main technological challenges are achievable within five to ten years. In particular, the study identifies fuel cell-powered propulsion as the most energy-efficient, climate-friendly, and economic option for a regional aircraft with a capacity of 80 passengers, foreseeing CO_2 reductions up to 100% with 5% to 15% of additional costs (per seat kilometer) and a maximum take-off weight increase of around 10%. However, these numbers are not the result of a detailed performance evaluation of a specific concept design, but they represent rather the potential results of the "most promising" design based on expert discussions, high-level calculations and a survey of academic literature.

Despite the common belief that hydrogen fuel cells could significantly reduce aviation environmental footprint, to the best of the authors' knowledge, the literature seems to lack of studies about hybrid electric configurations using fuel cells instead of batteries for electrical power generation. Among the few hybrid/full electric aircraft concepts and studies comprising hydrogen fuel cells found in the literature, the most relevant ones are introduced hereafter. ENFICA-FC [23], funded by European Commission, is a project which served to demonstrate through flight tests the feasibility of a full electric 2-seat aircraft based on a hydrogen fuel cell power system. HY4 aircraft [24], developed by DLR and manufactured by Pipistrel, is a fuel cell-powered 4-seat passenger aircraft that can

be used as electric air taxis. ZeroAvia HyFlier [25] is a zero-emission 6-seat airplane that provides a proof-of-concept platform that the company intends to grow into the 15-20 seat platform aimed at the regional airline market (up to 500 NM). All those concepts however belong to the aircraft category certified according to the CS-23, thus with a much smaller capacity than the ATR72 which is the reference for the aircraft category under study.

1.2 Survey of technology enablers

A comprehensive analysis of both batteries and hydrogen as alternative power sources to jet fuel has been conducted in order to get an insight into these technologies and to assess their performance in terms of energy content and CO_2 emissions. A review of the different types of batteries as well as various ways of producing and storing hydrogen is also provided in this section.

1.2.1 Battery

A battery is a device consisting of one or more electrochemical cells capable of generating electrical energy from chemical reactions (battery discharge) and vice-versa (battery charge). They can be classified into primary (disposable) batteries which can only be used once till full discharge and secondary or rechargeable batteries which can be discharged and recharged multiple times. The number of charges and discharge cycles a battery is able to perform depends mainly on the battery chemistry. Secondary batteries are clearly more suitable for the envisioned application, therefore a specific review of this type of battery is provided next.

In a battery system, several cells are connected in series and/or in parallel to increase the electrical power generated. A generic battery cell is composed of a positive electrode (cathode) which is paired with a negative electrode (anode) and an electrolyte to separate the electrodes and enable the motion of ions from one electrode to another. The electrodes are connected through an external circuit, which, if closed, allows the transfer of electrons from the anode to the cathode (reduction reaction at the cathode), while the ions move in the opposite direction through the electrolyte (oxidation reaction at the anode). When global electroneutrality is reached, the battery is fully discharged. By applying electric current, the chemical reactions that occur during discharge are reversed and the battery (re)charges (see Fig. 1.6).
Rechargeable batteries come in different sizes and shapes (see Fig. 1.7) and they can be made with all sorts of different chemical electrolytes and electrodes. The main figures of merit to describe battery performances are:

– Specific energy, E_{sp} $[Wh/kg]$

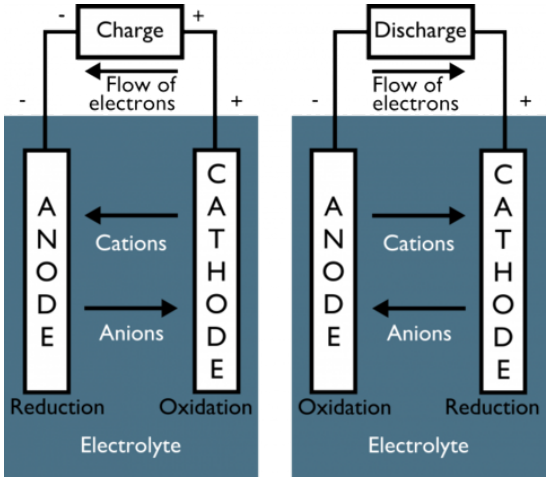

Figure 1.6: Battery charge and discharge process [26].

- Specific power, P_{sp} $[W/kg]$
- Energy density, ρ_E $[Wh/l]$
- Cyclability

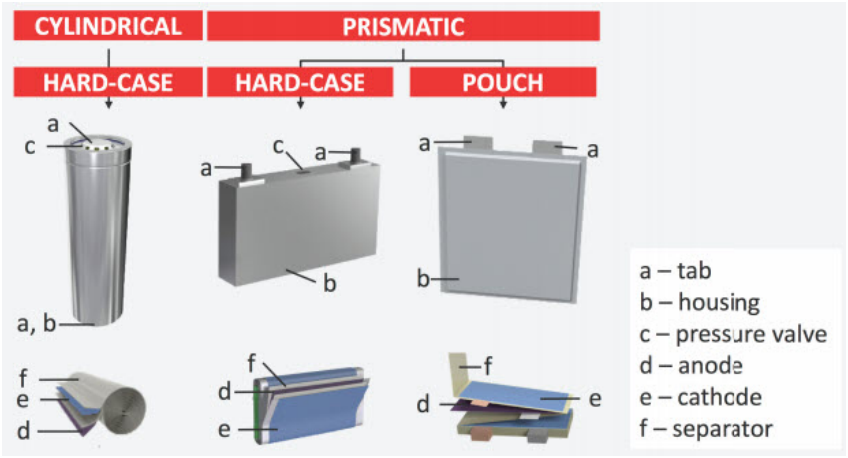

Figure 1.7: Shapes of battery cells [27].

Figure 1.8 shows a comparison of specific energy and power for different batteries. The values refer to battery cell performance, therefore do not take into account the mass of all the additional components of a battery pack (e.g. housing, electrical connections, etc.). An integration factor of 1.35 is commonly used as reference [28] to estimate the specific energy and power of the battery pack.

Battery chemistry

Among the battery technologies available to date, only lithium-based batteries (LiB) may satisfy the power and energy requirements necessary for hybrid electric propulsion

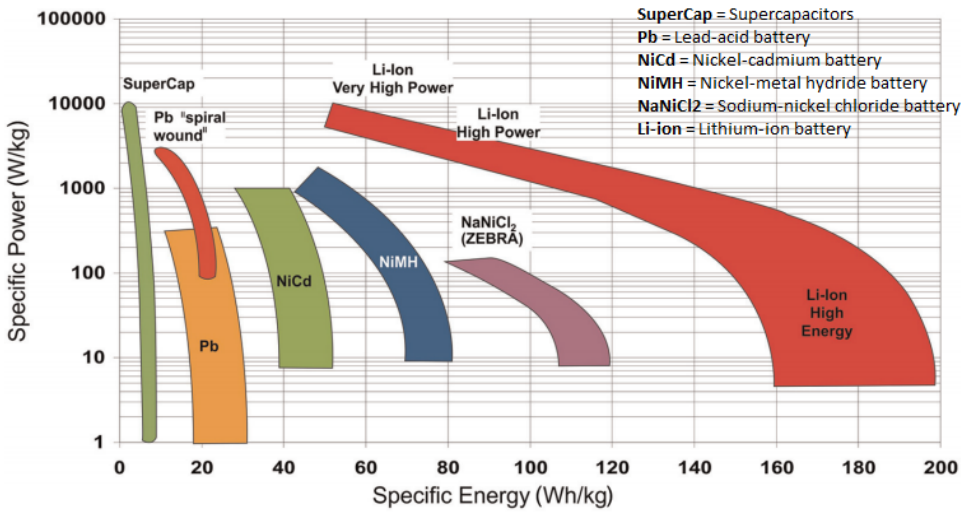

Figure 1.8: Ragone plot of various current battery technologies [29].

applications. Of all available metals for battery chemistry, lithium has the highest electrochemical potential and energy-to-weight ratio, which makes lithium-based batteries a good candidate for high-energy storage for hybrid (electric) propulsion.

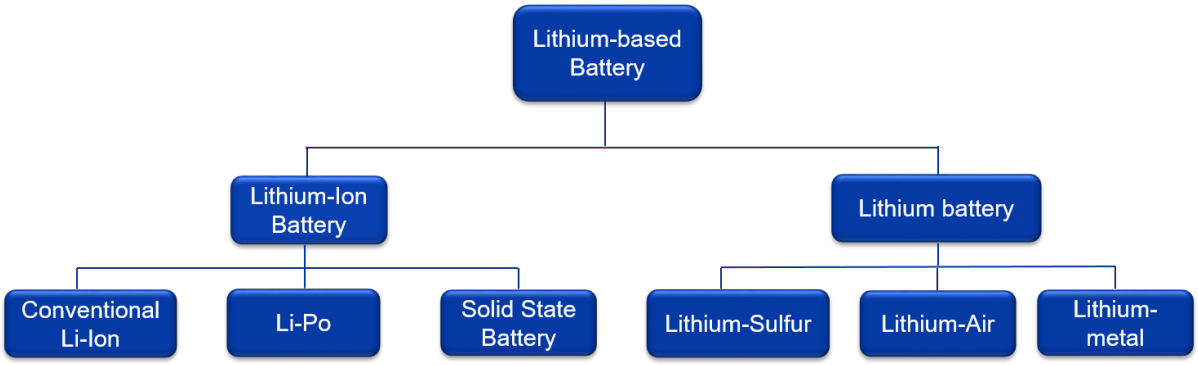

Figure 1.9: Lithium-based batteries classification.

Lithium-based batteries can be classified into lithium batteries and lithium-ion batteries (see Fig. 1.9). The main difference is that only the former type actually uses lithium metal as electrode material (anode), showing extremely high values of theoretical specific energy (up to 11680 Wh/kg for lithium-air [30]). However, lithium metal is highly reactive, which poses important challenges to managing safety risks. Growth of lithium dendrites, shown in Fig. 1.10, is a common issue in this kind of battery causing short circuits, therefore fire hazards. This is only one of the many obstacles to overcome for the commercialization of this breakthrough but still very immature battery technology [31].
To work around this issue, in lithium-ion batteries, lithium metal is replaced with "intercalating" compounds capable of accommodating lithium ions in their structure combined with an "intercalating" cathode that donates lithium ions. Li-ion battery is a mature technology and most of its potential is exploited, leaving little room for improvements.

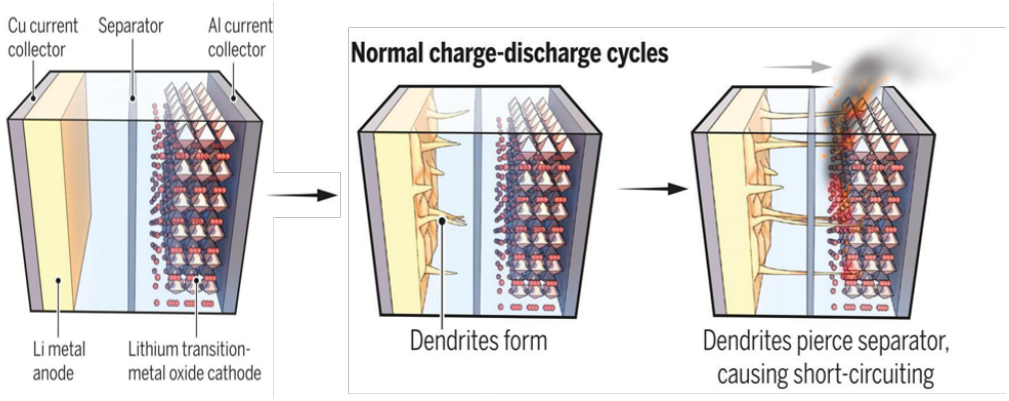

Figure 1.10: Growth of dendrites during charge-discharge cycles in lithium batteries. Modified from [32]

However, their performances are much lower than lithium batteries and they are mainly determined by the choice of the electrodes and the electrolyte. Current commercial batteries are named after the cathode, as this is the main determinant of cell properties. Regarding the anode, the current dominant intercalation material is graphite (C_6), although other options are TO (titanate - TiO_2), LTO (lithium titanate, $Li_4Ti_5O_12$) or lithium alloys such as $Li - Sn$. Table 1.1 summarizes the main Li-ion batteries and their characteristics are shown in Figs. 1.11 and 1.12 .

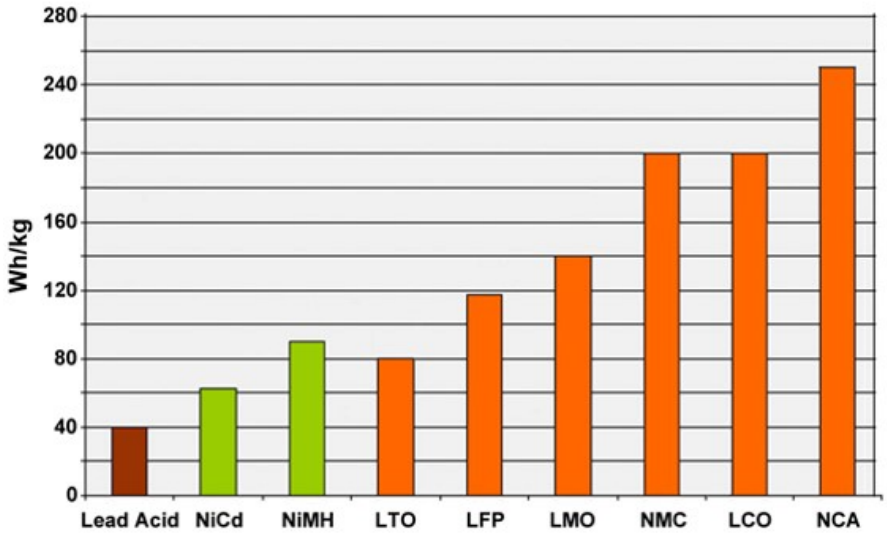

Figure 1.11: Typical specific energy at the cell level of li-ion batteries compared to lead acid and nickel-based (in green) batteries. Figure from batteryuniversity.com.

Li-ion batteries can also be categorized according to the type of electrolyte they are composed of. Conventional li-ion batteries are composed of a liquid electrolyte formed by lithium salts and an organic solvent. Common lithium salts include $LiPF_6$, $LiClO_4$ and $LiAsF_6$. The electrolyte can be a polymer (Li-Po batteries) or a solid material (Solid-State Li ion battery) which both offer slightly higher specific energy and can result in

Li-ion battery	Cathode material	Application
LCO	$LiCoO_2$	Portable electronics, B787 startup/backup power
LMO	$LiMn_2O_4$	e-bikes, medical devices
NCA	$LiNiCoAlO_2$	Electric vehicles (Tesla)
NMC	$LiNiMnCoO_2$	Electric vehicles (Toyota, Volkswagen, etc)
LFP	$LiFePO_4$	e-bikes, power supply systems

Table 1.1: Li-ion batteries.

Figure 1.12: Main characteristics of commercial Li-ion batteries [33].

thinner batteries than conventional Li-ion, at the price of higher manufacturing cost.

Although Li-ion battery is nowadays a mature technology, widely used and commercialized for many applications from medical devices to electrical vehicles, it is not completely exempt from safety issues. Potential hazards include toxic gas release, corrosive electrolyte release and fire. Risks of fire ignition are related to the so-called "thermal runaway": due to external fire, shocks or manufacturing defects in the electrode design, a cell may achieve elevated temperatures which would trigger a chain of exothermic reactions leading to a further temperature increase and therefore fire. However, safety is ensured by a combination of prevention, mitigation and protection systems which depend on the type of application and therefore the corresponding certification requirements. Regarding the certification specifications for large airplanes (CS-25), there is still a lack of standards and acceptable means of compliance to provide the safety requirements for the implementation of lithium-ion battery as a propulsive power source for aircraft.

Battery emissions

The use of batteries to generate propulsive power through electricity does not produce any on-flight emissions. However, battery manufacturing is an highly energy-demanding

process that produces greenhouse gas emissions. Many studies have been done to evaluate the environmental impact of battery production, however, sometimes the results differ significantly. Based on a review of available life-cycle assessments (LCA) on lithium-ion batteries performed by Romare et al. [34], a likely value of greenhouse gas emissions ($kgCO_{2eq}/kWh$) for battery production has been identified. This value will be used for the assessment of the emissions of a hybrid electric aircraft using batteries as a secondary power source.

The CO_2 equivalence (CO_{2eq}) is a measure of the global warming impact of $GHGs$ gases which uses the global warming potential (GWP) of CO_2 as reference. The carbon dioxide equivalency for a gas is obtained by multiplying the mass and the GWP of the gas. Table 1.2 gives the equivalence for the main $GHGs$ gases.

Greenhouse gas	$kg\ CO_{2eq}$**/kg**
CO_2	1
Methane (CH_4)	25
Nitrous oxide (N_2O)	298

Table 1.2: Global warming potential for 100 years time horizon relative to CO_2 [35].

Battery production can be divided in 3 stages:

- Stage 1: Raw material mining and refining
- Stage 2: Material processing (electrodes, electrolyte, etc.)
- Stage 3: Manufacturing and assembly (from components to full battery)

Based on the data provided by different studies [36, 37, 38, 39, 40], Romare et al. [34] concluded that the stages 2 and 3 are responsible for the greatest environmental impact (more than 80%) due to the large amount of electricity needed. However, large discrepancy arises regarding the total value of $GHGs$ emissions given from the different studies. This is mainly due to the different assumptions and calculation methods of the electric energy required for manufacturing, but also due to the different cell designs and relative amount of cells and support material considered in each study. Moreover, the emissions from the electricity vary a lot between countries, therefore another important assumption is the production location with the corresponding electricity mix.

Figure 1.13 shows the impact of different electricity mixes world-wide on the battery production emissions. In order to give an idea of the importance of this last assumption, the data and the assumptions of the work of Ellingsen et al. [36] are used. By varying only the value of the electricity mix, the emissions due to battery manufacturing are obtained for different countries. A reference total value of 172 $kgCO_{2eq}/kWh$ for battery production was used as calculated by [36]. Assuming that 586 MJ of electricity is needed

for each kWh of battery, they calculated that 107 $kgCO_{2eq}/kWh$ of these emissions were coming from manufacturing and only 65 $kgCO_{2eq}/kWh$ from the remaining stages.

Electricity mix	g CO_2-eq/ kWh el	kg CO_2-eq/kWh battery from electricity	% of Ellingsen manufacturing	% of Ellingsen total*
Sweden	50	7	7%	42%
Brazil	300	46	43%	65%
Ellingsen ref		107	100%	100%
USA	700	112	105%	103%
China	1000	159	149%	130%
Poland	1050	169	159%	136%
India	1400	226	212%	170%

Figure 1.13: Electricity mix impact on battery manufacturing and total battery production emissions [34].

The results in Fig. 1.13 show that even with the same assumptions about cell design, cell components, the energy required and manufacturing processes, the total greenhouse gas emissions may vary between 72 and 291 $kgCO_{2eq}/kWh$. Those values are obtained by adding the 65 $kgCO_{2eq}/kWh$ produced during stages 1 and 2 to the lower and higher values of Fig. 1.13 produced during stage 3. However, according to [34] a range of 150-200 $kgCO_{2eq}/kWh$ may be considered as the most likely impact. Therefore, the upper bound of this interval was used for the evaluation of the emissions related to the battery production process.

An additional consideration to take into account for the evaluation of battery-related emissions is that batteries are only an energy vector and have limited life, therefore their end-of-life treatment is an additional life cycle stage to be considered. After a certain amount of charge and discharge cycles, the electrode material degradation significantly affects battery performance, making them unsuitable for applications demanding high-performance standards (e.g. electric vehicles). When less than 80% of the initial capacity remains, the batteries are no longer good enough to be used in vehicles and can be either recycled or reused in a less demanding application.

Recycling of batteries is encouraged by the elevated costs of certain electrode materials, and it probably represents the only solution to face supply risks of some materials used for their production. However, in most cases, recycling represents an added greenhouse gas burden to the life cycle, since, with the conventional recycling process (pyrometallurgy), materials are extracted in their elemental form and therefore need to be re-processed for

batteries [34]. Basically, producing a battery using recycled materials would only result in skipping the first stage of the production process (mining and refining), which, as already anticipated, is a minor contributor to $GHGs$ emissions. Moreover, since incineration with pyrometallurgy is also responsible for $GHGs$ emissions, recycling does not change the results for the life-cycle assessment of greenhouse gas emissions of the battery.

Prolonging battery life by reuse may be the only way to improve the life cycle environmental impact of the batteries. When batteries no longer meet electric vehicle performance standards, they could be used as stationary energy-storage devices such as renewable energy grid storage and backup power systems. However, as of today, there is no established business of second-life batteries. Moreover, it would be very difficult to quantify the actual reduction of environmental impact due to battery reuse. Therefore, for this study, the value of 200 $kgCO_{2eq}/kWh$, found for battery production, is used for the evaluation of the emissions of the battery-based hybrid aircraft configuration.

1.2.2 Hydrogen

With a low heating value (LHV) almost three times higher than jet fuel, despite its low energy density (see Table 1.3), hydrogen seems to be a reasonable candidate to replace carbon-based fuels. The minimum ignition energy of hydrogen in air is not a real safety issue, because even a weak ignition source that is present in almost every accident releases enough energy to cause ignition also for a kerosene-air mixture [41].

Fuel	**Low heating value** (Wh/kg)	**Energy density** (Wh/l)	**Minimum ignition energy** (mJ)
Kerosene	11889	9167	0.24
CNG 250bar	14888	2500	0.33
L-H_2	33330	2358	0.02
C-H_2 700 bar	33330	1400	0.02

Table 1.3: Main properties of some alternative fuels for aviation.

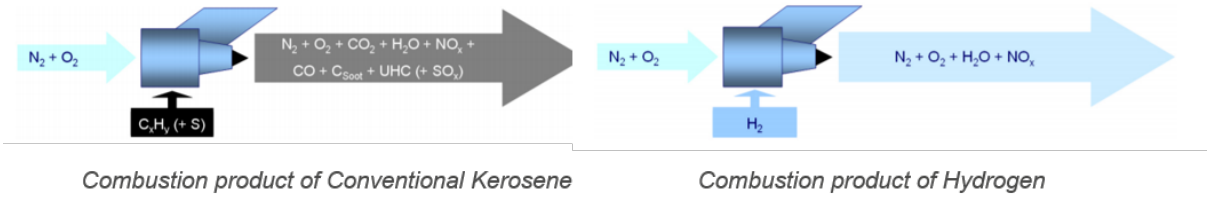

Figure 1.14: Combustion products of kerosene and hydrogen combustion [42].

Hydrogen can either be used with oxygen or another oxidizing agent to react in a fuel cell

and produce electricity or injected directly into a modified internal combustion engine (ICE) and produce thermal power. Modifying a conventional gas turbine engine to run on both kerosene and hydrogen is possible but requires some modifications, especially regarding sealing and structural reinforcements. The main advantage of burning hydrogen in the gas turbine instead of kerosene is related to its low pollutant emissions. Combustion products of hydrogen only include water vapor (H_2O) and oxides of nitrogen (NO_x). Emissions of NO_x depend on the air/hydrogen ratio: higher hydrogen concentration gives higher power, but also higher NO_x production. Figure 1.15 shows a typical NO_x emission trend of hydrogen combustion as a function of relative air/fuel ratio (λ) defined by:

$$AFR = (\frac{m_{air}}{m_{fuel}}) \tag{1.1}$$

$$AFR_{st} = (\frac{m_{air}}{m_{H2}})_{st} \tag{1.2}$$

$$\lambda = \frac{AFR}{AFR_{st}} \tag{1.3}$$

where:

- $\lambda = 1$, the air/fuel mixture is at the stoichiometric value (both the reactants are completely used within the combustion)
- $\lambda > 1$, lean combustion (not all the oxygen is used in the combustion)
- $\lambda < 1$, rich combustion (not all the hydrogen is used in the combustion)

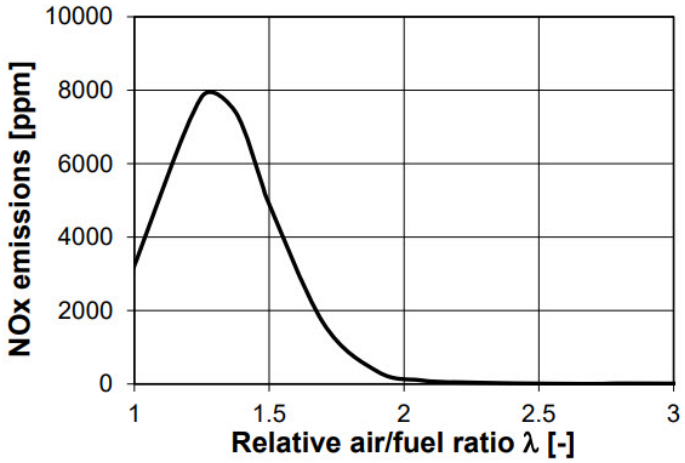

Figure 1.15: NO_x emission as function of relative air/fuel ratio [43].

At high relative air/fuel ratio ($\lambda > 2$) the combustion of hydrogen generates nearly zero NO_x emissions. However, since the density of hydrogen is much lower than the one of kerosene, the output power can be as low as half of that generated by kerosene combustion for the same engine size [44]. Decreasing the air/fuel ratio to values closer to the stoichiometric ratio would result in an increase of the output power, but also in a

dramatic increase of the combustion temperature, which would be responsible for NO_x emissions comparable to or even higher than NO_x emissions due to jet fuel combustion. Moreover, the efficiency of a gas turbine is a function of the combustion temperature (higher temperature gives higher efficiency), which, however, is limited by the material technology and the cooling capacity of turbine blades. Low efficiency implies elevated quantities of needed hydrogen, which, due to its low volumetric energy density, results in high volumes of hydrogen tanks to carry on board. This is one of the main challenges in the development of hydrogen-powered aircraft.

Hydrogen fuel cells have therefore received a lot of attention during the past decade due to the need for a power source that combines zero pollutant emissions and has high energy efficiency. It only emits water vapor and heat, with efficiency about twice that of gas turbines. Fuel cells also exhibit higher part-load efficiency, which is opposed to gas turbines which have peak efficiency at design conditions and show a rapid decrease at part-load. Moreover, fuel cells do not display a sharp drop in efficiency as the power-plant size decreases. In fact, the thermodynamic efficiency of gas turbines tends to decrease - power specific fuel consumption (PSFC) increases - as the engine size decreases (see Fig. 1.16).

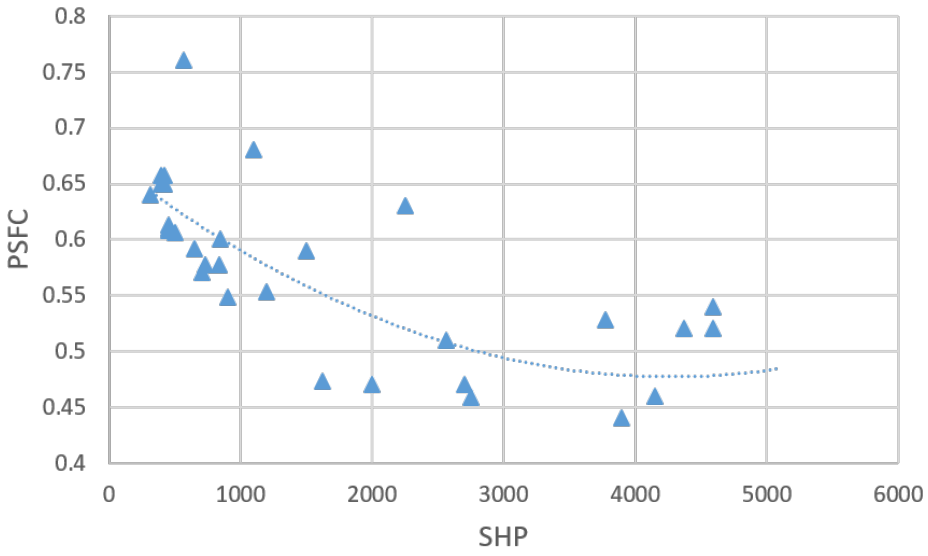

Figure 1.16: General trend of power specific fuel consumption (PSFC) as a function of engine shaft horsepower (SHP). Data from jet-engine.net

This is related to the inherent degradation of component efficiencies associated with the decrease in size. The degradation is caused by:

- Tip clearance losses for compressor
- Friction and heat losses

Compressor tip clearance cannot be scaled down as the engines get smaller, therefore the

relative impact these losses have on the engine efficiency is greater for smaller engines. Friction and heat losses are proportional to the surface area while combustion energy is proportional to the volume of the combustion chamber. For a cylindrical shape, the lower the radius the higher the area/volume ratio, and the higher the relative impact of these losses on the engine efficiency.

Fuel cell technology seems therefore a potentially ideal candidate for the generation of electrical power from hydrogen. In order to get more insight into this technology and to identify the main drawbacks and challenges, a more in-depth analysis of the working principle of this technology has been carried out and is presented hereafter.

Fuel cell

The fundamental working principle of a hydrogen fuel cell is the reverse of the electrolysis of water: hydrogen fuel is combined with oxygen to produce electricity, heat and water. A typical fuel cell consists of a negatively charged electrode (anode) and a positively charged electrode (cathode) separated by an electrolyte. Hydrogen is oxidized on the anode and oxygen is reduced on the cathode. The electrolyte is an ion conductor that, depending on the fuel cell type, moves ions either from the anode to the cathode or vice-versa, while the electrons are carried to the cathode over the external circuit to power the load.

Anode:	H_2	$\rightarrow 2H^+ + 2e^-$
Cathode:	$\frac{1}{2}O_2 + 2H^+ + 2e^-$	$\rightarrow H_2O$
Overall:	$H_2 + \frac{1}{2}O_2$	$\rightarrow H_2O$ + electric energy + waste heat

Similarly to batteries, the power obtainable from a single fuel cell is rather low since the maximum theoretical voltage is 1.223 volts, therefore multiple cells are stacked to achieve higher voltage and power.

Two main fuel cell types are under consideration for aircraft applications (see Fig. 1.17): PEMFC (Proton Exchange Membrane Fuel Cell) and SOFC (Solid Oxide Fuel Cell). The main design features which differentiate these two fuel cell types are:

- Type of electrolyte
- Electrodes catalyst material
- Operating temperature

PEMFCs work with a polymer electrolyte in the form of a thin, permeable sheet which allows the passage of positive hydrogen ions from the anode to the cathode. The operating temperature is between 80 and 200 $°C$ and a platinum catalyst is used to increase the rate of reaction at both the anode and cathode. SOFCs are characterized by the use of a solid oxide material for the electrolyte to conduct negative oxygen ions from the cathode

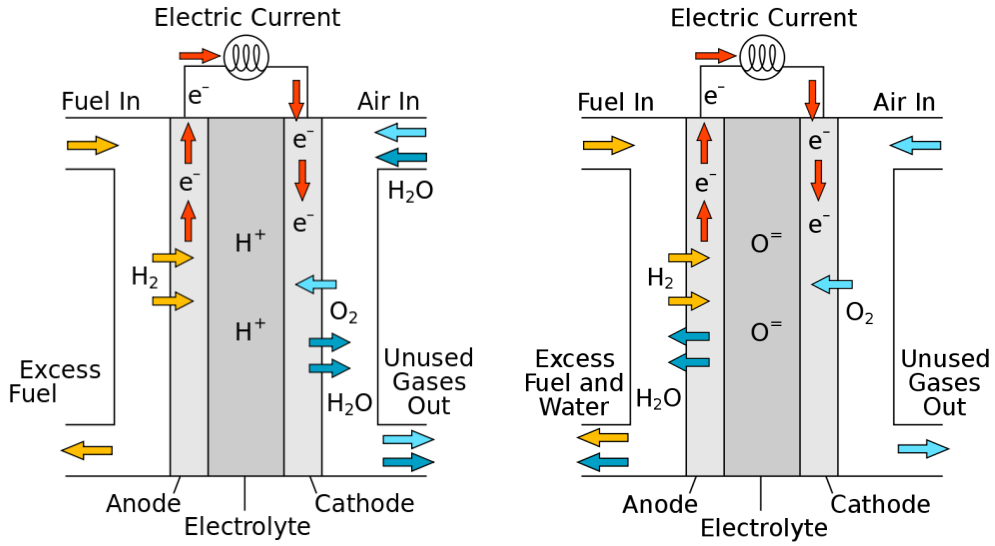

(a) PEMFC (b) SOFC

Figure 1.17: Schemes of a PEMFC (Proton Exchange Membrane Fuel Cell) and a SOFC (Solid Oxide Fuel Cell). Images from wikipedia.com.

to the anode. They operate at very high temperatures between 700 and 1000 $°C$, which provides an advantage compared to PEMFC by replacing the expensive platinum for catalyst material by nickel, therefore reducing costs. However, SOFCs present a number of disadvantages that make PEMFCs a more attractive option for on-board aircraft power generation:

- Long start-up time
- Short lifetime due to corrosion caused by high heat
- Low maturity level

PEMFCs are indeed used in most of the hybrid/full electric aircraft concepts [23, 24, 25]. For the sake of simplicity and for the different advantages of PEMFCs over SOFCs, only the former technology is investigated more in detail. Given the large range of operating temperature of PEMFCs, it is possible to distinguish between two types: low-temperature fuel cells ($LT\text{-}PEMFC$) operating at less than 100 $°C$ and high-temperature fuel cells ($LT\text{-}PEMFC$) with an operating temperature above 100 $°C$. $LT\text{-}PEMFC$ is a mature technology that is already used for automotive applications and recent hydrogen aircraft demonstrators. On the other side, $HT\text{-}PEMFC$ is still in the very early stages of development. While it still presents a number of issues to be solved such as fast degradation and increased start-up time, its advantages are multiple and considerable: high tolerance to hydrogen impurities, improved reaction rates and, most importantly, easier waste heat rejection due to the higher temperature difference between the fuel cell and the ambient environment [45]. Thermal management of the fuel cells is indeed one of the biggest challenges for the development of high-power fuel cell systems, which require a voluminous

and heavy cooling system to evacuate the waste heat and keep the fuel cell at its nominal operational temperature.

The heat generation in the fuel cell is associated with voltage losses and it is mostly created in the catalyst layers. There are three types of voltage losses occurring in the fuel cell:

- Activation losses
- Ohmic losses
- Concentration losses

These voltage losses are a function of the current density. The evolution of the net voltage against the current density is known as the polarization curve and it is an important indicator of the fuel cell performance. Figure 1.18 shows an example of typical polarization and power curves (respectively voltage and power as a function of current density). Activation losses are nonlinear with current and they occur due to the slow electrochemical reactions taking place on the surface of the electrodes. These losses are directly related to the energy barrier for oxidation and reduction at the electrodes. Ohmic losses are related to the transport of charge through the fuel cell. The two major types of charged particles are electrons and ions and they are both responsible for voltage losses. Finally, concentration losses are related to mass transport. These losses result from the change in concentration of the reactants at the surface of the electrodes as the fuel is used.

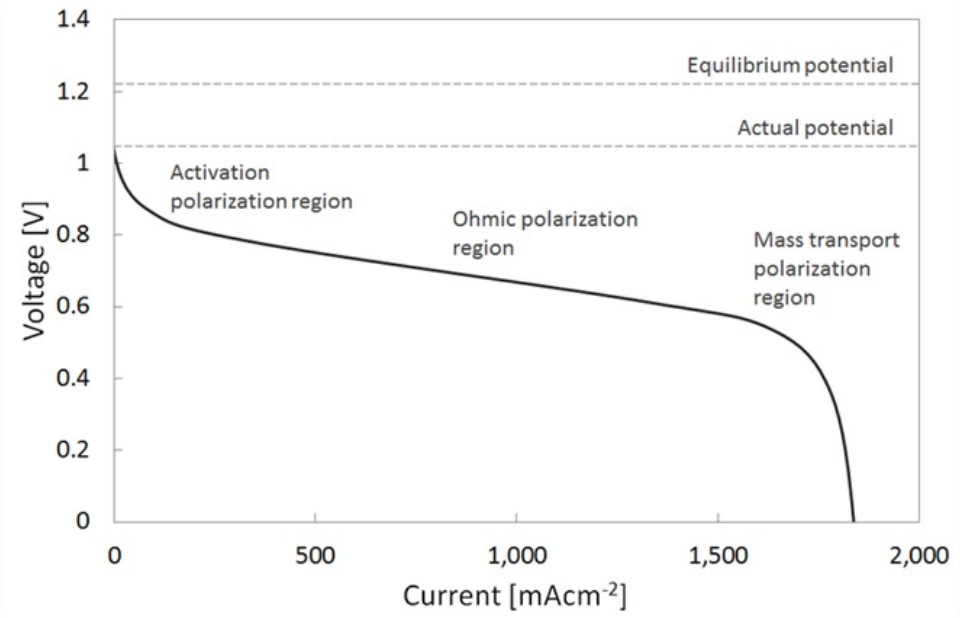

Figure 1.18: Example of polarization curve [46].

Due to such losses, fuel cell efficiency ranges between 40% and 60%, and unlike the gas turbine, it shows higher efficiency at part-load operation. The polarization curve gives

also the trend of the electrochemical efficiency η of the fuel cell with the operating current. Since η is proportional to the voltage, the lower the current, the higher the efficiency. Therefore, one strategy to improve the efficiency could be the oversizing of the fuel cell: designing a fuel cell with a nominal power that is lower than the maximum power it can actually deliver would result in lower currents and therefore higher efficiency. However, for aircraft design, another important parameter is the mass of the fuel cell. In fact, while oversizing the fuel cell determines an increase in efficiency, it also results in a heavier and bigger system: a trade-off between fuel cell size and efficiency is required for an optimal design.

The specific power of the fuel cell is actually one of the main drawbacks of this technology. In fact, even if the fuel cell stack has a state-of-the-art specific power of 3.5 kW/kg, which is equivalent to the one of a 2 MW class gas turbine engine, there are other components required for its operation. The set of all the required systems and components for the correct functioning of a fuel cell is usually referred to as the balance of plant (BoP) of the fuel cell. The fuel cell BoP includes:

- Fuel cell stack
- Fuel management system (e.g. pipes, heat exchanger, fans, etc.)
- Air and water management system (e.g. compressor, humidifier, pumps, etc.)

A simplified schematic of a balance of fuel cell power plant is given in Fig. 1.19.

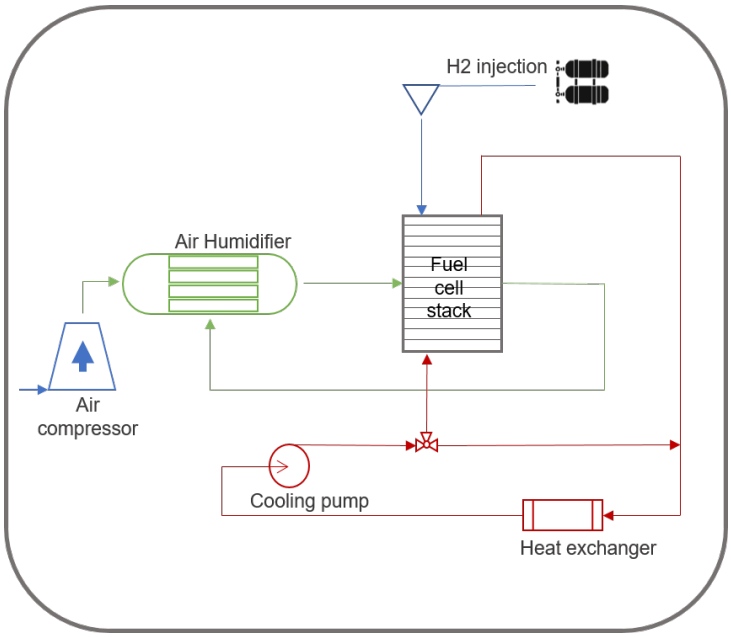

Figure 1.19: Balance of fuel cell power plant.

All these components not only increase the mass of the fuel cell but also use some of the output electrical power of the fuel cell to work. Therefore both the efficiency and the specific power of the fuel cell system decrease, thus posing big challenges for their

integration in an aircraft propulsive system. Different values of specific power for the fuel cell BoP have been found in literature, going from 0.6 kW/kg up to 2 kW/kg [47]. This large discrepancy is due to the diverse kind of applications as well as different fuel cell sizes, for which, the required BoP components may differ. Other important issues that engineers are facing to use fuel cells for aeronautical applications concern the decrease of oxygen partial pressure due to the operation at high altitudes, causing a general degradation of fuel cell performance. Moreover, system reliability, humidity management and hydrogen purity are additional technical challenges that are currently being addressed by researchers and engineers [48].

Hydrogen production pathways and related emissions

Hydrogen production is a big challenge when it comes to economical and environmental considerations. Natural hydrogen emissions from sedimentary basins have been documented in different parts of the world [49], but as of today only one area with large natural hydrogen accumulation has been discovered [50]. Therefore, in order to meet market and industry needs, hydrogen has to be extracted at the expense of energy. There exist different ways to produce hydrogen which needs different amounts of energy and emits varying quantities of $GHGs$. Figure 1.20 gives an overview of the different methods currently used to produce hydrogen. Steam methane reforming (SMR) represents 48% of worldwide hydrogen production. Widely used processes are also the coal gasification (18%) and the reforming of liquid hydrocarbons (30%), while hydrogen production from the electrolysis of water represents only 4% of H_2 production [51].

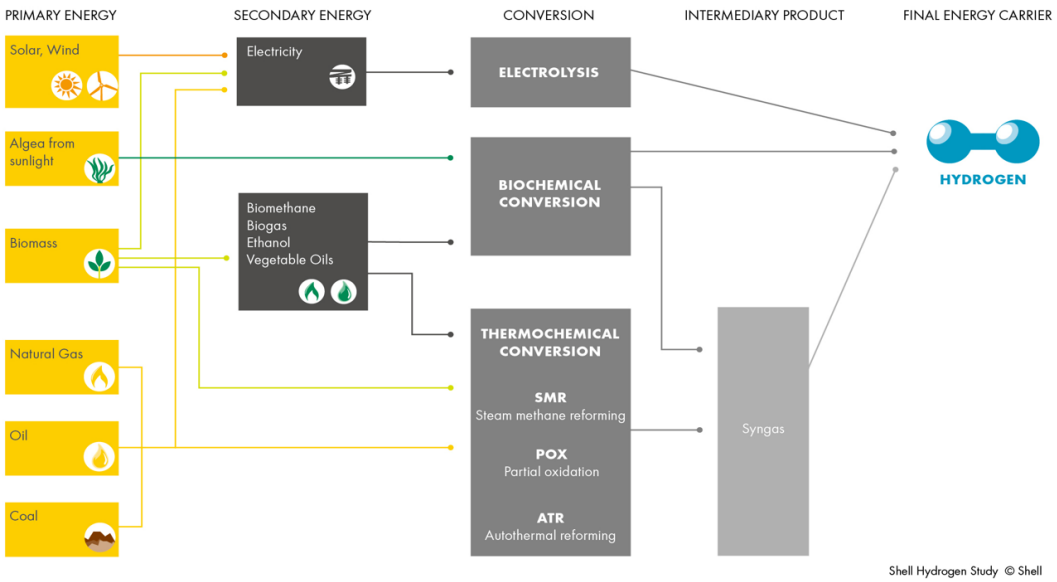

Figure 1.20: Hydrogen production pathways [52].

The objective of this paragraph is not to give an exhaustive description of the different processes, but to show and to understand the environmental impact of each method. For

that, a study performed by the JEC (JRC-Eucar-Concawe) collaboration [53] is used as the main reference. This work aims at describing the process of producing, transporting, manufacturing and distributing a number of fuels suitable for transport powertrains. It provides an evaluation of the energy consumed and the *GHGs* emissions for different production pathways, taking into account all the steps from extracting, capturing, or growing the primary energy carrier to refueling the vehicles with the finished fuel (see Fig. 1.21). The combination of steps necessary to turn a resource into fuel and bring this fuel to a vehicle is defined as "Well-to-Tank" pathway (WTT). Instead, the utilization of this fuel within the air-vehicle is referred to as "Tank-to-Wake" pathway (TTW).

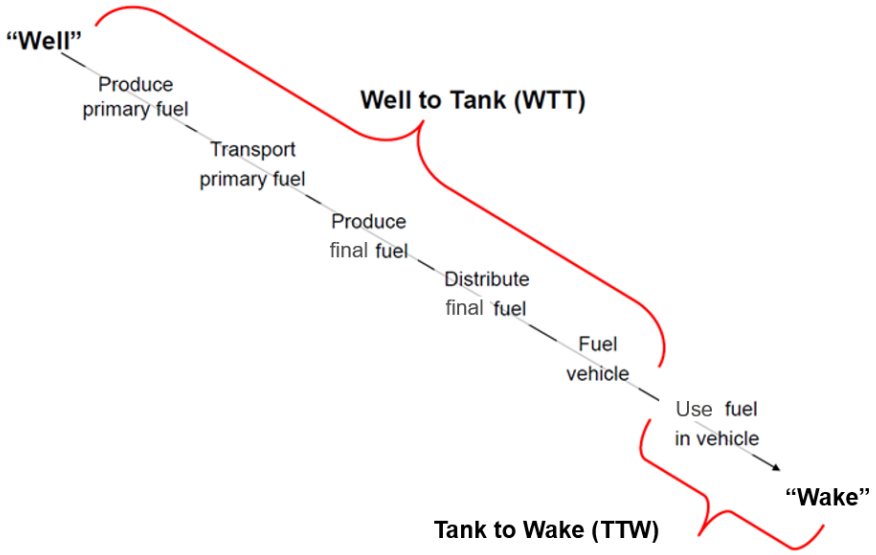

Figure 1.21: Well-to-Tank and Tank-to-Wake pathways. Modified from [53]

In [53], WTT emissions have been accurately calculated for different hydrogen pathways, each of them being identified by a code. The most representative pathways have been chosen for the main primary energy sources, such as natural gas, coal, biomass (waste wood), and wind. Figure 1.22 shows the energy expended and the WTT greenhouse gases emitted for the chosen pathways. Each pathway is briefly described in Table 1.4.
As can be seen in Fig. 1.22, due to the high energy-demanding process for producing hydrogen, related emissions can be as high as twice the ones coming from the entire kerosene cycle (from production to combustion). Only if green energy sources are used these emissions can actually be reduced, which is the case for biomass and wind. Moreover, it seems still possible to reduce *GHGs* emissions using steam methane reforming in combination with CO_2 capture and storage (CCS) process. CCS is the concept of isolating the CO_2 produced in combustion or conversion processes and injecting it into suitable geological formations. The process includes:

– Separation of CO_2 from other gases

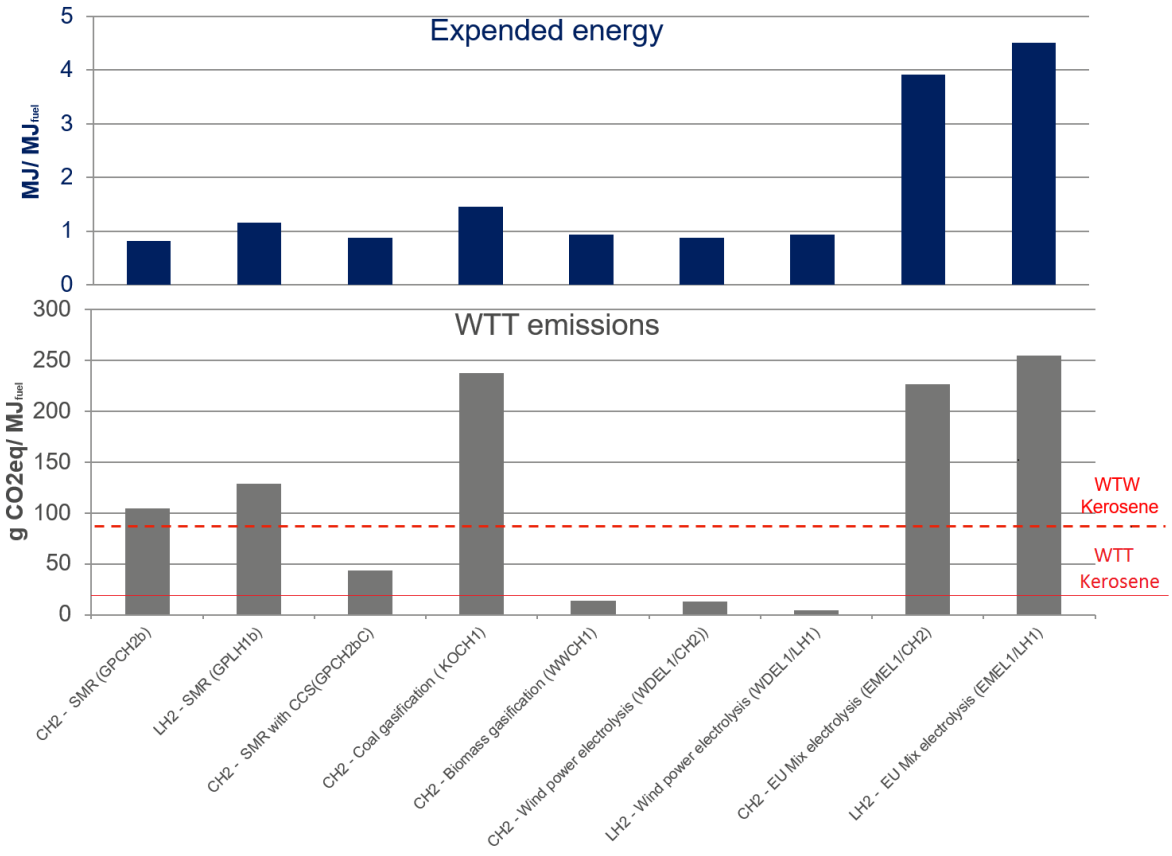

Figure 1.22: WTT *GHGs* emissions and energy expended of hydrogen pathways.

- Compression (15 MPa)
- Transport (by pipeline or ships) to the point of injection
- Injection under pressure.

However, CCS has so far only been applied on a limited scale in very few locations worldwide, therefore the presented figures should be regarded as very preliminary and indicative of the potential of the technology.

Hydrogen storage

On-board hydrogen storage is a relevant challenge considering that it has the lowest gas density of all known substances and it is among the elements with the lowest boiling point (see Fig. 1.23). Hydrogen density at standard temperature and pressure is 0.084 kg/m^3 whereas jet-A fuel density is about 800 kg/m^3. Therefore, in order to store gaseous hydrogen within an acceptable volume it is mandatory to compress it at high pressures. Standard pressure values widely used for compressed hydrogen storage are 350 bars and 700 bars. Increasing the pressure improves the energy density of the storage system, but it also increases the mass of the pressurized tanks, therefore affecting its specific energy. Compressed storage system performances in terms of mass and volume depend on the

Code	**Primary energy source**	**Final fuel**	**Description**
GPCH2b	Natural gas	C-H_2	Piped natural gas supply, transport to EU by pipeline (4000 km), distribution through high-pressure trunk lines, central large scale reformer, hydrogen pipeline, compression to 88 MPa at retail station.
GPLH1b	Natural gas	Cc-H_2	Piped natural gas supply, transport to EU by pipeline (4000 km), distribution through high-pressure trunk lines, central reforming, hydrogen liquefaction, liquid hydrogen road transport to the retail station, hydrogen cryo-compression into vehicle tank (35 MPa).
GPCH2bC	Natural gas	C-H_2	CO_2 Capture and Storage (CCS) option for GPCH2b.
KOCH1	Coal	C-H_2	EU-mix hard coal, hydrogen pipeline transport, hydrogen compression at a retail site.
WWCH1	Biomass	C-H_2	Waste wood, small scale gasifier in retail site, hydrogen compression to 88 MPa at a retail site.
WDEL1/CH2	Wind	C-H_2	Electricity from wind energy central electrolysis, hydrogen pipeline transport, hydrogen compression to 88 MPa.
WDEL1/LH1	Wind	Cc-H_2	Electricity from wind energy, central reforming, hydrogen liquefaction, liquid hydrogen road transport to the retail site, hydrogen cryo- compression into vehicle tank (35 MPa).
EMEL1/CH2	EU elec. mix	C-H_2	EU-mix electricity supply, central electrolysis with hydrogen pipeline transport, hydrogen compression to 88 MPa.
EMEL1/LH2	EU elec. mix	Cc-H_2	EU-mix electricity supply, central reforming, hydrogen liquefaction, liquid hydrogen road transport to a retail site, hydrogen cryo-compression into vehicle tank (35 MPa).

Table 1.4: Hydrogen pathways codes description [53].

compression pressure and on the tensile strength of the tank material. Composite tanks show good performances with best-in-class values of 1.7 kWh/kg and 0.8 kWh/l for an operating pressure of 700 bars [54]. These performances could be further improved using high-quality aviation composite materials (up to 2.5 kWh/kg according to [55]), with a dramatic increase in the price of the tanks which is already a weak spot of this technology. Liquid hydrogen has a density of around 70 kg/m^3 which is almost twice the density of compressed gaseous hydrogen at 700 bar. This liquid state is obtained by cooling the hydrogen at 22K at low pressure (1-5 bars). The main advantage is that there is no need for heavy tanks to provide high mechanical resistance since the internal pressure is low.

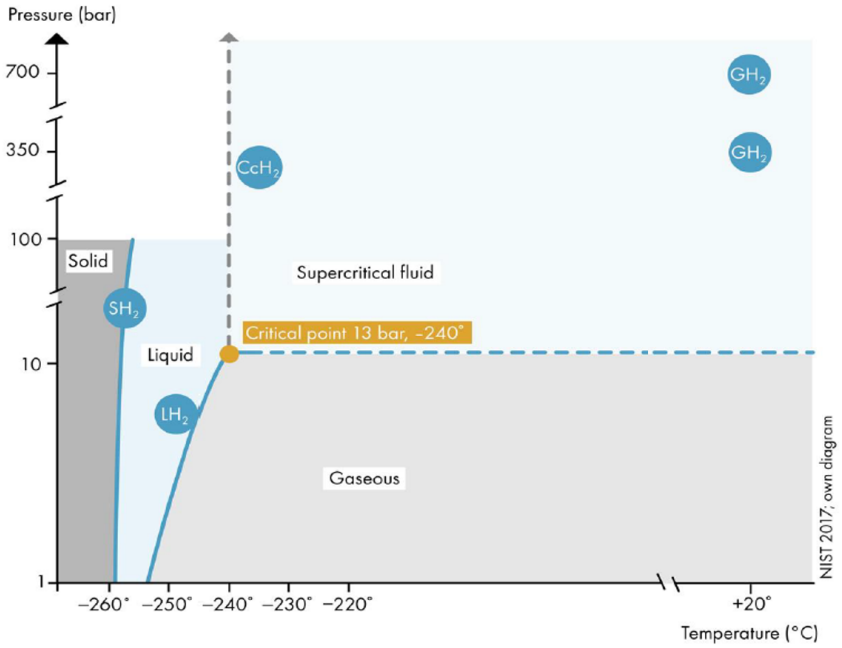

Figure 1.23: Hydrogen phase diagram.

However, the insulation material is needed to reduce heat inputs from the environment and therefore boil-off losses. Heat inputs from the environment warm up the hydrogen in the tank, which partially evaporates, increasing the internal pressure of the tank. In order to avoid over-pressures, the tank is designed with valves that allow the venting of the hydrogen gas when the internal pressure reaches a certain threshold value. The gaseous hydrogen released from the vessel is called "boil-off gas", therefore boil-off losses refer to the hydrogen energy lost to keep the cryogenic tank at constant pressure. Liquid hydrogen storage performances are shown in Fig. 1.24 as a function of the tank size (hydrogen payload).

The gravimetric index expresses the ratio between the mass of hydrogen and the total mass of the storage system (including hydrogen). Therefore, by multiplying this index by the hydrogen heating value, one obtains the specific energy (Wh/kg) of the storage system. According to [56], the specific energy of a system storing around 50 kg of liquid hydrogen is around 5300 Wh/kg, which is still approximately half of the specific energy of Jet-A1 fuel. Figure 1.24, however, shows how the gravimetric index of liquid hydrogen storage increases for larger tanks. This is confirmed also by the characteristics of the huge hydrogen tanks which equipped the Space Shuttle. With a total empty mass of 26500 kg, the external tank has a capacity of around 100 tons of liquid hydrogen, which translates into a gravimetric index of more than 80%.

However, due to the lack of data about existing liquid hydrogen tanks with a capacity between 50kg and 100 tons, it has not been possible to provide a state-of-the-art value for

the gravimetric index of liquid hydrogen tanks suitable for short-range regional aircraft. For such an application, the order of magnitude of hydrogen required is of few hundreds of kilos. Nevertheless, results of the structural and thermal analysis performed by different studies [57, 42] suggest that gravimetric indices between 30% and 60% may be applicable to tanks with a capacity to store between 100 and 300$kg$of hydrogen.

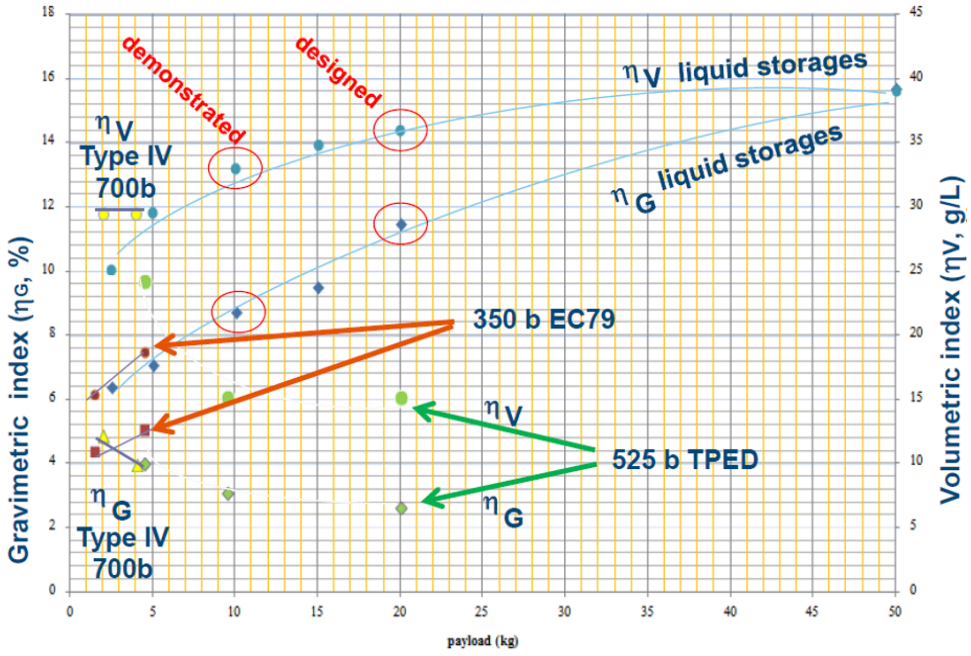

Figure 1.24: Hydrogen storage gravimetric and volumetric indexes [56].

For the sake of completeness, other non-traditional storage methods not suitable for on-board aircraft storage are shortly presented hereafter (see Fig. 1.25). Physical adsorption methods (physical storage) rely on the adsorption of the hydrogen molecule to high surface area materials. These are generally solid materials such as activated carbons, carbon nanotubes, zeolites, and material organic frameworks (MOFs). Currently, there are no known materials that contain adequate amounts of hydrogen at near ambient temperature and low pressures. A great deal of research is currently underway to improve the hydrogen storage densities in materials that demonstrate hydrogen physisorption. In chemical storage methods, hydrogen is bonded to other atoms within the material. A catalyst is generally required to break those metal-hydrogen bonds to allow the hydrogen molecule to form. The most critical issue regarding these methods is the hydrogenation of the spent fuel. This process needs to be performed off-board and depending on the material it may be complex, inefficient and/or expensive. Moreover, the on-board dehydrogenation of the fuel may pose other challenges: the need for high temperatures ($T > 300°C$ for LOHCs) and limited kinetics (low hydrogen production rates).

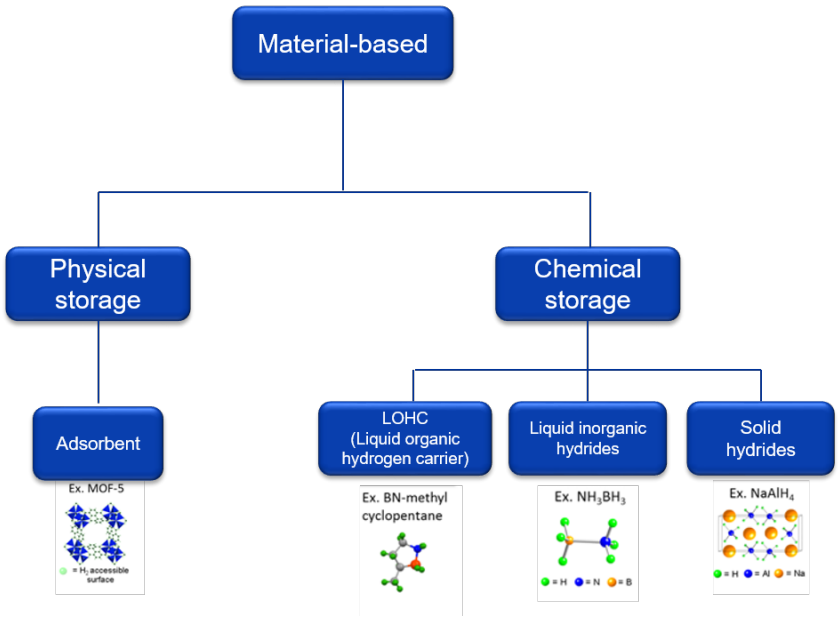

Figure 1.25: Material-based hydrogen storage methods.

1.2.3 Technology Survey

The main technological bricks which could be incorporated into the next-generation aircraft propulsion system are batteries, fuel cells, electric motors, generators and power electronics. Batteries and fuel cells have been widely discussed in the previous sections because they are considered the technology enablers which could allow the introduction of innovative systems such as hybrid/electric and hydrogen propulsion. While a comprehensive investigation of all the other components is out of the scope of this thesis, a technology survey to identify the main performance characteristics of such components in terms of mass and efficiency is hereby provided.

The electric motor, which converts electric power into mechanical power, can be fully characterized knowing only a few parameters such as power-to-weight ratio and efficiency. The generator does exactly the opposite of an electric motor, converting mechanical power into electric power. However, its characteristic parameters are assumed to be the same as those of the motor. Most often, motors and generators are indeed the same physical components that can work in both ways. It is the case for example for the 2.5 MW serial hybrid architecture of the E-Fan X developed by Rolls-Royce in collaboration with Airbus[1]. The electric motor and the generator of the E-Fan X are indeed the same component and this helps to reduce the complexity of the system as well as the maintenance costs. The main purpose of power electronics is to control and convert electrical power either by changing the voltage and the current. Similarly to the motor/generator, its

[1] flightglobal.com/E-FanX

performance parameters are efficiency and power-to-weight ratio.

The assumed state-of-the-art technological performance of these components are shown in the first column of Table 1.5. Assuming a reasonable development time, from initial design to flight tests and certification, for a short-haul commercial aircraft of 5 to 15 years, assumptions about the main technological evolution of components need to be done in order to properly estimate their performances. Some components may have steeper development curves than others, therefore design engineers have to take into account the projected state-of-the-art performance of the components at the expected entry into service date of the aircraft.

However, especially for novel technologies, for which little historical data exist, accurately forecasting their future performances may be a very challenging task. Table 1.5 summarizes the predicted technological levels of the main powertrain components. When possible, these values were taken from established technology road maps, otherwise, reasonable values according to some relevant studies from the literature were assumed.

	SoA 2020	**Projection 2025**	**Projection 2030+**
Fuel cell			
Specific power @BoP	0.5 kW/kg	1 kW/kg	1-2 kW/kg
Battery [58]			
Specific energy @cell	235 Wh/kg	350 Wh/kg	500 Wh/kg
Energy density @cell	630 Wh/l	750 Wh/l	1000 Wh/l
Life-cycle	1500	1500 cycles	2000 cycles
Electric motor/Generator [13] [59]			
Specific power	5 kW/kg	7 kW/kg	10 kW/kg
Peak efficiency	95%	97%	98.5%
Power electronics [13] [59]			
Specific power	7 kW/kg	11 kW/kg	15 kW/kg
Peak efficiency	95%	98%	99.5%

Table 1.5: Technology road map of the main technological bricks of the next generation aircraft propulsive system.

1.3 Conclusion of the chapter

- Most of the efforts of the aviation sector towards the development of greener aircraft concepts focus on disruptive aircraft configurations which will most likely enter into

service starting from 2035 on-wards.

- This thesis focuses on a forward-fit approach to aircraft design which is considered key for a rapid development and entry into service of a lower emissions aircraft in the short term.

- The key technology enablers that have been identified to reduce aircraft emissions in the short term are hybrid/electric and hydrogen propulsion systems.

- Several studies have been published concerning the potential of hybrid-electric aircraft concepts powered by batteries. However, the design approach consisted more of an overall re-design of the aircraft, rather than an assessment of the potential of the propulsion system on the existing aircraft platform.

- A lack of studies has been found concerning the assessment of hybrid-electric or full-electric aircraft powered by hydrogen fuel cells, particularly for the CS25 aircraft class.

- Although featuring zero on-flight emissions, both batteries and hydrogen are still responsible for pollutant emissions during their whole life cycle. The quantity of those emissions can be significant and is strongly affected by the production and manufacturing processes employed.

- Life-cycle emissions of both batteries and hydrogen must be taken into account to provide a reliable assessment of the true potential of those technologies to reduce aircraft-related emissions. Average emission indices have been identified in order to assess the life-cycle emissions of both technologies according to different production processes.

Chapter 2

Methods and tools for unconventional aircraft design

Contents

2.1 Overall Aircraft Design

Overall aircraft design is a multidisciplinary and simulation-based process with the objective to design an aircraft that meets the top-level aircraft requirements (TLARs) and which is optimized with respect to some criteria (e.g. costs, fuel consumption, etc). Typical requirements are:

- Passenger capacity
- Design and maximum range
- Cruise speed
- Take-off field length and approach speed
- Time to climb

OAD includes three main phases: conceptual design, preliminary design and detailed design. During the first phase of conceptual design, the main activity is the design space exploration of different overall aircraft concepts in order to select the most promising solutions and discard the configurations that are not feasible or not interesting. Due to the large number of potential configurations to be investigated, the tools employed to assess the performances of each aircraft configuration rely on empirical or simple analytical models which feature low computational time over high accuracy. The outcome of this phase is a selection of very few number of airplane configurations that will be further studied in the preliminary design phase. This second phase, not only deals with the whole aircraft system but also aims at defining all the required subsystems. In general, the process is very similar to the one of the conceptual phase, however, it uses more refined models (e.g. CFD, FEM, etc.) which are costly in terms of computational time and require the competencies of specialists from the various functional disciplines. Validation and verification of the airplane configuration performance are also performed through wind tunnel testing and structural testing before entering the detailed design phase. At the end of the preliminary phase, the identified optimal configuration is committed to production. Therefore, the objective of the detailed design phase is to conceive all the pieces and systems which will be actually built and installed on the aircraft. Once the geometry of all components is specified and their manufacturing processes are planned, the design phase officially ends. The following steps are manufacturing of components, final assembly, flight-testing and certification.

However, OAD is not only dedicated to completely new aircraft projects. It can be used when the evolution of an existing aircraft is at stake. It is the case for this thesis, where the objective is not to design a completely new regional aircraft but to improve the performance of an existing turboprop aircraft by means of innovative propulsion technology. This particular approach somehow involves tasks and processes from both conceptual and preliminary design phases. The baseline aircraft already exists, therefore plenty of

information and data are available. Nevertheless, the introduction of a completely new propulsion system raises challenges in the design of the aircraft inherent to its integration and installation on the existing platform. Changes in the propulsion system may affect both the aerodynamics and structural aspects of the aircraft, therefore multidisciplinary analysis and optimization techniques are still needed to handle all the possible interactions between the different disciplines.

For this thesis, a conceptual aircraft design platform named FAST-OAD has been used to develop the analysis processes and models for the design of a reference turboprop aircraft as well as for the forward-fit design of such aircraft with innovative low-emission propulsion systems. FAST-OAD is completely developed in python and is the evolution of FAST, a software program initially developed in 2015 by ONERA and ISAE-SUPAERO for aircraft design teaching purposes. It is based mostly on semi-empirical equations and models involving conventional OAD disciplines such as aircraft geometry, aerodynamics, structure/weight and propulsion as shown in Fig. 2.1 using an eXtended Design Structure Matrix (xDSM) diagram [60]. Under this format, each green box represents an analysis (e.g. a function for a rectangular or a group of functions for an octagonal box). The initial execution order of those functions is from the top left to the bottom right. Input variables relative to each analysis are placed vertically while outputs are placed horizontally. Finally, the thick gray lines trace data dependencies between the functions.

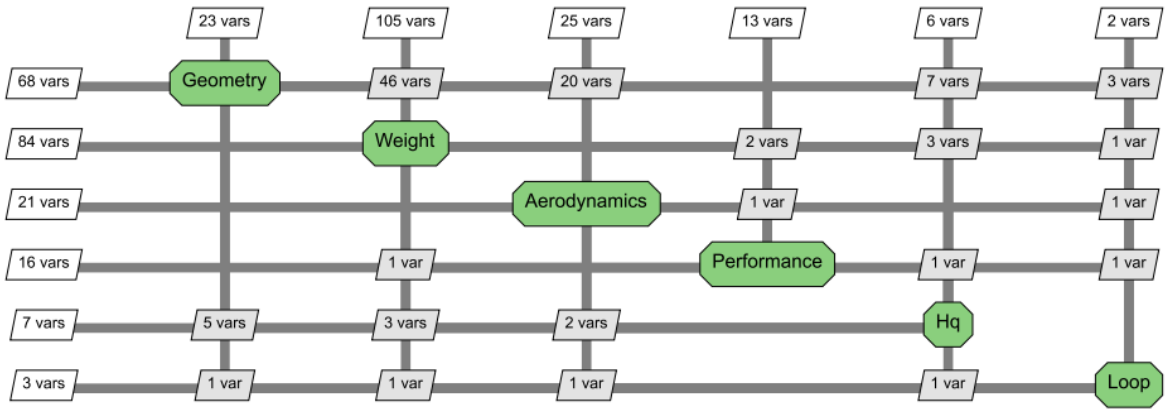

Figure 2.1: FAST-OAD disciplines interrelationships [61].

The main feature of FAST-OAD is the preliminary sizing of an aircraft with the TLARs and a few main geometrical parameters as inputs: wing, fuselage, horizontal and vertical tailplanes are sized and positioned, taking into account also longitudinal stability considerations. The computational models of such disciplines available in the open-source version are particularly suited for traditional single-aisle jet airliners such as the A320, for which the tool has been initially developed and validated. These models are based on typical aircraft design literature [62, 63], as well as on Airbus experience collected in the ISAE-SUPAERO handbook [64]. They are briefly presented in Fig. 2.2. Additional

details about those models and the equation used can be found in Section 3 as well as in the following references [65, 66].

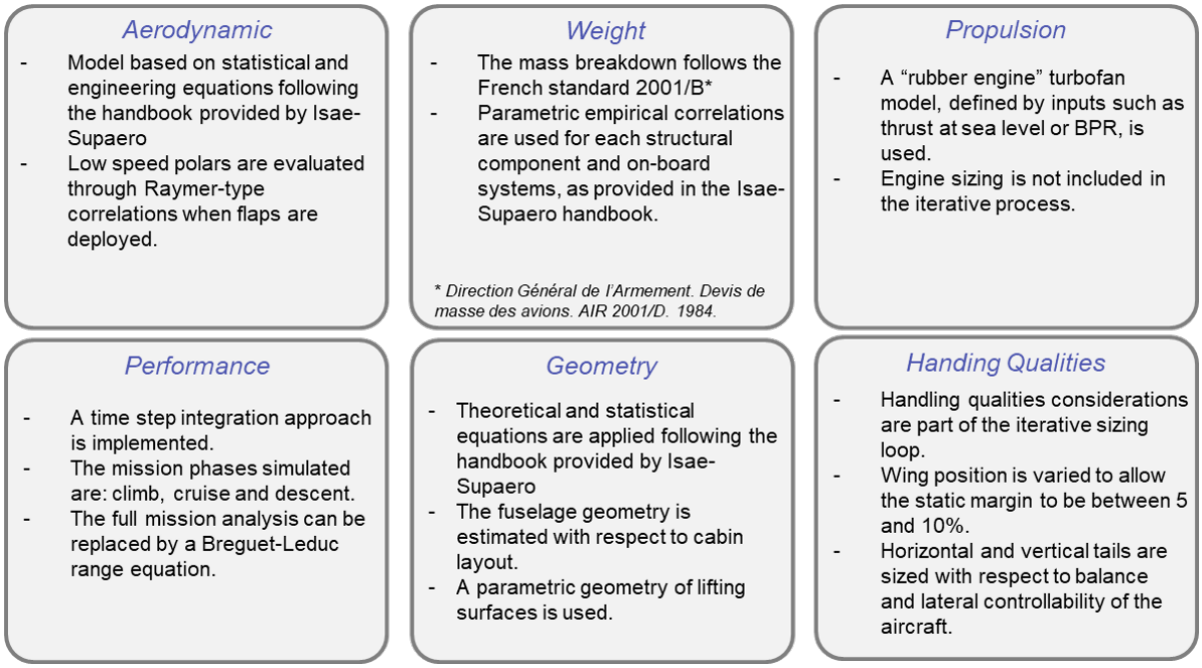

Figure 2.2: FAST-OAD computational models for each discipline.

As already anticipated, the objective of this work is the design of a turboprop aircraft and its forward-fit with different propulsion systems. Developments are therefore needed in order to adapt the MDA process for the envisioned application and to implement additional models for the sizing and performance evaluation of the new propulsion systems.

2.2 Multidisciplinary Design Optimization

Aircraft sizing and performance evaluation is a key output of the MDA process. Design optimization is however another essential task for the identification of the best aircraft configurations with respect to the defined optimization criteria. The method using numerical optimization techniques to design complex systems involving multiple disciplines is called multidisciplinary design optimization (MDO). The MDO problem starts with the definition of the objective of the optimization. This objective can be a simple parameter (e.g. fuel burn) or multiple variables (e.g. costs and emissions) which will result in a domain of multiple optimal designs. Design variables (also called decision variables) are then provided as inputs to the optimizer which explores the design space by changing their values. Finally, constraints need to be provided in order to be sure that the optimal solutions identified by the optimization process satisfy all the requirements. The convergence to the optimal solutions (and so the optimal set of design variables) is driven by the optimization algorithm. Different optimization strategies can be adopted, using either

gradient-based or gradient-free algorithms as well as different architectures (monolithic or distributed) each one offering specific advantages and drawbacks [67].

To perform aircraft design optimization, FAST-OAD relies on the OpenMDAO platform [68], an open-source framework coded in python dedicated to MDO. OpenMDAO features high-performance computing capabilities, using distributed memory to speed up serial computations, but it also enables efficient parallel execution as demonstrated in [69]. The efficiency and reliability of this platform have been demonstrated by its large users community for different optimization problems, concerning for example tightly coupled aero-structural [70, 71] and aero-propulsive [72] optimizations, as well as overall design optimization problems e.g. for small satellites [73] and blended wing body with distributed electric ducted fans [66]. Although OpenMDAO allows the adoption of both gradient-based or gradient-free algorithms, its major feature is the possibility to compute total derivatives very efficiently, by relying upon the modular analysis and unified derivatives (MAUD) architecture [74]. The major interest in the use of gradient-based algorithms lies in their high computation efficiency. In [66], results of the design optimization process show that the use of gradients in the procedure speeds up the process against a gradient-free method up to 70%. However, in the open source version of FAST-OAD the analytic derivatives of the analysis functions are not provided and thus must be estimated using finite difference which is costly in terms of computation effort.

Therefore, for this thesis, the idea has been to use a gradient-free algorithm, such as a Bayesian optimizer, which treats the MDA developed in FAST-OAD as a black box, for which no derivatives are available. Bayesian optimization is usually employed to optimize expensive-to-evaluate functions in a reduced amount of time by minimizing the number of evaluations of the expensive black boxes. The specific algorithm used is named SEGOMOE, an in-house optimizer developed in python thanks to a collaboration between ONERA and ISAE-SUPAERO. The optimization algorithm SEGOMOE stands for Super Efficient Global Optimization using Mixture Of Experts and it combines the Efficient Global Optimization [75] and the constraints handling introduced in [76]. SEGOMOE is a constrained Bayesian optimizer where the expensive black boxes (objectives and constraints functions) are approximated by some adaptive mixture of Kriging-based models. For high dimensional problems, the Partial Least Square technique is combined with Kriging to build KPLS models [77] in order to reduce the number of hyperparameters associated with the classical Kriging surrogates. The adaptive optimization process, shown in Fig. 2.3, starts with the generation of an initial set of evaluations of the objective and constraint functions, called Design of Experiments (DoE). Surrogate models of both functions are then created with Mixture Of Experts (MOE) technique [78] based on Kriging or KPLS models, using the open-source toolbox SMT[1]. Once created, those models are used

[1] github.com/SMT

to provide, with a cheap computational cost, a prediction of the optimum and associated uncertainty. The information about the optimum and the uncertainty associated to it are then combined in an acquisition function, denoted by α_f. The optimization problem, initially consisting in minimizing the objective function $f(\boldsymbol{x})$ under a certain number of constraints $c_i(\boldsymbol{x})$ (formalized in Eq. (2.1)), is thus changed into the problem defined by Eq. (2.2). Indeed, the Bayesian optimization consists of maximizing the acquisition function $\alpha_f(\boldsymbol{x})$, which is used to determine the point to be added to the DoE, representing an optimal trade-off between exploration of the highly uncertain domain that can hide a minimum and exploitation of the minimum of the surrogate model prediction. The Expected Improvement [75]) or WB2 [79] criteria are one of the well-known acquisition functions. Each constraint function $c_i(\boldsymbol{x})$ in Eq. (2.1) is replaced by its associated surrogate model $\hat{c_i}(\boldsymbol{x})$ in Eq. (2.2).

$$\begin{cases} \min\limits_{\boldsymbol{x}\in\mathbb{R}^d} \quad f(\boldsymbol{x}) \\ \text{s.t.} \\ c_1(\boldsymbol{x}) \leq 0 \\ \vdots \\ c_i(\boldsymbol{x}) = 0 \\ \vdots \\ c_m(\boldsymbol{x}) \leq 0 \end{cases} \tag{2.1}$$

$$\begin{cases} \max\limits_{\boldsymbol{x}\in\mathbb{R}^d} \quad \alpha_f(\boldsymbol{x}) \\ \text{s.t.} \\ \hat{c_1}(\boldsymbol{x}) \leq 0 \\ \vdots \\ \hat{c_i}(\boldsymbol{x}) = 0 \\ \vdots \\ \hat{c_m}(\boldsymbol{x}) \leq 0 \end{cases} \tag{2.2}$$

The search of the optimum point of the acquisition function can be done using different optimizers such as COBYLA (Constrained Optimization By Linear Approximation) [80], SLSQP (Sequential Least Squares Programming) [81] or SNOPT (Sparse Nonlinear OPTimizer) [82]. The DoE is thus enriched of points until the maximum number of iterations is reached and the final optimal point provided is the best point of the DoE.

A full description of SEGOMOE has been provided in [83], where its capabilities have been evaluated using five analytic benchmark problems as well as an aerodynamic shape optimization problem. The study proves the better performance of the optimization approach with respect to more conventional gradient-based optimization. Moreover, in [84], the authors show the application of SEGOMOE to two industrial study cases, testing

its capabilities with respect to the optimizers available within a commercial design optimization software named Isight. The obtained results prove the great advantages of SEGOMOE both in terms of required computational effort as well as on the CPU running time. Additional applications such as nacelle optimization [85], fuel burn optimization of a hybrid electric propulsion aircraft [86] and overall aircraft design bi-objective optimization [87], have confirmed its competitiveness with respect to more conventional optimization methods.

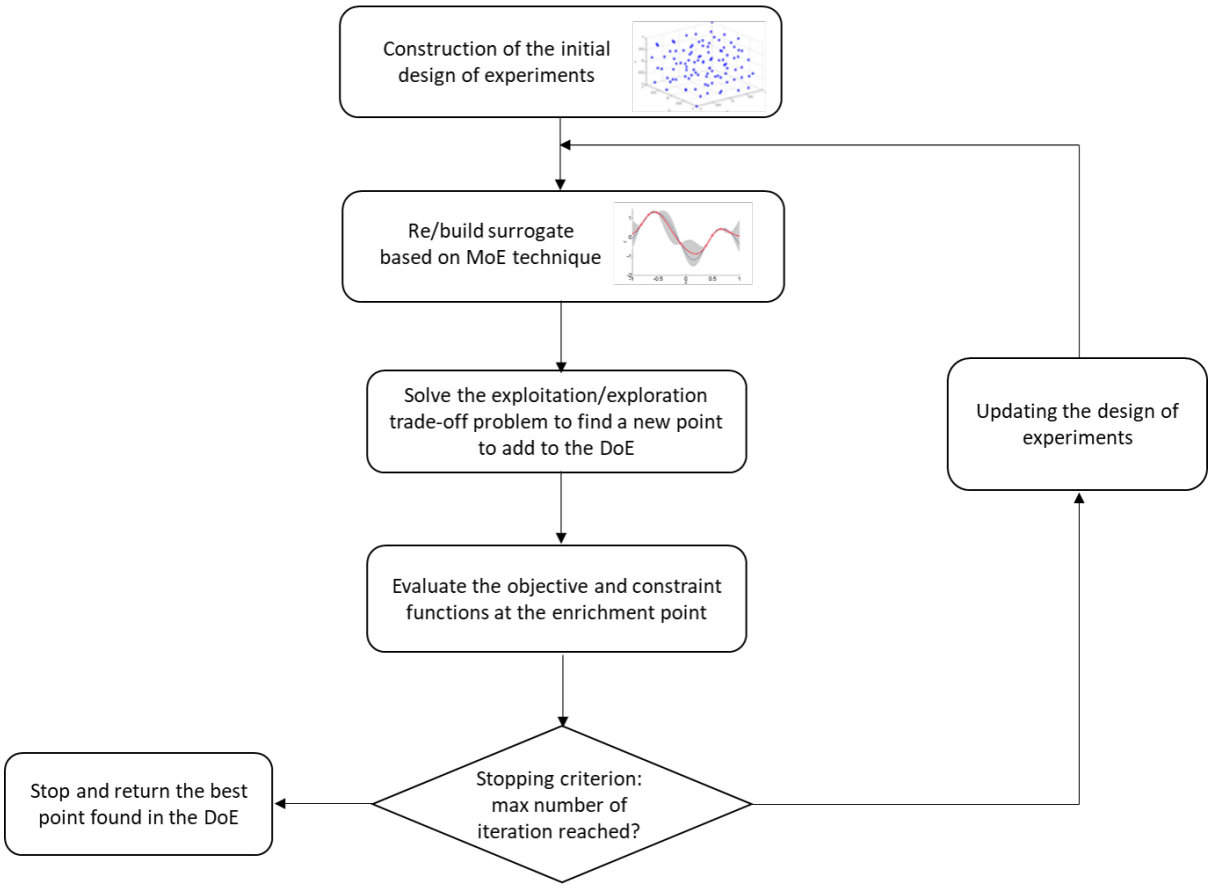

Figure 2.3: Overview of SEGOMOE algorithm. Modified from [83].

2.3 Uncertainty management

Conceptual aircraft design is a discipline that is inevitably subject to uncertainty because of the reduced amount and reliability of information available. This lack of data is addressed by developing and integrating into the design process evaluation methods and models, which are able to predict the performance and the behavior of the technology to investigate. However, numerical models are generally constituted of a set of parameters and equations, which can only partially represent the complexity of the real physical phenomenon. Consequently, there generally exists a discrepancy between the model estimation and the actual experimental observations. However, this discrepancy

could be reduced by gaining more information about the data and the system, increasing the number of parameters of the models and adding more equations to be able to capture more aspects of the phenomenon of interest. This kind of reducible uncertainty is called epistemic uncertainty and is in opposition with aleatory uncertainty which is due to the inherent physical variability in all processes, thus irreducible. Epistemic uncertainty can be further divided in:

- **Model uncertainty**, caused by the model from assumptions, imprecise model parameters, simplifications as well as numerical approximations.
- **Data uncertainty**, due to insufficient information, e.g. imprecise data and model inputs, technological assumptions.

Traditionally, engineers address this problem by performing sensitivity analyses and eventually taking margins or safety factors on some design parameters to mitigate technical risks. However, at the conceptual design stage, these margins are often assessed according to engineering judgment and know-how, which in the case of unconventional technologies may lead to inaccurate assessments, resulting in either too conservative or too ambitious designs. An explicit method to quantify the uncertainty introduced by each model and to propagate it through the aircraft simulation process is needed to improve the accuracy of the results and to help make the right design choices very early in the design process, so as to reduce the number of design iterations between the different design phases. Uncertainty management can be done in two major steps: identification and quantification of main uncertainty sources at the model level and uncertainty propagation. Propagating the uncertainty through the entire design process is important to assess its impact on the overall aircraft performance. Indeed, by identifying the uncertainty sources with the greatest repercussion on the final results, efforts can be properly targeted to efficiently improve the accuracy of the results.

In [88], the authors present an approach to managing uncertainties divided into two steps. Model uncertainty, as defined in this section, is referred to in the reference study as predictive uncertainty. The proposed methodology is summarized hereafter:

1. Uncertainty quantification and identification
   (a) Calculation of errors between model predictions and experimental values using available reference data.
   (b) Probability distribution fitting of the calculated sample errors.
2. Uncertainty propagation
   (a) Probabilistic approach: Monte Carlo Simulations (MCS) are used, which provide a confidence interval around the estimated value, giving a measure of the degree of precision of the estimation.

This approach, however, for the uncertainty quantification relies on the availability of at least few experimental data that are used, somehow, to correct the model outputs to provide more accurate and reliable results. Therefore, if no experimental or reliable data are available at all, the approach is not applicable. This is the case for this thesis where unconventional technologies are under study, for which there is no previous knowledge available in literature. The probabilistic approach proposed for the uncertainty propagation instead may be used in this thesis to propagate the uncertainties identified at component level to the aircraft performance level. Other studies [89, 90, 91] also use Monte Carlo Simulation for propagating uncertainties in the MDA, showing the effectiveness of such approach. MCS, however, is known to be time consuming, which is particularly an issue when the evaluation function is computationally expensive.

A different approach, more suitable to the scope of the work of this thesis concerning uncertainty quantification, is presented by [92]. The management of model uncertainty is done in the following steps:

1. Uncertainty quantification and identification
   (a) Identification of the model inputs which represent the main source of incertitude on the model outputs.
   (b) Association of sensitivity factors (K-factors) to the model parameters to take into account the error. The K-factors are determined within a certain range. The ranges are assigned through engineering judgment and based on the perceived accuracy of the computational models used.
2. Uncertainty propagation
   (a) Deterministic approach (min-max): The number of simulations to be performed is a function of the number of K-factors used (number of identified sources of incertitude). A full factorial set of K-factors combinations is considered, where the K-factors can only assume the lower or the upper bound value of the range. For example, with 5 sources of uncertainty identified, the full domain of possible solutions is given by performing 2^5 simulations.

Concerning the first step of uncertainty quantification, [92] proposes the same method also to manage data uncertainty (other than model uncertainty), for which technology level assumptions are considered associating K-factors to the model inputs of the components that may see fairly rapid development. Thus, both data uncertainty and model uncertainty quantification is treated, in this thesis, with the same approach, assigning K-factors or varying the model inputs or parameters within a specified range.

Instead, both approaches to uncertainty propagation (deterministic and probabilistic) are computationally expensive, requiring a large number of simulations. This is particularly

the case when the simulation models used are themselves time-consuming which can potentially lead to prohibitive computation time. A way to reduce the computation time of uncertainty propagation analyses is to replace the complex simulation model with a much simpler meta-model. Meta-models, also known as surrogate models, are obtained by evaluating the output of the simulation model at selected input points and interpolating or smoothing the output values obtained. Some popular meta-modeling techniques are polynomial regression models, artificial neural networks and Kriging models [88]. Meta-modeling techniques have been widely used for design evaluation and optimization in many engineering applications and have been proven to be very efficient in cutting down the computational cost [93]. In [94], uncertainty propagation is performed using stochastic expansion instead of sampling methods such as MCS, in order to provide a better compromise between cost and accuracy [95]. In particular, the paper introduces a semi-intrusive polynomial chaos expansion (PCE) formulation to solve the MDA under uncertainty. The efficiency of the proposed method is demonstrated by showing comparisons with Monte Carlo reference results, first on an academic example and then on two conceptual aircraft design test cases.

In this thesis, PCE is thus chosen to surrogate the response of the MDA with random input variables. To quantify the effect of input random variables on the variance of the response of the MDA, Sobol' indices are analytically determined as a post-processing of the PCE coefficients [96]. Those indices decompose the variance of the output of a model into fractions that can be attributed to inputs, thus providing a measure of the sensitivity of the model output to each input. The possibility to derive analytically those indices from the PCE coefficients is key to the reduction of the computational cost of the uncertainty propagation analysis. Indeed, the computation time is basically limited to the generation of the training set of the MDA response outcomes, which is used to fit the PCE model.

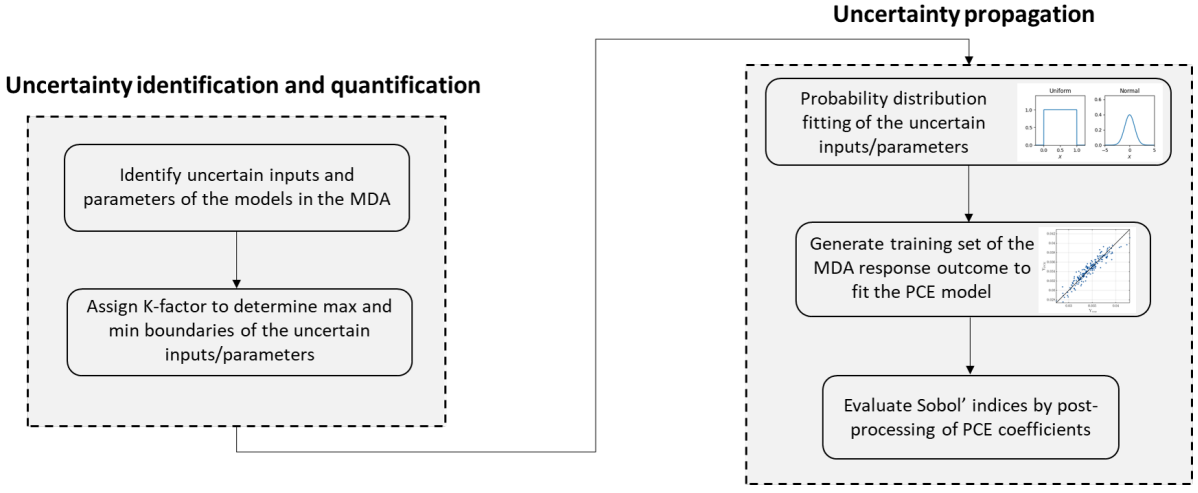

Figure 2.4: Uncertainty management process.

Figure 2.4 shows, step-by-step, the uncertainty management process adopted in this thesis. First, the uncertain model parameters and inputs are identified. According to engineering judgment or literature review, K-factors are assigned, together with a probabilistic distribution function. The next step consists in the creation of the PCE metamodel by giving the polynomial basis orthogonal with respect to the input distribution and using sparse least squares for the computation of the coefficients. Finally, Sobol' indices are computed as post-processing of the PCE coefficients.

2.4 Conclusion of the chapter

- The design of a disruptive propulsion system for an existing aircraft raises big challenges for engineers, inherent to its integration (mass and volume) as well as its characteristics that may affect aircraft performance (aerodynamics, propulsive efficiency, etc.).

- A multidisciplinary analysis and optimization framework is needed to handle all the possible interactions between the different OAD disciplines and to address the lack of data about innovative propulsion technologies by integrating into the design process new evaluation models.

- FAST-OAD, developed by ONERA and ISAE-SUPAERO, is the open-source conceptual aircraft design platform that has been chosen as the initial framework for the developments of the MDA processes to design a regional turboprop aircraft and its forward-fit with low-emission propulsion systems.

- Multidisciplinary design optimizations are to be performed with an in-house optimizer named SEGOMOE, a Bayesian optimizer characterized by an enrichment strategy based on a mixture of experts coupled with adaptive surrogate models, that has proven to be highly efficient both in terms of computation effort and CPU running time.

- Uncertainties introduced by the new evaluation models, due to the lack of means of validation inherent to the novelty and maturity level of the propulsion technologies, are to be properly managed.

- An approach to uncertainty management, consisting of uncertainty quantification and propagation, is well identified and set in place. Global variance-based sensitivity analyses are to be performed, computing Sobol sensitivity indices by polynomial chaos expansion.

Part II

From FAST-OAD to RHEA: Development of the design methods suitable for a regional propeller aircraft

Chapter 3

Analytic models for conventional aircraft design disciplines

Contents

3.1 RHEA versus FAST-OAD: Computational Models

In FAST-OAD, the overall design process as well as the methods used for the different disciplines are particularly suited for a single-aisle turbofan aircraft, for which FAST-OAD has been initially developed and validated. For this reason, both the evaluation models and the design process have been modified or added, when needed, in order to adapt the MDA to the design of turboprop regional aircraft. Overall, the set of new/-modified evaluation models and design processes, developed within the framework of this PhD, has been named RHEA (Regional Hybrid Electric Aircraft) design tool. RHEA includes sizing modules for several propulsion systems and comprises design processes for the overall design of a conventional turboprop aircraft as well as the forward-fit design of a given aircraft with low-emission propulsion systems.

In order to design a 70-seat twin-propeller aircraft and to evaluate its performances with different propulsion systems, several simulation models have been developed during this thesis and integrated into RHEA design tool. The objective of this chapter is to show the main modifications that have been done compared to the classical evaluation models already available in FAST-OAD in order to best suit the design of a regional twin-propeller aircraft. Figure 3.1 provides an overview of the main additions or adaptations that have been done to the evaluation models for each discipline.

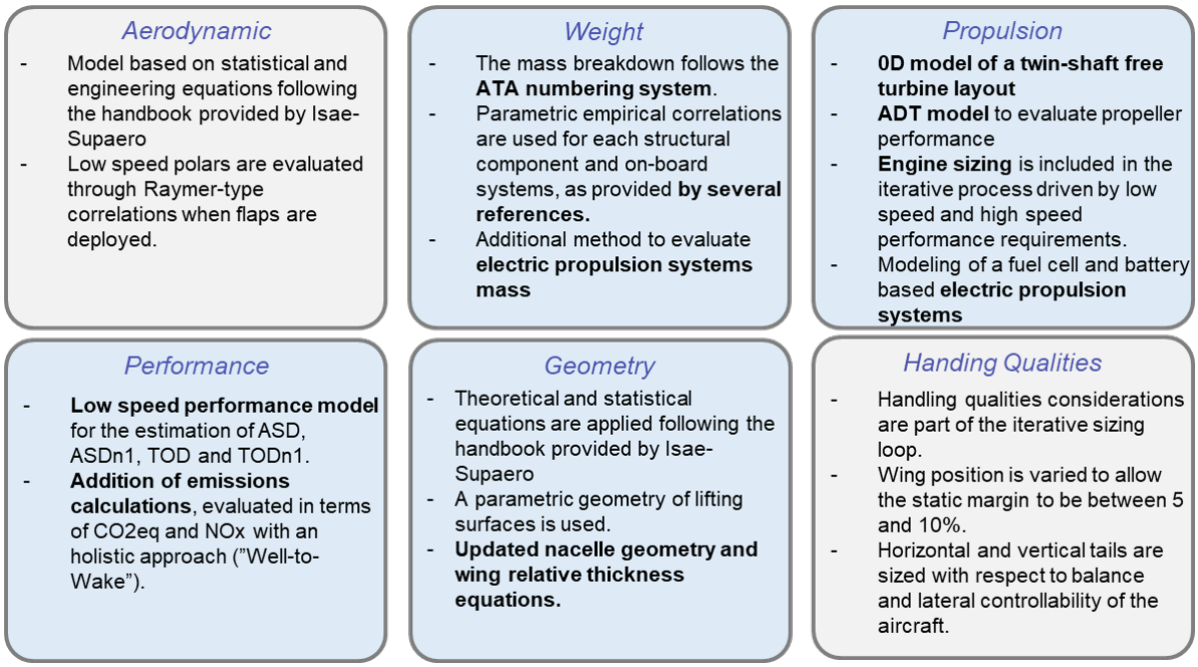

Figure 3.1: RHEA computational models for each discipline. In light blue are highlighted the disciplines that have undergone major changes with respect to FAST-OAD.

3.2 Geometry modelling

The geometry module evaluates aircraft dimensions by decomposing them into five elements: fuselage, wing, horizontal and vertical tail, and nacelle. Each element is initially defined by a set of input parameters which feeds an iterative sizing process. Fuselage, wing and tail geometries have been obtained using the equations already available in FAST-OAD and shown in [66]. Concerning the wing geometry, an important parameter that has a significant effect on the aerodynamic and weight characteristics of the wing is the relative thickness. The computational model for the wing geometry available in FAST-OAD estimates the relative thickness using a semi-empirical equation which is a function of a reference cruise Mach number and the wing sweep angle measured at the 25% of the chord. The equation provided, however, produces unfeasible estimations of the relative thickness for Mach numbers lower than 0.7, thus given that a twin-propeller regional aircraft features typical Mach numbers around 0.5, a more suitable correlation has been found in the literature. Equation (3.1) is a non-linear regression for the estimation of the wing thickness ratio (t/c) provided by [97], built as a combination of three parameters: the design cruise Mach number (M_{des}), the sweep angle at the 25% of the chord (ϕ_{25}) and the design lift coefficient (Cl_{des}), defined as the lift coefficient when the lift over drag ratio is maximum.

$$(t/c) = 0.127 M_{des}^{-0.204} cos(\phi_{25})^{0.573} Cl_{des}^{0.065} 0.921^{0.556} \tag{3.1}$$

Moreover, for the nacelle geometry, different equations were used because they are more representative of a turboprop engine. The geometry parameters of the nacelle are assumed to be equal to the gas turbine ones which are determined using Eqs. (3.2) and (3.3), derived by Raymer [62] (SI units).

$$D_{gt} = 0.241 \left(\frac{P_{gt}}{745.7} \right)^{0.12} \tag{3.2}$$

$$L_{gt} = 0.105 \left(\frac{P_{gt}}{745.7} \right)^{0.373} \tag{3.3}$$

At the conceptual design phase, the definition of the geometry of each aircraft system is not required since it is not relevant for overall aircraft performance studies.

3.3 Weight modelling

For the estimation of the characteristics masses of the aircraft, the mass breakdown used in RHEA follows the ATA numbering system, as shown in Table 3.1, which differentiates it from the French norm AIR 2001/D19 used in FAST-OAD. The operating weight empty (OWE) is divided into five groups: airframe, propulsion, systems, operational and furniture items. Except for the propulsion, the models used for mass estimation of the

components rely on semi-empirical methods collected in the Airbus note [64] or in other aircraft design books such as [62, 98].

Group	ATA	Description
Airframe	ATA32	Landing gears
	ATA53	Fuselage
	ATA54	Nacelles
	ATA55	Empennage
	ATA57	Wing
Propulsion	ATA28	Fuel lines
	ATA61	Propellers
	ATA72	Engine turbine
	ATA73	Engine Fuel and Control
Aircraft Systems	ATA21	Environmental constrol system
	ATA22	Auto flight system
	ATA23	Communication system
	ATA24	Electrical power system
	ATA26	Fire system
	ATA27	Flight controls system
	ATA29	Hydraulic power system
	ATA30	De-ice system
	ATA34	Navigation system
Operational and Furniture items	ATA25	Furnishing
	ATA33	Lights
	ATA35	Oxygen
	ATA38	Water
	N/A	Crew
	N/A	Documents and toolkit

Table 3.1: Mass breakdown standard implemented in RHEA.

For the propulsion part, the method proposed by [99] was used for the prediction of gas turbine and propeller masses. The conventional turboprop propulsion model divides the propulsive unit into four main components: gas turbine including gear box, nacelle, propeller and propulsive control system. The propulsive control system is further decomposed into: engine controls, starting systems and engine provisions (oil system and oil cooler). The total propulsion mass m_{pp} is the sum of each component:

$$m_{pp} = m_{eng} + m_{nacelle} + m_{prop} + m_{ps} \tag{3.4}$$

The mass of each component is evaluated using statistical relations between take-off power and engine mass which are similar to the formula that can be found in Roskam [63] and Raymer [62]. However, some of the methods in these handbooks are somewhat dated, therefore the authors in [99] updated certain models with more recent statistical data for aircraft engines. The trend of engine-specific power as a function of take-off power, obtained with this method, is illustrated in Fig. 3.2 for both dry engine and installed engine masses.

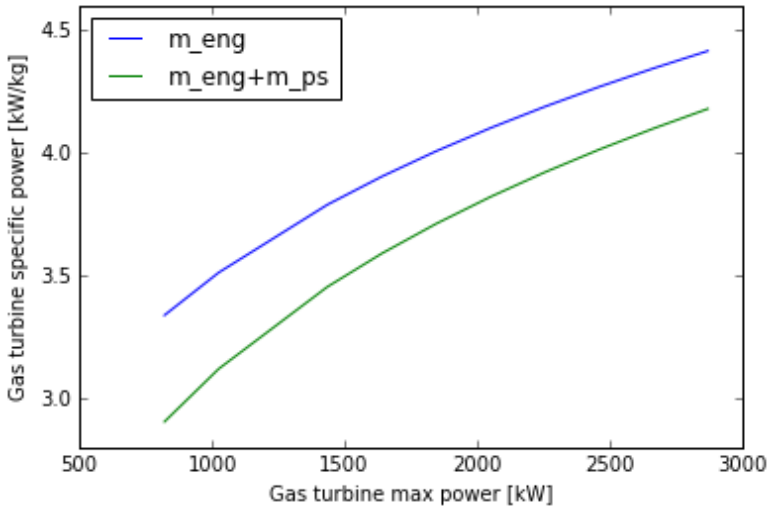

Figure 3.2: Gas turbine specific power curves

3.4 Aerodynamics modeling

The aerodynamics module consists of low-fidelity models based on semi-empirical equations allowing for extremely fast computation of the aerodynamic performance of the aircraft. It is devoted to the computation of the drag polar $C_D = f(C_L)$ for both high-speed and low-speed conditions. As shown in Eq. (3.5), the total drag is decomposed into four components: friction drag D_0, induced drag D_i, wave drag D_w and trim drag D_{eq}. Each drag component is estimated according to the methods proposed by Roskam [63]. More details about the model and the formulas used can be found in [66].

$$C_D = C_{D_0} + C_{D_i} + C_{D_w} + C_{D_{eq}} \tag{3.5}$$

The introduction of batteries or fuel cells for the production of electrical power leads to the need for a cooling system that requires a certain amount of external airflow to evacuate the heat produced in order to keep all the systems at their operational temperature. Therefore air scoops are needed in order to provide the required airflow to heat exchangers, which may be responsible for an additional cooling drag that leads to a degradation of the aerodynamic performance of the aircraft.

However, the installation of the heat exchanger in a duct with a diffuser and a nozzle generates appreciable thrust utilizing the so-called Meredith effect [100, 101]. This effect is well known since the beginning of WWII and the Mustang P-51D and Messerschmitt Bf 109 are examples of aircraft making use of this effect to efficiently cool down their piston engines without significantly increasing the overall aircraft drag. No attempt was made during this thesis to quantify both the drag and the thrust generated by such ducted heat exchangers since that would require efforts in the geometrical design of both the heat exchanger and the duct which is out of the scope of the thesis. Nevertheless, those considerations led to the strong assumption of neglecting any additional cooling drag, provided that it is entirely counter-balanced by the additional thrust generated by making use of the Meredith effect as proved by [100].

3.5 Traditional propulsion modeling

The propulsion module includes all the methods for the estimation of propulsion performance in terms of available thrust and fuel consumption. The gas turbine model consists in the characterization of a twin-shaft free turbine engine architecture (see Fig. 3.3). This configuration is chosen because a representative of the PW100 aircraft engine family, used by a large number of turboprop aircraft and covers a wide power range between 1100 to 3700 kW. Assuming that these engines have similar designs, the model can scale the engine to lower or higher powers within the PW100 engines power range, while providing the same specific fuel consumption characteristic at design conditions.

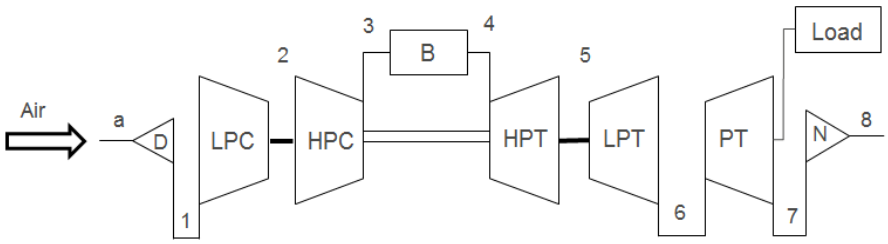

Figure 3.3: Gas turbine architecture

The gas turbine model evaluates the available power and the specific fuel consumption by computing the thermodynamic properties of the airflow at the inlet and the outlet of each engine component and by solving the power balance equations of the low-pressure and high-pressure spools. At the design point, available data from the engine's manufacturer were used to characterize the engine components, such as compressor pressure ratios, max turbine inlet temperature and compressors bleed airflow. The efficiencies of components were estimated using representative values relative to the state-of-art engine technology according to [102]. The main thermodynamic equations as well as the sizing

process for the determination of the turbine engine parameters used to evaluate the gas turbine performance in off-design conditions are given in Appendix A.

In order to reduce the computational time needed to evaluate the turboprop performance at each time step of the flight mission profile, a surrogate model is built to approximate the results of the 0D model presented above, which is computationally expensive. The surrogate modeling approach chosen is a polynomial regression of the third degree which takes as input the flight conditions in terms of flight altitude (x_1 in feet) and Mach number (x_2) as well as the engine throttle setting (x_3 with values between 0 and 1) and evaluates the power lapse coefficient (P_{lapse}) and specific fuel consumption in $kg/hp/hr$, as given in Eqs. (3.6) and (3.7). The coefficients c_i of both equations are provided in Table 3.2. The power lapse coefficient is defined as the ratio between the available power at the given condition and the max power available at static conditions (sea level and Mach=0) to take into account the change in atmosphere air density that affects engine performance.

$$\begin{aligned} P_{lapse} = c_0 + c_1x_1 + c_2x_2 + c_3x_1^2 + c_4x_1x_2 + \\ + c_5x_2^2 + c_6x_1^3 + c_7x_1^2x_2 + c_8x_1x_2^2 + c_9x_2^3 \end{aligned} \tag{3.6}$$

$$\begin{aligned} PSFC = c_0 + c_1x_1 + c_2x_2 + c_3x_3 + c_4x_1^2 + c_5x_1x_2 + \\ + c_6x_1x_3 + c_7x_2^2 + c_8x_2x_3 + c_9x_3^2 + c_{10}x_1^3 + \\ + c_{11}x_1^2x_2 + c_{12}x_1^2x_3 + c_{13}x_1x_2^2 + c_{14}x_1x_2x_3 + \\ + c_{15}x_1x_3^2 + c_{16}x_2^3 + c_{17}x_2^2x_3 + c_{18}x_2x_3^2 + c_{19}x_3^3 \end{aligned} \tag{3.7}$$

P_{lapse} Eq. (3.6)	PSFC Eq. (3.7)	
c_0: 1.015	c_0: 0.9533	c_{10}: $-2.497e^{-15}$
c_1: $-2.806e^{-6}$	c_1: $-1.4739e^{-5}$	c_{11}: $1.132e^{-10}$
c_2: $-8.498e^{-2}$	c_2: $-1.285e^{-1}$	c_{12}: $-9.598e^{-11}$
c_3: $-8.928e^{-10}$	c_3: -2.257	c_{13}:$-1.182e^{-6}$
c_4: $2.253e^{-5}$	c_4: $1.887e^{-10}$	c_{14}: $-3.861e^{e-6}$
c_5: $1.943e^{-1}$	c_5: $-4.882e^{-8}$	c_{15}: $-1.471e^{-5}$
c_6: $1.914e^{-14}$	c_6: $2.685e^{-5}$	c_{16}: $6.02e^{-2}$
c_7: $-8.816e^{-10}$	c_7: $-2.707e^{-1}$	c_{17}: $2.522e^{-1}$
c_8: $1.919e^{-5}$	c_8: $4.479e^{-1}$	c_{18}: $-3.248e^{-1}$
c_9: $-3.257e^{-1}$	c_9: 2.511	c_{19}: $-9.402e^{-1}$

Table 3.2: Coefficients of the 3rd degree polynomial regressions for the determination of P_{lapse} and PSFC.

The model validation shows a coefficient of determination R^2 equal to 0.996. A scatter plot of predicted values versus true values is given in Fig. 3.4.

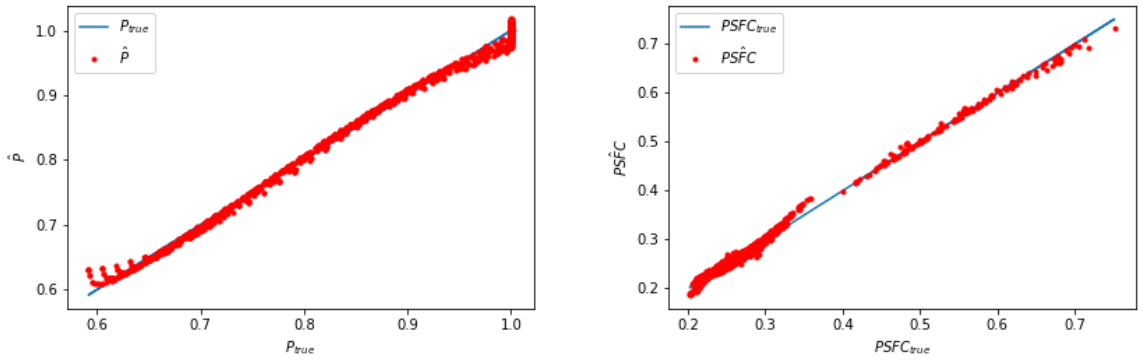

Figure 3.4: Validation results for the prediction of the power lapse coefficient (left) and specific fuel consumption (right).

The thrust produced by the propeller is evaluated using Eq. (3.8), where the propeller efficiency is determined at each condition during the flight mission using an analytic model based on the actuator disk theory (ADT) for a propeller sized for a max shaft power of $1.1P_{gt_{RTO}}$

$$\mathcal{T} = (\eta_{prop} P_{shaft})/speed \tag{3.8}$$

For takeoff performance, when the aircraft speed is close to 0, Eq. (3.8) is not applicable. The actuator disk theory can be considered valid starting from Mach values of 0.2. A linear interpolation model between the static thrust value evaluated using Eq. (3.9) proposed by [103] and the thrust at Mach 0.2 evaluated with the ADT model has been used in order to estimate the thrust for all the Mach numbers between 0 and 0.2

$$\mathcal{T}_0 = \frac{K_{\mathcal{T}_0} P_{shaft}[hp]}{rpm \times d_{prop}[ft]} \tag{3.9}$$

where $\mathcal{T}_0$ is the static thrust in pounds and $K_{\mathcal{T}_0}$ is the static thrust coefficient which according to [103] was estimated to be 55000.

3.6 Performance modelling

Based on a segment-by-segment simulation using time step integration, the performance module solves the equations of motion to evaluate the performance of the vehicle throughout the mission in terms of fuel consumption and emissions. For the conventional aircraft flight mission, no particular modifications were applied to the existing performance module of FAST-OAD as described in [66]. For each time step, the performance module performs the analyses illustrated in Fig. 3.5 using an eXtended Design Structure Matrix (xDSM) scheme [60].
However, for the new propulsion system using batteries or hydrogen as an energy source, some modifications were required. For example, with a hybrid propulsion system using two different fuels, at each time step the aircraft is not only consuming kerosene but

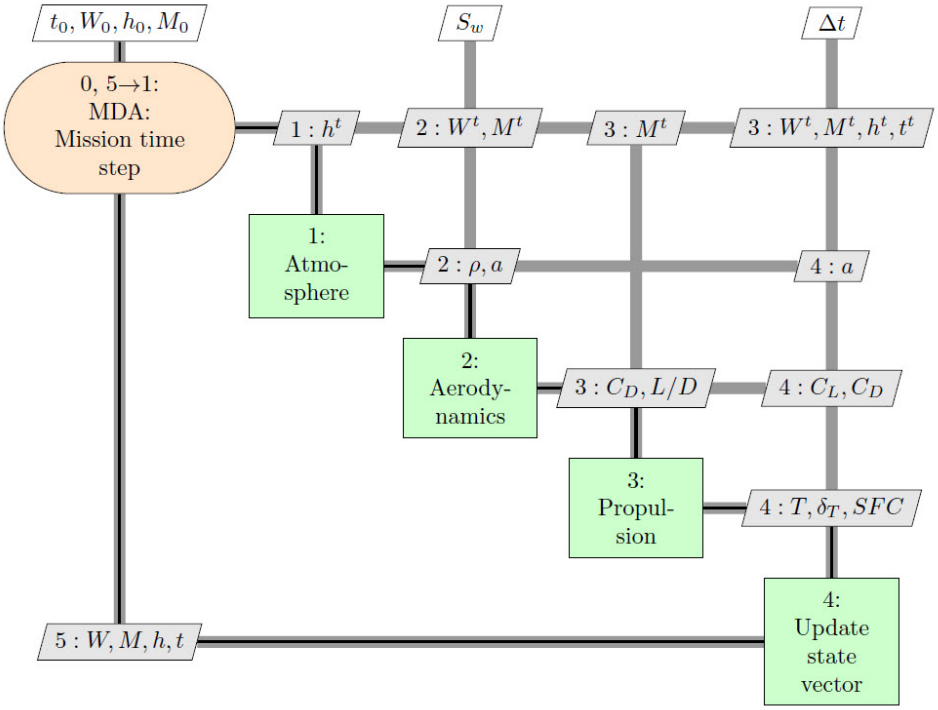

Figure 3.5: xDSM diagram for the time step performance analysis [66].

also hydrogen, therefore the mass variation of the aircraft at each time step takes into account both jet fuel consumption and hydrogen consumption. The propulsion module in Fig. 3.5 therefore provides additional inputs to the state vector, which are functions of the specific propulsive system used.

Additionally, the performance module evaluates the aircraft emissions in terms of CO_2 equivalence which are obtained by multiplying the mass of the substance emitted by the CO_{2eq} emission index. The such index accounts for all the emissions generated by the production of the fuel till its use on board the aircraft, called Well-to-Wake (WTW) emissions. For the hydrogen fuel cells, the only product of the reaction between hydrogen and oxygen is water vapor, therefore the WTW CO_{2eq} emissions correspond to the Well-to-Tank (WTT) emissions. Moreover, those emissions vary significantly according to the different processes used to generate hydrogen. More insights into those processes and the related emissions can be found in Section 1.2.2. For the electrical batteries instead, as shown more in detail in Section 1.2.1, CO_{2eq} emissions are generated by its production process as well as by the production electricity which is needed to recharge them before each flight.

In addition to the calculation of CO_{2eq}, the model also evaluates H_2O emissions for both hydrogen-based and jet fuel propulsion systems, as well as NO_x emissions due to jet fuel combustion. The indexes used to calculate these emissions are summarized in Table 3.3.

NO_x formation from Jet-A combustion does not exclusively depend on the amount of nitrogen in the fuel but also on the air-fuel mix ratio. High temperatures and oxidation-rich conditions generally favor NO_x emission in combustion. Therefore, the correlation for the NOx emission index ($kg\ NO_x/kg$ fuel) is calculated as a function of burner entrance pressure (kPa) as well as combustion chamber entrance and exit temperatures (K), as shown in the following equation:

$$EI_{NOx} = 5.4728 \times 10^{-9} T_4 P_3^{0.37} e^{\frac{T_3}{191.67}} \tag{3.10}$$

Jet-A emissions			
WTW	3.79 $kgCO_{2eq}/kg$ Jet-A		
Hydrogen emissions ($kgCO_{2eq}/kg\ H_2$)			
	$EMEL1/LH2$	$GPLH1b$	$WDEL1/LH1$
WTW	30.53	15.45	0.50
Battery emissions			
Battery production	200 $kgCO_{2eq}/kWh$ battery @ 1500 cycles (= 0.13 $kgCO_{2eq}/kWh/cycle$)		
Battery recharge	0.42 $kgCO_{2eq}/kWh$		

Table 3.3: Fuel-specific emission indexes

Concerning H_2O emissions, the emission indexes EI_{H_2O} for kerosene combustion and the hydrogen reaction in the fuel cells are respectively 1.26 and 9 kg H_2O per kg of fuel. Assuming rough values of gas turbine efficiency η_{gt} of 30% and fuel cell efficiency η_{fc} of 50%, in order to produce the same amount of propulsive energy, hydrogen fuel cells emit roughly 50% more water vapor than a conventional kerosene gas turbine.

– Kerosene gas turbine H_2O emissions

$$\frac{EI_{H_2O}}{FHV_{Jet-A} \times \eta_{gt}} = 0.35 g H_2O/Wh \tag{3.11}$$

– Hydrogen fuel cell H_2O emissions

$$\frac{EI_{H_2O}}{FHV_{H_2} \times \eta_{fc}} = 0.54 g H_2O/Wh \tag{3.12}$$

The residence time of water vapor emitted at the typical cruise altitude of turboprop aircraft (less than 25000 ft) is of a couple of weeks, whereas the residence time for CO_2 is of 100 years, so the environmental impact of CO_2 emissions is a function of the total emissions over the past 100 years. Moreover, the direct radiative effect of water vapor emissions is believed to be negligible [104, 105]. The primary concern about water vapor emissions is the indirect effects which are complex and uncertain, one of these being contrails formation. However:

– "*Contrails formation do not scale directly with the amount of H_2O emitted because aircraft H_2O emissions just act as a trigger for contrail formation*" [104]: more H_2O emissions do not imply more or bigger contrails.

– "*Contrails formation depends on what is emitted from the engines in addition to water vapor*" [104]: the only emission of hydrogen fuel cells is water so the absence of sulfurs compounds should reduce the probability of contrails formation.

Therefore, given the typical flight altitudes of the considered aircraft class, it is assumed that an increase of water vapor emissions of 50% does not have a significant environmental impact. Obviously, more research is needed to confirm this preliminary consideration, however, for this thesis only NO_x and CO_{2eq} emissions are used as a performance metric for the assessment of the different propulsive architectures under study.

3.7 Conclusion of the chapter

- Development efforts were needed in order to best suit FAST-OAD to the design of a regional twin-propeller aircraft.
- The main disciplines undergoing major modifications were the weights module and the propulsion module. Concerning the former, the estimation of the characteristics masses of the aircraft was based on a mass breakdown which follows the ATA numbering system. For the propulsion module instead, analytical models were developed for the evaluation of the gas turbine and propeller performances.
- Overall, the set of new/modified evaluation models and design processes, based on the existing multidisciplinary design platform, was named RHEA design tool.

Chapter 4

Additional models for the design and analysis of low-emission propulsion technologies

Contents

4.1 Fuel cell system

The balance of the plant of a fuel cell is the set of all the required systems and components for the correct functioning of a fuel cell (see Fig. 4.1). Due to the uncertainty regarding the choice of the right value for fuel cell-specific power and considering the huge impact this parameter has on the electric propulsion system mass, it was decided to carry out a component-by-component modeling of the fuel cell system rather than arbitrarily choosing a mean value among the ones found in the literature.

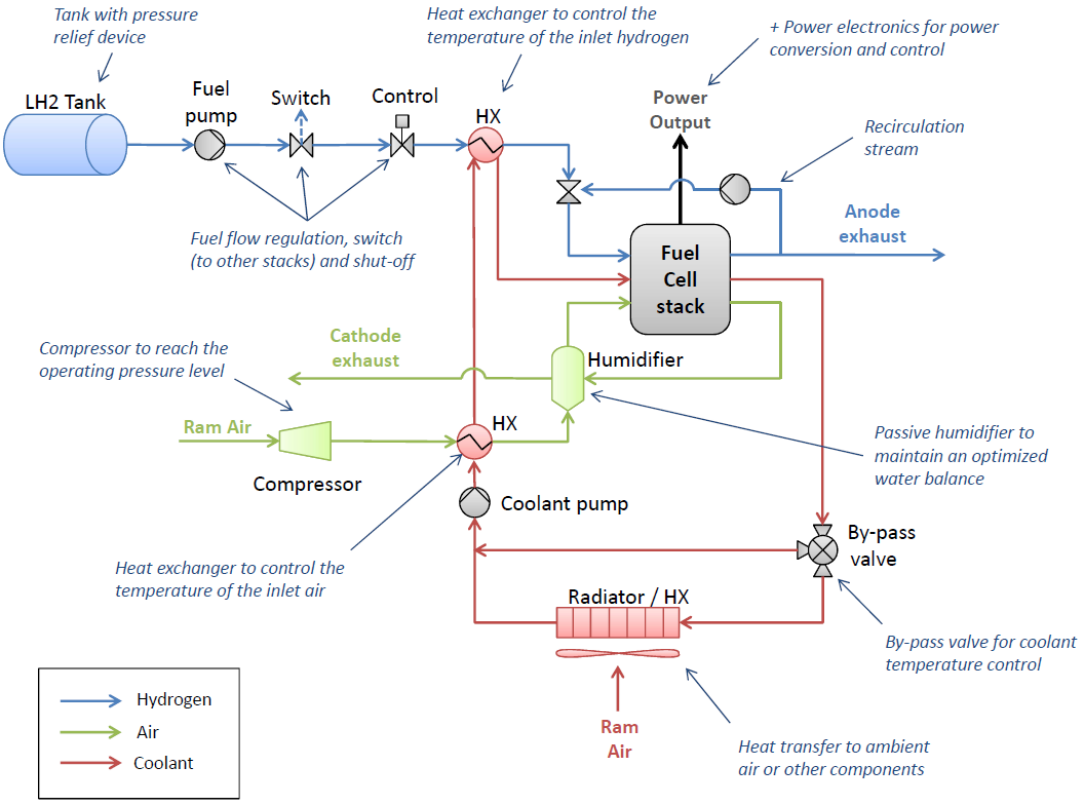

Figure 4.1: Schematic layout of the fuel cell BoP including hydrogen tanks.

The method used consists of the development of statistical and analytical relationships for the determination of the mass of each component of the fuel cell balance of the plant. Regarding the fuel cell stack, multiple manufacturers (e.g. Ballard, PowerCell) seem to achieve a state-of-the-art specific power of 3.5 kW/kg, for a net power output of 100 kW. The specific power of the fuel cell stack is therefore really close to the one of a 2 MW class gas turbine engine as shown in Fig. 3.2. However, due to the BoP components, the specific power of the fuel cell system decreases, as it will be shown in the following.

According to [106], the power value of 100 kW is the highest a low-temperature PEM fuel cell stack can generate. Consequently, to obtain high levels of electrical power, it is necessary to connect in series or in parallel multiple stacks.

In Fig. 4.1, valves and pressure regulators are required to supply hydrogen to the fuel cell with the right flow rate. In terms of weights, according to [41], each valve weighs about $1kg$ and the actuators not more than $3kg$. Therefore, a total of $7kg$ per fuel cell stack (to include inlet and outlet valves) has been considered. A cooling system is used to dissipate the heat generated by the fuel cell stack and the other components. The mass of the cooling module (which includes coolant, pumps and air/hydrogen heat exchangers) is calculated based on the results from the *Inn-Balance fuel cell project* [107] using the following equation:

$$m_{cool} = \frac{P_{fc}}{P_{sp_{cool}}}, \quad P_{sp_{cool}} = 5.56kW/kg \tag{4.1}$$

where P_{fc} is the fuel cell power and $P_{sp_{cool}}$ is the specific power of the cooling module of the stack. On the cathode side, the reactant air is supplied by a compressor and humidified in a humidity exchanger to prevent the fuel cell membrane from drying, which would reduce the efficiency of the stack. The humidifier mass is scaled from experimental and commercial products (see Fig. 4.2a). The compressor weight is estimated from a linear interpolation over the results from Teichel [108]. The preliminary design carried on by Teichel leads to a relation between the mechanical power of a single-stage axial compressor and its weight, as depicted in Fig. 4.2b.

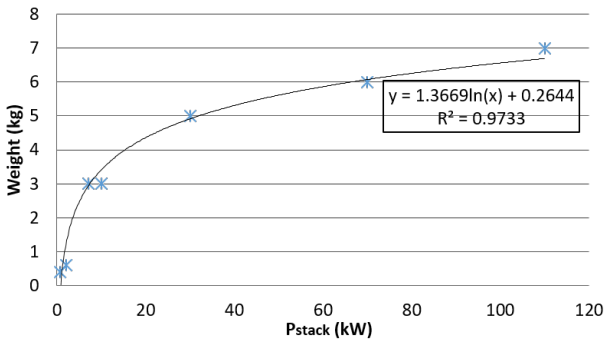

(a) Humidifier weight from Fumatech [109].

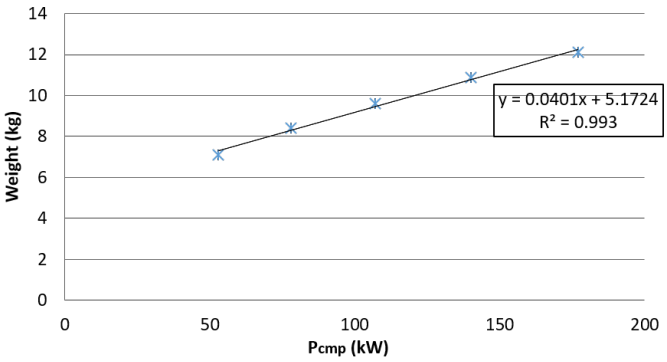

(b) Compressor weight from [108].

Figure 4.2: Empirical laws for the estimation of compressor and humidifier masses.

The mechanical power of the compressor is derived from thermodynamics relations. Given the fuel cell power P_{fc} and the average cell voltage V_{cell}, the air mass flow $dotm_{air}$ needed to supply the fuel cell with the oxygen for the reaction with hydrogen is calculated based on the following equation provided by Larminie [110]

$$\dot{m}_{air} = \frac{2P_{fc}3.57 \times 10^{-7}}{V_{cell}} \tag{4.2}$$

The temperature variation is obtained from the pressure ratio β, the compressor efficiency η and the inlet air temperature T_{in} as shown in the following equation

$$\Delta T = \frac{T_{in}}{\eta}(\beta^{\frac{\gamma-1}{\gamma}} - 1) \tag{4.3}$$

Finally, the mechanical power of the compressor P_{cmp} is proportional to the flow rate and the temperature variation

$$P_{cmp} = C_p \dot{m}_{air} \Delta T \tag{4.4}$$

In addition, the mass of the electrical motor driving the compressor has to be taken into account. Teichel [108] provides the following equation for an air-cooled electric motor

$$m_{em}[kg] = 6.08 + 0.077\frac{P_{cmp}}{\eta_{em}}[kW] \tag{4.5}$$

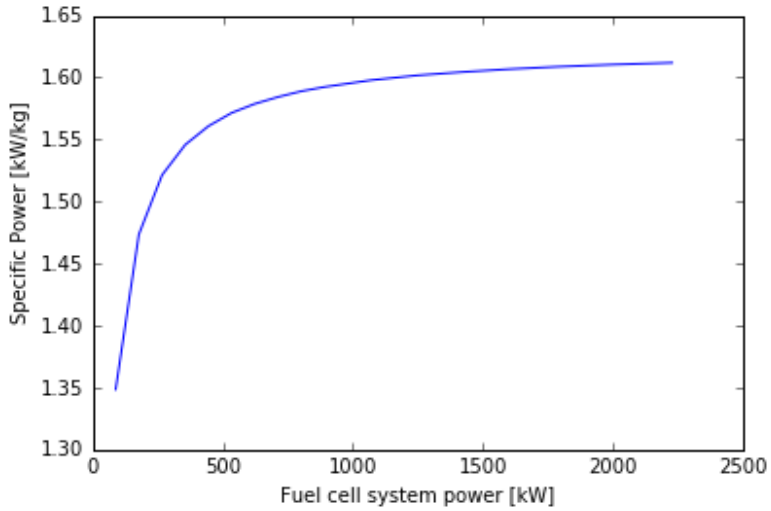

Figure 4.3: Fuel cell system specific power trend with fuel cell power (radiator mass not included).

The sum of all these components masses gives the total mass of the fuel cell system m_{fc}:

$$m_{fc} = m_{stack} + m_{humidifier} + m_{cmp} + m_{cool} + m_{acc} \tag{4.6}$$

The resulting fuel cell-specific power is shown in Fig. 4.3 as a function of the net output power. From the results, it can be observed that there is a scaling effect since the higher

the power, the better the specific power. Indeed, not all the components masses scale directly with the output fuel cell power, moreover, some of these components may be used by multiple stacks. For example, a fuel cell system of 2 MW is actually composed of 20 fuel cell stacks of 100 kW and each stack needs cooling, pumps and all the other components as shown in Fig. 4.1. Nevertheless, instead of using one compressor for each stack, a single bigger compressor may be used to supply pressurized air to all the stacks, reducing significantly its impact on the total mass of the system.

The hydrogen consumption depends on the overall efficiency of the electric propulsive chain:

$$\dot{m}_{H2} = \frac{P_{shaft}}{\eta_{fc}\eta_{pe}\eta_{em}FHV_{H2}} \tag{4.7}$$

Both the electric motor and power electronics efficiencies were assumed to be constant and equal respectively to 97% and 98%, which are representative values of state-of-the-art technology levels [13]. For the fuel cell system, the efficiency is assessed by considering the different components and thermochemical equations. As shown in Fig. 4.1, a fuel cell system is composed of a fuel cell stack and of a certain number of components that significantly increase the mass of the fuel cell, but also use some of the output electrical power of the fuel cell stack to work. Therefore, the net output power of the fuel cell system P_{fc} is lower than the gross output power of the fuel cell stack P_{stack}. In terms of efficiency, it translates into the following mathematical formulation:

$$\eta_{fc} = \eta_{stack}\frac{P_{fc}}{P_{stack}} \tag{4.8}$$

As shown by [111], the main power consumer of the BoP is the compressor. For this study, all the secondary power consumers have been neglected. The compressor power requirement is calculated using Eq. (4.4). With this method, the resulting ratio between net and gross output power is $\frac{P_{fc}}{P_{stack}} = 0.89$. Finally, Eq. (4.9) is used to evaluate the fuel cell stack efficiency:

$$\eta_{stack} = \eta_{cell} = \eta_{ideal}\frac{V_{net}}{E_{OCV}} \tag{4.9}$$

where V_{net} is the fuel cell net output voltage and E_{OCV} is the fuel cell open circuit potential. The ideal fuel cell efficiency at standard conditions is obtained by dividing maximum work output by the enthalpy input (Eq. (4.10)). In these ideal conditions, the fuel cell reversible potential E_r is given by:

$$\eta_{ideal} = \Delta G/\Delta H = 83\% \tag{4.10}$$

$$E_r = -\Delta G/nF = 1.229V \tag{4.11}$$

At non-standard conditions, E_{OCV} is given by:

$$E_{OCV} = E_r + \frac{\Delta S}{2F}(T - T_{ref}) + c\log(P/P_{ref}) \tag{4.12}$$

V_{net} is evaluated considering the voltage losses due to $v_{activation}$, v_{ohmic} and $v_{concentration}$, obtained using the following equations:

$$v_{activation} = \frac{2RT}{nF} sinh^{-1} \frac{i}{2i_0} \tag{4.13}$$

$$v_{ohmic} = iR_{ohmic} = i(R_{elec} + R_{ionic}) \tag{4.14}$$

$$v_{concentration} = \frac{2RT}{nF}(1 + \frac{1}{\alpha}) log \frac{i_l}{i_l - i} \tag{4.15}$$

$$V_{net} = E_{OCV} - (v_{concentration} + v_{activation} + v_{ohmic}) \tag{4.16}$$

These voltage losses are a function of the current density. The evolution of the net voltage against the current density is known as the polarization curve and is an important indicator of the fuel cell performance. Figure 4.4a shows the resulting polarization curve obtained for different operating pressures.

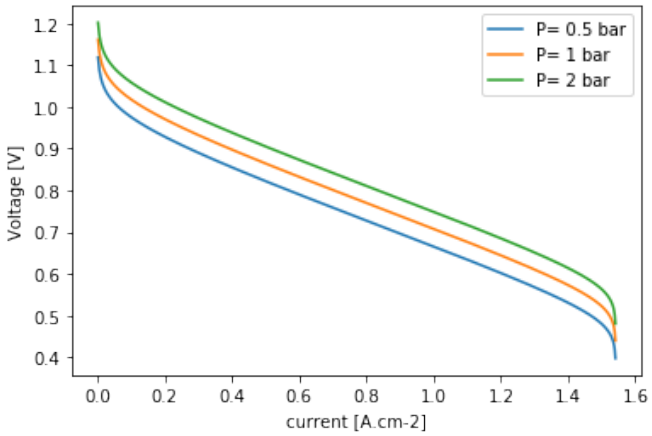

(a) Fuel cell polarization curves.

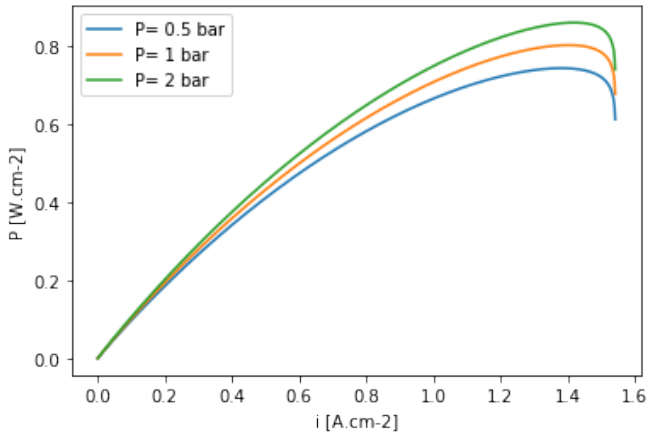

(b) Fuel cell power curves.

Figure 4.4: Dependency of fuel cell polarization curve and power on the operating pressure.

The polarization curve gives also the trend of the electrochemical efficiency of the fuel cell with the operating current. Since η_{cell} is proportional to V_{net}, the lower the current, the higher the efficiency. As shown in Fig. 4.4 the maximum power point does not correspond to the maximum efficiency point. The choice of the operating point is not straightforward. Therefore, the optimum operating current is obtained using a weight parameter, w_p, which defines the relative importance of fuel cell power density over efficiency. With this weight parameter, an overall objective function is calculated

$$f(\eta_{cell}, P_{cell}) = w_p P_{cell} + (1 - w_p)\eta_{cell} \tag{4.17}$$

If the objective is to optimize only the weight of the fuel cell, then a w_p of 1 should be chosen. Values of w_p between 0 and 1 are chosen if a compromise between maximum power and efficiency is required.

4.2 Liquid Hydrogen storage

For hydrogen-powered aircraft configurations, the geometrical design of the hydrogen tanks has a non-negligible impact on their masses. Therefore, a set of input parameters for hydrogen tank design is required to define its shape. The dimensionless parameters - λ, ϕ, ψ - needed to characterize the shape of the tank is shown in Fig. 4.5. This mathematical

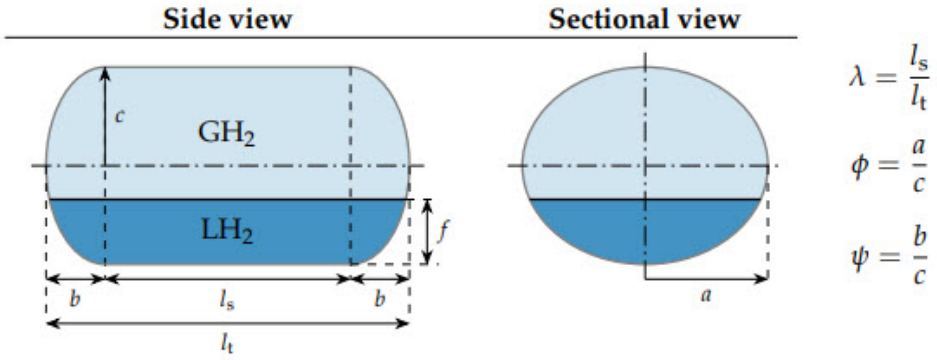

Figure 4.5: Parameters defining hydrogen tank geometry [112].

description of the geometry, which corresponds to an elliptical shell with ellipsoidal heads, ensures a flexible design because it can also characterize simpler ellipsoidal ($\lambda = 0$) or spherical ($\phi = 1, \psi = 1, \lambda = 0$) shapes. These parameters, together with the tank internal volume V_t, are needed to determine the actual dimensions of the tank using Eqs. (4.18) to (4.21).

$$a = \left(\frac{3V_t \phi^2 (1 - \lambda)}{\pi \psi (2\lambda + 4)} \right)^{1/3} \tag{4.18}$$

$$b = \psi c \tag{4.19}$$

$$c = \frac{a}{\phi} \tag{4.20}$$

$$l_s = \frac{V_t - (4/3)\pi abc}{\pi ac} \tag{4.21}$$

The tank internal volume V_t is the total volume occupied by the hydrogen and it can be calculated with Eq. (4.22) knowing the tank filling pressure p_{fill}, the venting pressure p_v and the mass of hydrogen to be stored given as inputs [112].

$$V_t = \frac{y m_{H_2}}{\rho_{LH_2}} + \frac{(1-y) m_{H_2}}{\rho_{GH_2}} \tag{4.22}$$

ρ_{LH_2} and ρ_{GH_2} are hydrogen density respectively in liquid and gaseous states. They are evaluated as a function of the filling pressure using the linear regressions derived from [112]. The same approach has been used for the determination of the volume fraction of gaseous and liquid hydrogen in the tank, denoted by y, which is a function of both the venting and the filling pressure of the tank.

Typical values of the tank nominal pressure found in the literature are between 1.2 and 2 bar [57], however, those values refer to tanks with a capacity of more than 1000 kg of H_2. Compared with those studies, due to the much lower energy requirements of the aircraft under study, the hydrogen tanks designed in this thesis are much smaller, which leads to a higher surface-to-volume ratio of the tank. Thus, the relative impact of the tank wall area on the tank mass and thermal resistance is higher, leading to lower gravimetric efficiencies and higher boil-off ratios (ratio between the boil-off rate in kg/h and mass of hydrogen stored in kg). In order to limit excessive hydrogen venting during flight, liquid hydrogen tanks can be designed with higher venting pressures. Verstraete [57] suggests that for small tanks storage pressure of up to 8 bar may be used. For this study, a venting pressure of 4 bar was considered high enough to withstand the amount of boil-off that is expected over the duration of the aircraft mission, without needing to vent gaseous hydrogen into the atmosphere. The fill pressure instead represents also the minimum pressure allowed inside the tank and it has been set to 2 bar. This pressure must be higher than the atmospheric pressure to avoid air entering the tank which would lead to an explosion. The choice of these two pressure values is critical for the tank design because it affects not only the actual hydrogen capacity of the tank as shown by Eq. (4.22) but also its mass.

As for the geometry, also the model used to evaluate the cryogenic hydrogen tank mass is derived from [112]. It takes as inputs the total hydrogen mass to be stored and the tank shape defined by the parameters ϕ, ψ and λ. Based on the venting pressure, the tank material and the geometry, the model yields the calculation of the wall thickness. Finally, a thermal analysis provides a relation between the thickness of the insulation and the hydrogen boil-off resulting from the heat leaks. Single-layer foam insulation is

modeled, which offers low thermal conductivity, reduced weight, and sufficient damage resistance [57]. In order to determine the boil-off losses, thermodynamic equations have been used to calculate the heating flux Q that is exchanged across the tank wall and insulation. The following phenomena have been taken into account:

- internal heat convection between hydrogen and internal surface of tank wall;
- heat conduction through the tank wall;
- heat conduction through the insulation material;
- external heat convection between the air outside the tank and the external surface of tank insulation.

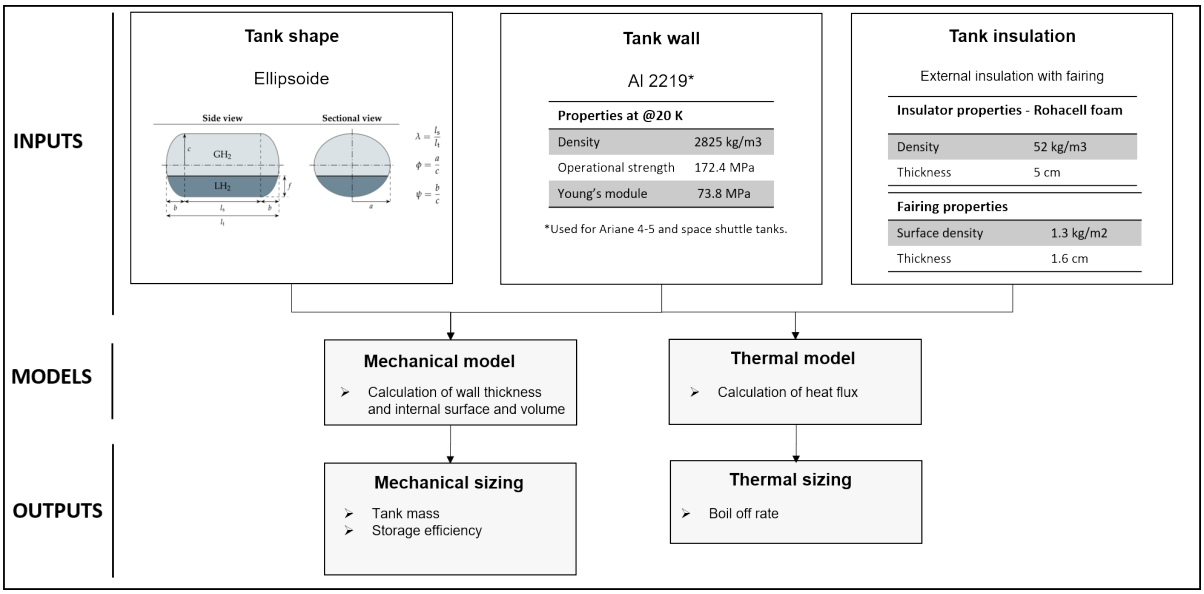

Figure 4.6: Flowchart of tank design

The model calculates the temperature value at each interface and, consequently, the heat exchanged through the tank. Then, knowing the hydrogen latent heat of vaporization λ_{H_2}, the boil-off rate is calculated as follows

$$BOR = \frac{Q}{\lambda_{H_2}} \tag{4.23}$$

A simplified flowchart with the main inputs used for this study is shown in Fig. 4.6. In order to choose the input tank shape parameters, a sensitivity analysis was performed to evaluate the dependency of the storage efficiency on the shape parameters. The storage efficiency is defined as

$$\eta_g = \frac{m_{H_2}}{m_{H_2} + m_{tank}} \tag{4.24}$$

Due to its low area-to-volume ratio, the spherical shape clearly offers the best solution in terms of weight, volume and heat loss. However, the integration of such tanks in the

aircraft is not practical, therefore cylinders with rounded edges ($\psi = 1$) are preferred. Results of the sensitivity study in Fig. 4.7 show that a cylindrical shell ($\phi = 1$) provides a much better storage density than elliptical ones ($\phi \neq 1$). The parameter λ has a lower impact on the storage efficiency. Moreover, while a greater value of λ provides slightly better efficiency, it also increases the boil-off rate as shown in Fig. 4.8a. Therefore, the choice of λ must result from a trade-off between tank mass and boil-off requirement, but could also be derived from operational as well as installation constraints. For this study, a value of $\lambda = 0.5$ is chosen. The full set of shape parameters is therefore selected: $\lambda = 0.5$, $\phi = 1$ and $\psi = 1$. The choice of these parameters, together with the previously shown assumptions regarding tank wall material and tank insulation, gives the tank storage efficiency as a function of tank capacity as illustrated in Fig. 4.8.

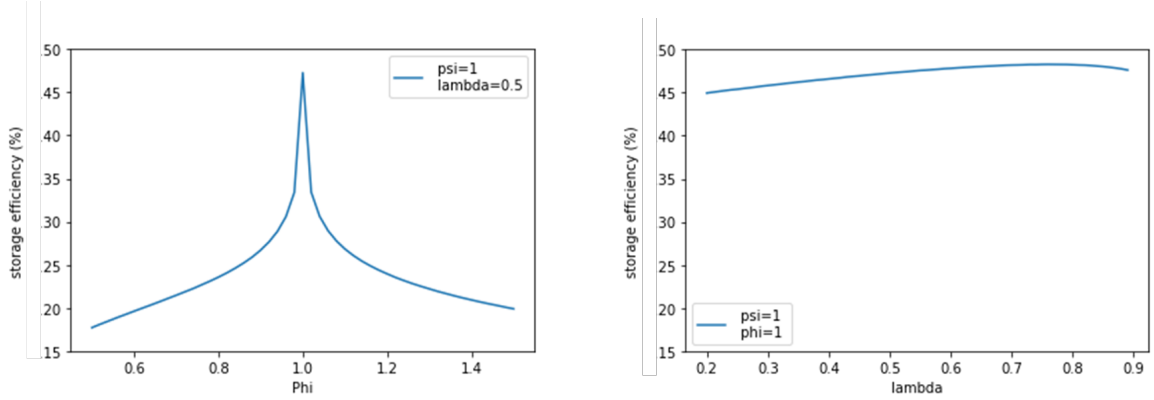

(a) Evolution of η_g with ϕ.

(b) Evolution of η_g with λ.

Figure 4.7: Dependency of storage efficiency on the shape parameters for a tank capacity of 60 kg of H_2.

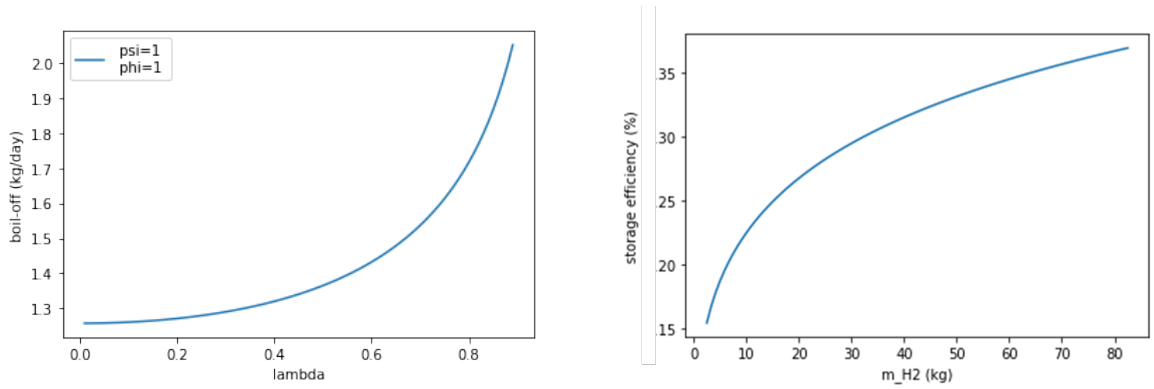

(a) Dependency of boil-off rate on λ.

(b) Scale effect of η_g with tank capacity.

Figure 4.8: Effect of tank shape and tank capacity on boil-off and gravimetric efficiency.

4.3 Hydrogen distribution

Hydrogen distribution from the cryogenics tanks to the fuel cell stacks is ensured by cryogenic pipes with Rohacell ® foam insulation. This type of insulation has been selected because it is lightweight, cheap and with good mechanical properties. Other insulation architectures exist in the literature but provide limited properties (e.g. Aerogel ®) or operate in peculiar conditions which would require efficient monitoring to prevent failures (e.g. multi-layer insulation). The preliminary design of Rohacell ® foam insulated pipes is done in two steps. First, the inner diameter of the pipes is derived from the flow rate, according to the method proposed by [113]. Then, a heat transfer analysis is performed to evaluate the performance of the insulated pipes. The model evaluates the mass of the pipes (m_{distr}) by evaluating the mass of the pipe wall and of the required insulation layer given a total required length as input. The results of the model in terms of linear density variation with hydrogen flow rate are shown in Fig. 4.9. This includes a pipe wall made of 304L steel and insulation with Rohacell ® foam.

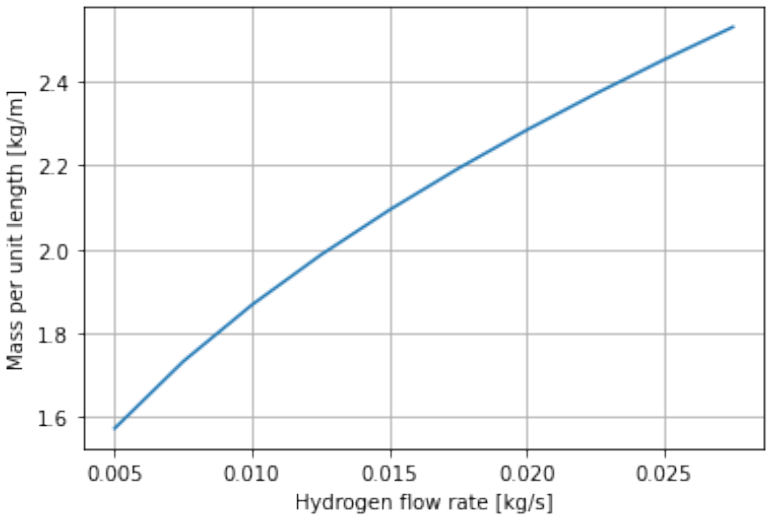

Figure 4.9: Pipe linear density variation with hydrogen flow rate

4.4 Cooling system

A propulsive system comprising fuel cells for the generation of electrical power requires the integration of cooling systems to evacuate the waste heat produced by the fuel cells. Figure 4.10 presents the energy flow inside a typical fuel cell system. For a given electric power output, a fuel cell with an efficiency of around 50% generates roughly the same amount of power in the form of heat. Part of the generated heat is removed from the stack by the extra air and hydrogen that have not reacted, while some may be used to vaporize the produced water for the inlet air humidification. Natural convection from the fuel cell body removes a few additional percent of the heat.

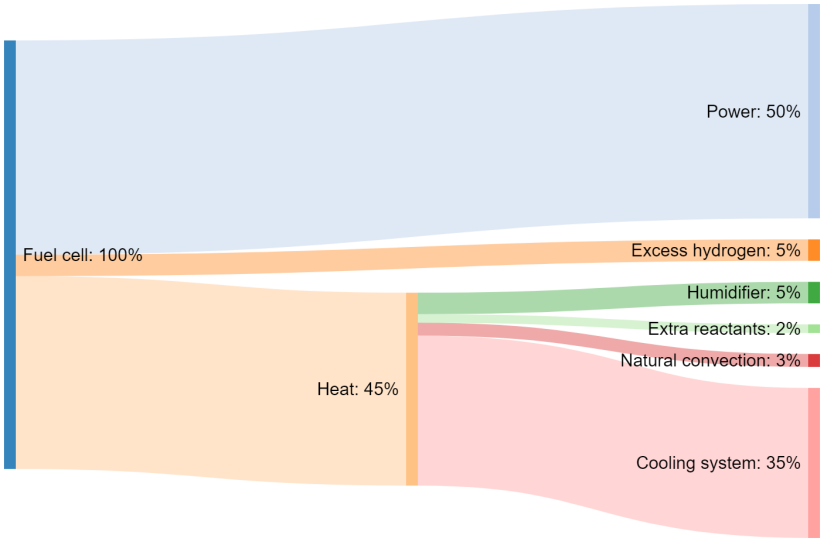

Figure 4.10: Energy flows for a typical PEM fuel cell, derived from [114], [115].

Moreover, part of the waste heat from the fuel cells can be recovered in order to vaporize and heat the cryogenic hydrogen prior to its reaction in the fuel cell stacks. Based on the cooling ability of hydrogen, the required hydrogen flow rate and the required temperature increase fixed by the fuel cell operating temperature, it was estimated that between 13% and 17% of the heat to be rejected by the liquid cooling system could be recovered for hydrogen heating and vaporization (see Fig. 4.11). Therefore, the remaining heat that must be dissipated by the cooling system Q_{RAHX} is less than 35% of the incoming hydrogen energy which is supplied to the fuel cells.

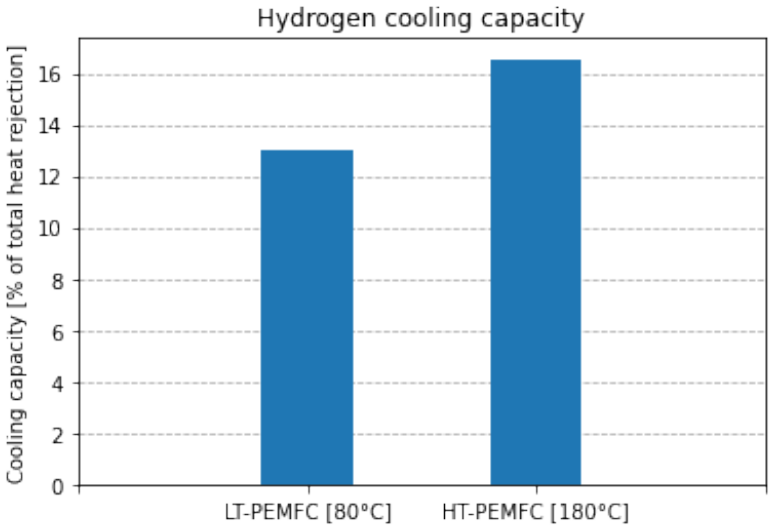

Figure 4.11: Hydrogen cooling capacity.

The cooling ability of the hydrogen is determined by its flow rate $\dot{m}_{H_2}$ and temperature increase. The hydrogen flow rate is derived from the stacks power P_{fc} and the mean

voltage V_{cell} of each cell in the stacks.

$$Q_{H_2} = \dot{m}_{H_2} L_{H_2} + \dot{m}_{H_2} c_{p,H2} (T_{hot} - T_{cold}) \tag{4.25}$$

$$\dot{m}_{H_2} = 1.05e^{-8} \frac{P_{fc}}{V_{cell}} \tag{4.26}$$

The average values of the parameters are summarized in Table 4.1.

Parameter	**Value**
Latent heat of hydrogen, L_{H2}	455 kJ/kg
Specific heat capacity of hydrogen, $c_{p,H2}$	14.30 $kJ/kg/K$
Hydrogen temperature leaving the tank, T_{cold}	22 K
Hydrogen temperature before injection for $HT\text{-}PEMFC$, T_{hot}	180 C
Hydrogen temperature before injection for $LT\text{-}PEMFC$, T_{hot}	80 C

Table 4.1: Values of the parameters needed for the evaluation of hydrogen cooling capacity.

For a given fuel cell power output, the hydrogen flow rate is determined using Eq. (4.26). Then, the heat recovered for hydrogen heating and vaporization is derived from Eq. (4.25). The higher the temperature difference between T_{cold} and T_{hot}, the higher the heat recovered, thus the lower the waste heat Q_{RAHX} to be dissipated by the heat exchanger. Moreover, for the sizing of the heat exchanger, given the same operating conditions and the same output power, the use of $HT\text{-}PEMFC$, instead of $LT\text{-}PEMFC$, not only implies lower waste heat to dissipate but also higher temperature difference between coolant temperature $T_{coolant}$ and the cooling airflow temperature T_{air}^{tot}. This higher delta temperature further decreases the required specific heat rejection, thus the heat exchanger sizing requirements, resulting in a smaller and lighter system.

In order to evacuate the waste heat generated by the fuel cells and to maintain the stacks at their operational temperature, air-liquid heat exchangers are used. They allow the transfer of the heat from the coolant to the airflow which is granted by the installation of air scoops. The mass of the heat exchangers is directly determined by the specific heat rejection according to Fig. 4.12.

$$\text{Specific heat rejection} = \frac{Q_{RAHX}}{T_{coolant} - T_{air}^{tot}} \tag{4.27}$$

Q_{RAHX} is the waste heat that must be transferred from the liquid coolant at the temperature $T_{coolant}$ to the ram air at the temperature T_{air}^{tot}, which is the total temperature of ambient air with ΔISA = 30K to account for aircraft operations in hot weather. The specific heat rejection, whose unit is kW/K, is related to the size and type of radiator.

In this study, data sheets from commercial products [116] have been used to derive the sizing laws in Fig. 4.12. In the picture, the blue points represent the weight/frontal area of the radiator assembly (including fan and motor) listed in the AKG catalogue [116]. The solid blue lines are obtained by means of a linear regression over the given points. The orange line gives the weight estimation of the radiator alone.

For specific heat rejection values greater than 8 kW/K, radiator mass and frontal area values are linearly extrapolated from the curves. In order to operate the fuel cells during ground operations, fans are required to provide sufficient airflow to the radiators. Thus, restricting the fuel cell system operation to in-flight conditions only would allow reducing considerably the weight of the assembly. The weight savings due to the removal of electric motors and fans from the radiator assembly are estimated to be around 30%. This weight reduction has been taken into account for the estimation of the radiator mass.

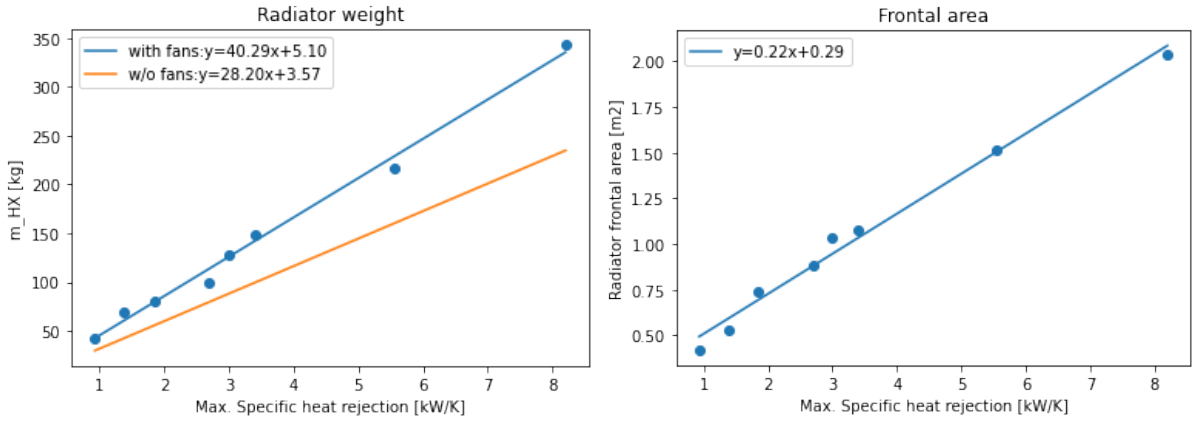

Figure 4.12: Empirical laws for the estimation of radiators weight and frontal area.

4.5 Electric power conversion

The components of the electrical power chain such as power electronics and electric motors are modeled using simple equations and are fully characterized by two parameters: specific power P_{sp} and efficiency. Those parameters are used to evaluate their mass and the power losses given the following equations:

$$m_{em} = \frac{P_{em}}{P_{sp_{em}}} \tag{4.28}$$

$$m_{pe} = \frac{P_{pe}}{P_{sp_{pe}}} \tag{4.29}$$

$$P_{output} = \eta P_{input} \tag{4.30}$$

where m is the mass of the component and P is the nominal power and η is the component efficiency. The values of efficiency and specific power of these components are given as

inputs according to the technological scenario assumed. The assumptions used together with their scenario are shown in Section 1.2.3.

Concerning the evaluation of the electric cable mass, the results from a study conducted by Vratny [111] were used in order to size the electric transmission cables. Given the total cable length, sizing electric current and conductor material as inputs, the cable mass is evaluated using the value of linear density from Fig. 4.13.

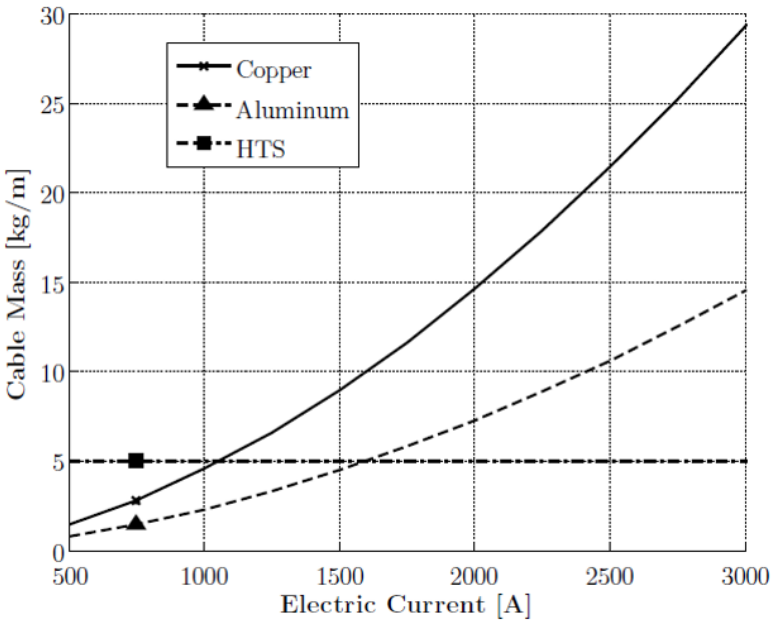

Figure 4.13: Linear density of cables using different conductor material [111].

4.6 Conclusion of the chapter

- This chapter showed the development and integration into RHEA of all the models needed to predict the performance and behavior of the different low emission propulsion technologies

- Main focus is given to the hydrogen-based model, including the thermal management and liquid hydrogen storage systems modeling.

Chapter 5

Set-up of the process for the design of a turboprop aircraft

Contents

5.1 RHEA versus FAST-OAD: Overall Aircraft Design Process

The Multidisciplinary Design Analysis implemented in the open-source version of FAST-OAD for the aircraft sizing process is illustrated in Fig. 5.1 using an xDSM diagram [60].

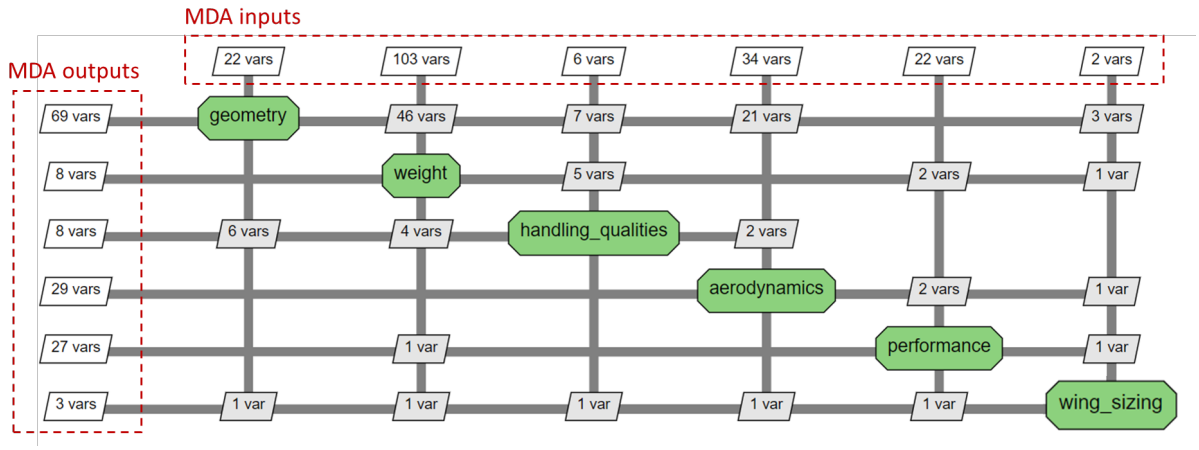

Figure 5.1: Overall aircraft design process implemented in FAST-OAD.

Starting from a set of input data and aircraft requirements (red dashed box on top in Fig. 5.1), this overall aircraft design process evaluates aircraft geometry, masses and in-flight performances (red dashed box on the left). A brief description of those inputs and outputs divided by discipline is given in Table 5.1.

In FAST-OAD, the multidisciplinary couplings that must be dealt with to obtain a consistent design are solved with numerical solvers providing a complete multidisciplinary analysis for the sizing of the vehicle. The main sizing loops present in the FAST-OAD act on the wing position, the main landing gear position, and the sizing of the control surfaces in order to reach the targeted static margin. Moreover, the green box in Fig. 5.1 named "wing sizing" deals with the evaluation of the wing surface to meet low-speed lift for a given approach speed and the maximum fuel weight requirements. The weight module instead provides the loop for the convergence between the Maximum Take Off Weight (MTOW) computed as the sum of all the aircraft systems and air-frame components and the one computed after the performance analysis which includes the mass of the fuel required for the mission. The performances of the propulsion system are directly computed in the performance module, which performs the mission analysis taking into account the aerodynamic, weight and propulsion characteristics of the aircraft. In FAST-OAD, however, the engine sizing is not included in the iterative process. The size of the engine is fully determined by one input variable, the max engine take-off thrust. Its performance characteristics - specific fuel consumption (SFC) and available thrust- are evaluated using a "rubber" engine model which scales its performance with respect

	Inputs	**Outputs**
Geometry 22 Inputs 69 Outputs	Nb of passengers Cabin dimensions requirements Main geometric char. of lifting surfaces	Airframe geometry Wetted areas Cl_{alpha} of lifting surf.
Weight 103 Inputs 87 Outputs	Cabin dimensions requirements Wing load cases Wing spar ratios Nb of engines Tuning factors	Wing sizing loads A/C weight breakdown MTOW
Handling qualities 6 Inputs 8 Outputs	Type of empennage Target static margin CG range	Empennage surfaces Static margin Aero center
Aerodynamics 34 Inputs 46 Outputs	Cl_{max2D} clean Main geometric char. of lifting surfaces Tuning factors	High/Low speed polars Drag breakdown
Performance 22 Inputs 27 Outputs	Range requirement Max Thrust and engine characteristics Flight mission profile	Fuel consumption High speed performances
Wing sizing 2 Inputs 3 Outputs	Wing aspect ratio Approach speed	Wing Area Additional fuel Additional Cl

Table 5.1: Main inputs and outputs of the design process implemented in FAST-OAD.

to some engine parameters, also provided as inputs (e.g. ByPass Ratio (BPR), Overall Pressure Ratio (OPR), turbine inlet temperature, etc.).

This chapter focuses on the presentation of RHEA design processes for the design of a turboprop aircraft, highlighting the main differences with respect to the multidisciplinary analysis already implemented in FAST-OAD. First, the input data and top-level aircraft requirements (TLARs) provided in the `xml` input file and used to initialize the design process have been changed. Those inputs, when possible, have been derived from publicly available data of the ATR72 aircraft, since this aircraft is considered as the most representative of the regional turboprop market with more than 75% of the market share. The main TLARs given as inputs to the aircraft design process are given in Table 5.2. The additional inputs required by the design process are the set of geometrical parameters for the preliminary sizing of the wing, the tails and the cabin as well as the set of design parameters for the sizing of the turboprop engine. These inputs have not been included in the table to simplify its reading, however, the complete `xml` input file is provided in Appendix B .

TLARs	
Number of passengers	72
OEI net ceiling	>2900 m
Take off distance AEO	<1200 m
Time to climb to FL200	<24 min
Approach speed	116 $knots$
Max cruise Mach @MTOW	0.45
Design range @72PAX	750 NM
Flight mission inputs	
Min. control speed (V_{MCA})	99 $knots$
Climb speed CAS	170 $knots$
Cruise flight level	20000 $feet$
Descent speed CAS	250 $knots$
Diversion distance	100 NM
Diversion flight level	10000 $feet$
Holding duration	30 min

Table 5.2: Top level aircraft requirements and inputs parameters.

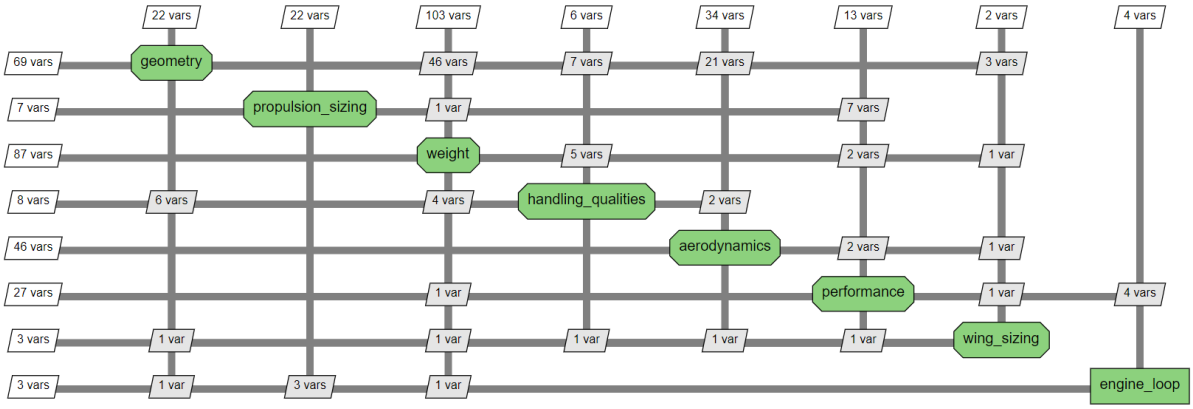

Figure 5.2: Overall aircraft design process implemented in RHEA.

Those inputs are then provided to the modified design process shown in Fig. 5.2. The main difference with respect to the original MDA in FAST-OAD lies in the implementation of the propulsion sizing loop. For that, two modules have been added to the MDA: a propulsion sizing module to characterize both propeller and gas turbine systems and a loop function that iterates the propeller sizing power and maximum gas turbine power to match the aircraft performance requirements in terms of take-off distance (TOD), time to climb (TTC), maximum cruise speed and one engine inoperative (OEI) ceiling. The

propulsion sizing group comprises a propeller sizing function to evaluate the required propeller diameter for a given sizing power as well as a gas turbine sizing function to evaluate the off-design coefficients needed for the turbine performance calculations.

	Inputs	**Outputs**
Propulsion sizing 22 Inputs 7 Outputs	Propeller disk loading Turbine design parameters: Turbine efficiencies Compressors efficiencies Turbine inlet temperature, etc.	Propeller diameter Off-design turbine coefficients
Engine loop 4 Inputs 3 Outputs	Target TOD Target TTC Target max cruise speed Target OEI ceiling	Propeller sizing power Max turbine thermodynamic power Max turbine shaft power

Table 5.3: Main inputs and outputs of the new implemented functions in RHEA.

5.2 Designed baseline aircraft

RHEA design process applied to a turboprop regional aircraft results in a baseline model. In order to provide a general validation of the design process and to check the validity of the models, this baseline model is compared to the ATR72 aircraft. In Table 5.4, general characteristics of the baseline model are compared with published data of the ATR72. As can be seen in the table, the discrepancies are relatively low, with the highest deltas being less than 10%. More accurate results may be obtained by using calibration factors applied, for example, to engine performance parameters. However, such faithful reproduction of the original ATR72 aircraft is beyond the scope of this study, therefore the obtained turboprop aircraft design can be considered as a valid representation of a typical 70-seat turboprop aircraft.

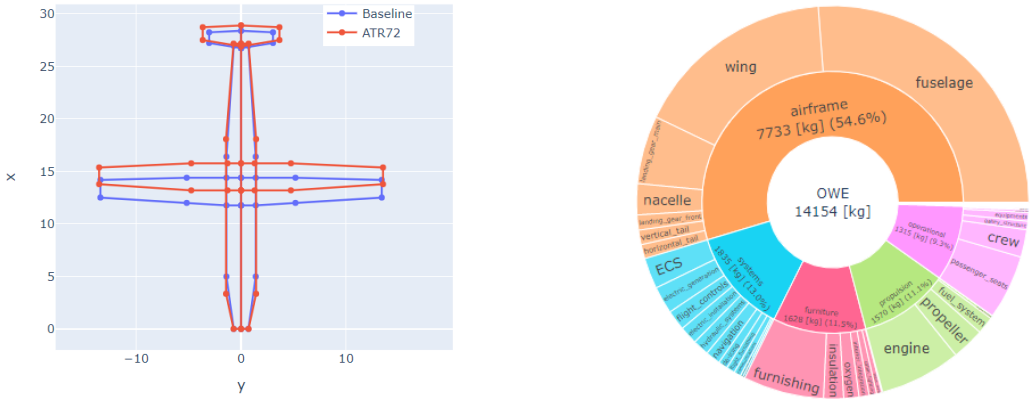

Figure 5.3: Main dimensions and weight breakdown of the baseline aircraft.

Parameter	ATR72 [117]	Baseline aircraft	Delta
MTOW	23000 kg	23572 kg	+2.5%
OWE	13500 kg	14154 kg	+4.8%
Wing area	61 m^2	59.9 m^2	-1.8 %
Take-off Power	2475 hp	2415 hp	-2.4%
Fuel flow at cruise speed	762 kg/h	699 kg/h	-8.3 %
Cruise glide ratio	Not disclosed	13-16	N/A
Block fuel for 200 NM	618 kg	609	-2.3%
Block fuel for 300 NM	859 kg	849	-1.2%

Table 5.4: General aircraft characteristics

The main dimensions of the baseline aircraft and the obtained weight breakdown are shown in Fig. 5.3. Its aerodynamic performance is illustrated in Fig. 5.4, where both a drag polar and a cruise drag breakdown are provided. Engine performance is shown in Fig. 5.5, where power-specific fuel consumption is plotted against altitude for different values of Mach number and throttle. Moreover, at flight idle (10% rated power) the specific fuel consumption increases up to 0.46 $kg/hp/kW$ at 25000 feet, which, compared to the rated cruise power at the same altitude, constitutes a twofold increase. These results are obtained using the 0D model of a twin-shaft free turbine engine presented in Section 3.5, which computes the thermodynamic properties of the airflow at the inlet and the outlet of each engine component and solves the power balance equations of the low pressure and high-pressure spools. Those results are integrated into the propulsion performance evaluation process through the use of a surrogate model as explained in Section 3.5.

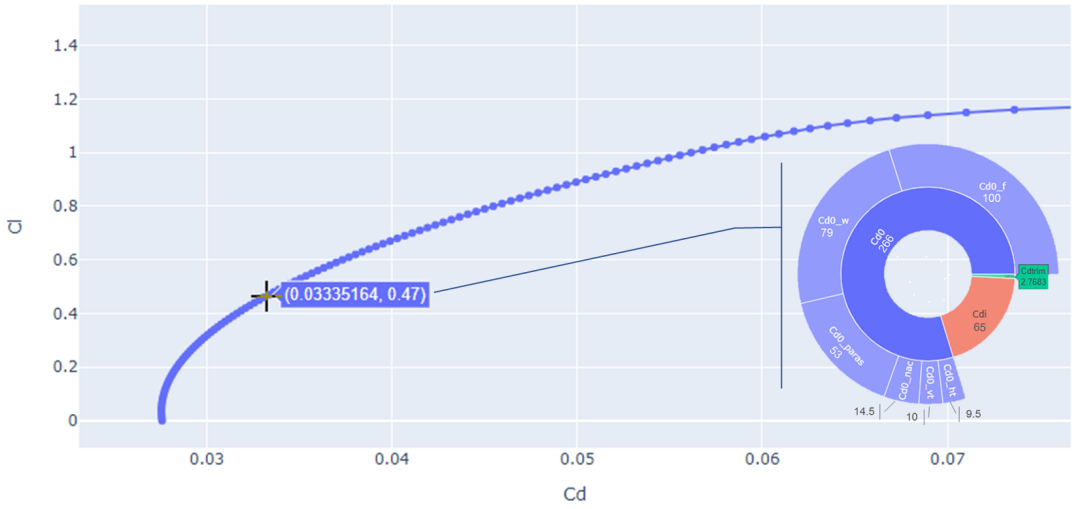

Figure 5.4: Aerodynamic performance of the baseline aircraft (Drag breakdown in drag counts).

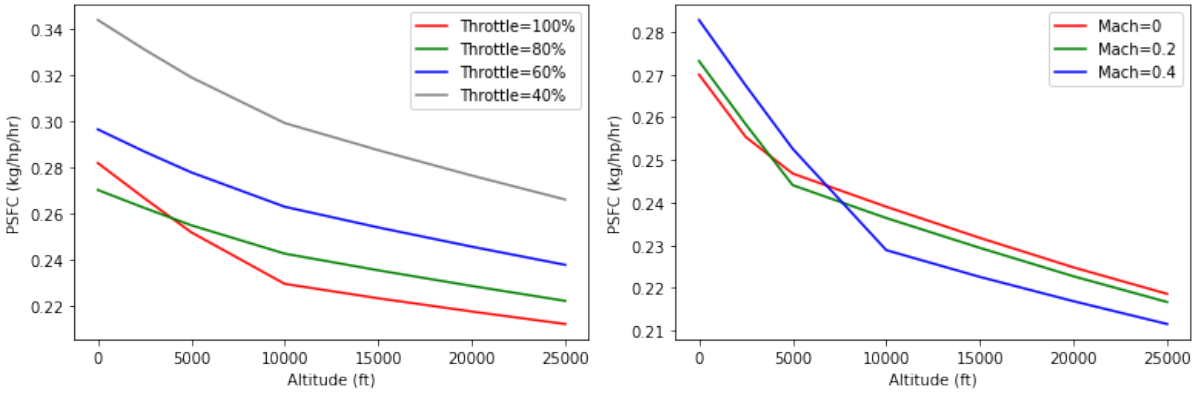

Figure 5.5: Gas turbine specific fuel consumption for different part-load operation conditions (left) and mach numbers (right).

5.2.1 Flight mission profile

Figure 5.6 shows the flight profile of a typical mission of 200 NM, where the altitude is represented by the black solid line and the flight speed and the total shaft power delivered by the two engines throughout the mission are illustrated respectively using dashed blue and red lines. The figure shows the flight mission profile starting from the end of the take-off segment at an altitude of 35 $feet$ and at a flight speed of roughly 115 $KCAS$.

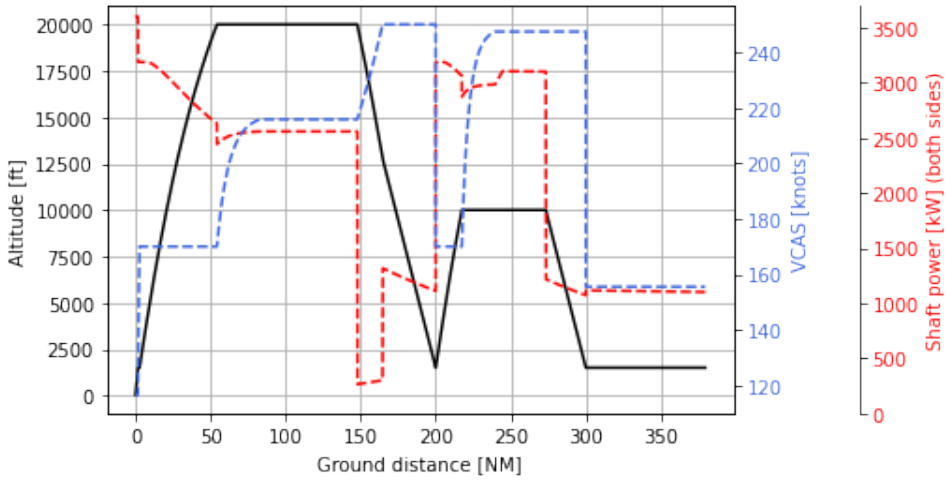

Figure 5.6: Baseline aircraft flight profile for 200 NM mission. The altitude is represented by the black solid line and the flight speed and total shaft power are illustrated respectively using the dashed blue and red lines.

The ground segments are not evaluated by the simulation but are taken into account in estimating flat-rate quantities of fuel needed for each phase as shown in Table 5.5. During the initial climb segment, the aircraft climbs to 1500 $feet$ where it accelerates to the target climb speed of 170 $KCAS$. Once the target climb speed has been reached,

the engine shaft power decreases from 1800 kW to 1600 kW due to the engine rating change from NTO (Normal Take-Off) rating - used for take-off and initial climb segments - to MCL (Max Climb) rating used for the climb segment. The climb phase is performed at a constant CAS speed of 170 *knots* and the shaft power delivered during this phase changes due to the change of altitude and Mach number, according to the thermodynamic limits of the gas turbine. At the end of the climb phase, once the target cruise altitude is reached, the engine rating switches from MCL to MCR (Max Cruise) rating and the aircraft accelerates to the max cruise speed. At a given altitude, this speed is a function of the aircraft payload and mission range, however for the typical mission of 200 NM under consideration the max cruise speed is about 295 $KTAS$ which is equivalent to a Mach number of 0.48. Finally, the descent phase is performed in two steps. First, the flight idle rating is used to allow the aircraft to descend and at the same time accelerate to the defined descent speed of 250 $KCAS$. Then, the descent is performed at constant CAS speed with the engines delivering enough thrust to keep the aircraft at a constant descent slope of -3°. The flight profile also shows the reserve mission comprising a 100 NM diversion and 30 min holding.

5.2.2 Aircraft in-flight performance

The simulation of a flight mission as described above allows for the evaluation of aircraft in-flight performance such as TTC (time to climb), block time, block fuel, reserve fuel, max cruise speed, etc. The main performance figures are shown in Table 5.5.

Ground segments allowances	
Taxi-out	9 kg 6 min
Take-Off	10 kg 1 min
Approach and Landing	20 kg 4 min
Taxi-in	3 kg 2 min
Aircraft performance	
Time to climb to FL200 @MTOW	16.9 min
Max cruise mach	0.48
Block fuel for 200 NM	609 kg
Block time for 200 NM	58 min
TOFL @MTOW, SL, ISA	1384 m
OEI net ceiling	2943 m

Table 5.5: Ground segments and aircraft performance.

OEI net ceiling and TOFL are evaluated using dedicated simulation models which take into account the event of an engine failure and its impact on both the available propulsive

power and additional trim drag as well as parasite drag from the feathered propeller.

The OEI ceiling performance provided in Table 5.5 has been evaluated with an iterative single-point calculation of the maximum altitude that the aircraft can reach by flying at the optimal climb speed with only one engine operating at MCT rating. According to section 25.123 of the certification specifications for large aeroplanes [118], the net ceiling is evaluated by applying a climb gradient penalty of 1.1% in order to conservatively account for aircraft performance degradation and pilot average skills. It is the altitude at which:

$$\frac{Thrust}{Weight} - \frac{Drag}{Lift} - 0.011 = 0 \tag{5.1}$$

The take-off segment is divided into three main phases: ground acceleration, rotation and airborne acceleration. The end of each phase is delimited by characteristics speeds which are described in Table 5.6. The take-off model evaluates the required speeds for given operating conditions according to the regulations for a CS25/FAR25 aircraft:

$$V_R > V_1$$
$$V_R > 1.05 \max\left(V_{MCG}, V_{MCA}\right)$$
$$V_2 > 1.13 V_{SR}$$
$$V_2 > 1.1 \max\left(V_{MCG}, V_{MCA}\right)$$

The take-off field length, defined as the shortest runway length that complies with safety regulations, is the most limiting of each of the following four criteria [119]:

- TOD_{N-1} = Take off distance with one engine inoperative. It is the distance covered from the brake release to a point at which the aircraft is 35 feet above the takeoff surface, assuming the failure of the critical engine at V_{EF} and recognized at V_1.
- 1.15 TOD_N = 115% of the take-off distance covered from brake release to a point at which the aircraft is 35 feet above the takeoff surface, assuming all engines operating.
- ASD_{N-1} = Accelerate stop distance with one engine inoperative. It is the sum of the distances necessary to:
  - Accelerate the airplane with all engines operating to V_{EF},
  - Accelerate from V_{EF} to V_1 with one inoperative engine,
  - Come to a full stop,
  - Plus a distance equivalent to 2 seconds at constant V_1 speed.
- ASD_N = Accelerate stop distance with all engine operatives. It is the sum of the distances necessary to:
  - Accelerate the airplane with all engines operating to V1,
  - With all engines still operating come to a full stop,
  - Plus a distance equivalent to 2 seconds at constant V1 speed.

Takeoff Speed	Definition
V_{MCA}	Minimum control speed in the air.
V_{MCG}	Minimum control speed on ground.
V_{EF}	Engine Failure speed at which the critical engine is assumed to fail.
V_1	Decision speed limit at which the pilot can interrupt takeoff = V_{EF} + 1s.
V_R	Rotation speed at which the aircraft is rotated for lift off.
V_{LOF}	Lift Off speed at which the aircraft lifts off the ground.
V_2	Takeoff climb speed to be reached before the 35ft takeoff height to meet the 2.4% gradient, with one engine inoperative.
V_{SR}	1 g stall speed for a specified configuration. It is a function of aircraft weight.

Table 5.6: Take-off speeds

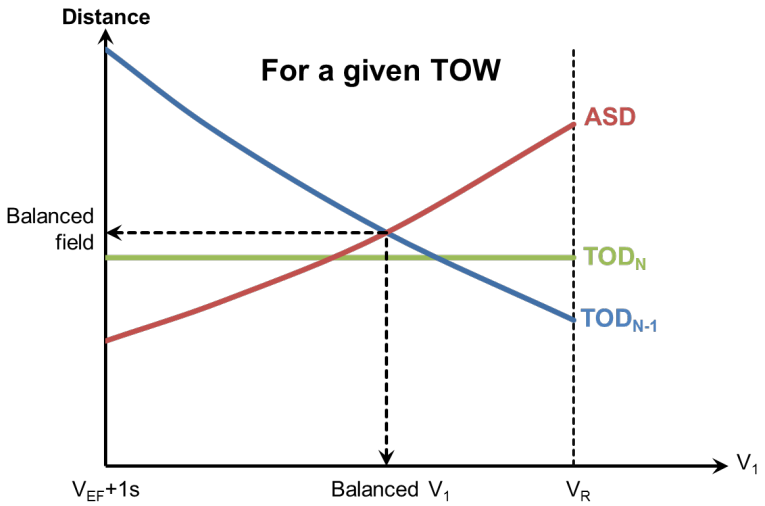

Figure 5.7: Balanced field length.

When the decision speed V_1 is such that the accelerate-stop distance equals the takeoff distance, the corresponding distance is called the Balanced Field Length (BFL). This distance depends on the operating conditions and weight. It is the minimum runway length on which the aircraft can take off. However, the balanced decision speed may be greater than the rotation speed, which is out of range. In that case, the minimum field length is the largest value between the take-off distance ($TOD = \max[TOD_{N-1}; 1.15\ TOD_N]$) and the accelerated stop distance ($ASD = \max[ASD_N;\ ASD_{N-1}]$) with

$V_1 = V_R$. The take-off field length of the baseline aircraft with a TOW of 23572 kg is 1384 m, which corresponds to the take-off distance with one engine inoperative. At this TOW there is no balanced field length, as V_1 would have to be greater than V_R. The take off lengths evaluated at $V_1 = V_R$ are: TOD_{N-1}= 1384 m, 1.15 TOD_N= 1209 m and ASD= 1325 m (see Figs. 5.8 and 5.9).

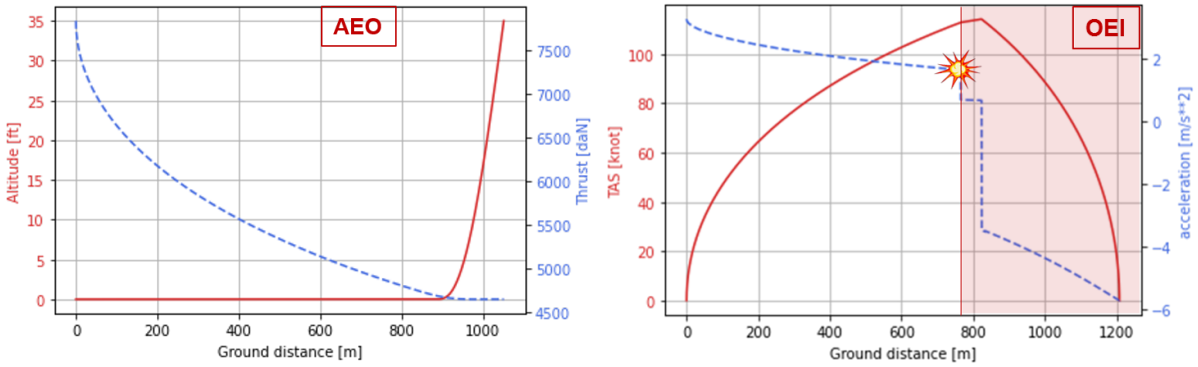

Figure 5.8: (left) Take off distance with all engine operative: altitude (red solid line) and total aircraft thrust (dashed blue line) versus ground distance. (right) Accelerate-stop distance with one engine inoperative: true airspeed (red solid line) and acceleration (dashed blue line) versus ground distance.

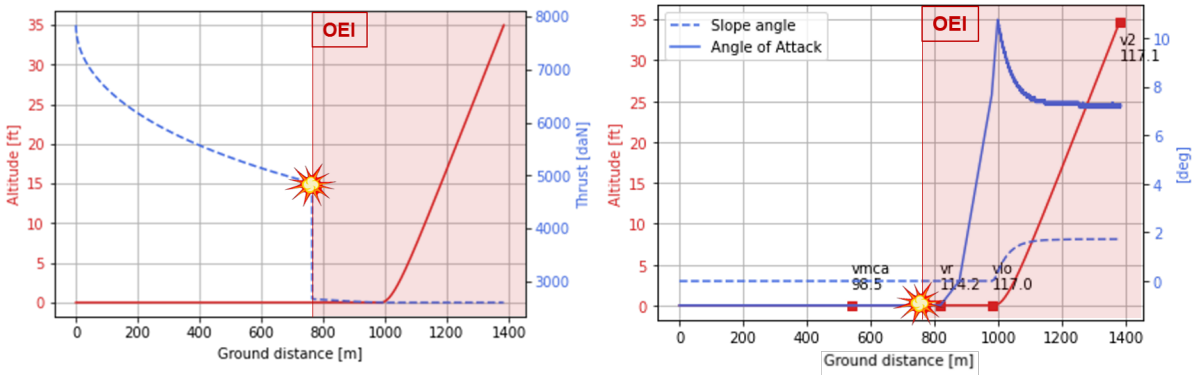

Figure 5.9: Take off distance with one engine inoperative: (left) altitude (red solid line) and aircraft thrust (blue dashed line) plotted against ground distance. (right) Altitude (red solid line), angle of attack (blue solid line) and slope angle (blue dashed line) plotted against ground distance.

5.3 Conclusion of the chapter

- The overall aircraft design process available in the open-source version of FAST-OAD is particularly suited for the design of a single-aisle aircraft such as the Airbus A320.

- In order to design a regional turboprop aircraft and to perform the forward fit design with innovative propulsion systems, new design processes have been implemented. The development of those processes and of the simulation models needed for the analysis of the new propulsive system culminated in an evolution of the FAST-OAD design tool which is named RHEA.

- The overall aircraft design process implemented in RHEA has been used to design a 70-seat regional turboprop aircraft similar to the ATR72. The main results and performances of the obtained aircraft have been presented in this chapter. The resulting aircraft design denoted as baseline aircraft has been validated by comparing the obtained aircraft characteristics with the available published data of the ATR72.

Part III

Exploration of low-emission propulsion technologies design space for regional air transport

Chapter 6

Set-up of the processes for the performance assessment of low-emission regional aircraft

Contents

6.1 Overall approach to the design space analysis

This chapter deals with the analysis of the different propulsive configurations suitable for the regional aircraft under study. According to the main findings of the previous studies summarized in Section 1.1, three main categories of propulsion systems have been identified to replace the conventional gas turbine in order to provide better environmental performance: battery electric, hydrogen and turbo/hybrid-electric propulsion.

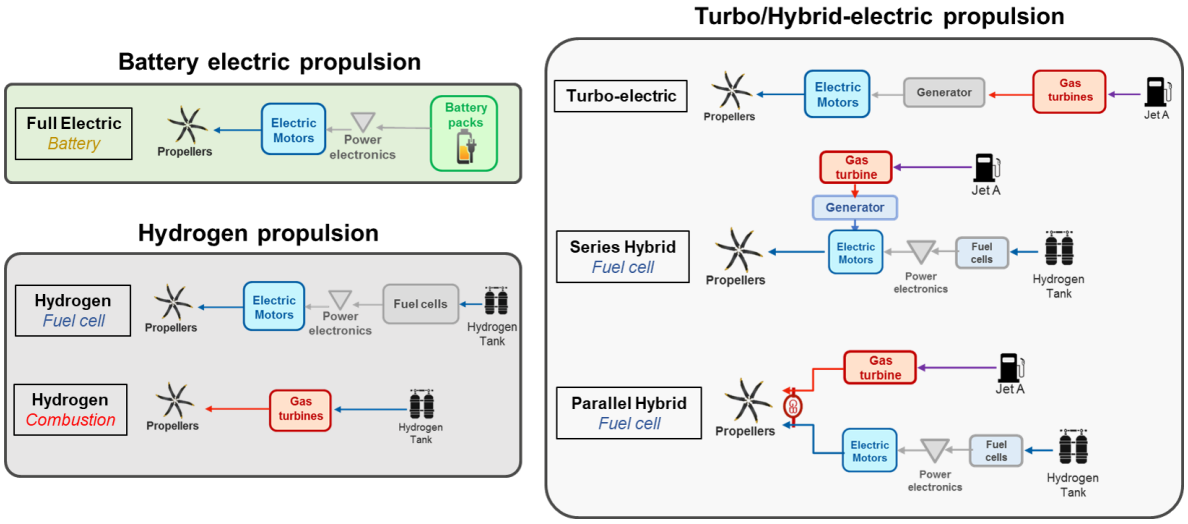

Figure 6.1: Overview of three different propulsive configurations suitable for the regional aircraft.

Battery electric propulsion relies exclusively on batteries for the generation of the required propulsive power. Hydrogen propulsion instead uses hydrogen as fuel and can generate the required propulsive power either by burning hydrogen in a gas turbine or through the use of electric motors and fuel cells. Finally, hybrid propulsion comprises all the propulsive systems making use of at least two power sources. This category can be further subdivided according to the propulsive layout and energy source used. All the propulsive architectures are shown in Fig. 6.1. The series and parallel hybrid architectures with batteries have been omitted from Fig. 6.1 for an easier representation of the architectures, but are nonetheless under study. Therefore, a total of eight propulsion systems has been identified to potentially replace the conventional gas turbines. Given the large number of architectures, a down-selection process consisting of three steps is established as shown in Fig. 6.2:

- *Step 1 - Conceptual studies*: high-level studies are performed using spreadsheets, rather than more complex aircraft design tools, to identify the main challenges and benefits to be expected from the architecture under study. For the configurations analyzed at this stage, data about the propulsive system and component performance derived from previous studies are used to understand the impact of the propulsive system at the aircraft level. Moreover, global sensitivity analyses are

carried out to identify the parameters that trigger the switch in the design process to higher fidelity analyses, based on uncertainty propagation.

- *Step 2 - Preliminary design studies*: more detailed analysis and calculations are performed both at the system and aircraft level. Dedicated models of the propulsive systems are created to characterize their behaviors and evaluate their performances. Those models are integrated into RHEA in order to size the systems and evaluate aircraft performance throughout a given flight mission. Trade studies are also performed in order to identify the most influencing and significant design variables.

- *Step 3 - Design optimization studies*: at this stage, optimizations are performed in order to determine the propulsive system design variables to enhance the selected aircraft performance metrics. Global sensitivity analyses are carried out in RHEA to identify and propagate the uncertainties through the simulation in order to increase the reliability of the aircraft performance assessment and to give additional meaning to the results.

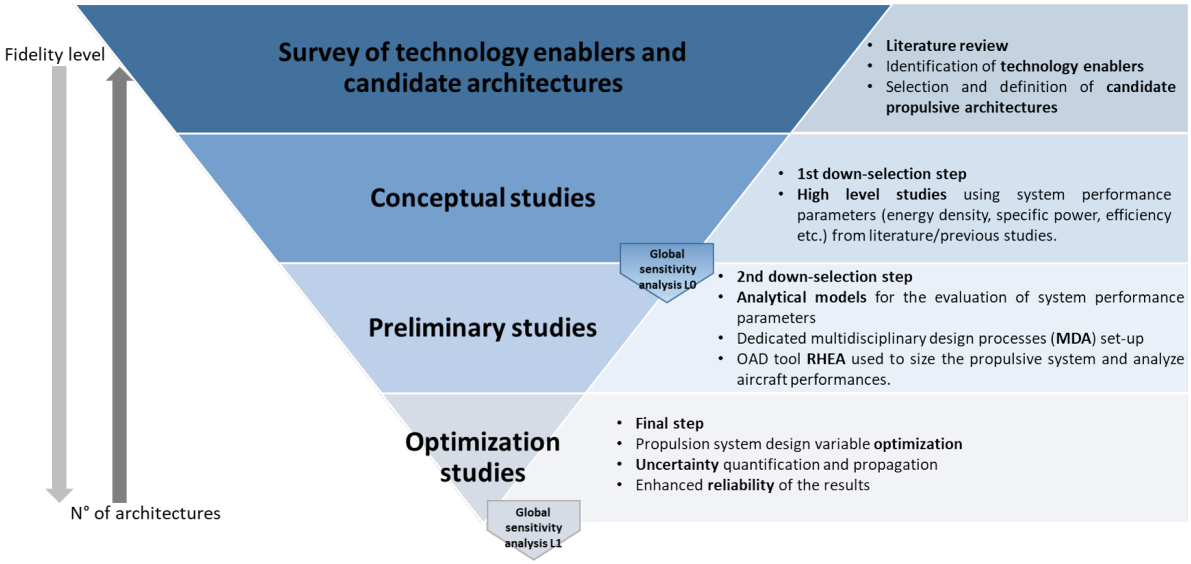

Figure 6.2: Down-selection process for the exploration of the propulsive system design space

At each step, main results and conclusions are used to select the most promising configurations and direct the modeling and research efforts on those which are further studied in the next step with an improved version of the multidisciplinary design process. Therefore, only few architectures are analyzed at the highest level of detail, with design optimization studies. With this approach, only the most promising architectures are deeply analyzed with the level of fidelity of the studies and the quantity of information which increase at each down-selection process. However, when adding complexity to the models does not lead to a better understanding of the system and/or does not improve the accuracy of

the results, the architecture is not further studied and its assessment stops. Indeed, the process is only valid if the models used to determine the performance of a given propulsive architecture can be further developed to provide more insights into the system, leading to more accurate and precise analyses.

The design philosophy of the new aircraft configurations equipped with the propulsive architectures under study consists of a "forward-fit" approach rather than ex-novo design, meaning that the air-frame geometry (wing, fuselage, tails and undercarriage) and weight are kept unchanged with respect to the baseline turboprop aircraft designed in Section 5.1. The objective is to provide a reliable preliminary assessment of the performance of such propulsion systems applied on a large turboprop passenger aircraft and to assess its impact on the overall aircraft performance.

6.2 Design process for the forward-fit of the baseline aircraft

The design of a regional 70-seat aircraft featuring a low-emission propulsion system is carried on using a forward-fit approach. It means that the aircraft is designed starting from the characteristics of the obtained baseline turboprop aircraft design presented in Section 5.2 but integrates a new propulsion system (among the ones identified in Section 6.1. The overall design process is shown in Fig. 6.3.

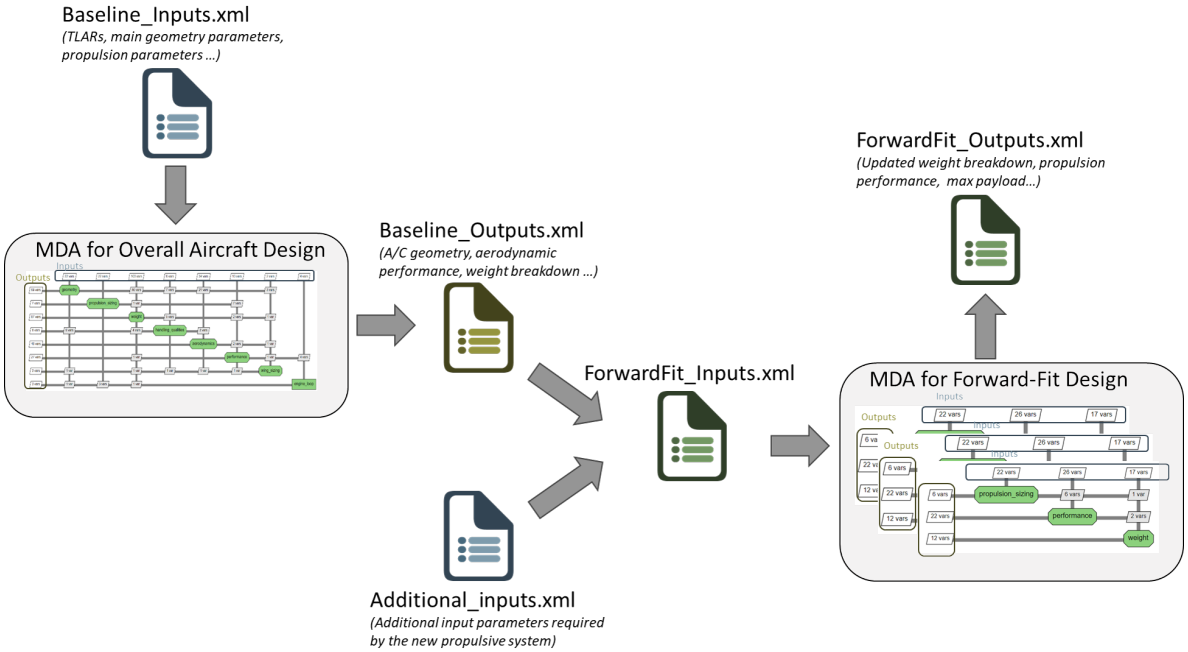

Figure 6.3: Overall process: from the overall design of the baseline aircraft to its forward fit with the new propulsion system.

The MDA introduced in Section 5.1 and used to design the baseline aircraft provides all the information needed to characterize the aircraft performances, among which the aerodynamic polars, weight breakdown and maximum takeoff weight, and collect them in an output `xml` file, which, after the addition of few extra parameters required for the new propulsion system, becomes the input file of a new multidisciplinary design analysis. The MDA for forward-fit design is used to size the new propulsive system and to assess its impact on aircraft weights and performances. Although the MDA process is specific to each propulsion system to be designed, there are some commonalities that can be found. Indeed, regardless of the propulsion system, the MDA for the forward fit design can always be represented using three main groups of functions: propulsion sizing, performance and weight. The specific functions contained in each group as well as the interrelationships between them are specific to each system. Figure 6.4, for example, shows the MDA process for the forward fit of the baseline aircraft with parallel hybrid propulsion with batteries for the generation of electric power.

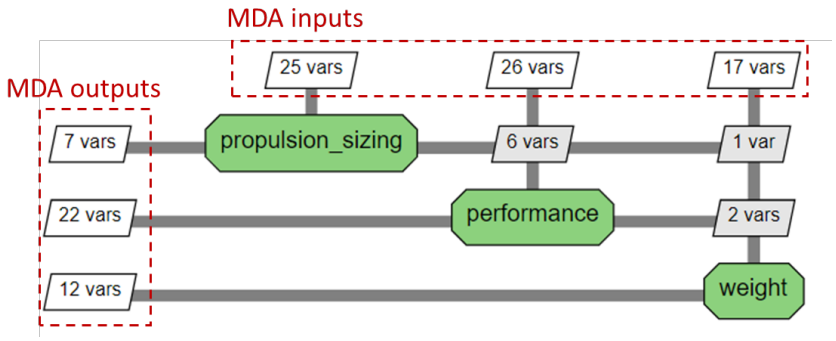

Figure 6.4: MDA for the forward-fit design of the baseline aircraft with the battery-based parallel hybrid propulsion system.

In such a process, the geometry and aerodynamic modules are not used because all the necessary data for the mission performance calculation (such as aerodynamic polars, wing reference area, etc.) are directly provided as inputs to the performance module. Moreover, there is no iterative loop required between the performance module and the weight module because the MTOW of the aircraft is also provided as an input, thus it is not a function of the fuel weight and the battery weight required by the aircraft to fly the given mission. Therefore, the weight module is used only to provide the new weight breakdown of the aircraft, updating its OWE due to the change in the propulsion system weight. Given that the MTOW is fixed, the change in OWE leads to the calculation of a new max payload that the aircraft can carry, thus the maximum number of passengers is obtained as an output of this module. Other outputs of the MDA shown in Fig. 6.4 are, for example, the mass of the new gas turbine and of the batteries as well as the power profiles and energy consumption of both gas turbines and electric motors throughout the flight.

Figure 6.5 shows the MDA process used for the retrofit of the baseline aircraft with a parallel hybrid propulsion system featuring hydrogen fuel cells instead of batteries for the generation of electric power. The overall process is really similar, with only the propulsion sizing, performance and weight modules being used and all the aerodynamic and geometric characteristics of the aircraft being provided as inputs in the `xml` file. Nevertheless, unlike the MDA shown in Fig. 6.4, the design process of the fuel cell hybrid electric aircraft comprises a feedback loop between the performance and the propulsion sizing module. This iteration is related to the sizing of the hydrogen tank which, in order to determine its gravimetric efficiency, needs as input the total hydrogen quantity to be stored. Such a variable is indeed evaluated in the performance module which receives from the propulsion sizing module all the required inputs to determine fuel cell efficiency at each flight point during the mission.

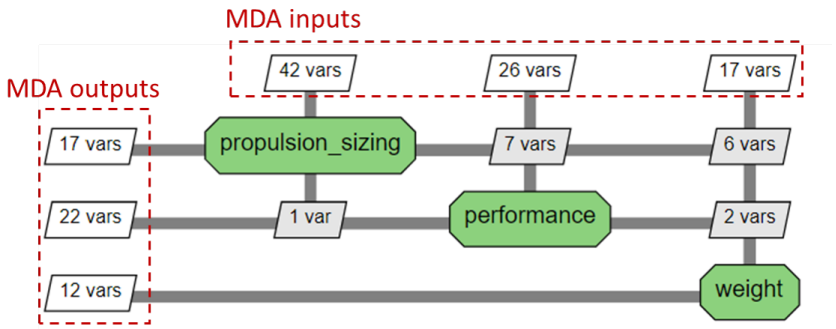

Figure 6.5: MDA for the forward-fit design of the baseline aircraft with hydrogen fuel cell-based parallel hybrid propulsion system.

It can be noted that the number of inputs provided to the propulsion sizing groups in the two processes (battery-based and fuel-cell based) is significantly different, as shown in Fig. 6.6. That is because, in the case of the battery-based hybrid propulsion system, such a module is only composed of the gas turbine sizing function (the same as the one in the baseline aircraft design process in Section 5.1) and a battery sizing function which simply evaluates the specific energy of the battery pack taking into account the input integration factor, the specific energy of the battery cell and the minimum state of charge allowed. On the other side, the propulsion sizing group for the fuel cell hybrid propulsion system is composed of the gas turbine sizing function, the fuel cell stack sizing function and the fuel cell balance of plant (BoP) sizing function. The fuel cell stack sizing function determines the polarization curve of the fuel cells, the number of cells to be stacked and the optimal operating point based on several inputs such as the input nominal power, active cell surface, weight parameter, etc., as described in Section 4. The fuel cell BoP sizing function instead is used to determine the specific power of the fuel cell system including all the components required for its operation (e.g. compressor, humidifier, valves, etc.) as well as to determine the main characteristics of the hydrogen

tank (geometry and gravimetric efficiency) and distribution system (linear density in kg/m).

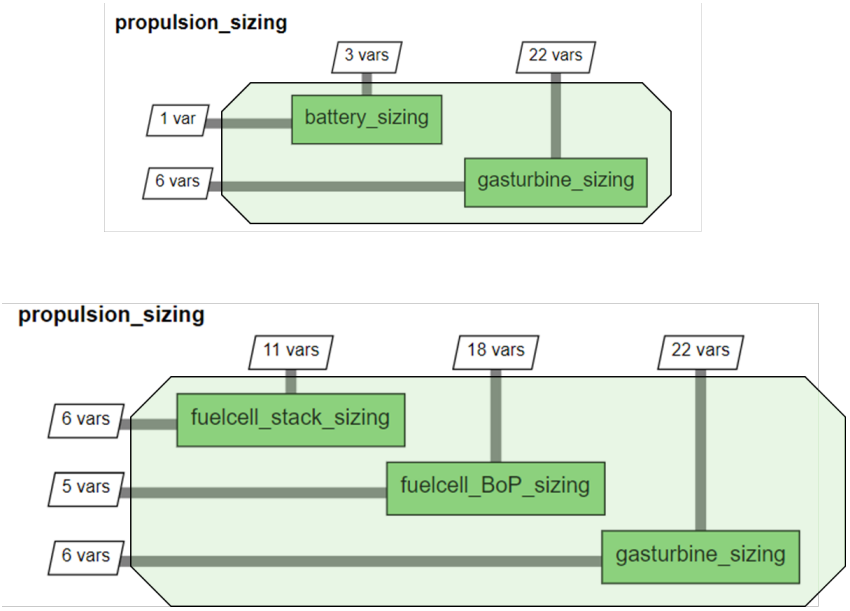

Figure 6.6: Function breakdown of the propulsion sizing group for the battery-based (top) and fuel cell-based (bottom) hybrid propulsion systems.

6.3 Conclusion of the chapter

- The overall approach employed for the analysis of the design space of low-emission propulsion systems to forward-fit the baseline aircraft consists of three steps. At each step, the number of propulsion architectures to be analyzed is reduced and the level of fidelity of the analyses is increased.

- The process from the overall design of the baseline aircraft to its forward fit with the new propulsion system has been set in place. From a few sets of inputs and top-level aircraft requirements, the process first designs the baseline conventional aircraft and then uses the output files produced as inputs for the "forward-fit" MDA, which performs the sizing of the given propulsion system and evaluates aircraft performance and weight breakdown.

- In the following, each chapter presents the studies of all the architectures that have been analyzed and intermediate conclusions are provided to support the selection of the propulsion architecture which are further analyzed in the next step.

Chapter 7

Conceptual studies

Contents

7.1 Battery electric propulsion: *FE-EB* architecture

The full electric architecture using batteries (named *FE-EB*) for electrical power generation has aroused great interest among the research community. It has been a preferred solution in the automotive sector and it has been subject to several studies and publications also in the aviation sector [13, 19, 120]. This solution offers great benefits in terms of ease of integration and economic viability with respect to much more complex electric propulsion systems based on hydrogen fuel cells.

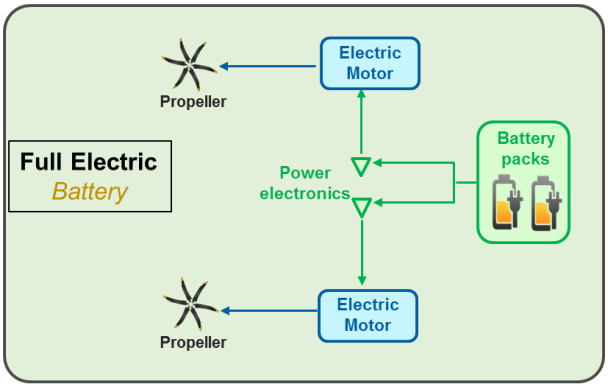

Figure 7.1: *FE-EB*: Full electric architecture layout with batteries.

A simplified layout of the propulsive architecture is shown in Fig. 7.1, where the term "battery pack" refers to the fully integrated power generation module including battery cells, housing, electrical connections and cooling system. In order to investigate the technical viability of this propulsive architecture to power the regional aircraft designed in Section 5.1, the mass and the volume of the batteries required to power the electric motors that drive the propellers are assessed. For that, three generations of battery technology have been considered: commercial Li-Ion, Advanced Li-Ion and Solid State batteries. The specifics of those battery technologies are given in Section 1.2.1, however, their performances are shown once again in Table 7.1. The evaluation of the mass and volume of the battery pack are obtained by dividing the battery cell values by an integration factor of 1.35.

	Current Li-Ion	**Advanced Li-Ion**	**Solid State**
Specific energy @cell	235 Wh/kg	350 Wh/kg	500 Wh/kg
Energy density @cell	630 Wh/l	750 Wh/l	1000 Wh/l
Specific energy @pack	174 Wh/kg	259 Wh/kg	370 Wh/kg
Energy density @pack	467 Wh/l	556 Wh/l	741 Wh/l

Table 7.1: Indicative performance of potential technological advancement of battery cells [58].

The evaluation of batteries mass and volume starts from the estimation of the total

energy that those batteries need to provide to the propellers for the generation of the required thrust. Figure 7.2 shows the flight profile of the baseline turboprop aircraft with a TOW=MTOW for a 200 NM mission (plus 100 NM diversion and 30 min holding) at the typical flight speeds presented in Section 5.1. The figure gives the evolution of the shaft power and the expended energy monitored at the gas turbine shaft at any point during the mission.

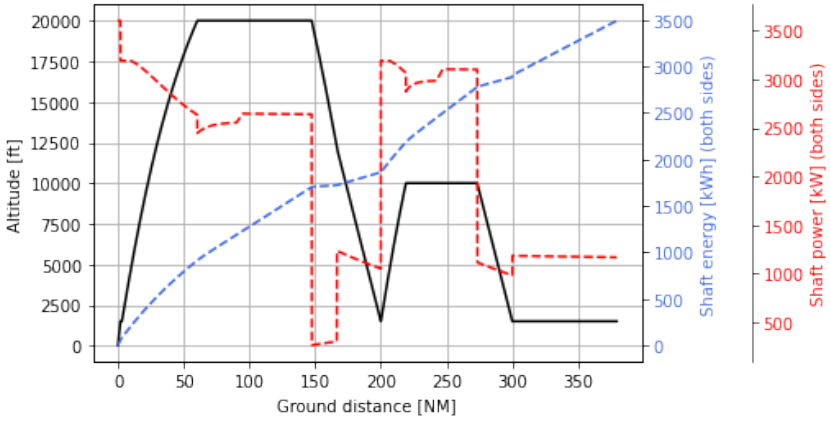

Figure 7.2: Flight profile of the baseline aircraft for a 200 NM mission. The black solid line shows the flight altitude, while the red and blue dashed lines show respectively the total propeller shaft power and the total energy expended by the propellers.

The total shaft energy expended by the baseline aircraft with turboprops to fly both the main and the reserve missions is about 3500 kWh. For the same aircraft equipped with full electric propulsion (thus the same geometry, TOW and aerodynamics performance as the baseline aircraft), the evolution of the shaft power (and thus energy) would look slightly different for two reasons. First, during the climb, the increase in altitude would not lead to a decrease in shaft power because, unlike the gas turbines, the performances of electric motors are not affected by the change of air density with altitude, thus the output power would be constant throughout the climb phase. Then, by using batteries instead of burning fuel to generate propulsive power, the aircraft weight remains constant and equal to the TOW, thus the power required to fly at the same altitude and speeds during the cruise and holding phases would be higher for the electric aircraft. Nevertheless, the value of 3500 kWh, which refers to the total energy expended by the baseline turboprop aircraft to fly 200 NM (plus 100 NM diversion and 30 min holding), gives a first approximation of the total energy that must be supplied by the electric propulsion system. Assuming efficiencies of 97% and 98% respectively for the electric motor and power electronics, the total energy that will be used to size the electric batteries is given by:

$$\text{Required battery energy} = \frac{3500\,kWh}{0.97 \times 0.98} = 3682\,kWh \tag{7.1}$$

The mass of the full electric propulsion system is given in Table 7.2, where the mass of the electric motors and power electronics are evaluated considering specific power

	Current Li-Ion	**Advanced Li-Ion**	**Solid State**
Electric motors mass	514 kg		
Power electronics mass	328 kg		
Battery packs (cells) mass	21152 (15668) kg	14202 (10520) kg	9941 (7364) kg
Battery packs (cells) volume	7889 (5844) l	6627 (4909) l	4971 (3682) l
Total mass	21994 kg	15044 kg	10783 kg

Table 7.2: Electric propulsion mass breakdowns for three battery technologies to supply two 2415 hp electrical motors and a total of 3682 kWh of energy.

values of 7 and 11 kW/kg, respectively. The results obtained show that due to the mass of the electric propulsion system, none of the three battery technologies investigated gives feasible results. Indeed, given that the baseline aircraft OWE without the gas turbines and fuel system is about 13000 kg, even considering the solid-state battery technology, almost 10000 kg of batteries is required. Therefore, the total mass of the electric propulsion system would be as high as 10783 kg, leading to an OWE of 23783kg, which is higher than the aircraft MTOW of 23572 kg. In order to give a preliminary estimation of the battery performance that would be required to allow full electric flight for a regional 70-seat aircraft, the same calculations of Table 7.2 were repeated using specific energy values of battery cells between 600 and 1500 Wh/kg. The results are shown in Fig. 7.3 where both battery mass (m_{Bat}) and maximum payload are plotted versus the battery specific energy assumption. Given the aircraft MTOW of 23572 kg and OWE (without batteries) of 13842 kg, the maximum payload is simply estimated by the following difference:

$$Payload = MTOW - OWE - m_{Bat} \tag{7.2}$$

Assuming 95 kg for each passenger, Fig. 7.3 shows that, for example, in order to carry more than 50 passengers, at least a two-fold increase is needed in battery performance with respect to the best technological projection for the Li-Ion technology. Moreover, these results were obtained considering a full discharge of the batteries during the flight, therefore if a minimum state of charge (SOC_{min}) is imposed to preserve battery life, then a further increase of battery mass (thus a decrease in max payload) is to be expected.

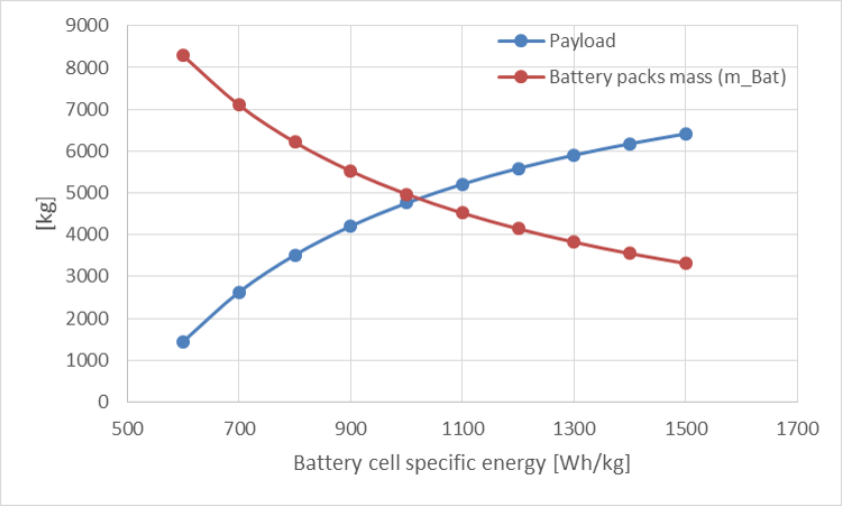

Figure 7.3: Evolution of batteries mass and max payload with the battery specific energy assumption for a 200 NM mission. Calculations are performed for an aircraft with a MTOW of 23572 kg and an OWE (without batteries) of 13842 kg.

7.2 Hydrogen propulsion

7.2.1 Full Electric - Hydrogen Fuel Cells (FE-FC) architecture

Full electric propulsion can also be realized by means of hydrogen fuel cells instead of batteries. However, while batteries fulfill both functions of energy storage and electrical power generation, an electric propulsion system based on hydrogen fuel cells is composed of hydrogen tanks for energy storage and fuel cells for electrical power generation.

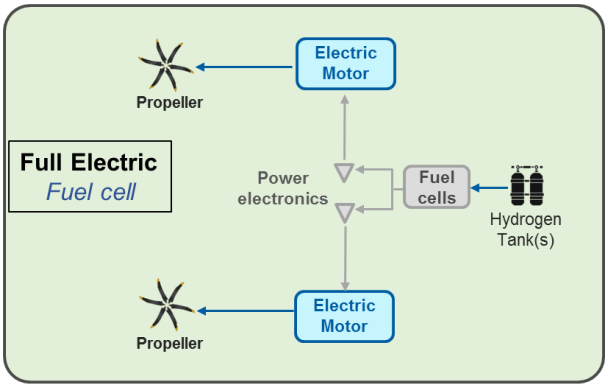

Figure 7.4: FE-FC: Full electric architecture layout with hydrogen fuel cells.

This study aims at providing a preliminary assessment of the weight impact of fuel cell propulsion for a regional aircraft. In order to be able to easily compare its performance to battery-powered aircraft, the entire hydrogen system upstream of the electric power conversion system will be considered as a whole. The mass breakdown is therefore composed of the masses of the following components: propellers, electric motors, power electronics

and hydrogen system (incl. fuel cells and hydrogen tank). As for the full electric battery configuration study, it is assumed that the fuel cell electric propulsion system shown in Fig. 7.4 equips the baseline aircraft designed in Section 5.1, replacing the conventional gas turbines with no modifications to its external geometry, MTOW and aerodynamics performance. The take-off power of this aircraft is 1800 kW, therefore the fuel cells as well as the electric motors and power electronics are sized accordingly. For that, the same specific power values as for the full electric battery study are used for the electric motor and power electronics, while three technological scenarios are considered for the fuel cells and for the hydrogen tank gravimetric efficiency. Table 7.3 summarizes the technological assumptions used.

	Scenario 1	**Scenario 2**	**Scenario 3**
Electric motor specific power	7 kW/kg		
Power electronics specific power	11 kW/kg		
Fuel cells specific power	1 kW/kg	1.5 kW/kg	2 kW/kg
Hydrogen tank gravimetric efficiency	15 %	30 %	45%

Table 7.3: Technological assumptions for the full electric fuel cell architecture.

The total energy required by this aircraft to fly a given mission is given in Fig. 7.5 as a function of the flight distance.

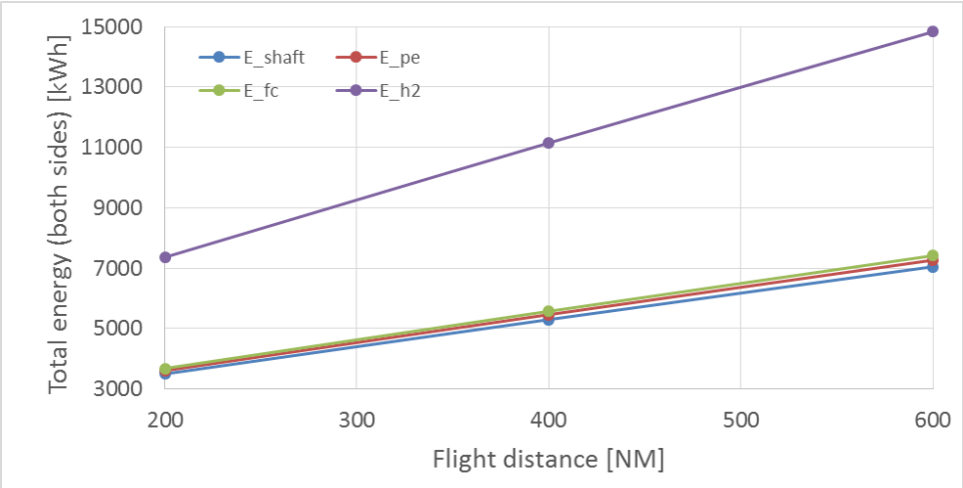

Figure 7.5: Total energy expended by the baseline turboprop aircraft versus flight distance. The energy values take also into account the energy required to fly 100 NM of diversion flight and 30 min of holding.

The shaft energy (E_{shaft}) values given in the picture have been obtained by simulating the flight mission of the baseline aircraft for any given distance and by tracking the power output of the gas turbine and integrating this power over the whole flight duration to obtain the energy value. Of course, these values are a rough estimation of the total energy

that must be supplied by the electric propulsion system, but for the purpose of this study, they are considered valid approximations. The total hydrogen energy (E_{h2}) required is evaluated starting from the shaft energy and assuming the component efficiencies as shown in Fig. 7.6. Then, the hydrogen tank mass is calculated using different assumptions for gravimetric efficiency.

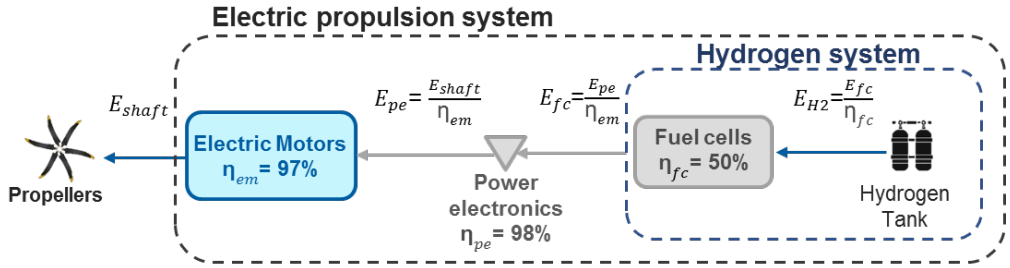

Figure 7.6: Energy conversions for full electric fuel cell propulsion architecture.

Given the total energy and the total power to be provided, the propulsion system mass is then evaluated using the component performance given in Table 7.3. Figure 7.7 shows the values of specific energy of the hydrogen systems for each technological scenario. Regardless of the scenario, the specific energy of the hydrogen system is always higher than the battery. Moreover, contrarily to the battery system, it tends to increase with longer flight distances, because, even if the mass of the fuel cells is constant, increasing the range leads to an increase in energy requirement and thus an increase in hydrogen and tank mass.

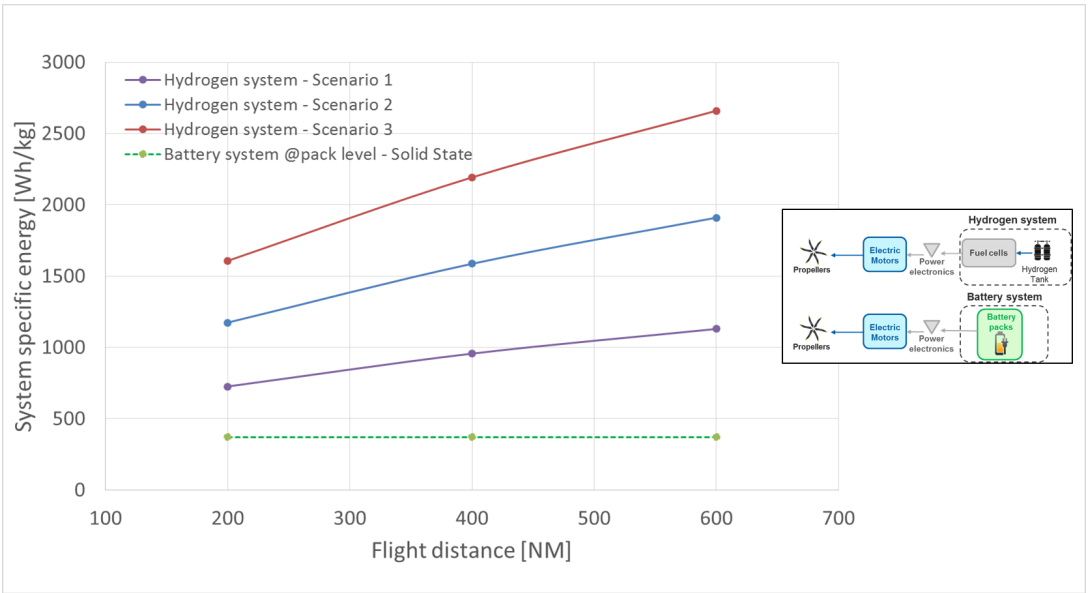

Figure 7.7: Comparison between the most advanced battery technology and three hydrogen systems in terms of system specific energy. Each solid colored line represents a different technological scenario for the components of the hydrogen system.

Compared to the gas turbine system (see Fig. 7.8), the full electric fuel cell system shows satisfactory performance with values of specific energy and power that are as high as for the gas turbine system in the most optimistic scenario.

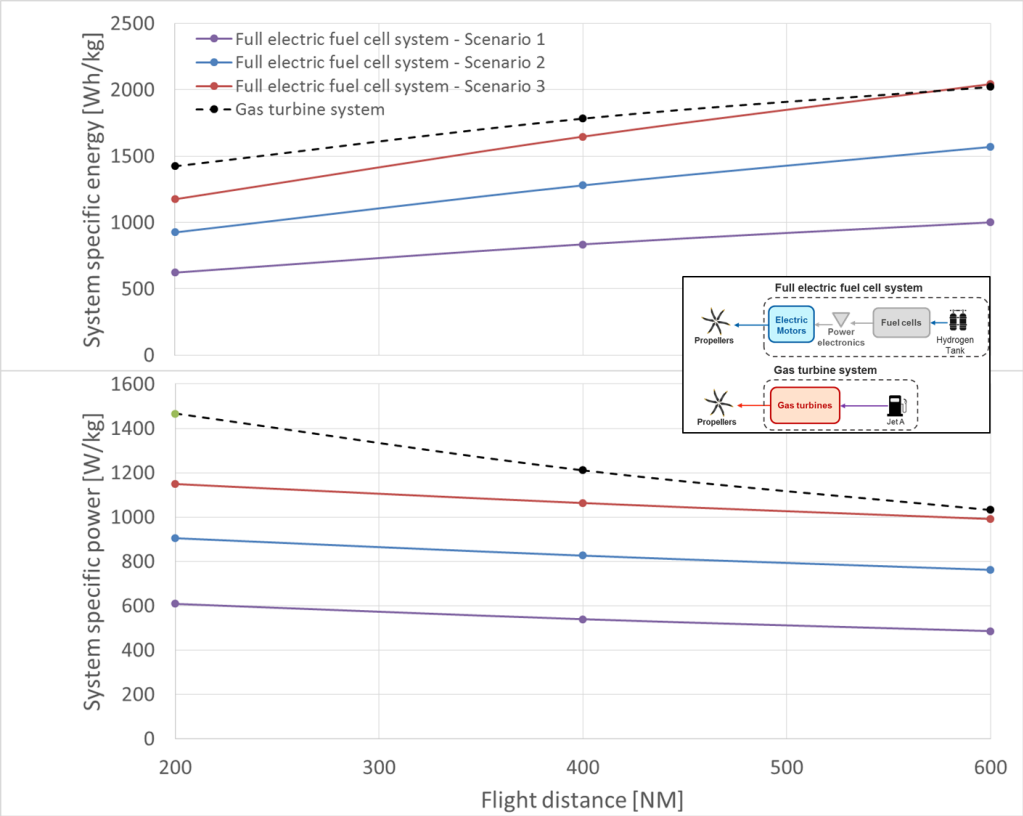

Figure 7.8: Evolution of specific energy and power characteristics of a fuel cell electric propulsion system of 1.8 MW designed for different design ranges. The solid colored lines represent the fuel cell system performance with the different technological scenarios and the black dotted line represents the conventional gas turbine system.

Hydrogen is indeed known for its high specific energy (Wh/kg) which is almost three times higher than jet fuel. Nevertheless, it raises significant concerns for its low energy density (Wh/l). Given a certain amount of energy, a volume almost four times higher than jet fuel is needed for liquid hydrogen. Moreover, while jet fuel is easily stored in the wings, hydrogen is not a viable solution due to the limited space available and the complex shape the hydrogen tanks would require. Thus, hydrogen tanks would more likely be stored at the back of the fuselage, potentially in a non-pressurized environment, obtained for example by moving forward the rear pressure bulkhead. This would clearly result in a reduction of the passenger cabin volume and/or in the integration of external pods that could be installed under the wings, leading to additional drag forces. A first estimation of the cabin volume that would be required to store the needed amount of hydrogen is provided in Table 7.4 and is evaluated knowing the hydrogen mass needed for the three flight missions of the previous calculations and the density of liquid hydrogen ($= 0.071\ kg/l$). Although the mass of hydrogen is nearly a sixth of the mass of jet fuel,

its volume is considerably higher (more than double) and, as previously said, it cannot be stored in the wings, which complicates its integration on board the aircraft.

	200 NM	**400** NM	**600** NM
Hydrogen mass	221 kg	335 kg	445 kg
Hydrogen volume	3111 l	4712 l	6267 l
Jet fuel mass	1306 kg	1820 kg	2335 kg
Jet fuel volume	1633 l	2275 l	2918 l

Table 7.4: Hydrogen mass and volume required by the baseline aircraft equipped with the fuel cell propulsion system to fly three mission distances. The values for the jet fuel have been evaluated simulating the three missions with the baseline aircraft with its conventional gas turbine system.

Moreover, those figures are considerably underestimated since they only take into account the volume of the liquid hydrogen, thus neglecting the volume occupied by additional components such as valves, heat exchangers, piping and attachments to the air-frame. Furthermore, other parameters such as tank geometry, venting pressure and fill pressure, play a significant role in the sizing of the hydrogen tank itself. In fact, due to boil-off losses, hydrogen tanks need to have a minimum volume of gaseous hydrogen at the venting pressure, which limits the maximum allowable fill percentage of the tank with liquid hydrogen. The liquid volume fraction of the tank is strongly influenced by the combination of filling and venting pressure and can be as low as 65% as shown by Verstraete [57]. Considering that the hydrogen density in a gaseous state at 1 bar is as low as 0.00009 kg/l (three orders of magnitude lower than liquid hydrogen), the concerns about hydrogen tank integration are justified.

7.2.2 Hydrogen gas-turbine (TP-$H2B$) architecture

Another possibility of using hydrogen as an energy carrier on board an aircraft is to burn it directly into the gas turbine. Although much simpler and lighter than fuel cell propulsion, such a propulsive system is significantly less efficient.

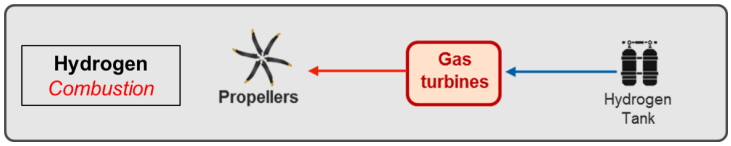

Figure 7.9: TP-$H2B$: Hydrogen gas turbine architecture

For the regional aircraft under study, assuming that the gas turbine efficiency when burning hydrogen is equivalent to the efficiency of traditional kerosene turbines [121], the hydrogen needed to propel the aircraft over three flight distances is given in Table 7.5.

	200 NM	**400** NM	**600** NM
Jet fuel mass	1306 kg	1820 kg	2335 kg
Hydrogen mass	466 kg	649 kg	833 kg

Table 7.5: Hydrogen mass required by the baseline aircraft equipped with hydrogen gas turbines to fly three mission distances. The values for the jet fuel have been evaluated simulating the three missions with the baseline aircraft with its conventional gas turbine system.

Given its specific energy almost three times higher than jet fuel, the hydrogen mass required to produce a certain amount of mechanical power is about a third of the jet fuel mass. However, due to the mass of the tank needed to store the liquid hydrogen, the use of hydrogen as fuel still leads to an increase of the OWE of the aircraft, as shown in Fig. 7.10.

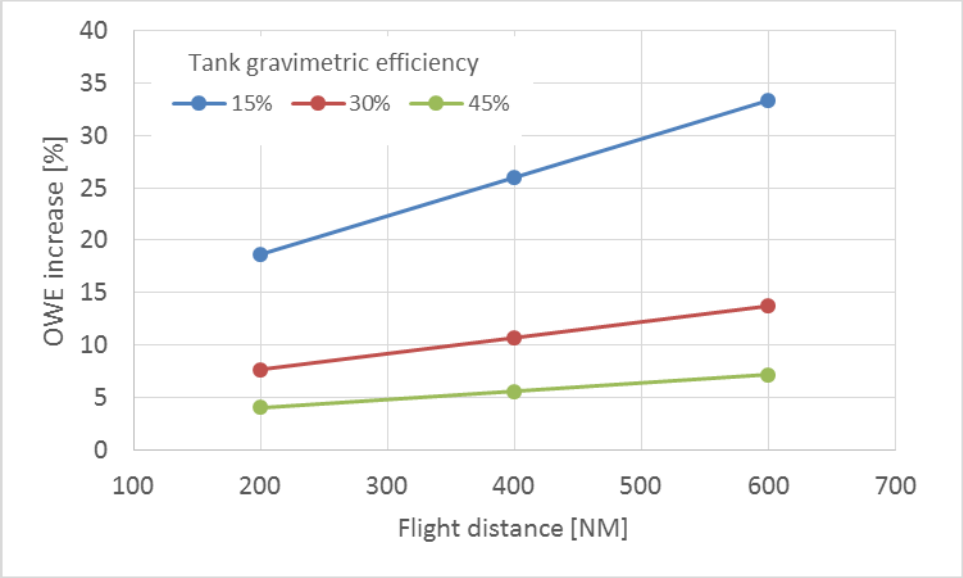

Figure 7.10: Percentage of OWE increase of the baseline aircraft equipped with hydrogen gas turbine according to the design mission distance and the technological scenario assumed for the tank gravimetric efficiency.

With such increases of OWE, except for the most optimistic scenario with a gravimetric efficiency of the liquid hydrogen tank of 45%, the mass saving resulting from the use of a fuel with much higher energy content such as hydrogen is always balanced off by the additional mass of the tank. Moreover, given the significant quantities of hydrogen involved, it is worth making some considerations about the actual emissions related to the hydrogen life cycle. Indeed, although hydrogen combustion is not responsible for the emission of greenhouse gases with the exception of water vapor, the whole process from its production to conditioning and distribution may be responsible for significant

emissions of gases contributing to global warming (see Section 1.2.2). Emissions are hereby evaluated for the propulsive system under study in terms of CO_{2eq}, by taking into account the combination of all the steps necessary to turn a resource into a fuel and bring this fuel to a vehicle, which is defined as *Well-to-Tank* pathway (WTT). As introduced in Section 1.2.2, liquid hydrogen can be produced in different ways, however, the most representative pathways have been chosen for this study: electrolysis using wind power ($WDEL1/LH1$), electrolysis using the EU electricity mix ($EMEL1/LH2$) and steam methane reforming process ($GPLH1b$). The emission indexes used for the calculation of the CO_{2eq} emissions of the aircraft running on hydrogen or jet fuel are given in Table 7.6.

Jet-A emissions ($kg\ CO_{2eq}/kg$ **Jet-A**)			
WTT	0.64		
TTW	3.15		
Hydrogen emissions ($kg\ CO_{2eq}/kg\ H_2$)			
	$EMEL1/LH2$	$GPLH1b$	$WDEL1/LH1$
WTT	30.53	15.45	0.50
TTW	0	0	0

Table 7.6: *Well-to-Tank* (WTT) and *Tank-to-Wake* (TTW) fuel-specific CO_{2eq} emission indexes derived from [53].

Figure 7.11 shows that when taking into account the entire life-cycle of hydrogen, the emission of the $TP\text{-}H2B$ configuration can be as high as three times the emissions of the baseline aircraft if hydrogen is produced by electrolysis using EU-mix electricity.

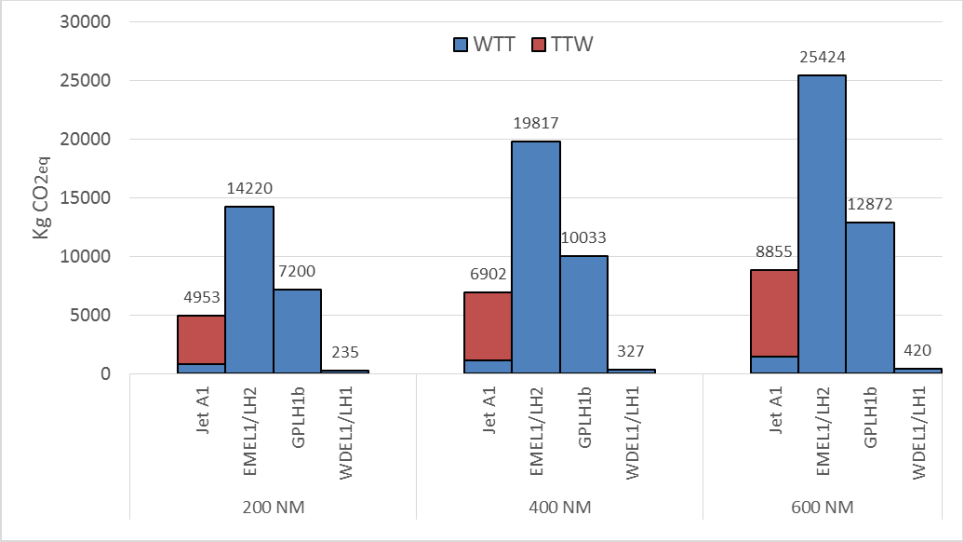

Figure 7.11: CO_{2eq} emissions generated by the hydrogen gas turbines for three flight distances and considering three H_2 production pathways. Emissions generated by the conventional baseline aircraft burning jet fuel are also given as a reference.

The expended energy required to produce hydrogen with this process is about four times higher than the steam methane reforming, which justifies why its emissions are so considerably higher. Moreover, considering that, together with the increase of OWE, the integration of the voluminous H_2 tank would result in a reduction of the maximum number of passengers, the evaluation of the CO_{2eq} emissions per passenger and per nautical mile would show an even worse outcome for hydrogen combustion. With such propulsive architecture, the production of hydrogen by electrolysis, using electricity generated by renewable sources such as wind energy, is the only possible solution to actually improve the environmental performance of the aircraft.

Nevertheless, the reduction of the passenger cabin volume due to the installation of the hydrogen tanks is still an issue that needs to be assessed. According to the aircraft cabin dimensions and the total cabin length occupied by the hydrogen storage compartment, it is of utmost interest to evaluate the number of seat rows that would need to be removed. At this stage, some assumptions regarding hydrogen tank design and cabin geometry must be made. Concerning the hydrogen tanks, a simple spherical design is considered to allow an easier evaluation of their size compared to a more complex ellipsoidal shape. Additionally, some data about the geometry of the baseline aircraft fuselage are needed to calculate the available cabin volume. External fuselage dimensions have been calculated by the geometry module of RHEA, however, the internal dimensions of the cabin are not available. The cabin height is indeed an important parameter that sets the maximum hydrogen tank diameter. A value of 1.9 meters is assumed for the cabin height, which is equivalent to the one of the ATR72 aircraft. By taking a few centimeters of clearance margin, the maximum diameter of the hydrogen tank is set to 1.7 meters. The total mass of hydrogen that can be stored in a spherical tank with the aforementioned characteristics is calculated using Eqs. (7.3) and (7.4).

$$V_{tank} = \frac{4\pi R^3}{3} = 2572l \tag{7.3}$$

$$m_{H2} = \rho_{LH2} V_{tank} = 173kg \tag{7.4}$$

where m_{H2} is the hydrogen mass that can be stored in each tank.

First, the spherical tank volume is derived using the maximum radius (R) of 0.85 meters. Then, the liquid hydrogen mass that the tank can store is evaluated multiplying the LH_2 density (ρ_{LH2}) by the tank volume (V_{tank}). As suggested by [112], a mean density of 0.0673 kg/l for hydrogen is chosen to consider the hydrogen gas fraction needed for venting as introduced in the previous paragraph.

The results obtained with the given assumptions show that three spherical tanks would be needed to store the amount of hydrogen needed for a 200 NM mission given in Ta-

ble 7.5. The total length of the H_2 storage compartment would then be around three times the tank diameter, which gives 5.1 meters. With a seat pitch of 30" (0.8 meters), the installation of such tanks would result in the removal of approximately 7 rows of passenger seats, thus in a reduction of 28 passengers. For the 600 NM with 833 kg of hydrogen needed, the installation of five tanks would lead to a reduction of 44 passengers. These numbers represent a very preliminary estimation of the passenger capacity of the $TP\text{-}H2B$ architecture, which is a function of the assumptions taken for the tank design and cabin geometry, however, they are provided to give an idea of the challenging integration of the liquid hydrogen tanks on board a 70-seat regional aircraft. Moreover, it has to be pointed out that the technical viability of such a solution is also subject to weight and balance considerations, considering that the position of those tanks in the fuselage would significantly impact the location of the center of gravity of the aircraft.

In order to mitigate those challenges, a gas turbine system with the flexibility of being capable of working with a mixture of hydrogen and kerosene could be used instead, splitting the total energy input to the engine among the two fuels. The main advantage of this multi-fuel engine concept is that the hydrogen tanks could be designed only with respect to the hydrogen required for the main mission, thus during the reserve mission, the turbine would operate burning only kerosene. For such a system, emissions are related to the fuel blend used, meaning the relative quantity of hydrogen and jet fuel that are injected into the combustion chamber. Clearly, higher percentages of hydrogen would lead to lower CO_{2eq} emissions (assuming H_2 produced by renewable energy sources), therefore a compromise would have to be found between emission reduction and passenger carrying capacity.

7.3 Turbo/Hybrid-electric propulsion

7.3.1 Turbo-electric (TE) architecture

The general working principle of a turbo-electric system consists of the use of jet fuel as an energy carrier which is burnt in a gas turbine for the generation of thermal power, which is first converted into mechanical power and successively into electric power through the use of a generator. The electric power is finally transferred to the propellers by means of electric motors.

The electric generator produces AC power that can be either directly transmitted to the electric motors (such as shown in Fig. 7.12), or converted first into DC at the output of the generator and back into AC power at the input of the electric motors. The latter configuration allows for reducing conduction losses of the electric wires, however, it requires additional electrical components such as power converters. For both turbo-

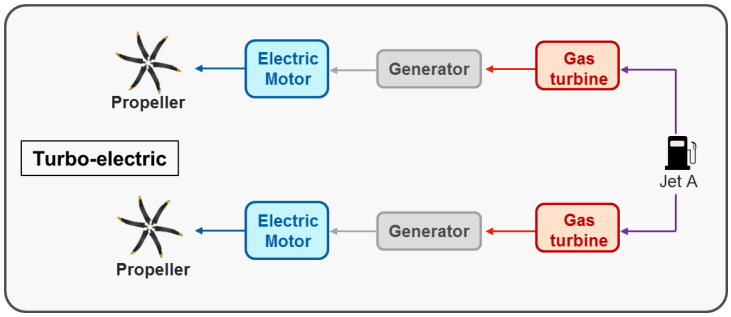

Figure 7.12: *TE*: Example of turbo-electric architecture with AC power transmission

electric variants, the additional components for electrical power generation, distribution and conversion lead to an increase of the propulsive system mass, but also to a decrease in the overall system efficiency, since more energy conversions are needed (see Fig. 7.13). Considering the simplest turbo-electric architecture with direct AC power transmission between a generator and an electric motor of Fig. 7.12, its installation on the regional aircraft under study would lead to an increase of OWE of at least 7%. Such an increase has been obtained by adding to the original OWE, only the mass of the two electric motors and generators while neglecting the mass of the electric wires and electric circuit protection that may be needed. A specific power value of 7 kW/kg is assumed for both components, given that most often, motors and generators are indeed the same hardware which can work in both ways.

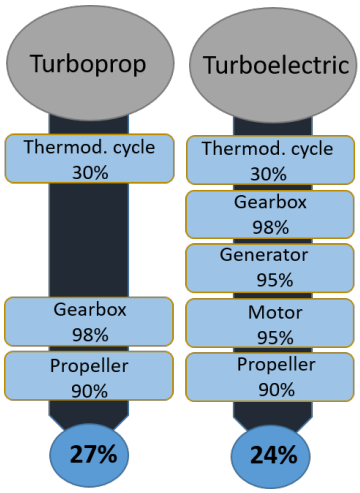

Figure 7.13: Overall average efficiency of turboprop and turbo-electric systems.

7.3.2 Series Hybrid-electric (SH) and Parallel Hybrid-electric (PH) architectures

With the term hybrid-electric propulsion, the author refers to those systems where the electricity is generated by hydrogen fuel cells or batteries rather than gas turbine generators. The use of such systems for the generation of electrical power is key to the design of

a low-emission propulsive system because they are characterized by very high efficiencies and do not generate carbon emissions. The term hybrid indicates that a second power source is used for the generation of the required propulsive power, which in this case is the conventional gas turbine. The characterization of such a system comprising two power sources comes with different challenges in terms of design choices to be made. Indeed, depending on how the energy is transferred from the carriers to the propellers, several architecture layouts are possible. Two of the most common and interesting hybrid electric architectures are the series hybrid and parallel hybrid layouts.

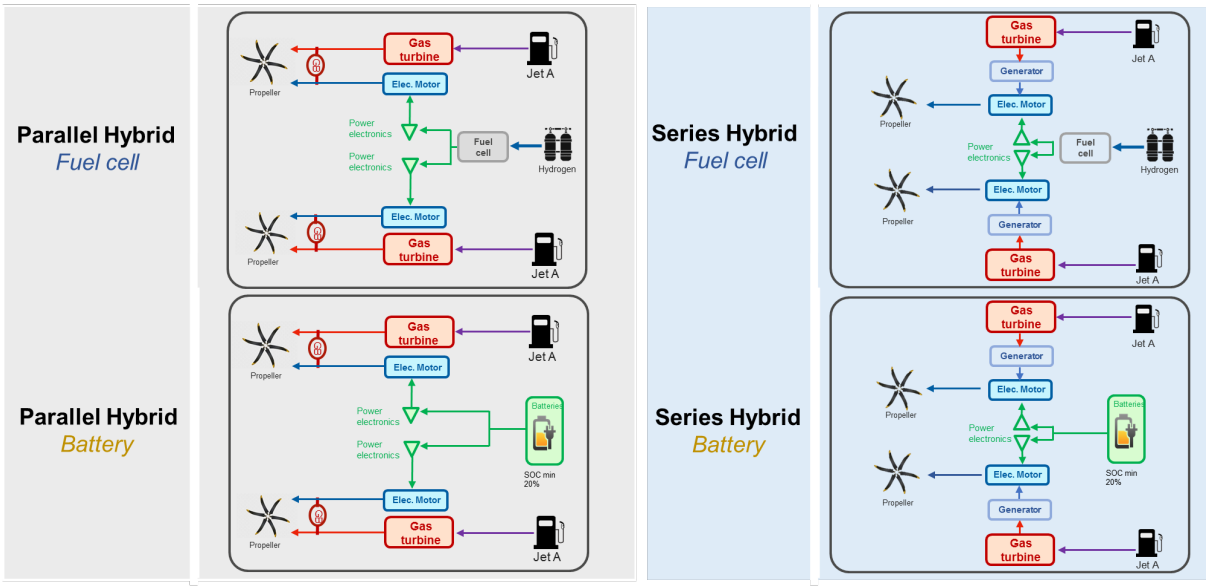

Figure 7.14: Series and parallel hybrid-electric architectures with batteries and fuel cells.

As it can be seen in Fig. 7.14, the series hybrid architecture presents additional components such as the generators that are not needed in the parallel architecture, where the turbine shaft power is directly transferred to the propeller by means of a double input gearbox. Therefore, most of the considerations done for the turbo-electric also apply to the series hybrid system with electrical batteries or hydrogen fuel cells ($SH\text{-}EB/FC$) since the installation of additional components in the power chain leads to higher mass and lower efficiency. Thus, given the increase of OWE combined with a decrease in overall efficiency, no potential benefit in terms of $GHGs$ emissions and block fuel reduction can be expected from those architectures for the envisioned application. These types of architecture only make sense if there is an interest in exploiting electric power in such a way to have significant aerodynamics gains or synergy effects with other aircraft systems, which could more than offset the system mass and efficiency penalties (e.g. distributed electric propulsion [122]).

The parallel hybrid configurations with electrical batteries or hydrogen fuel cells ($PH\text{-}EB/FC$) instead are much more promising because the electric propulsion system is completely independent of the gas turbine and it does not affect the overall efficiency of

its power conversion chain. However, the performance of such an architecture layout is influenced by several design variables:

- Electric energy source
- Degree of hybridization, H_p
- Power management strategy

The first and probably most important variable which impacts the performance of a parallel hybrid propulsion system is the choice of the secondary energy source, which can be either batteries or hydrogen fuel cells. Then, the degree of hybridization, defined as the ratio between the nominal power supplied by the electric motor and the total power transferred to the propeller, determines the sizing of the gas turbine and the electric propulsive system. Finally, the power management strategy of the two power sources is defined by the combination of electric and thermal power outputs throughout the flight. The power output of those components is determined by the throttle (or power rate) applied during each segment of the mission. Given all those variables, it is not possible at this stage to give a preliminary assessment of the system performance and of its impact on the mission fuel consumption. More in-depth analyses are needed to size and analyze each architecture with different combinations of such design variables. The next section is dedicated to such studies that have been performed using the aircraft design process and methods introduced in Section 6.2.

7.3.3 Global sensitivity analysis L0

Given the uncertainty on the main performance of the electric propulsion system components and the impossibility to validate the results using existing aircraft data, a global sensitivity analysis is hereby performed to identify the variables with the greatest impact on the aircraft energy consumption (E_c) and OWE. This analysis focuses on the *PH-FC* architecture, because of the complexity of such a system due to the higher number of subsystems compared to a hybrid architecture using batteries for the generation of electrical power. In order to perform this analysis, a simple hybrid electric propulsion model has been developed in RHEA to evaluate the OWE and the aircraft fuel consumption over the reference 200 NM mission. This model evaluates the mass and the performances of the propulsion system components using a few key performance parameters. These components are the electric motors, power converters, fuel cell systems (including BoP) and hydrogen storage. Their key performance parameters (efficiency, specific power, gravimetric efficiency) are inputs of the sensitivity analysis, for which the upper and lower bounds are set according to the technology survey provided in Section 1.2.3.

Before carrying out the sensitivity analysis, the main design variables of the hybrid propulsion system need to be set. For that, the following assumptions have been used: gas turbine maximum rated power of 1500 kW and fuel cell maximum rated power of 500 kW

(per side). Concerning the power management strategy, the fuel cells deliver maximum power during the climb and cruise phases, whereas the gas turbines deliver maximum power during the climb and only the required power needed to fly at the given speed and descent rate respectively for the cruise and descent phases. The flight mission profile considered is the same as the one defined for the baseline turboprop aircraft in Section 5.1. It is important to note that such design variables are not optimized in any way and have only been fixed at this stage to be able to perform the global sensitivity analysis. Indeed, the objective of this study is simply to understand where the modeling efforts should be focused, so as to attempt at reducing the uncertainty on the systems with the greatest impact by increasing the fidelity of the models used, allowing a better understanding of the system behavior.

The uncertain parameters of the sensitivity analysis are shown in Table 7.7, together with the probabilistic model associated. All those inputs are concatenated in a vector denoted by $\vec{x}$, defined by its components x_i for $i = 1, \ldots, 7$. The global sensitivity analysis of the quantity of interest $\vec{y}$, where $y_1 = E_c$ and $y_2 = OWE$ with respect to $\vec{x}$ is then performed as follows.

$\vec{x}$: Parameters	Distribution	Range	Unit
x_1: Electric motor efficiency	Uniform	$[0.95, 1]$	
x_2: Electric motor specific power	Uniform	$[5, 10]$	kW/kg
x_3: Power electronics efficiency	Uniform	$[0.95, 1]$	
x_4: Power electronics specific power	Uniform	$[7, 15]$	kW/kg
x_5: H_2 tank gravimetric efficiency	Uniform	$[0.2, 0.4]$	
x_6: Fuel cell specific power	Uniform	$[1, 2]$	kW/kg
x_7: Fuel cell efficiency	Uniform	$[0.4, 0.6]$	
Total parameters	**7**		

Table 7.7: Uniform probability distribution characteristics of the input parameters of the sensitivity analysis.

The first step consists in modeling the vector $\vec{x}$ with a suitable probabilistic model. It is hereby assumed that those parameters are uniformly distributed between the minimal and the maximal values provided in Table 7.7. Moreover, the parameters are assumed to be independent. The relative importance of uncertain input variables onto the output quantities of interest of the model is quantified through the calculation of the Sobol' indices. These indices are usually computed by Monte Carlo simulation, which is costly in terms of computational time due to the number of simulations needed which are defined by the number of uncertain parameters and the level of accuracy needed. Therefore, the approach used hereafter consists in substituting the model under consideration with an analytical approximation, named metamodel. In particular, sparse polynomial chaos

expansion is the method employed to build the metamodel (using OpenTURNS [123]), which has proven to be very effective both in terms of computational time and accuracy by previous studies [124, 125, 94]. The accuracy of the sensitivity indices depends on the degree of the basis of the polynomial and on the size of the design of experiments (DOE) used. Section 2.3 recalls some basic theories about the computation of Sobol sensitivity indices by PCE. In this study, various PCE metamodels are built using different polynomial degrees (from 2nd order degree up to 8th degree). The DoE size is composed of 1100 points, of which 1000 are used for the computation of the unknown coefficients of the PCE (training set) and 100 points are used as a validation set for the computation of the predictivity factor Q_2, defined by:

$$Q_2 = 1 - \frac{\sum_{i=1}^{N}(y_i - \hat{y}_i)^2}{N\,Var(y)} \tag{7.5}$$

where N is the sample size, y the true output of the model and $\hat{y}$ the estimated output of the metamodel. Validation results for each polynomial degree are shown in Table 7.8.

Degree	Q_2 **w.r.t.** E_c	Q_2 **w.r.t. OWE**
2nd	0.988341	0.989654
3rd	0.989961	0.990964
4th	0.99601	0.991644
6th	0.999065	0.994022
8th	0.999921	0.999542

Table 7.8: Predictivity factors of the metamodels built using different polynomial degrees.

Given the linearity of the problem, all metamodels are able to provide approximations with really low error, however in order to calculate the Sobol indices the 3rd-degree model is chosen. The associated Sobol indices are shown in Fig. 7.15 as well as in Table 7.9. The higher the index value, the largest the impact on the output. The first order sensitivity indices are used to measure the impact on the output variability due to the parameter x_i alone, while the total order indices take also into account the impact on the output of the interactions of x_i with all the other parameters x_j. The first conclusion that can be drawn looking at the results on Fig. 7.15 is that there is almost no interactions between variables: first order and total order indices have almost the same values.

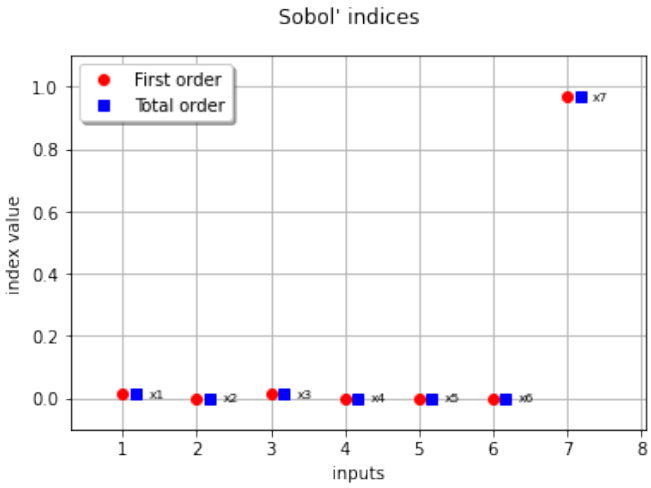

(a) Results for E_c

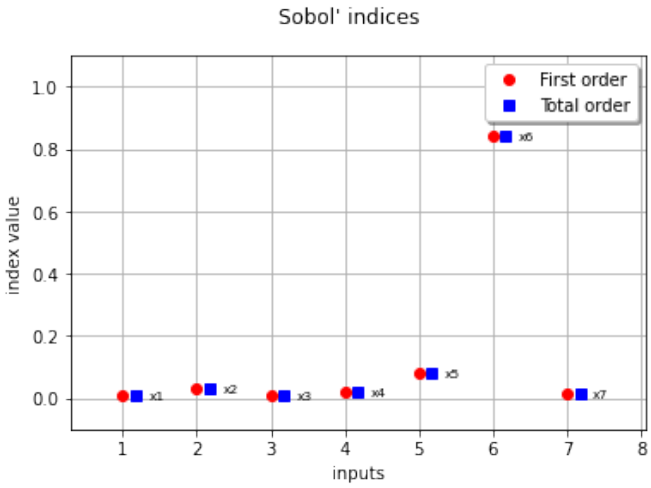

(b) Results for OWE

Figure 7.15: Plotted values of first and total order Sobol indices for each parameter x_i.

	Sobol indices	
$\vec{x}$: Parameters	E_c	**OWE**
x_1: Electric motor efficiency	0.01543	0.0083
x_2: Electric motor specific power	0.0	0.03038
x_3: Power electronics efficiency	0.01541	0.00674
x_4: Power electronics specific power	0.0	0.0183
x_5: H_2 tank gravimetric efficiency	0.0	0.07989
x_6: Fuel cell specific power	0.0	**0.84117**
x_7: Fuel cell efficiency	**0.9687**	0.01369

Table 7.9: Tabulated values of first-order Sobol indices for each parameter x_i. The highest indices are in bold.

Results clearly show that the overall propulsive efficiency of the aircraft and thus the energy consumption over the flight mission is mostly affected by the uncertainty on the fuel cell efficiency. The main contribution to OWE sensitivity instead is given by the uncertainty on the fuel cell specific power which represents the biggest percentage of the propulsion weight. The second most important contribution to OWE is given by the tank gravimetric efficiency which determines the mass of the hydrogen tank. Overall it can be said that the main sources of uncertainty that mostly affect the aircraft performances both in terms of energy consumption and OWE are related to the hydrogen systems rather than the electric components such as the motor and the power inverters. Therefore the modeling efforts for the analyses and simulation performed in the second step of the down-selection process have been focused on the development of models to better characterize the hydrogen systems including hydrogen tanks, fuel cell BoP and thermal management.

7.4 Conclusion of the chapter

For the first down-selection step, as the number of options is large, only low-fidelity analyses or models have been used. Battery electric, hydrogen and hybrid propulsion systems have been considered leading to a total of eight propulsive configurations which have been analyzed. As shown in Fig. 7.16, only two architectures have been selected for the next step of the down-selection process: the parallel hybrid architectures with battery or fuel cells (*PH-EB* and *PH-FC* architectures). Those architectures will be investigated at a higher level of detail in the next steps of the process. The remaining configurations have been discarded for different reasons which are discussed hereafter.

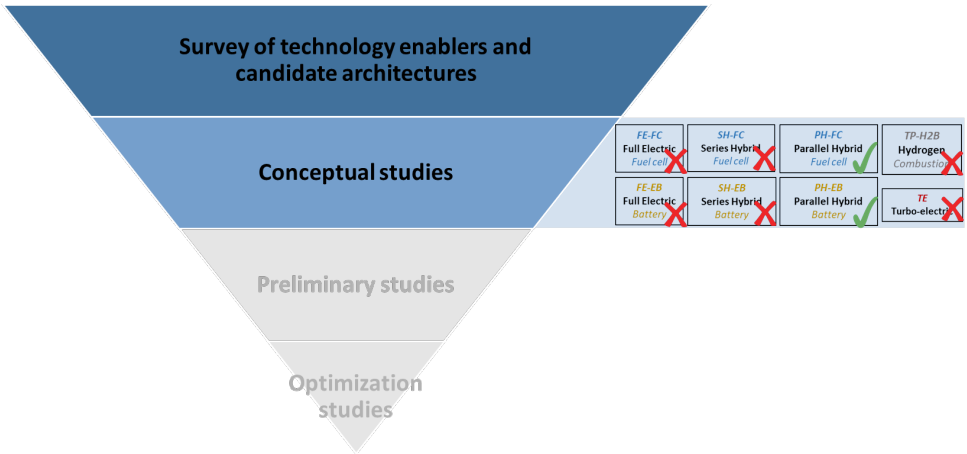

Figure 7.16: Synthesis of the propulsive architectures analyzed in the first step of the down-selection process.

The results obtained for the *FE-EB* architecture (full electric with batteries) show that with the current state-of-the-art battery technology, the conversion of a 70-seat regional aircraft with a full electric propulsion system with batteries is not feasible, thus it is not

further explored in the next steps. Indeed, even considering the most advanced generation of the Li-Ion technology which is expected to be available by the year 2025, the mass of the propulsive system that is required to provide the power and energy to propel such aircraft for a 200 NM mission is so high that its OWE is already greater than the certified MTOW. This propulsive architecture, for the considered aircraft class, could only make sense with a battery technology featuring at least 1000 Wh/kg. With such performance, a regional aircraft able to carry around 50 passengers seems feasible. Only lithium-air technology shows theoretical specific energy values that could potentially provide satisfactory payload-range capabilities. Nonetheless, such batteries are still in the early stages of development with many issues and challenges yet to be solved [31].

On the other hand, the $FE\text{-}FC$ architecture has shown much higher potential both in terms of specific energy and power, which makes its payload-range performances comparable to the conventional turboprop configuration. The main concern about this architecture lies with the challenging volume integration of all the powertrain components. Fuel cells and their balance of plant, thermal management systems and hydrogen tanks are voluminous and interdependent systems that have to be properly allocated within the aircraft, in compliance with functional and safety requirements. Although this architecture has shown promising results, it is not further studied within the framework of this PhD. Indeed, the work needed to generate additional meaningful results to increase the reliability of the assessment goes beyond the scope of this thesis. This would require space allocation and cabin layout analyses as well as modeling some non-propulsive systems. Digital mock-ups of the aircraft and of all the powertrain components shall be available to establish an engineering diagram of the aircraft fuselage interior that shows the arrangement of all the elements to be installed in the aircraft. This includes the conventional cabin equipment (e.g. passenger and flight attendant seats, emergency equipment, exits, lavatories, and galleys) and all the powertrain systems that would not fit in the nacelles (e.g. hydrogen tanks and potentially components of the balance of plant). Additionally, replacing the gas turbine with the fuel cells for propulsive power generation has an impact on all the non-propulsive systems that rely on the bleed air. Existing turboprop aircraft, for example, use compressed air taken from the compressor stage of the gas turbine to provide de-icing capabilities through the operation of inflatable boot sections installed on the leading edge surfaces of wings and tailplanes. The modeling and design of an alternative air supply system and/or the design of an electric de-icing system are essential activities that are needed to quantify their impact on aircraft performance, so as to assess the actual potential benefit of such propulsive architecture. All these activities are not compatible with the time frame and objective of this PhD, which consists rather of a wide exploration of several propulsion concepts.

Similar considerations can be made for the $TP\text{-}H2B$ architecture (turboprop with hydro-

gen combustion). Indeed, while it shows impressive payload capabilities due to the low increase in OWE with respect to the baseline configuration, the H_2 tanks integration is even more challenging than for the $FE\text{-}FC$ architecture, given the much higher quantity of H_2 which would be needed. This challenge may be mitigated by the introduction of a multi-fuel turbine technology providing the capability to operate both with kerosene and H_2-kerosene fuel mixture. However, the maturity level of such engine technology is very low and little information has been found in the literature as already pointed out in Section 1.2.2. Therefore, further investigation of this architecture was not envisaged for the continuation of this thesis.

Concerning the propulsive architectures falling into the turbo/hybrid-electric propulsion category, only the parallel hybrid configurations have shown the potential to improve the environmental performance of the regional aircraft under study and are further investigated in the next steps of this thesis. With the envisioned retrofit design approach, no potential benefit in terms of $GHGs$ emissions and block fuel reduction can be expected by the series hybrid or the turbo-electric configurations. Indeed, replacing a conventional turboprop engine with such systems would only result in an increase in the propulsive system mass due to the introduction of additional components, but also in a decrease in the overall system efficiency, since more energy conversions are needed. However, those architectures may prove beneficial if an ex-novo design of the aircraft is envisaged, for which the exploitation of the electric power may allow, for example, an highly efficient unconventional design featuring boundary layer ingestion and distributed electric propulsion as shown by [122]. Parallel hybrid configurations instead are more suitable to the retrofit design approach, for which the expected performance improvements of the aircraft only rely on the characteristics of the propulsive system. The results for these architectures, shown in the next chapter, have been obtained by developing and integrating into the multidisciplinary design tool RHEA dedicated models to characterize the behavior of the powertrain components and to assess their impact on the overall aircraft performance.

Chapter 8

Preliminary design studies

Contents

8.1 Parallel-hybrid electric batteries: *PH-EB*

The propulsive architecture under study is shown in Fig. 8.1. In this hybrid-electric configuration, each propeller is supplied with mechanical power provided by both the electric motor and the gas turbine through the use of a dual input/single output gearbox. The fuel burnt by the engine produces mechanical power which is directly converted into kinetic energy by the propeller. At the same time, the electric power supplied by the batteries is transferred to the electric motor via the electric core and the DC-AC converters. This power is finally transferred to the propeller by means of the gearbox.

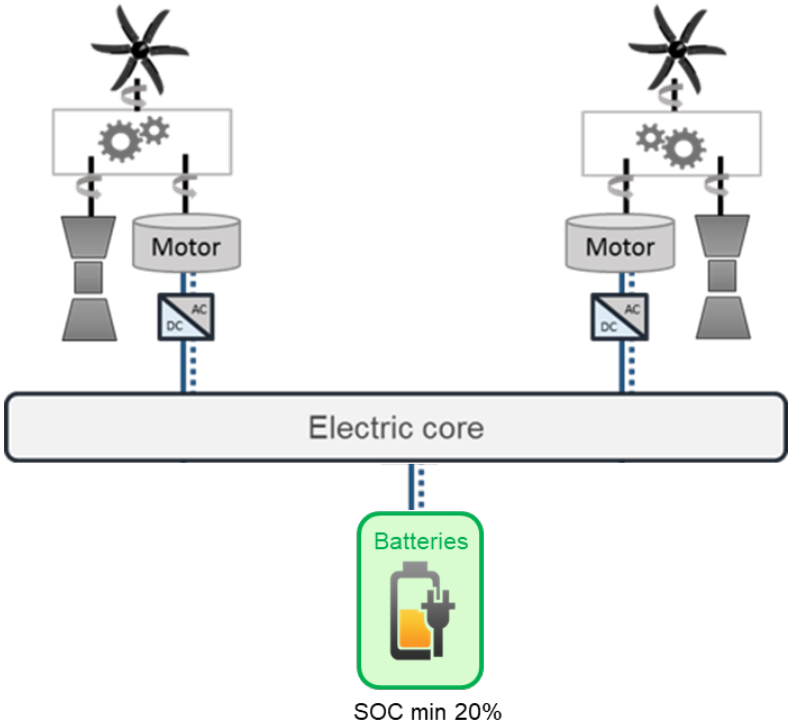

Figure 8.1: *PH-EB*: Schematic layout of the parallel hybrid architecture with Jet-A1 gas turbines and batteries.

The sizing of the gas turbine and of the electric power system, including batteries and power electronics, is determined by the power hybridization factor H_p. Also referred to as "degree of hybridization", H_p is defined as the ratio between the electric power supplied by the batteries and the required total system power. In the conventional case, when all the power is supplied by the gas turbine, H_p is 0, conversely, for a full electric aircraft, H_p is 1. The hybridization strategy employed for this study is the same used for the *PH-FC* configuration, where the electrical power installed is fully exploited during the climb and cruise segment of the main mission and the gas turbines provide the required power for the descent and reserve missions. As it can be seen in Fig. 8.2, batteries are not fully discharged at the end of the cruise, but a minimum state of charge (SOC_{min}) of 20% is imposed to preserve battery life.

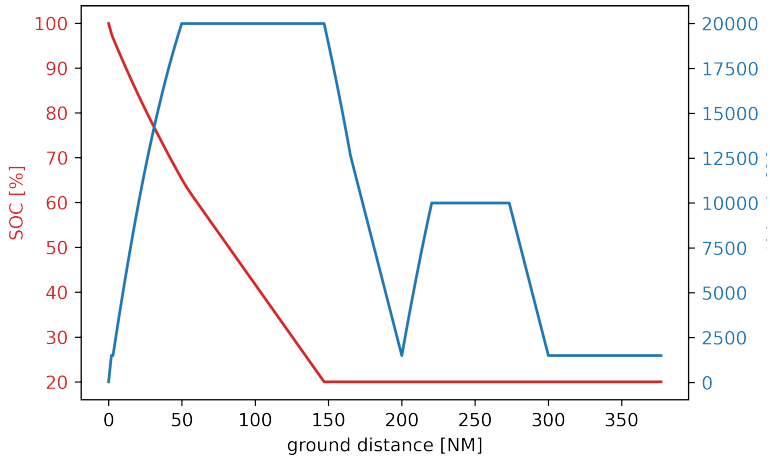

Figure 8.2: Example of battery state of charge evolution during flight for a 200 NM mission.

The objective of this analysis is to size the hybrid propulsion system using different degrees of hybridization, according to three different requirements in terms of aircraft range (200, 400 and 600 NM). For that, three technological scenarios for battery performance are considered, as done for the performance evaluation of the $FE\text{-}EB$ architecture (see Table 7.1), while the technological scenario relative to the year 2025 has been considered for electric motor and power electronics (see Table 1.5). Then, the performances of the aircraft in terms of CO_{2eq} emissions, fuel consumption and payload capabilities are investigated. The calculation of the aircraft emissions takes into account both the products of the fuel production and combustion and the emissions caused by the batteries life-cycle, including the generation of electricity to recharge the batteries. Electricity generation is characterized by an average OECD (Organization for Economic Co-operation and Development) measure of 0.42 $kgCO_{2eq}/kWh$ electricity [126]. Moreover, the emissions of CO_{2eq} due to the battery production are taken into account: 200 $kgCO_{2eq}/kWh$ is the cradle-to-gate emission index for the batteries (see Section 1.2.1). These emissions are amortized over their life cycle. For a fair comparison, it should be noticed that there are other sources of emissions that should be taken into account, such as battery disposal and manufacturing of the gas turbine. However, due to the lack of reliable calculation methods, these contributions are not considered. Table 8.1 summarizes the emission indexes used for this study.

CO_{2eq} **emission indexes**	
Jet-A (WTW)	3.79 $kgCO_{2eq}/kg$ Jet-A
Electricity generation	0.42 $kgCO_{2eq}/kWh$ electricity
Battery (cradle-to-gate)	200 $kgCO_{2eq}/kWh$ battery @ 1500 cycles (= 0.13 $kgCO_{2eq}/kWh/cycle$)

Table 8.1: Life-cycle CO_{2eq} emission indexes for Jet-A and batteries.

The longer missions of 400 NM and 600 NM imply high electric energy requirements which, for different combinations of hybridization factors and technology scenarios, led to unfeasible designs. Indeed, for such configurations, the calculated battery mass is so high that the OWE alone is higher than the $MTOW$. Table 8.2 shows only the results of the viable configurations for the two design ranges. All designs show poorer performance in terms of CO_{2eq} emissions per passenger.

Indeed, even if fuel consumption decreases with higher hybridization factors, the number of passengers is drastically reduced, thus increasing the emissions per passenger. The results also show that the CO_{2eq} emissions generated by the production of electricity to recharge the batteries are not negligible (between 5% and 25% depending on the range and H_p). However even considering electricity produced by green sources, thus assuming an electricity emission index equal to 0, as well as neglecting the life-cycle emissions of batteries, the total CO_{2eq} emissions per passenger would be still higher than the baseline aircraft.

The outcome is slightly different for a hybrid electric aircraft designed for a mission of only 200 NM. As shown in Fig. 8.3, the energy required for that mission implies the need for batteries with a total mass which does not always result in a severe reduction of passengers that offsets the benefit of the reduction of block fuel. This is true at least for the most advanced battery technology featuring a specific energy of 500 Wh/kg at the cell level (projection 2030+ according to the technology road map in Table 1.5).

A/C conf	**Range** NM	**OWE** kg	**Battery** kg	PAX	**BF** kg	$kgCO_{2eq}$ **Elec**	$kgCO_{2eq}$ **Battery**	$kgCO_{2eq}$ **Jet-A**	$kgCO_{2eq}/PAX$ **total**
Baseline	400	14154	0	72	1114	0	0	4222	58.6
Baseline	600	14154	0	72	1609	0	0	6098	84.7
Scenario 1: Current Li-Ion technology (235 Wh/kg **@cell)**									
H_p=0.1	400	17717	3830	42	1102	224	69	4176	106
H_p=0.2	400	21206	7651	7	943	447	138	3575	594
H_p=0.1	600	19521	5884	17	1581	344	106	5993	379
Scenario 2: Advanced Li-Ion technology (350 Wh/kg **@cell)**									
H_p=0.1	400	16579	2572	54	1102	224	69	4176	83
H_p=0.2	400	18933	5137	31	943	447	138	3575	134
H_p=0.3	400	21316	7696	8	785	670	207	2974	481
H_p=0.1	600	17778	3951	36	1581	344	106	5993	179
H_p=0.2	600	21390	7894	1	1341	688	213	5083	5983
Scenario 3: Solid State technology (500 Wh/kg **@cell)**									
H_p=0.1	400	15877	1800	61	1102	224	69	4176	73
H_p=0.2	400	17542	3596	46	943	447	138	3575	90
H_p=0.3	400	19227	5387	30	785	670	207	2974	128
H_p=0.4	400	20927	7175	14	631	893	276	2391	254
H_p=0.1	600	16702	2765	47	1102	344	106	5993	137
H_p=0.2	600	19242	5526	23	943	688	213	5083	260

Table 8.2: Main results of the viable hybrid electric aircraft configurations designed for missions of 400 NM and 600 NM computed with RHEA.

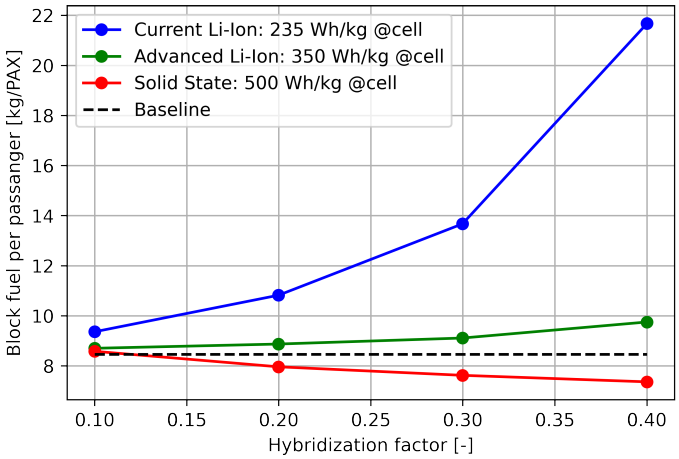

(a) Evolution of block fuel per passenger with H_p for the different battery technologies.

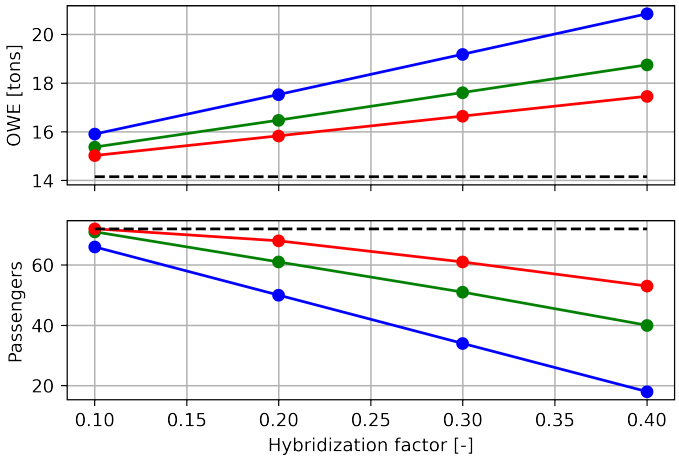

(b) OWE and passengers of the hybrid aircraft configurations for each H_p and battery technology.

Figure 8.3: Main results of the hybrid electric aircraft configurations designed for the 200 NM mission

Concerning the CO_{2eq} emissions, Fig. 8.4 shows that if battery life-cycle and electricity generation are taken into account, even for the 200 NM mission, there is no benefit to be expected by the *PH-EB* architecture. However, assuming the electricity is produced by green sources, a slight emissions reduction of the order of 5% may be obtained with such a propulsive system.

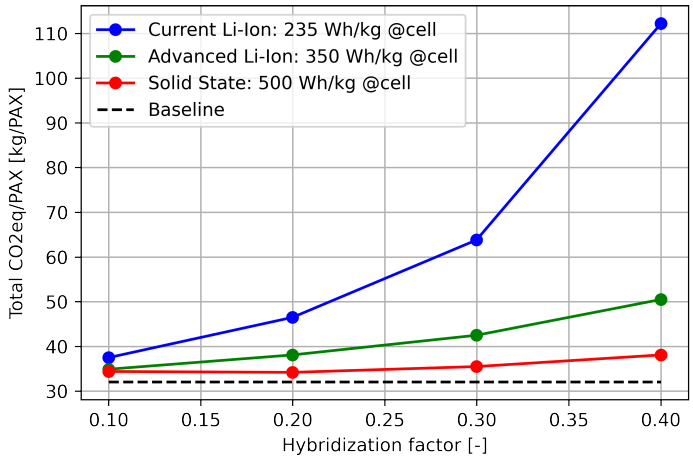

(a) Evolution of CO_{2eq} emissions per passenger with H_p for the different battery technologies.

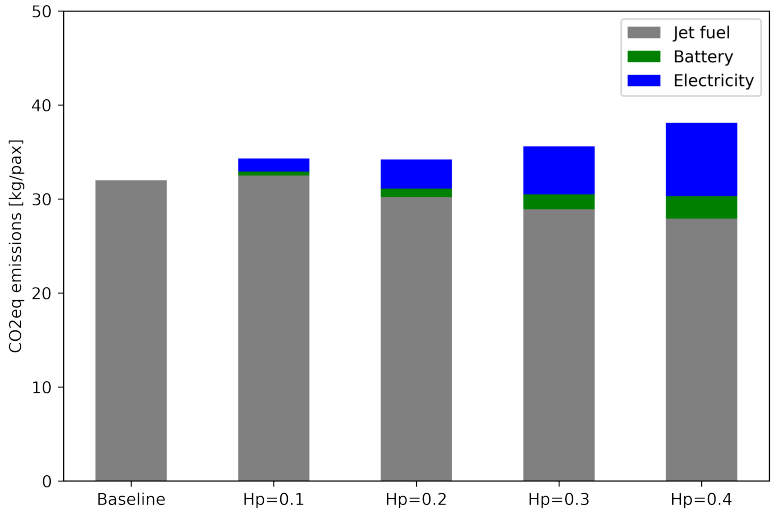

(b) CO_{2eq} emissions breakdown of the hybrid aircraft configurations with Solid State battery technology.

Figure 8.4: CO_{2eq} emissions of the hybrid electric aircraft configurations designed for the 200 NM mission

8.2 Parallel-hybrid fuel cell: *PH-FC*

The scope of this study is to explore the potential of hybrid electric propulsion comprising hydrogen fuel cells for the generation of electrical power. Starting from the baseline turboprop aircraft designed using RHEA and presented in Section 5.1, the *PH-FC* aircraft is designed by replacing the turboprop system with hybrid electric fuel-cell-based propulsion (see Fig. 8.5).

The MDA process shown in Section 6.2 is used to size the propulsion system according to the required design range and electric nominal power and to evaluate its performance with

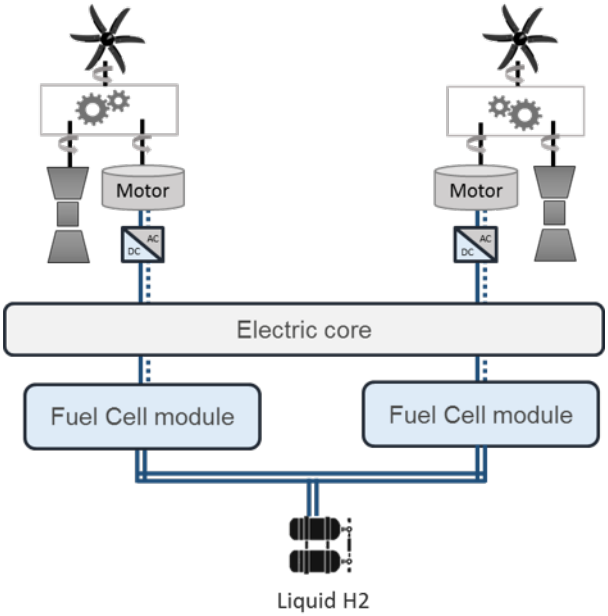

Figure 8.5: *PH-FC*: Schematic layout of the selected parallel hybrid architecture with Jet-A1 gas turbine and hydrogen fuel cells.

respect to the baseline conventional aircraft. Parametric studies are hereby conducted in order to understand the impact on the hybrid aircraft performance of the design range and nominal electrical power of the system.

Each propeller is supplied with mechanical power provided by both the electric motor and the gas turbine. The two power contributions to the required total system power are imposed by the power hybridization factor H_p. The electric motors converting the electrical power into mechanical power are alternating current (AC) motors which, compared with direct current (DC) motor drives, show several advantages such as lightweight, small volume, low cost, and high efficiency [127]. However, fuel cells are electrochemical devices providing DC current at their terminals, therefore DC-AC power converters are also needed. The electric core is a DC supply grid that includes power switches and circuit breakers for the protection system as well as all the electronic components needed for power management and control. The combination of electric core and DC-AC power converters is hereby referred to by the more generic term of power electronics.

The fuel cell modules which generate the electrical power have the layout shown in Fig. 8.6a. Each module is composed of a certain number of fuel cell systems connected in series which depends on the maximum electrical power for which the system has to be designed. The single fuel cell system unit designed for this study is composed of a low-temperature PEM fuel cell operating at a cell voltage of 0.60 Volts resulting in a cell efficiency $\eta_{cell} = 48\%$ at $T = 353\ K$ and $P = 2\ bar$. The overall fuel cell system efficiency η_{fc} including BoP is calculated as described in Section 4 and is approximately

equal to 43%. The actual output power of each cell depends on the assumed surface area of the cell. For this study, a cell surface area value of 650 cm^2 has been used from the estimation of fuel cell manufacturer data sheet [128]. The output power of a single cell at the chosen operating point is approximately 530 W. Therefore, each fuel cell system with a net output power of 100 kW is composed of a fuel cell stack with 211 cells stacked in series, producing a voltage of 127 V and a current of 882 A. The evolution of voltage and current values for different power levels of the fuel cell module is given in Fig. 8.6b in order to give an idea of the order of magnitude of the main properties of the electrical power grid.

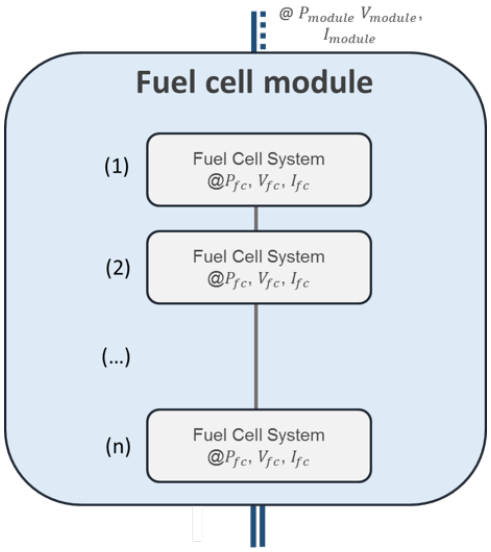

(a) Schematic of the module layout.

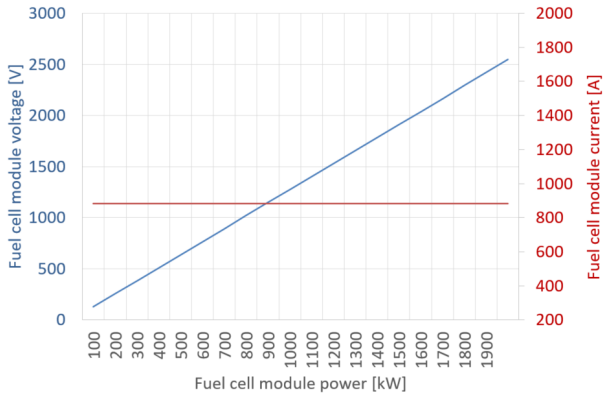

(b) Evolution of voltage and current with fuel cell module power.

Figure 8.6: Layout and electrical properties of a fuel cell module.

The hybrid propulsive system of the hybrid aircraft is sized relatively to the nominal electric power and the design range given as inputs. According to those inputs, the mass of the entire hybrid propulsive system is determined using the methods described in Chapter 4, using technological levels of electric motor and power electronics corresponding to the 2025 scenario (see Table 1.5). Due to the inevitable increase of OWE caused by the higher mass of the hybrid propulsive architecture, in order to comply with the characteristic MTOW of the baseline aircraft, the maximum payload is reduced accordingly. Therefore, for the hybrid electric aircraft design process, the number of passengers is not a given requirement, but rather an output of the process. The total take-off power of the hybrid aircraft is kept equal to the take-off shaft power of the baseline aircraft, therefore the definition of the nominal electric power implies also, by means of a simple arithmetic operation of subtraction, the definition of the gas turbine take-off power. Thus, the hybridization factor, H_p, at take-off is only a function of the electric power, given that the total installed power does not change.

Concerning the hybridization strategy, i.e. the power management strategy of the two power sources throughout the mission, the chosen approach consists in the full exploitation of the total power available during the flight phases of climb and cruise, whereas during the descent phase only the gas turbine is employed at idle rating. As a result, the hybridization factor will be slightly higher at higher altitudes since the available gas turbine power decreases due to the effect of lower air density while the electrical power output is not affected by the atmospheric conditions. Nevertheless, two different approaches are still viable: the first consists of the exploitation of electric power during all flight phases of climb and cruise, including diversion and holding, whereas with the second solution, the electric power will be used only during the climb and cruise phases of the design mission, leaving the gas turbine to provide with the required power throughout the reserve flight. For the sake of simplicity, these two approaches will be referred to as "full hybrid mission" and "main hybrid mission", respectively.

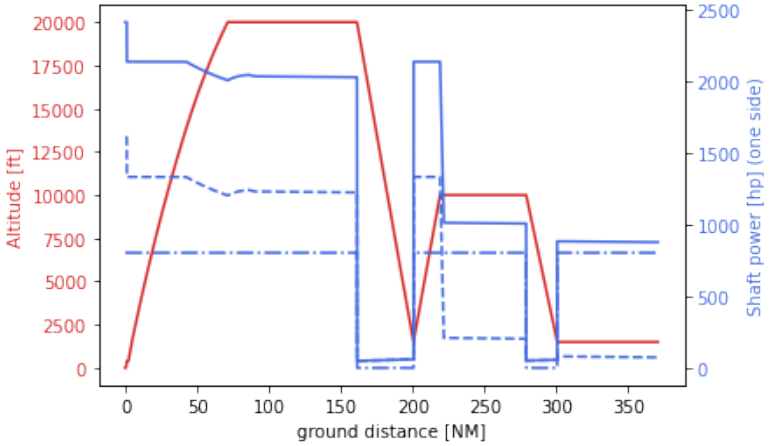

(a) Flight power profile for full hybrid mission.

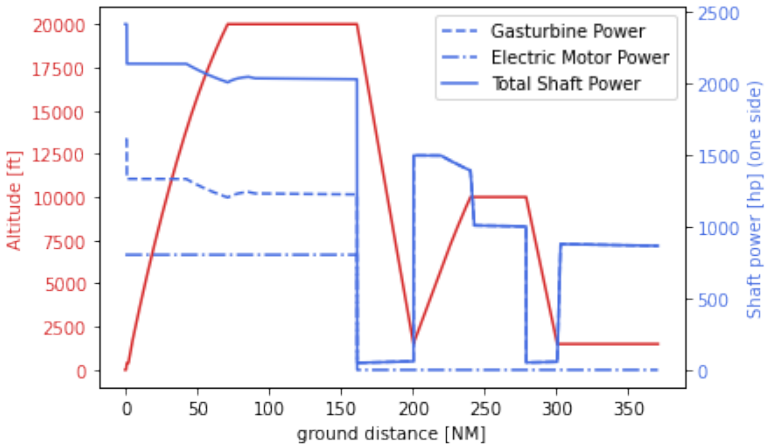

(b) Flight power profile for main hybrid mission.

Figure 8.7: Representation of power management for two hybridization strategies.

In Fig. 8.7, the flight power profiles for both strategies - for a design mission of 200 NM

with a nominal electrical power of 600 kW per side - are illustrated in order to give a better understanding of the concepts explained. Hybrid aircraft flight simulations are always performed with the same speeds and altitudes as the ones used for the baseline aircraft (illustrated in Table 5.2). However, the diversion cruise altitude was reduced to $10000ft$ and its speed to a Mach number of 0.25, in order to allow sufficiently high hybridization factors, which would otherwise lead to insufficient gas turbine power levels to perform the reserve flight.

A parametric study with the hybridization factor varying approximately between 0.1 and 0.5 (corresponding to nominal electric power varying between 200 kW and 1200 kW) was conducted for both strategies for a design range of 200 NM and the most relevant results are illustrated in Fig. 8.8. The graph 8.8a on the left-hand side shows that the mass penalty due to the installation of the hybrid electric architecture does not vary significantly with the choice of the hybridization strategies investigated herein. Indeed, for each specific hybridization factor, the only difference in the propulsive architectures designed for the two strategies is the size of the cryogenic hydrogen tank, which will be higher for the full hybrid mission design due to the higher quantity of hydrogen it needs to carry to cover the diversion and holding flight segments. As it can be seen in the graph 8.8b on the right, the mass of hydrogen is almost doubled for the full hybrid mission. Although not particularly inconvenient in terms of an added weight penalty, it is still seriously challenging in terms of volume. Moreover, the lower OWE for the main hybrid mission design also implies higher payload capabilities and therefore slightly better performances in terms of block fuel per passenger. For these reasons, it was decided to continue the analyses only using the main hybrid mission strategy.

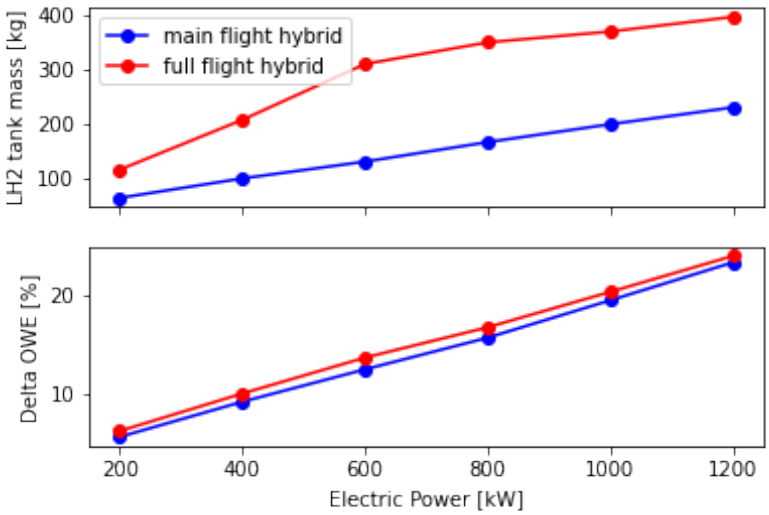

(a) LH_2 tank mass and delta OWE variation w.r.t. baseline.

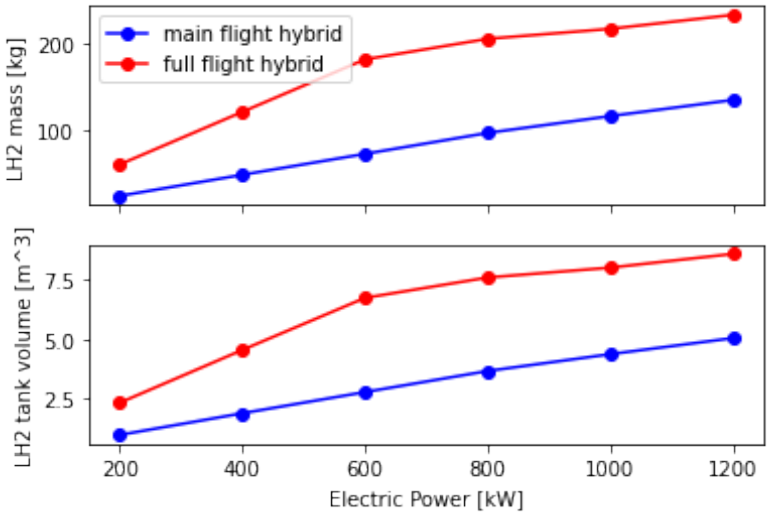

(b) LH_2 mass and tank volume variation.

Figure 8.8: Main results of the parametric study for the selection of the hybridization strategy.

Figure 8.9 shows the most relevant results of a second parametric study which was performed in order to evaluate the impact of the design range on the hybrid aircraft performance. Three design ranges have been considered for the study: 200 NM, 400 NM and 600 NM. By varying the electrical power between 200 kW and 1200 kW, the block fuel per passenger appears to decrease almost linearly with the increase of the hybridization factor for all the three design ranges investigated. At 800 kW, there seems to be an optimum, after which the increase of H_p leads to a deterioration of the performances, again for all three ranges. This optimum is given by a combination of two separate effects.
First, at 800 kW of nominal electric power, according to the sizing criteria of the gas turbine expressed at the beginning of this paragraph, the take-off power of the gas turbine is about 1200 kW, which appears to be the minimum power required to allow the execution

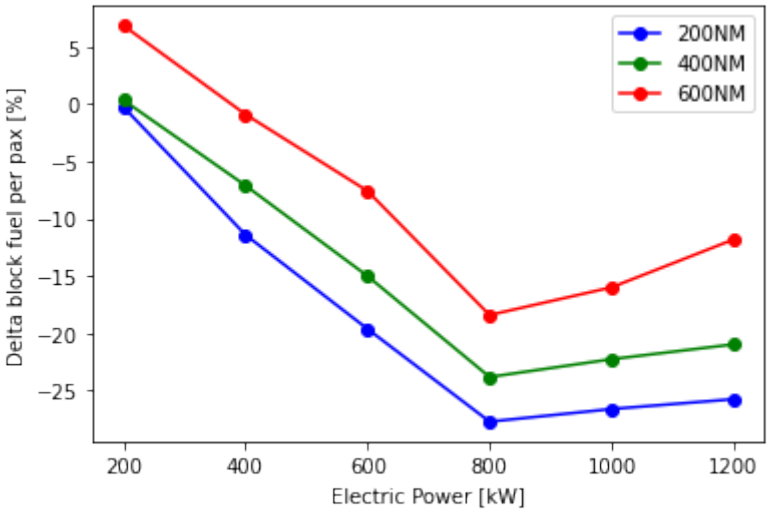

Figure 8.9: Delta block fuel per pax variation for main flight hybrid w.r.t. baseline aircraft

of the reserve flight mission without the aid of the electrical power. Therefore, for all the designs with nominal electrical power above 800 kW, the increase of the H_p does not lead anymore to a consequent reduction in gas turbine size, which thereby results in higher weight and fuel consumption.

The second effect is related to the variation of the specific energy of the hydrogen-based electric system with the increase of the H_p. This term refers to the combination of all the equipment and systems that are needed to generate and supply electrical power to the electric core and includes hydrogen liquid, hydrogen tank, hydrogen distribution, fuel cell systems (as defined in Eq. (4.6)) and radiators for cooling. The specific energy is therefore calculated as follows:

$$E_{sp} = \frac{m_{H_2} \times FHV_{H2} \times \eta_{fc}}{m_{H_2} + m_{tank} + m_{distr} + m_{fc} + m_{radiators}} \tag{8.1}$$

The aforementioned definition of specific energy is particularly meaningful because it can be considered as the equivalent specific energy required by the batteries in order to have the same performance as the hydrogen-based system herein designed. Figure 8.10 shows the variation of the specific energy of the system related to the change of design range and nominal electrical power. It can be seen, how for each range, there seems to be an optimal point that corresponds to the highest specific energy, this point being the 800 kW for which the hybrid aircraft design showed the best performance in Fig. 8.9. This behavior is given by the fact that most of the components of the system have masses that do not scale linearly with the electric sizing power, as shown in Fig. 4.3. The power-to-weight ratio of the fuel cell system increases rapidly till reaching an almost constant trend. Past this crucial point, increasing the electrical power leads to an increase of the radiator mass which already at 800 kW has become significantly high to be comparable to the fuel cell system mass (see Fig. 8.11: the radiator mass is referred to with the label "cooling").

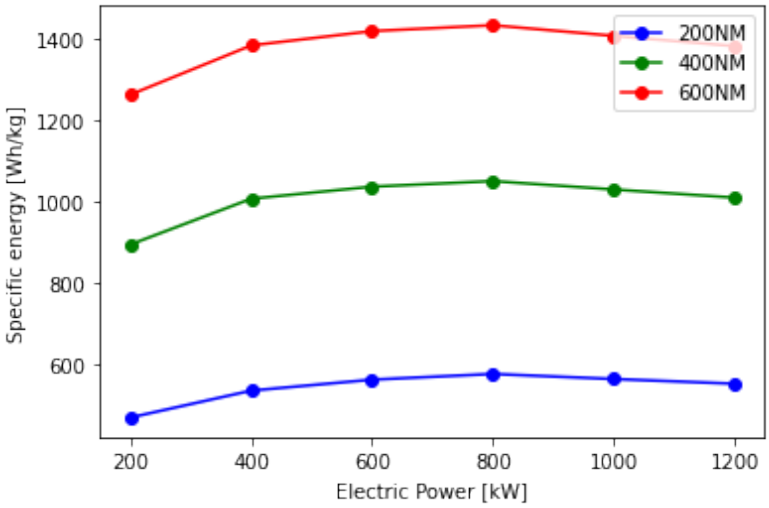

Figure 8.10: Variation of system specific energy

Furthermore, from Fig. 8.10, it can be observed that there is an appreciable variation of the system specific energy with respect to the range variation. The increase in design range has only an impact on the hydrogen consumption, and consequently on the mass of the hydrogen tank, but it does not affect cooling requirements and fuel cell system size which are driven mainly by the nominal electric power of the system. Since the tank mass is a relatively small percentage of the entire hybrid propulsion system, the aforementioned behavior is explained. Nevertheless, in terms of absolute values, the total mass of the propulsive system with a certain sizing electrical power is still higher with increasing design range, due to the bigger and heavier tanks. This added mass penalty results in a reduction of the max payload which translates in worse performance in terms of block fuel per passenger, as illustrated in Fig. 8.9. Considering also the volume constraints to integrate into the aircraft voluminous hydrogen tanks, the design range of 200 NM seems to be the most profitable and viable option. Therefore hereafter, additional analyses and considerations on the hybrid aircraft design are only given considering a design range of 200 NM. The main performance of different hybrid aircraft configurations corresponding to the baseline aircraft with six different hybridization levels is summarized in Table 8.3.

It shows, among others, the aircraft performance in terms of emissions, hydrogen consumption and trip time, meaning the time required to perform the flight segments of the climb, cruise and descent without taking into account the ground operations. With the exception of the last hybrid configuration, which is characterized by a higher installed total power due to the minimal gas turbine power requirement for the reserve flight, the time spent to carry out the flight is higher for the hybrid aircraft compared to the baseline aircraft due to the higher TOW which also affects the max cruise speed. However, the trip time decreases with increasing hybridization levels. This happens because the electric power output is not affected by the change in altitude and Mach number, contrarily

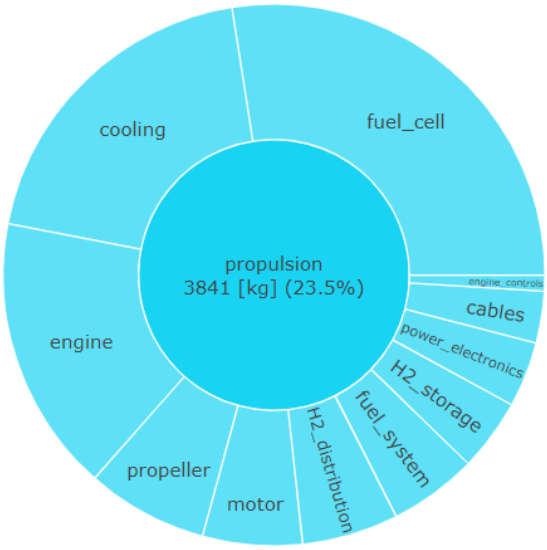

Figure 8.11: Propulsion weight breakdown of the architecture designed for 200 NM and 800 kW

A/C conf	$P_{elec}(P_{gt_{TO}})$	**TOW** kg	M_{cr}	PAX	**TT** min	kgH_2	$kgCO_{2eq}/PAX$	gNO_x/PAX
Baseline	0 (1.8) MW	22108	0.489	72	45.9	0	29.9	21.9
1: H_p=0.11	0.2 (1.6) MW	23020	0.442	72	50	24.5	30.7	21.5
2: H_p=0.22	0.4 (1.4) MW	23480	0.449	72	49.5	48.9	27.4	18.7
3: H_p=0.34	0.6 (1.2) MW	23573	0.457	69	48.9	72.9	25.1	16.4
4: H_p=0.45	0.8 (1.0) MW	23573	0.465	65	48.4	97	**22.8**	**13.9**
5: H_p=0.51	1.0 (1.0) MW	23573	0.486	59	46.1	116.3	23.3	13.1
6: H_p=0.56	1.2 (1.0) MW	23573	0.505	54	44.2	134.8	23.8	12.3

Table 8.3: Main aircraft performance for a mission of 200 NM for six different hybridization factors. Values in bold indicate the emissions of the most promising configuration.

to the gas turbine engine, therefore the total available power of the hybrid propulsion system at high altitude is greater for higher hybridization levels, despite having the same total take-off power. Concerning the emissions, for the first hybrid configuration, the hybridization level is not sufficiently high to offset the mass penalty of the hybrid system with a significant reduction of fuel consumption. However for all the other configurations, regardless of the decrease of the allowed number of passengers, appreciable reduction of both CO_{2eq} and NO_x can be observed, with peaks for the fourth configuration of -24% and -40%, respectively.

8.3 Conclusion of the chapter

In this second step of the down-selection process, preliminary studies have been performed to explore the potential of parallel hybrid electric propulsion to improve aircraft fuel efficiency and reduce its emissions during flight. For that, dedicated MDA processes

have been developed in RHEA to size the propulsion systems and to assess aircraft performance. Two architectures have been studied, both consisting of a parallel hybrid electric layout, but using different sources for the generation of electrical power: low-temperature PEM fuel cells or batteries. The battery-based system (named *PH-EB*) has shown very poor performance in terms of mass which have led to an important increase of OWE, thus to a significant reduction of passengers. The reduction of block fuel achieved thanks to the downsizing of the gas turbines is counterbalanced by a reduction of payload, which resulted in an increase of the emissions per passenger for all the different designs. As shown in Fig. 8.12, the battery-based architecture is thus discarded from further analysis.

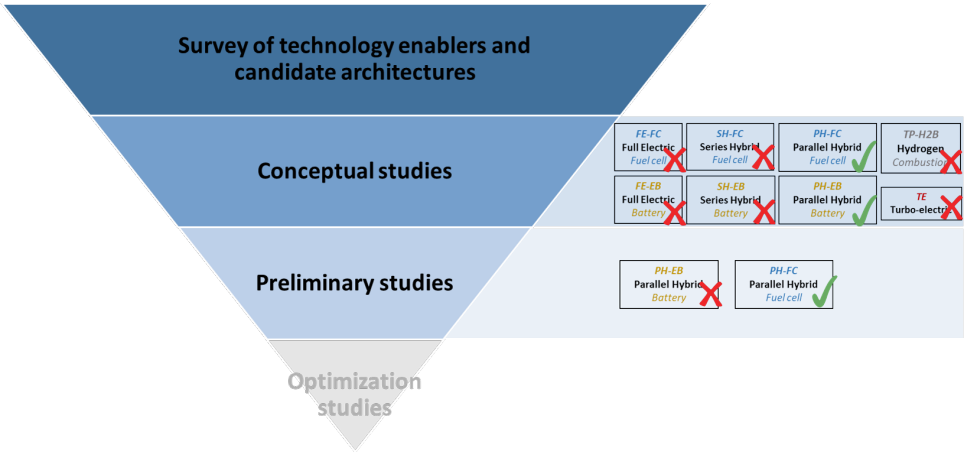

Figure 8.12: Synthesis of the propulsive architectures analyzed in the second step of the down-selection process.

While being much more complex than battery-based electric propulsion, hydrogen-based electric propulsion has shown the potential to considerably reduce aircraft emissions even with today's state-of-the-art technological levels. One of the main challenges of the *PH-FC* architecture is the thermal management of PEM fuel cells due to their low operating temperatures. The results showed that low-temperature PEM fuel cells require large and heavy radiators to evacuate the waste heat. Nevertheless, appreciable reductions of both CO_{2eq} and NO_x have been observed, with peaks for the best configuration of -24% and -40%, respectively. Moreover, considering that some of these technologies (e.g. electric motors, fuel cells) have seen a steep evolution and improvement curve in the past few years, thanks also to their application on serial production vehicles, higher benefits can still be expected for the next future. A new technology of PEM fuel cells operating at higher temperatures (named HT-PEM) could allow for reducing considerably the weight penalties of the thermal management system. Increasing the fuel cell operating temperature would lead to higher heat recovery for the heating of the liquid hydrogen as well as a reduction of waste heat due to the higher heat required to keep the fuel cell at the nominal operational temperature. In addition to that, the hybrid fuel cell system was sized according to design variables which were only chosen based on some preliminary

trade studies which do not necessarily guarantee optimal results.

The next step consists of the set-up of a dedicated multidisciplinary optimization to allow for a wider exploration of the design space of the hybrid propulsive system, which focuses exclusively on the *PH-FC* architecture and takes into account also the potential benefits of the high-temperature PEM fuel cells.

Chapter 9

Design optimization studies

Contents

9.1 Aims and objectives

The objective of this study is to design the *PH-FC* system to replace the conventional turboprop engine of the baseline aircraft and to define an optimal hybridization strategy that would minimize the block fuel consumption per passenger. The characterization of a hybrid propulsive system comprising two power sources for the generation of the required propulsive power comes with different challenges in terms of design choices to be made. The conventional propulsion system composed of gas turbine engines that equip existing aircraft is directly sized by its flight performance requirements. According to the total thrust needed to satisfy low-speed and high-speed performance requirements, the gas turbines are directly sized to provide the needed amount of power and thrust at the different flight conditions. However, when the required power must be provided by two power sources, the sizing of those systems, as well as the power management strategy, are not straightforward. For this study, it is decided to make use of an optimization algorithm to size the propulsive system and to identify the hybridization strategy that would minimize the aircraft fuel consumption while satisfying the given flight performance requirements. The obtained design and the hybridization strategy are the results of a Bayesian optimization (described in Section 2.2) in order to perform a global optimization (exploration/exploitation trade-off) with a minimum number of function evaluations.

Moreover, this study addresses the evaluation of fuel cell technology on the overall performance of hybrid aircraft. Although low-temperature PEM fuel cells have been the common choice in both automotive applications and recent hydrogen aircraft concepts and studies, the preliminary studies on the *PH-FC* architecture of the previous subsection showed that due to the low operating temperatures, the thermal management system would require large and heavy radiators to evacuate the waste heat. To overcome this issue, an option is to increase the operating temperature, which would result in an increase in the heat transfer rate due to the larger temperature gradient between the fuel cells and the external environment, thus reducing the size and weight of the cooling system. High-temperature PEM fuel cells, however, have many potential drawbacks including faster degradation and increased start-up time and they are still in the early stages of their development. In order to provide a reliable assessment of the potential benefits of PEM fuel cell technology for aircraft application and to quantify the potential advantages of higher operational temperatures, both technologies are hereby investigated.

9.2 *PH-FC* system design and assumptions

The propulsive system under study is the *PH-FC* architecture (see Fig. 8.5) which has already been introduced in the previous Chapter, where the results of the preliminary studies about the parallel hybrid electric configurations are shown. This study consid-

ers two variants of such architecture, one using low temperature *LT-PEMFC* and the other using high temperature *HT-PEMFC*. The performances of the fuel cells are represented by the polarization curve shown in Fig. 9.1, which has been obtained using the model introduced in Chapter 4 for the characterization of low-temperature PEM fuel cells performances.

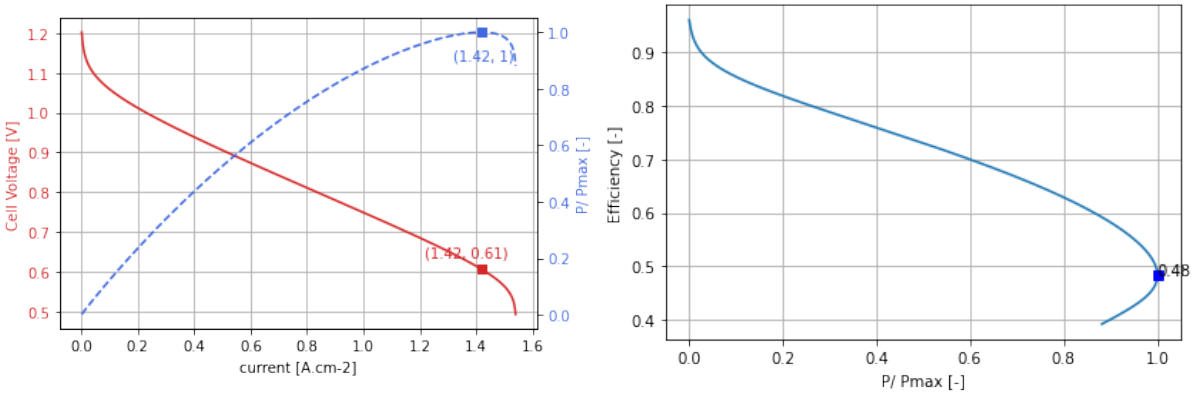

Figure 9.1: Fuel cell performance obtained using the model described in Chapter 4. On the left-hand side, the polarization curve and the normalized power output are represented respectively using the solid red and dashed blue lines. On the right-hand side, fuel cell efficiency is plotted against the normalized power output. The square marker indicated the nominal operation point.

It is reminded that, unlike the gas turbine, the fuel cell efficiency is lower at its nominal operation point with maximum power output than at part-load operation. This is a key feature of the fuel cells which is important to emphasize at this point because, unlike the previous studies on the *PH-FC* architecture, the hybridization strategy is to be optimized. Therefore, the fuel cell power output is not assumed to be constant throughout the flight, thus the operating conditions (voltage, current and efficiency) are not constant during the mission segments. Moreover, it is assumed that low and high-temperature PEM fuel cells share the same performance curves shown in Fig. 9.1. Although those technologies show different reaction kinetics, fuel impurity tolerance and other dissimilarities thoroughly investigated by [129], contradicting conclusions about the performance comparisons of *LT-PEMFC* and *HT-PEMFC* have been found in literature, especially regarding the electrode reaction kinetics given by the oxygen reduction reaction. The cited study also suggests that the different stack manufacturers have different development levels as well as specific stack design and optimization that may play a more significant role in the fuel cell performance than the difference of the intrinsic technology itself. Finally, great efforts are made to increase the performance of high-temperature PEM fuel cells in the short term. Consequently, it seems legitimate to consider the same efficiency for *LT-PEMFC* and *HT-PEMFC* fuel cells.

Similarly, for the determination of the *HT-PEMFC* system mass, the models presented in Chapter 4 that were specifically developed for *LT-PEMFC* systems have been used. Due to the operating temperature being above the boiling point of water, one of the main advantages of the *HT-PEMFCs* is that water is present in the vapor state, which allows getting rid of the water management system [130]. Even though there is common agreement in the literature that the higher operating temperature simplifies the fuel cell system, little was found about the mass of the stack of *HT-PEMFCs*. Several companies are developing commercial *HT-PEMFCs* for transport application in the $1kW$ - $10MW$ power range [131], among which Hypoint [132] who claims to reach high specific power values for its technology up to 2 kW/kg. However, due to the lack of available commercial products with detailed technical specifications, it was not possible to assess whether the *HT-PEMFC* stacks have significantly different specific power levels than the *LT-PEMFC* stacks. For this reason, as for their performance in terms of power and efficiency, also their mass is assumed to be equivalent. Therefore, the use of one technology over the other will only impact the cooling requirements, thus the size and the weight of the cooling system. Table 9.1 summarizes the main metrics used to size and evaluate the performance of the main powertrain components.

Fuel cell system	
System specific power ($\geq$500kW system)	$\approx$ 1.6 kW/kg
Stack nominal efficiency	48%
Net nominal efficiency	43%
Cryogenic hydrogen storage system	
Tank gravimetric efficiency (70 kg H_2 capacity)	$\approx$ 35%
Tank volume (70 kg H_2 capacity)	$\approx$ 2.7 m^3
Electric power systems	
Electric motor specific power	7 kW/kg
Electric motor efficiency	97%
Power electronics specific power	11 kW/kg
Power electronics efficiency	98%

Table 9.1: Summary of the main performance metrics of the electric powertrain.

The propulsive system is sized with respect to the nominal electric motor and gas turbine power and the design range given as inputs. According to those inputs, the mass of the entire hybrid propulsive system is determined using the methods and the results shown in Chapter 4. Due to the inevitable increase of OWE caused by the higher mass of the hybrid propulsive architecture, in order to comply with the characteristic MTOW of the baseline aircraft assumed unchanged, the maximum payload is reduced accordingly. Moreover, the resulting number of passengers takes also into account the fuselage volume and length which is required to accommodate the voluminous liquid hydrogen tank, considering that

the same geometry as the baseline aircraft is assumed (see Fig. 9.2). With a seat pitch of 30" (equivalent to 0.8m), the available space for the integration of the hydrogen tank is 0.8 meters for each seat row that is removed due to the lower payload. Moreover, a bonus length of 1.5 meter from the rear tail-cone zone is considered available for the installation of the hydrogen tank even with the full 72 passengers capacity. The most limiting requirement between the available payload mass and the available passenger cabin length will determine the maximum number of passengers in the aircraft. The mission performances of the hybrid aircraft are evaluated for a design mission of 200 NM at the same flight speeds as the baseline aircraft.

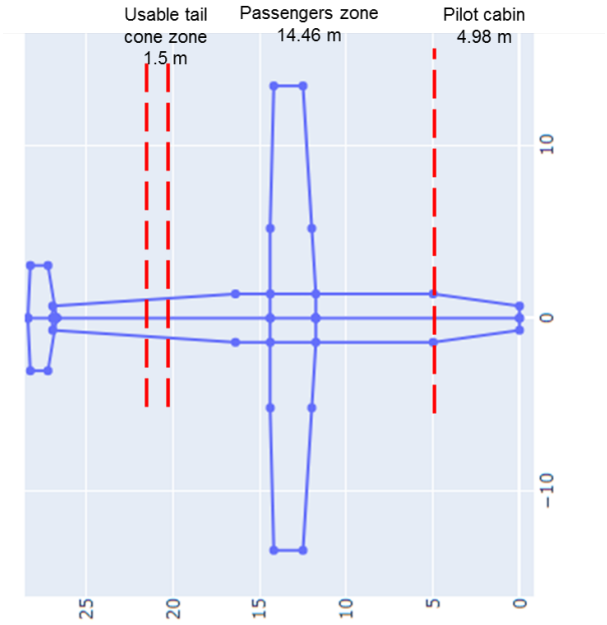

Figure 9.2: Fuselage length breakdown

The performance requirements of the aircraft under study take into account the one engine inoperative condition. Whilst the OEI denomination for the baseline turboprop aircraft may be self-explanatory, its definition for a hybrid aircraft needs to be further clarified. The parallel hybrid propulsion system shown in Fig. 8.5 is composed of two propellers (one per side) which convert the mechanical power into forward thrust. The electrical power provided to each propeller is generated by both an electric motor and a gas turbine by means of a double-input/single-output gearbox. Given the dependence between those components, it was assumed that the failure of one component would compromise the whole sub-system. Therefore, the OEI condition of the proposed propulsive architecture refers to the complete loss of thrust from one propeller. Regarding the fuel consumption for ground operations, the same fuel allowances as the baseline aircraft were considered. The required power for those segments would be provided exclusively by the gas turbines, easing the cooling requirement for the fuel cells. Due to the low speeds of the aircraft on the ground, electric fans would be required to provide the necessary airflow to the

radiator, therefore increasing electric power consumption and cooling system mass.

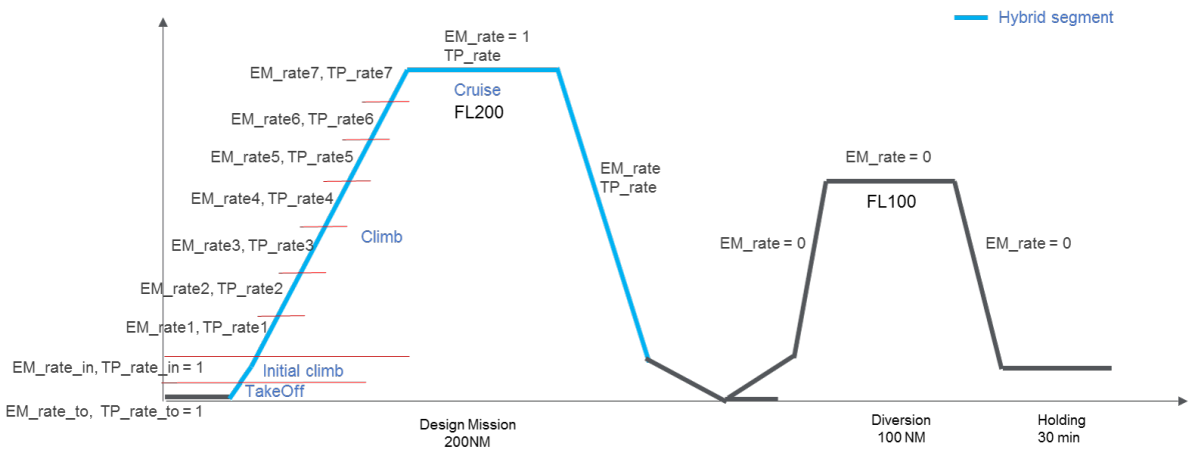

Figure 9.3: Representation of the different flight mission segments. The light blue line indicates a hybrid segment where both electric and gas turbine power is used. The dark grey line instead represents the flight segments that only use gas turbine power.

Concerning the hybridization strategy, it was decided to exploit the electrical power during the segments of take-off, climb, cruise and descent of the design mission (as shown in Fig. 9.3). Therefore, the gas turbine must be sized taking into account that it needs to provide all the required power and thrust to perform the reserve mission. Nevertheless, the hydrogen storage system is designed to take into account additional reserves that would be required in case of a go-around procedure with engine failure. This approach was chosen under the consideration that the employment of electrical power during the reserve missions would lead to higher hydrogen consumption, therefore to the need for a heavier and bigger tank. This would have a negative impact on the overall reduction of jet fuel consumption during the design mission, which is the performance metric to be optimized. During the descent, the specific fuel consumption of the gas turbine is considerably higher than the nominal cruise or climb rating due to its operation at a low throttle setting, which is far from the optimal operating condition of the turbine. Although the fuel cells would be able to provide alone the required propulsive power, turning off the gas turbines during this segment seems unfeasible. In fact, even if electrical and hydraulic power could be provided by the fuel cells, the turbines are still needed to provide bleed airflow for thermal control and cabin pressurization purposes. Moreover, even if a dedicated electric environmental control system was designed to ensure such function, with the proposed hybrid architecture, fuel cells alone may not be able to provide the required power in case of an aborted landing and go-around procedures. Therefore, the strategy employed consists of operating the gas turbine at idle rating during the whole duration of the descent segment, with the fuel cells providing the required propulsive power to guarantee a constant descent slope of -3°.

The power management strategy of the two power sources during the hybrid segments is defined by the combination of electric and thermal power outputs throughout the flight. The power output of those components is determined by the throttle (or power rate) applied during each segment of the mission. Considering that, during the climb, the flight conditions vary significantly and that those conditions affect both the fuel cell and the gas turbine performance, it seemed appropriate to split the climb in different smaller segments, increasing the degree of freedom of the propulsion operation strategy. As illustrated in Fig. 9.3, the simulated mission is composed of a total of 11 hybrid segments, for which the degree of hybridization is determined by the electric and thermal power rates:

$$PS = \frac{EM_{rate} \times P_{EMrated}}{EM_{rate} \times P_{EMrated} + TP_{rate} \times P_{TPrated}} \tag{9.1}$$

where PS is the power split defined as the ratio between the power supplied by the electric motor and the total power transferred to the propeller, $P_{EMrated}$ is the sizing power of the electric propulsive chain and the $P_{TPrated}$ is the max available power of the gas turbine at each flight point.

9.3 Optimization set-up

The optimization problem is given here by a single objective function, 18 design variables and 4 inequality constraints as described in Table 9.2.

	Function/variable	Quantity	Range
Minimize	Block fuel per passenger	1	
with respect to	Nominal electric power	1	$[500, 1000]$ (kW)
	Gas turbine RTO power	1	$[1200, 2000]$ (kW)
	Take-off electric power rate	1	$[0.6, 1]$
	Initial climb electric power rate	1	$[0.6, 4]$
	Climb electric power rates	7	$[0.6, 1]$
	Climb turbine power rates	7	$[0.4, 1]$
	Total design variables	**18**	
subject to	Operational ceiling $>$ 6096 m		
	OEI net ceiling $>$ 2943 m		
	TOFL $<$ 1384 m		
	TTC $<$ 16.9 min		
	Total inequality constraints	**4**	

Table 9.2: Definition of the optimization problem with 1 objective function to minimize, 18 continuous design variables and 4 inequality constraints.

To initialize a Bayesian optimizer, a design of experiments (DOE composed of inputs and

associated outputs) has to be chosen in order to build the first surrogate models for the objective and the constraints. As 18 design variables are considered here, an initial DOE of 60 (3 times the dimension of the problem) is built as suggested in [83] and the use of WB2s (Watson and Barnes 2nd criterion with scaling) as acquisition function is chosen as it is known to be more robust than the Expected improvement criterion, especially in high dimension [83]. The associated surrogate models with 18 inputs are built using Kriging with Partial Least Squares, known as KPLS models [77] in order to handle the input dimension. Here the number of PLS components is fixed to 4. To tackle multi-modal constraints, the Upper Trust Bound (UTB) criterion is used [133]. Concerning the optimization algorithms to solve the subproblem related to the acquisition function, SLSQP (Sequential Least Squares Programming) has been chosen.

The choice of the design variables listed above allows the optimization algorithm to explore a wide range of hybridization strategies, where the resulting electric and thermal powers at each flight point are determined independently of the maximum rated power of the electric motor and gas turbine. The components of the electrical power chain (e.g. fuel cells, power electronics, electric motors) are sized according to the nominal electric power, which is the electric power supplied by each electric motor during the cruise (cruise electric power rate = 1). During the cruise, the gas turbine throttle is automatically derived to match the thrust needed to fly at the defined flight speed and altitude. The gas turbine RTO power instead sizes the thermal engine for the take-off phase where the turbine power rate is set to 1. The lower bound of 1200 kW is imposed because it is the minimum power required to allow the execution of the reserve flight mission without the aid of electrical power.

By varying the design variables, the optimization algorithm explores different system designs with a total installed power between 1700 kW and 3000 kW per side. Moreover, considering that the throttle settings for both the electric motor and gas turbine may be lower than 1, the total power delivered by the propulsion system may be much lower than the rated 1700 kW. Therefore, in order to design a propulsive system capable of reducing fuel consumption while ensuring the same performance requirements as that of the baseline aircraft, the optimization is subject to some operational constraints.

9.4 Optimization results

Optimizations were run to design two parallel hybrid propulsive systems comprising either low-temperature or high-temperature PEM fuel cells. These configurations are referred to as *Hybrid-LT* and *Hybrid-HT*, respectively. The optimal results for both simulations are shown in Table 9.3.

Function/variable	*Hybrid-HT*	*Hybrid-LT*
Block fuel per passenger	4.5 kg/PAX	4.85 kg/PAX
Nominal electric power	1000 kW	1000 kW
Gas turbine RTO power	1200 kW	1200 kW
Take-off electric power rate	0.71	0.72
Initial climb electric power rate	0.77	0.75
Climb electric power rates	[0.97, 0.96, 0.98, 0.99, 0.98, 1, 0.99]	[0.88, 0.92, 0.93, 0.94, 0.99, 0.99, 1]
Climb turbine power rates	[0.56, 0.54, 0.53, 0.51, 0.5, 0.41, 0.4]	[0.6, 0.58, 0.61, 0.6, 0.4, 0.4, 0.4]

Table 9.3: Optimal design variables and objective function for both propulsive systems.

With an initial DOE of 60 points, for the *Hybrid-HT* configuration the optimum was found after 400 iterations. As shown in Fig. 9.4, the successive iterations did not lead to better results. The optimization algorithm found that the lowest fuel consumption per passenger is found when the electric power chain is sized according to the highest power allowed. On the contrary, the optimal sizing power of the gas turbine is the lower bound of the given range.

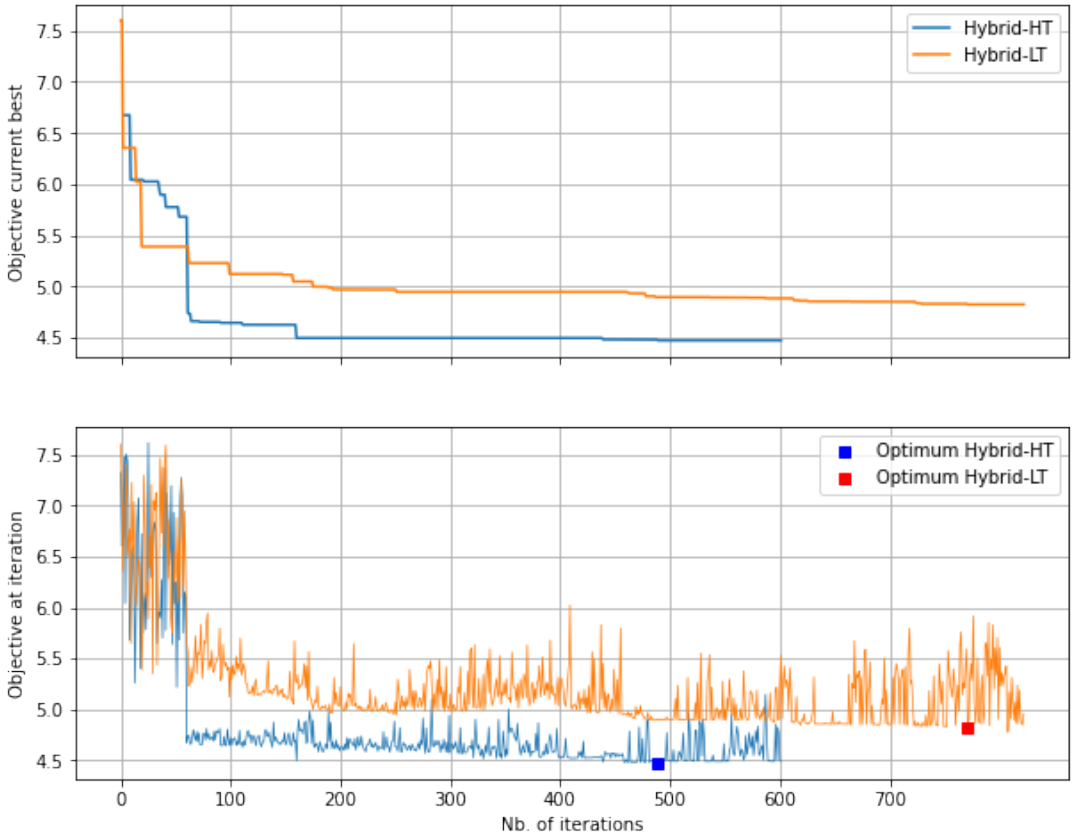

Figure 9.4: Current best objective function value found at given iteration (top) and all evaluations done during the optimization process (exploration or exploitation) (bottom) for the *Hybrid-LT* and *Hybrid-HT* optimization problems. The best point associated with each problem is given by a colored square. The 60 first iterations represent the initial DOE.

Although the electric power rates during the climb are close to 1, the optimal hybridization strategy does not consist in exploiting all the electric power available throughout the mission. The optimal design of the *Hybrid-HT* configuration consists in a minimal sizing of the gas turbine, used for power peak shaving of the climb and cruise phases, as shown in Fig. 9.5. Therefore, the gas turbine power rates during the climb are driven by the operational constraint of the required time to climb to reach the cruise altitude.

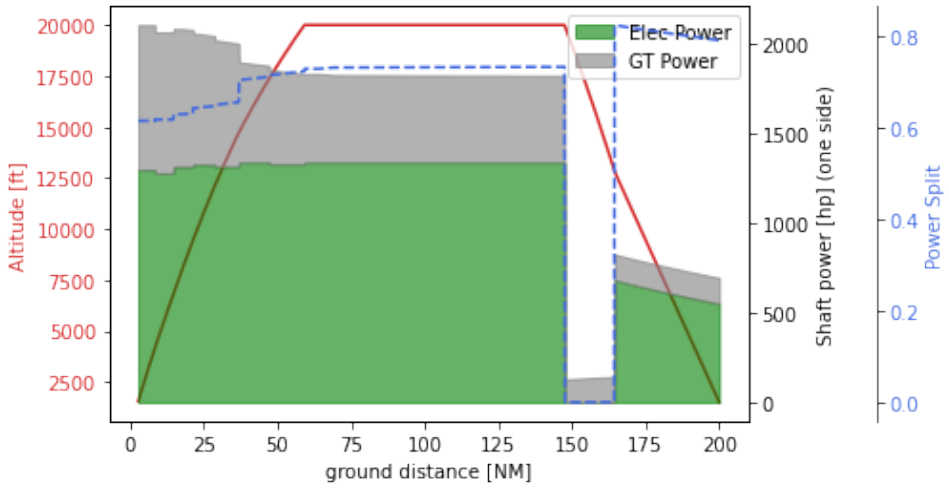

Figure 9.5: Hybridization strategy for the *Hybrid-HT* configuration. The dashed blue line represents the hybridization factor. The grey and green areas illustrate respectively the gas turbine and the electric motor power output all along the mission. Finally, the red solid line gives the evolution of the altitude during the flight.

As it can be seen in Fig. 9.6, TTC, together with TOFL, is the most stringent constraint that drives the powertrain design. The electric power rates during the climb are limited by a constraint that is not explicitly defined in the optimization problem, but that is integrated into the MDA process. As previously mentioned, the design process of the hybrid aircraft takes as inputs the airframe geometry and the characteristic MTOW of the baseline aircraft and it evaluates the maximum payload as well as the maximum number of passengers it can carry. While the maximum payload is only affected by the change of the OWE, the maximum number of passengers is also limited by the available length of the fuselage passenger zone. Since higher electric power output means higher hydrogen consumption, the larger hydrogen tank required reduces the fuselage passenger zone. The electric power rates found by the optimizer turn out to be the highest values possible before the size of the hydrogen tank imposes a further reduction of the maximum number of passengers.

The optimization of the *Hybrid-LT* configuration instead, leads to a different hybridization strategy. As for the *Hybrid-HT* configuration, Fig. 9.7 shows that TTC, together with TOFL, is the most stringent constraint that drives the powertrain design.

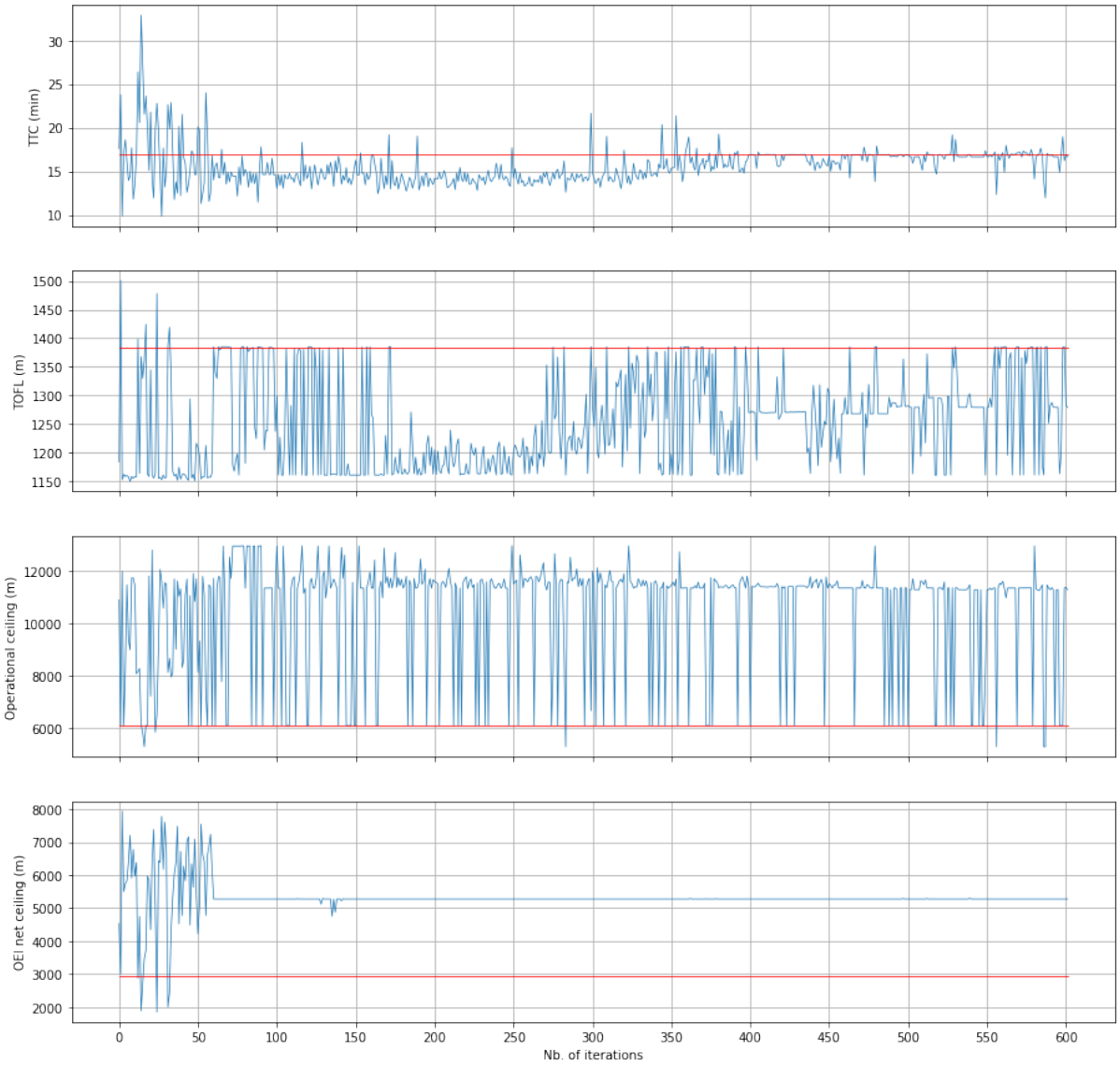

Figure 9.6: *Hybrid-HT* constraints function of iterations. The red line represents the maximum value allowed for the TTC and TOFL constraints (respectively first and second plots from the top), and the minimum value allowed for the operational ceiling and OEI net ceiling constraints (respectively third and fourth plots).

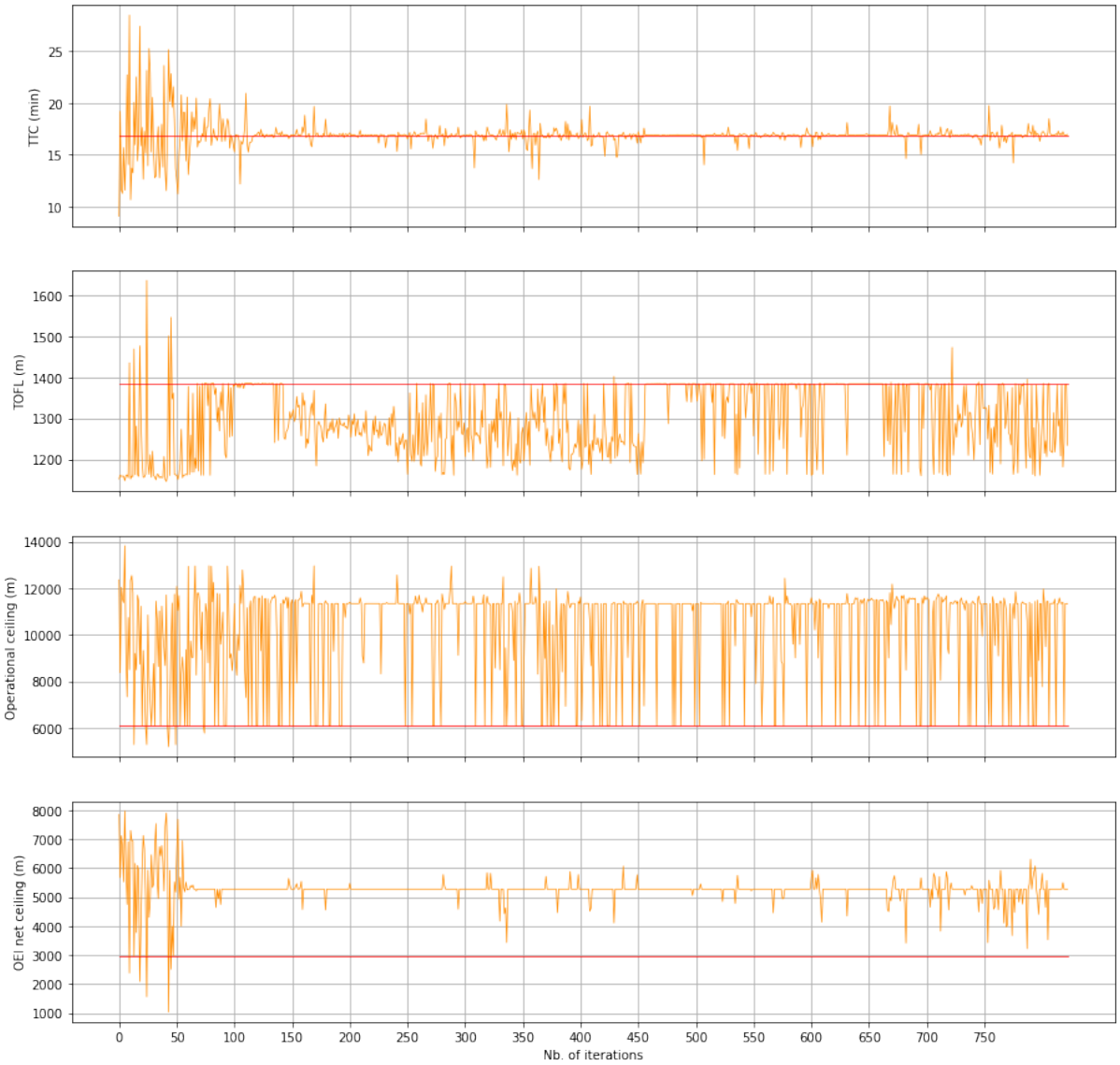

Figure 9.7: *Hybrid-LT* constraints function of iterations. The red line represents the maximum value allowed for the TTC and TOFL constraints (respectively first and second plots from the top), and the minimum value allowed for the operational ceiling and OEI net ceiling constraints (respectively third and fourth plots).

Whereas the nominal electric power and gas turbine RTO power is found to be the same as for the *Hybrid-HT* case, for this configuration, the minimum block fuel per passenger is given by a different power management strategy with lower electric power output at the beginning of the climb phase. This behavior is explained by the different cooling system designs, being the only difference between the two configurations. In fact, for the *Hybrid-LT* aircraft, the mass of the two radiators needed to evacuate the heat generated by the fuel cells is much higher than the *Hybrid-HT* configuration, which affects significantly its payload capability. As shown in Fig. 9.8, the mass of the cooling system of the propulsive system using LT-PEM fuel cells is double the mass of the *Hybrid-HT* configuration. In both cases, the maximum payload is determined by the increase of OWE and is not

constrained by the available volume in the cabin for the installation of the hydrogen tank.

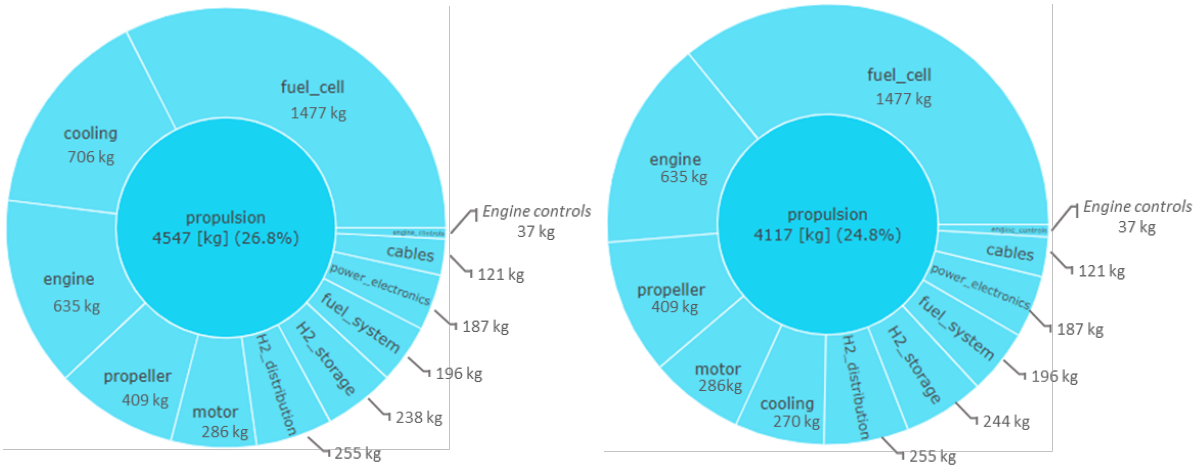

Figure 9.8: Propulsion weight breakdown of the resulting *Hybrid-LT* (left) and *Hybrid-HT* (right) optimal designs.

Higher electric power rates lead to lower fuel consumption, however, they also lead to higher radiator mass which is balanced off by a decrease in the payload. The main characteristics of the two configurations resulting from the optimization process are provided in Table 9.4.

Parameter	***Hybrid-HT***	***Hybrid-LT***	***Baseline***
OWE	16581 kg	16972 kg	14154 kg
Max Payload	6023 kg	5634 kg	6840 kg
Passengers	63	59	72
Block fuel 200 NM	283 kg	286 kg	609 kg
H2	143 kg	139 kg	-
Max waste heat Q_{RAHX} (one side)	750 kW	780 kW	-

Table 9.4: General characteristics of the different aircraft configurations.

The mass of the radiator is a function of the waste heat of the fuel cell as well as the ambient temperature. Decreasing the electric power rates during the climb reduces the radiator mass thanks to the combination of two effects. Not only it reduces the power output of the fuel cell, but it also increases its efficiency thus reducing the waste heat, hence the required radiator mass. Moreover, in Fig. 9.9, it can be observed how the electric power increases with increasing altitude. This is explained by the increase in the heat transfer rate due to the increase of the delta between the fuel cell operating temperature and the ambient temperature. The resulting hybridization strategy is the

optimal compromise between the fuel consumption during the mission and the fuel cell cooling system mass.

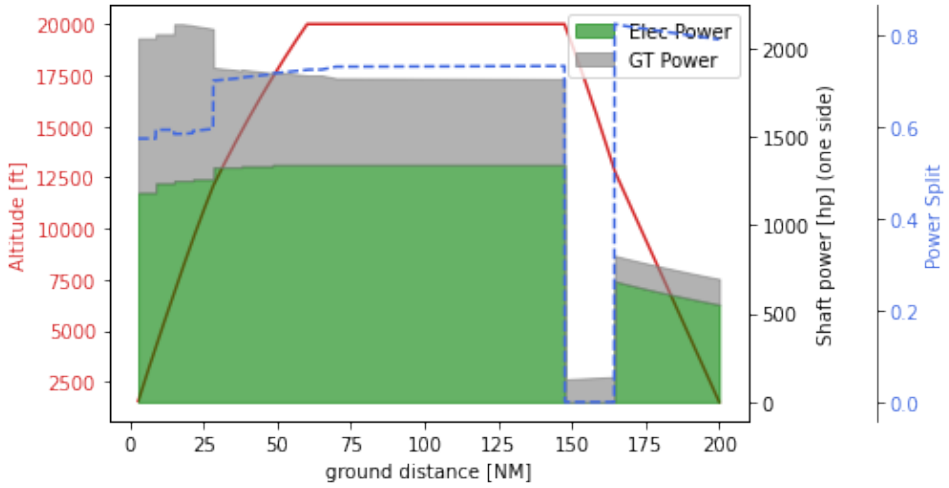

Figure 9.9: Hybridization strategy for the *Hybrid-LT* configuration. The dashed blue line represents the hybridization factor. The grey and green areas illustrate respectively the gas turbine and the electric motor power output all along the mission. Finally, the red solid line gives the evolution of the altitude during the flight.

9.5 Global sensitivity analysis L1

In the previous section, an optimization was performed to design the parallel hybrid fuel cell propulsion system and an associated power management strategy that would minimize the block fuel per passenger while ensuring the same high-speed and low-speed performance as the baseline conventional aircraft. The design variables used in the optimization problem have a direct impact on the outputs of the models developed for the sizing and performance evaluation of the propulsion system components. However, each model accounts for a certain level of modeling error, which induces a modeling uncertainty on the output of the model, and thus on the aircraft performance assessment. In this section, the objective is to quantify the uncertainty introduced by each model and to propagate it through the aircraft simulation process in order to identify the model parameters which have the greatest impact on the final quantity of interest (block fuel per passenger). Such a result would allow us to understand where the development efforts should be focused if higher accuracy of the results is needed.

Therefore, Polynomial Chaos Expansion method (described in Section 2.3) is used to perform a global variance-based sensitivity analysis by computing the Sobol indices. This analysis focuses on the *Hybrid-HT* which has shown better performances due to the reduced weight of the cooling system. Given the hybrid aircraft configuration under study, the first step of the method consists of the identification of the model parameters which

are likely to have an impact on the quantity of interest. For that, only the uncertainties introduced by the models used to analyze the new propulsive system are taken into account. The list of all the parameters identified, which are used to perform the global sensitivity analysis, is given in Table 9.5, together with the probabilistic model associated and the upper and lower boundary values. For the sake of clarity, all those parameters are concatenated in a vector denoted by $\vec{x}$, with the generic parameter x_i for $i = 1, \ldots, 11$.

$\vec{x}$: Parameters	Distribution	Range	Unit
x_1: Cables length	Uniform	$[20, 50]$	m
x_2: H_2 pipes length	Uniform	$[30, 70]$	m
x_3: Electric motor efficiency	Uniform	$[0.95, 1]$	
x_4: Electric motor specific power	Uniform	$[5, 10]$	kW/kg
x_5: Power electronics efficiency	Uniform	$[0.95, 1]$	
x_6: Power electronics specific power	Uniform	$[7, 15]$	kW/kg
x_7: K-factor H_2 tank length	Uniform	$[0.8, 1.2]$	
x_8: K-factor H_2 tank gravimetric efficiency	Uniform	$[0.7, 1]$	
x_9: K-factor cooling mass	Uniform	$[0.8, 1.2]$	
x_{10}: K-factor fuel cell specific power	Uniform	$[0.8, 1.2]$	
x_{11}: K-factor fuel cell efficiency	Uniform	$[0.95, 1.05]$	
Total parameters	**11**		

Table 9.5: Uniform probability distribution characteristics of hybrid propulsion parameters.

Those uncertain parameters can be either outputs or inputs of the component models. If they are inputs, the probabilistic model is associated directly with them, otherwise, sensitivity factors (K-factors) are multiplied by the parameters to modify their value. The ranges are assigned using different criteria. For example, engineering judgment is used to determine the range of parameters such as cables and hydrogen pipe length. Instead, when the parameter is an output of a model, which is the case for all the parameters for which a K-factor is defined, the perceived accuracy of the model is used to determine the range. Finally, reference values from the literature are used to determine the range of the remaining input parameters of the electric motor and power electronics [13, 59, 21]. Once the uncertain model parameters have been identified and a probabilistic distribution function has been associated to them, the next step consists in the creation of a metamodel for the estimation of the quantity of interest by polynomial chaos expansion (PCE). The PCE metamodel is created giving the polynomial basis orthogonal with respect to the input distribution and using sparse least squares for the computation of the coefficients. Different hyper-parameters are used (from 2nd order degree up to 8th degree) to obtain the better accuracy of the metamodel. The number of points used to train the metamodel is 918, while 50 points have been used for the validation.

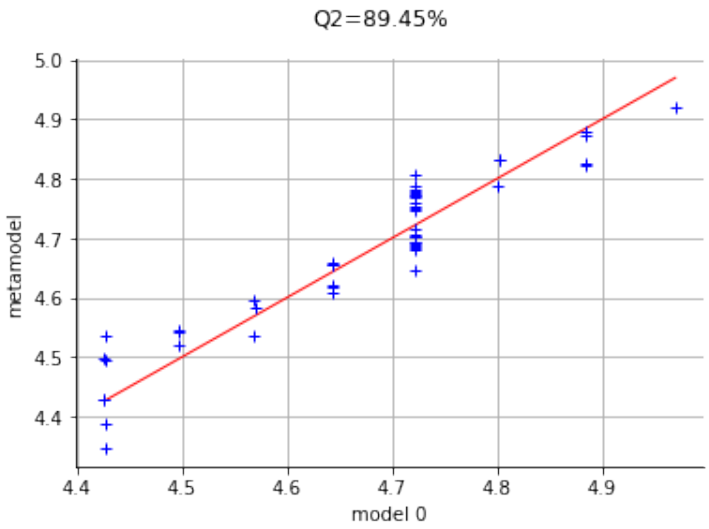

Figure 9.10: Validation results for the 8th degree PCE metamodel. Predicted results are plotted versus true results.

The best fit has been obtained using the 8th degree and the validation results are shown in Fig. 9.10. In the case of a perfect fit, all the points would lie on the first diagonal (red solid line). In this case, with a predictivity factor (defined by Eq. (7.5)) lower than 90%, the validation results show that the PCE could not approximate the original function with very high accuracy. Such difficulties in building an accurate metamodel must be related to the discontinuous nature of the quantity of interest. Indeed, while the block fuel varies continuously with the input parameters, the number of passengers is a discrete variable, thus the function the PCE is trying to approximate is discontinuous. Such behavior can be observed graphically in Fig. 9.11, where those variables, evaluated on the 918 training points, are sorted in ascending order. It can also be observed how the variation of block fuel is almost null, thus the actual output variable which is affected by the uncertainty of the model parameters is the maximum number of passengers.

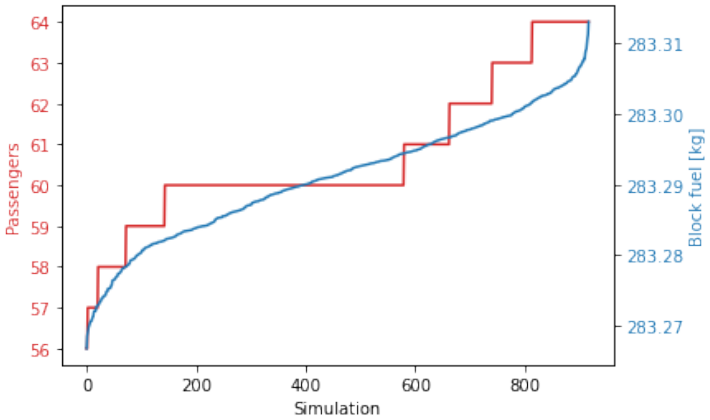

Figure 9.11: Number of passengers and block fuel results of the 918 training points sorted in ascending order.

In order to assess which of the parameters in Table 9.5 have the greatest impact on the maximum number of passengers, the Sobol indices associated with the polynomial chaos decomposition of the model are evaluated. The results obtained are shown in Fig. 9.12 and the values provided in Table 9.6.

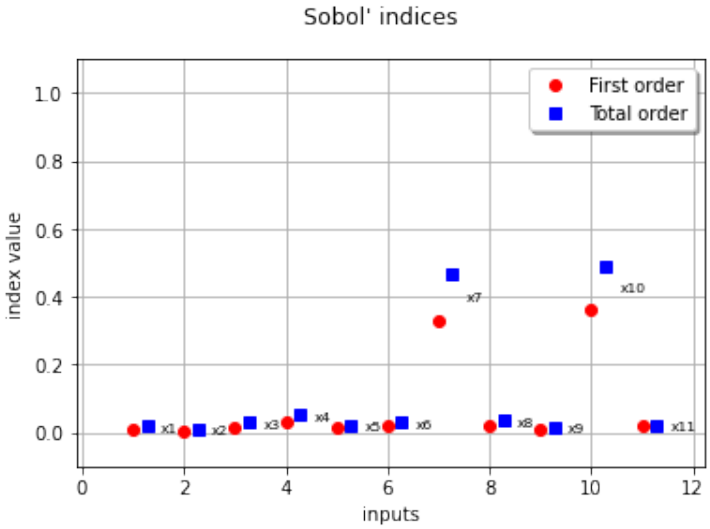

Figure 9.12: First and total order values of Sobol indices for each parameter x_i

	Sobol indices	
$\vec{x}$**: Parameters**	**1st order**	**Total order**
x_1: Cables length	0.0103268	0.0191047
x_2: H_2 pipes length	0.00269965	0.0101174
x_3: Electric motor efficiency	0.0164014	0.0287802
x_4: Electric motor specific power	0.0337231	0.0546075
x_5: Power electronics efficiency	0.0135952	0.0195697
x_6: Power electronics specific power	0.0202809	0.0296135
x_7: K-factor H_2 tank length	**0.33084**	**0.469735**
x_8: K-factor H_2 tank gravimetric efficiency	0.0223152	0.0390379
x_9: K-factor cooling mass	0.0088396	0.0160398
x_{10}: K-factor fuel cell specific power	**0.360833**	**0.490289**
x_{11}: K-factor fuel cell efficiency	0.0191649	0.0224588

Table 9.6: Tabulated values of first and total order Sobol indices for each parameter x_i. Bold values indicate the parameters with greatest impact on the quantity of interest.

Figure 9.12 shows that the two parameters with the greatest impact on the block fuel per passenger are the length of the hydrogen tank and the specific power of the fuel cell system. Indeed, both parameters strongly affect the payload capability of the aircraft. The former parameter determines the available passenger cabin space and thus the maximum

number of passenger seat rows, whereas the latter influences the OWE and thus the max payload capability of the aircraft.

The sensitivity of the output to the parameter variation can also be visually identified using scatter plots, as done in Fig. 9.13. These plots show the impact of each parameter x_i on the block fuel per passenger. Each plot shows the distribution of the results (block fuel per passenger) for each fixed value of the parameter x_i, while varying all the other parameters. If the output is not sensitive to the variation of x_i, an uniform distribution of the points can be observed between its minimum and maximum values for each fixed value of x_i. This is the case for all the plots in Fig. 9.13 except for the ones corresponding to x_7 and x_{10}. For example, in the first plot which shows the sensitivity of the output to the electric cables length, it can be seen that whatever the value of x_1, the block fuel per passenger always varies approximately between 4.4 and 5, suggesting that such parameter is not a determining factor for the output. On the contrary, when the parameter has a strong impact on the output, the points tend to show a trend. For example, the plot corresponding to the fuel cell specific power (x_{10}) shows a linear trend, with the block fuel per passenger that decreases with the increase in the fuel cell specific power. This is easily explained given that a higher specific power leads to lower OWE and thus a higher number of passengers. Instead, the interpretation of the plot corresponding to the second most dominant parameter, x_7, is a bit less straightforward. Being x_7 the K-factor of the H_2 tank length, a linear growing trend could be expected. Indeed, the greater the H_2 tank length, the lower the space available for the passengers and thus the higher the block fuel per passenger. However, as it can be observed in the plot, this is only partially true because the number of passengers is determined both by the available cabin space and the OWE of the aircraft. Therefore, when the H_2 tank length is low, this only results in a higher number of passengers if the OWE is low enough to allow it.

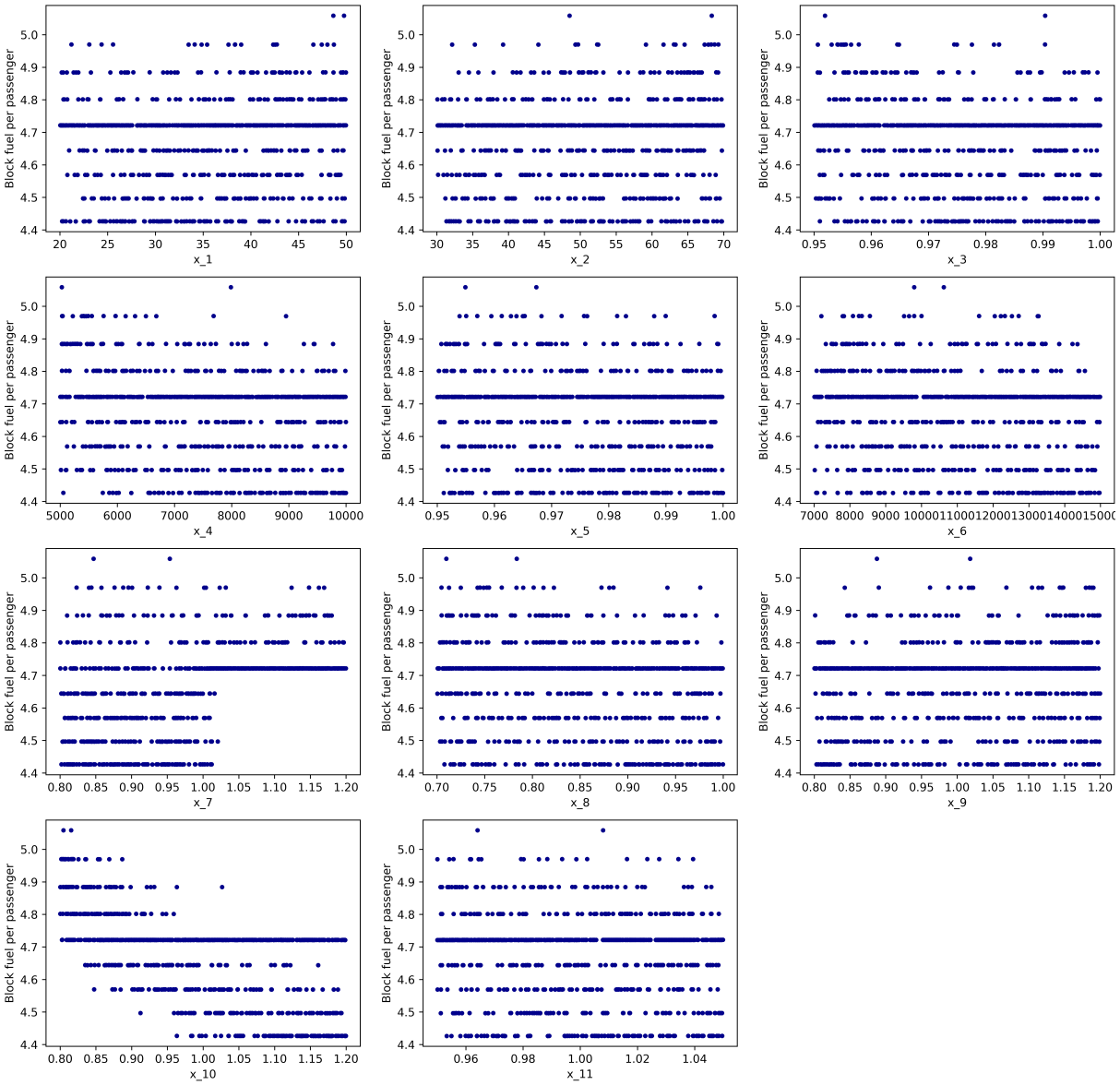

Figure 9.13: Effects of each parameter x_i on the block fuel per passenger.

9.6 Conclusion of the chapter

The objective of this study was to perform a constrained optimization in order to design the hybrid propulsion system and an associated power management strategy that would minimize the block fuel per passenger while ensuring the same high-speed and low-speed performance as the baseline conventional aircraft.

Two optimizations were performed to design two parallel hybrid propulsive systems comprising either low-temperature or high-temperature PEM fuel cells for the generation of electrical power. Both designs showed the capability to reduce fuel consumption per passenger by more than 30%, at the expense of less passengers, a lower range at maximum

payload and higher OWE than the same aircraft equipped with conventional propulsion. For both configurations, the total installed power of 2200 kW (1000 kW for the electric power and 1200 kW for the gas turbine power) is 22% higher than the baseline aircraft. In both cases, the optimization algorithm tends to maximize the sizing power of the fuel cell and minimize one of the gas turbines, both effects being beneficial to the two power-train designs. Minimizing the gas turbine power allows for increasing its efficiency when operated at low power since the operating point is close to the turbine nominal design point. Maximizing the fuel cell power leads to the increase of the hybridization factor in cruise but, above all, allows for increasing their efficiency when operated at low power rates. This higher efficiency is beneficial to both configurations in a different way. High efficiency of the fuel cells is key to the determination of the maximum number of passenger for both configurations, however for the *Hybrid-HT* configuration this is achieved through the increase of available cabin volume, while for the the *Hybrid-LT* the maximum number of passenger is achieved through the decrease of OWE.
Indeed, for the *Hybrid-HT* configuration, the higher efficiency of the fuel cells results in the reduction of the quantity of hydrogen needed to store on-board, and thus to an increase of the number of passengers the aircraft is able to carry. For the *Hybrid-LT* configuration, the higher efficiency leads to the reduction of waste heat to be dissipated, thus to the reduction of the cooling system mass, which is the key to increasing the payload for this aircraft configuration.

The optimal power management strategy identified for each configuration differs due to the higher cooling requirements of the *Hybrid-LT* system. Thermal management is a key aspect in the design of a propulsive system involving fuel cells for the generation of electric power. It is crucial in the determination of the performance of a fuel cell-based hybrid electric aircraft because its sizing has a first-order impact on the OWE of the aircraft and therefore on its payload capabilities which affects the block fuel reduction per passenger.

As the *Hybrid-HT* showed the capability to reduce even further the block fuel consumption per passenger due to the lower weight of the cooling system required, this architecture has been further analyzed by performing a global sensitivity analysis to quantify the uncertainty on its performance which is produced by the modeling errors and assumptions used. The study has shown that the propulsion parameters with the greatest impact on the quantity of interest in the aircraft performance are the length of the hydrogen tank and the specific power of the fuel cell system. Therefore, if higher accuracy is required, the efforts should be focused on enhancing the confidence level of the models used to determine such parameters.

General conclusion and future perspectives

Conclusion

The research work of this thesis was aimed to close the gap between the next generation zero-emissions aircraft and the existing carbon fossil fuel-based aircraft, employing a forward-fit rather than an ex-novo approach for aircraft design, which, given the reduced certification and development efforts, may allow an entry into service of more efficient air-vehicles well before 2035. In particular, the thesis focused on the forward-fit design of a 70-seat regional aircraft featuring low-emission propulsion.

As part of a PhD thesis in aircraft design, **the first goal** was to develop the capabilities, in terms of methods and tools, paving the way for a reliable design and sizing of future propulsive systems to be integrated on existing aircraft platforms. In order to reach such a goal, the research work covered three main activities:

- Survey of technology enablers
- Evolution of a conceptual aircraft design platform
- Set-up of multidisciplinary optimization and uncertainty management techniques

The first months of this research were dedicated to performing an extensive literature review of the suitable technologies that could have been used to reduce the emissions of a regional aircraft with the capability to carry between 50 and 100 passengers. Excluding the use of sustainable aviation fuel which does not require particular design efforts at the conceptual stage, two key technology enablers were identified: Li-Ion battery and liquid hydrogen. Several aircraft propulsive systems employing those technologies can be designed. In this thesis, three main propulsive groups were defined: battery-based electric propulsion, hydrogen-based propulsion and turbo/hybrid-electric propulsion. In total, those three propulsive groups are composed of eight propulsive systems which were identified in order to replace the conventional gas turbines of a regional turboprop aircraft.

A conceptual aircraft design platform named RHEA design tool was therefore developed in order to assess the performance of each system. RHEA is based on an existing multidisciplinary aircraft design and optimization tool named FAST-OAD, developed and

validated for the design of a single-aisle aircraft such as the Airbus A320. Therefore, the evaluation models as well as the overall design processes, in RHEA, were modified to be suitable for the design of the regional 70-seat turboprop aircraft to be used as baseline aircraft for the forward-fit designs. The obtained baseline aircraft was chosen to be representative of the ATR72 aircraft, to provide the design process inputs that were coherent with its characteristics in terms of range, payload and speed. The design process was therefore validated by comparing the baseline aircraft results with the available data of the ATR72 and proved to be sufficiently accurate and reliable. The main strength of the developed overall design process is its flexibility to reproduce any other regional twin-propeller aircraft such as the ATR42, Dash8-Q300, -Q400, Dornier 328, etc. This is possible simply by providing a new set of input top-level aircraft requirements which are representative of the aircraft to model. The same consideration is applicable to the forward-fit design process used for aircraft conversion with the new propulsion system. Indeed, such a process uses as inputs the output files generated for the baseline aircraft model and sizes the new propulsive system according to the new set of aircraft requirements provided for the modified aircraft.

Given the forward-fit approach employed, multidisciplinary design optimization and uncertainty techniques were not employed to optimize the overall aircraft design, but rather to provide a reliable assessment of the potential of the different propulsive systems for the same baseline aircraft platform. Indeed, only the parameters introduced by the new propulsive systems were used as design variables for the optimization in order to guarantee the best possible design for the given aircraft platform and operational scenario. For that, a Bayesian optimizer named SEGOMOE was used, which features very low computational effort and CPU running time, allowing for optimizations using up to eighteen design variables subject to four inequality constraints.

In the same way, only the uncertainties arising from the introduction of the new propulsion systems were quantified and propagated throughout the multidisciplinary design and analysis process. Uncertainty management techniques were employed in order to cope with the lack of means of validation inherent to the unavailability of data on the propulsion technologies used. Indeed, even if some of those technologies are currently mature enough to be used in other sectors (e.g. batteries and fuel cells are already used in the automotive industry), the aviation performance standards are often much more stringent both concerning their safety and reliability, which may lead to very different designs. The uncertainty management approach employed consisted in performing global variance-based sensitivity analyses, and computing Sobol sensitivity indices by polynomial chaos expansion. These analyses have allowed assessing the impact of both data uncertainty (related to the lack of reliable data) and model uncertainty (related to the inevitable errors between a real-life phenomenon and its computational model) on the

overall aircraft performance. These analyses were performed on the most promising architectures in order to identify the uncertainty sources with the greatest repercussions on the final results, so as to efficiently address the modeling efforts to increase the reliability of the results.

The results of those uncertainty studies suggested increasing the level of detail and thus the complexity of the model used to size and characterize the behavior of the fuel cell system. Indeed, while overall aircraft performances have shown to be significantly impacted by the batteries specific energy, the uncertainty concerning its value is more inherent to the battery chemistry rather than the ability of our model to reproduce its performance. The first global sensitivity studies performed on the fuel cell-based propulsive architecture have shown that the main contributor, among all the components of the entire propulsive system, to the uncertainties of both the propulsion system weight and efficiency is the fuel cell, followed by the hydrogen tank for its impact on the aircraft weight. Therefore, during this thesis, the modeling efforts of the electric propulsive chain focused on the development of models to better characterize the hydrogen systems including hydrogen tanks, fuel cell balance of plant and thermal management.

The second goal of this PhD was to provide some preliminary results to be used as a credible basis to drive the next generation of low-emission regional aircraft design choices. For that, a down-selection approach consisting of three steps was set in place to analyze a total of eight propulsive architectures in a time-efficient manner. At each step, the number of architectures is reduced and the level of fidelity of the analyses is increased. Figure 9.14 shows all the architectures analyzed at the different steps of the downselection process. Most of the propulsive architectures have been discarded after the first step of conceptual studies. Indeed, from a total of eight systems, only two were further analyzed in the second step of the process: the parallel hybrid configurations with batteries ($PH\text{-}EB$ architecture) and with fuel cells ($PH\text{-}FC$ architecture). The other configurations were discarded for different reasons. The full electric system using batteries ($FE\text{-}EB$) was discarded because it proved to be not technically feasible due to the poor performance in terms of the weight of the batteries. The study concludes that a two-fold increase of battery-specific energy, with respect to the most optimistic scenario of 500 Wh/kg, would be needed for the aircraft to carry at least 50 passengers with a maximum range of 200 NM. Similarly, the series hybrid and turbo-electric configurations were discarded, because although technically feasible, they only showed a degradation of the overall performance of the aircraft due to an increase in weight and decrease in propulsive efficiency, which lead to increase the fuel consumption. It must be specified, however, that the exactitude of such a statement is limited to the specific design approach used, which does not allow exploiting the electric power to enhance the efficiency of the airframe design (e.g. boundary layer ingestion, distributed electric propulsion, etc.). On the

other hand, the full hydrogen architectures such as the fuel-cell based full electric system ($FE\text{-}FC$) and the hydrogen gas turbine system ($TP\text{-}H2B$), although having shown the potential to comply with the top-level aircraft requirements in terms of range, payload, and CO_2 emissions, have not been further assessed in the next steps because in order to provide a true added value in the continued assessment of such architectures, more reliable information about such technologies would be needed.

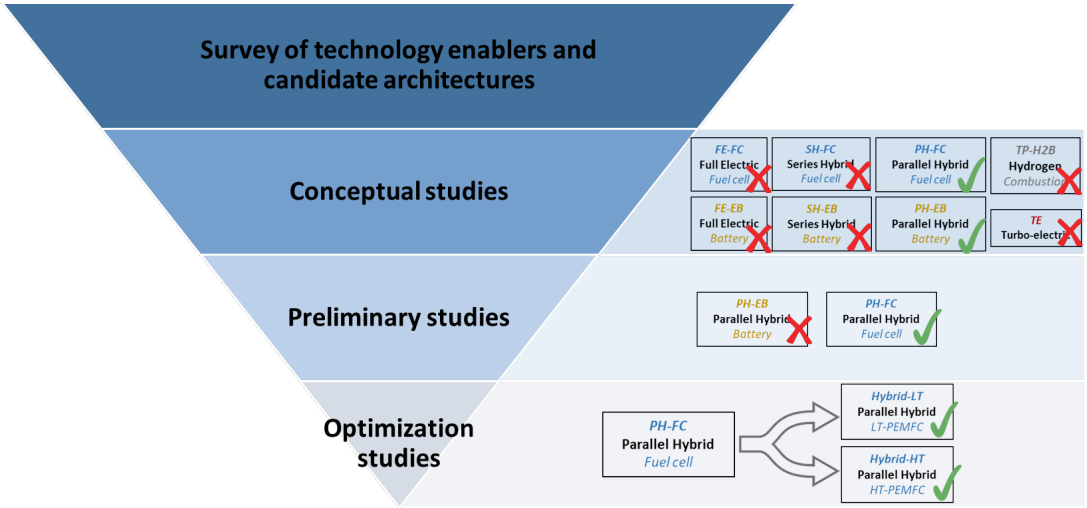

Figure 9.14: Synthesis of the propulsive architectures analyzed in the three steps of the down-selection process.

Of the two parallel hybrid systems analyzed in the second step of preliminary design studies, only the fuel cell-based configuration was selected and further analyzed in the last step of the process. Contrarily to the battery-based configuration, the parallel hybrid fuel cell system showed the potential to considerably reduce aircraft emissions (more than 20%) both in terms of CO_{2eq} and NO_x. This study also showed the significant impact of the thermal management system on the overall weight of the propulsive system. For this reason, in the last step of the down-selection process, the parallel hybrid fuel cell architecture was optimized also taking into account the technology of high temperature PEM fuel cells ($HT\text{-}PEMFC$). By optimizing the powertrain design and the associated power management strategy throughout the mission, the parallel hybrid fuel cell configurations either with low-temperature and high-temperature fuel cells, show the potential to reduce CO_{2eq} emissions by more than 30% on a 200 NM mission for a regional aircraft with the capability to carry around 60 passengers. However, the technology of PEM fuel cells operating at higher temperatures is more efficient insofar as it allows reducing considerably the weight penalties of the thermal management system.

Future perspectives

Nevertheless, many challenges still remain to be addressed.

The first limitation of this thesis lies in the aerodynamic model which does not evaluate

any additional drag caused by the introduction of the thermal management system of the fuel cells. Indeed, considerable air scoops are surely needed in order to keep the fuel cell at the nominal operating temperature and to provide the required airflow for the chemical reaction with hydrogen. These air scoops are responsible for the degradation of the aerodynamic performance of the aircraft, which has not been taken into account in this thesis based on the assumption that a good design exploiting the Meredith effect would result in a negligible increase in drag. This is clearly a strong assumption that has only been verified using results of previous studies on significantly different applications (e.g. military piston engine aircraft). It is therefore suggested for future works to enhance the aerodynamic modeling in order to quantify the additional drag due to the air inlets and the delta pressure across the radiators taking also into account an estimation of "thrust" generated by the Meredith effect.

Moreover, more advanced technologies for thermal management such as skin heat exchangers may be used rather than or in combination with the traditional ram air radiators. This technology exploits the heat sink potential of the aircraft surface to cool down the coolant fluid. Such technology is very promising both in terms of weight savings and reduced aerodynamic penalties since it does not require the integration of ram air inlets. To the knowledge of the authors, skin heat exchangers have been developed and manufactured by Liebherr Aerospace who successfully tested the system on an A320 provided by the DLR institute in 2014 [134]. At the time of this thesis, the technology readiness level of skin-heat exchangers is probably not mature enough to have reliable information, but their promising performance could be among the key enablers for the development of a fuel cell-based hydrogen propulsion system in the future.

The same consideration is also applicable to the high temperature PEM fuel cells. Despite the difficulties to retrieve reliable information about such technology, a parallel hybrid configuration featuring high temperature fuel cells (*Hybrid-HT*) has been studied and has proven to be the architecture with the highest potential to reduce aircraft emissions. However, due to the scarcity and often contradictory information found, many assumptions had to be made concerning their efficiency and specific power at stack level. The results obtained for the *Hybrid-HT* architecture are thus highly uncertain and a more reliable assessment could be made in the future. Only with additional knowledge about such technology and by taking into account also aerodynamics considerations for the fuel cell cooling, the high temperature PEM fuel cells may prove to be the game-changer technology that can pave the way to full electric regional aircraft.

Another way of improvement would be to work on the design of a specific gas turbine for the hybridized regional aircraft. Indeed, the performance of the gas turbine representative of existing designs shows significantly higher specific fuel consumption when operated at

partial load. The specific design of a gas turbine with higher efficiency, when operated at a lower power setting than its nominal power, would have a considerable impact on the overall fuel consumption.

Other future work could concern safety requirements, space allocation of these voluminous systems on board an aircraft and their impact on the aircraft center of gravity, thus its stability and handling qualities. A method for rapid allocation of the propulsion components within the aircraft could be set in place in order to allow more refined cabin layout studies and center of gravity diagrams of the aircraft.

Also the uncertainty of the results, in terms of block fuel per passenger, as shown in Section 9.5 is still high and could be further reduced by improving the accuracy of the models used for the sizing of the hydrogen tank and the fuel cell balance of plant. Moreover, a different approach concerning optimization and uncertainty quantification may be used. For example optimization under uncertainty techniques may be used, such as robust design optimization (RDO) and reliability-based design optimization (RBDO). Those methods differ in the way the constraints are handled. Moreover, RBDO adds probabilistic constraints based on probability of failure, while RDO considers the effects of uncertainty in the objective and constraints through statistical moments, e.g., mean and variance. Both methods allow to fully integrate uncertainty within the optimization problem, therefore they provide a more efficient and robust way to perform optimization studies taking into account uncertainties.

Bibliography

[1] Scott Delbecq et al. "ISAE-SUPAERO Aviation and Climate: a literature review". In: (2022).

[2] Jeff Overton. "The Growth in Greenhouse Gas Emissions from Commercial Aviation". In: *EESI, url: https://www. eesi. org/papers/view/fact-sheet-the-growth-ingreenhouse-gas-emissions-from-commercial-aviation [accessed: 2021-04-23]* (2019).

[3] R IEA. "Energy technology perspectives 2020". In: *Special Report on Carbon Capture, Utilisation and Storage.* (2020).

[4] Nateri Madavan et al. "A NASA perspective on electric propulsion technologies for commercial aviation". In: *Proceedings of the Workshop on Technology Roadmap for Large Electric Machines, Urbana-Champaign, IL, USA*. 2016, pp. 5–6.

[5] Xochitl Cruz-Nunez. "Transport. In: Climate Change 2014: Mitigation of Climate Change. Contribution of Working Group III to the Fifth Assessment Report of the Intergovernmental Panel on Climate Change". en. In: (2014).

[6] M Darecki et al. "Flightpath 2050 Europes Vision for Aviation". In: *Off. Eur* (2011).

[7] Ramesh K Agarwal. "Review of technologies to achieve sustainable (green) aviation". In: *Recent advances in aircraft technology* 19 (2012), pp. 427–464.

[8] ETN. *The path towards a zero-carbon gas turbine.* https://etn.global/wp-content/uploads/2020/01/ETN-Hydrogen-Gas-Turbines-report.pdf. 2020.

[9] Emilio M Botero et al. "Suave: An open-source environment for conceptual vehicle design and optimization". In: *54th AIAA Aerospace Sciences Meeting*. 2016, p. 1275.

[10] Alessandro Sgueglia et al. "Preliminary Sizing of a Medium Range Blended Wing-Body using a Multidisciplinary Design Analysis Approach". In: *MATEC Web of Conferences*. Vol. 233. EDP Sciences. 2018, p. 00014.

[11] Kristof Risse et al. "An integrated environment for preliminary aircraft design and optimization". In: *53rd AIAA/ASME/ASCE/AHS/ASC Structures, Structural Dynamics and Materials Conference 20th AIAA/ASME/AHS Adaptive Structures Conference 14th AIAA*. 2012, p. 1675.

[12] CM Osterheld, W Heinze, and P Horst. "Preliminary design of a blended wing body configuration using the design tool PrADO". In: *DGLR BERICHT* 5 (2001), pp. 119–128.

[13] Jérôme Thauvin. "Exploring the design space for a hybrid-electric regional aircraft with multidisciplinary design optimisation methods". PhD thesis. 2018.

[14] PACE Aerospace Engineering and Information Technology GmbH. *Pacelab APD 3.0.0. Release Note*. 2012.

[15] X Zheng and Dan Rutherford. *Fuel burn of new commercial jet aircraft: 1960 to 2019*. 2020.

[16] FlightGlobal in association with CFM. *Commercial Engines - Turbofan focus 2016*. 2016. URL: https://www.flightglobal.com/download?ac=79070.

[17] Pedro David Bravo-Mosquera, Fernando Martini Catalano, and David W. Zingg. "Unconventional aircraft for civil aviation: A review of concepts and design methodologies". In: *Progress in Aerospace Sciences* (2022).

[18] Hendrik Gesell, Florian Wolters, and Martin Plohr. "System analysis of turbo-electric and hybrid-electric propulsion systems on a regional aircraft". In: *The Aeronautical Journal* 123.1268 (2019), pp. 1602–1617.

[19] Jacopo Zamboni et al. "A method for the conceptual design of hybrid electric aircraft". In: *AIAA Scitech 2019 Forum*. 2019, p. 1587.

[20] D Felix Finger, Carsten Braun, and Cees Bil. "Comparative assessment of parallel-hybrid-electric propulsion systems for four different aircraft". In: *Journal of Aircraft* (2020), pp. 1–11.

[21] Stefan Stückl. "Methods for the design and evaluation of future aircraft concepts utilizing electric propulsion systems". PhD thesis. Technische Universität München, 2016.

[22] McKinsey & Company. "Hydrogen-powered aviation: A fact-based study of hydrogen technology, economics, and climate impact by 2050". In: (2020).

[23] G Romeo et al. "ENFICA-FC: Design of transport aircraft powered by fuel cell & flight test of zero emission 2-seater aircraft powered by fuel cells fueled by hydrogen". In: *International journal of hydrogen energy* 38.1 (2013), pp. 469–479.

[24] Josef Kallo. "DLR leads HY4 project for four-seater fuel cell aircraft". In: *Fuel Cells Bulletin* 2015.11 (2015), p. 13.

[25] Tony Osborne. "Startup sees fuel cell future for regional aviation: ZeroAvia planning 300-mi. endurance flight in early 2020; hydrogen production facilities could be sited at airports and use renewable energy". In: *Aviation Week & Space Technology* (2019).

[26] Simon Engelke. "Current and future sodium-ion battery research". In: *Int. Journal of Energy Storage.–Draft* 1 (2013).

[27] Robert Schröder, Muhammed Aydemir, and Günther Seliger. "Comparatively assessing different shapes of lithium-ion battery cells". In: *Procedia Manufacturing* 8 (2017), pp. 104–111.

[28] Jeffrey C Chin et al. "Battery Cell-to-Pack Scaling Trends for Electric Aircraft". In: *2021 AIAA/IEEE Electric Aircraft Technologies Symposium (EATS)*. IEEE. 2021, pp. 1–15.

[29] Heide Budde-Meiwes et al. "A review of current automotive battery technology and future prospects". In: *Proceedings of the Institution of Mechanical Engineers, Part D: Journal of Automobile Engineering* 227.5 (2013), pp. 761–776.

[30] G Girishkumar et al. "Lithium- air battery: promise and challenges". In: *The Journal of Physical Chemistry Letters* 1.14 (2010), pp. 2193–2203.

[31] Zahoor Awan et al. "Lithium Air Battery: Alternate Energy Resource for the Future". In: *Journal of Electrochemical Science and Technology* 3 (Mar. 2012). DOI: 10.5229/JECST.2012.3.1.14.

[32] Amartya Mukhopadhyay and Manoj K Jangid. "Li metal battery, heal thyself". In: *Science* 359.6383 (2018), pp. 1463–1463.

[33] Ghassan Zubi et al. "The lithium-ion battery: State of the art and future perspectives". In: *Renewable and Sustainable Energy Reviews* 89 (2018), pp. 292–308.

[34] Mia Romare and Lisbeth Dahllöf. "The life cycle energy consumption and greenhouse gas emissions from lithium-ion batteries". In: *Stockholm. Zugriff am* 23 (2017), p. 2017.

[35] S Solomon et al. "IPCC fourth assessment report (AR4)". In: *Climate change* (2007).

[36] Linda Ager-Wick Ellingsen et al. “Life cycle assessment of a lithium-ion battery vehicle pack”. In: *Journal of Industrial Ecology* 18.1 (2014), pp. 113–124.

[37] Guillaume Majeau-Bettez, Troy R Hawkins, and Anders Hammer Strømman. “Life cycle environmental assessment of lithium-ion and nickel metal hydride batteries for plug-in hybrid and battery electric vehicles”. In: *Environmental science & technology* 45.10 (2011), pp. 4548–4554.

[38] Hyung Chul Kim et al. “Cradle-to-gate emissions from a commercial electric vehicle Li-ion battery: a comparative analysis”. In: *Environmental science & technology* 50.14 (2016), pp. 7715–7722.

[39] Hanjiro Ambrose and Alissa Kendall. “Effects of battery chemistry and performance on the life cycle greenhouse gas intensity of electric mobility”. In: *Transportation Research Part D: Transport and Environment* 47 (2016), pp. 182–194.

[40] Shanika Amarakoon, Jay Smith, and Brian Segal. *Application of life-cycle assessment to nanoscale technology: Lithium-ion batteries for electric vehicles*. Tech. rep. 2013.

[41] Airbus Deutschland GmbH. *Liquid Hydrogen Fuelled Aircraft â€“ System Analysis*. Final report GRD1-1999-10014. 2003.

[42] Kolja Seeckt. “Conceptual design and investigation of hydrogen-fueled regional freighter aircraft”. PhD thesis. US-AB, 2010.

[43] Sebastian Verhelst et al. “Update on the progress of hydrogen-fueled internal combustion engines”. In: *Renewable hydrogen technologies* (2013), pp. 381–400.

[44] Shang Hsiung et al. *Hydrogen fuel cell engines and related technologies*. Tech. rep. 2001.

[45] RE Rosli et al. “A review of high-temperature proton exchange membrane fuel cell (HT-PEMFC) system”. In: *International Journal of Hydrogen Energy* 42.14 (2017), pp. 9293–9314.

[46] K. Gurbinder. “Solid oxide fuel cell components: Interfacial compatibility of SOFC glass seals.” In: *Springer*. (2016).

[47] Joey Hoogendoorn. “Fuel Cell and Battery Hybrid System Optimization: Towards Increased Range and Endurance”. In: (2018).

[48] Ahmad Baroutaji et al. “Comprehensive investigation on hydrogen and fuel cell technology in the aviation and aerospace sectors”. In: *Renewable and sustainable energy reviews* 106 (2019), pp. 31–40.

[49] Alain Prinzhofer et al. “Natural hydrogen continuous emission from sedimentary basins: The example of a Brazilian H2-emitting structure”. In: *International Journal of Hydrogen Energy* 44.12 (2019), pp. 5676–5685.

[50] Alain Prinzhofer, Cheick Sidy Tahara Cissé, and Aliou Boubacar Diallo. “Discovery of a large accumulation of natural hydrogen in Bourakebougou (Mali)”. In: *International Journal of Hydrogen Energy* 43.42 (2018), pp. 19315–19326.

[51] Kalathur SV Santhanam et al. *Introduction to hydrogen technology*. John Wiley & Sons, 2017.

[52] Jörg Adolf et al. “Energy of the future?: Sustainable mobility through fuel cells and H2; Shell hydrogen study”. In: (2017).

[53] Robert Edwards JRC et al. “Well-to-wheels Report Version 4.a JEC Well-to-wheels analysis”. In: *Institute for Energy and Transport, Joint Research Centre, Luxembourg: Publications Office of the European Union* 2014 (2014).

[54] G Ordaz, C Houchins, and T Hua. “Onboard type IV compressed hydrogen storage systemsâ€”cost and performance status 2015”. In: *DOE Hydrogen and Fuel Cells Program Record* (2015).

[55] Strategy Advisory Committee of the Technology Roadmap for Energy Saving, New Energy Vehicles, and the Society of Automotive Engineers of China. *Hydrogen Fuel Cell Vehicle Technology Roadmap*. Tech. rep. 2016.

[56] Emmanuel Bensadoun. "Hydrogen Storage on board aeronef and ground infrastructure". In: *Air Liquide Advanced Technologies* (2015).

[57] Dries Verstraete. "The potential of liquid hydrogen for long range aircraft propulsion". PhD thesis. Cranfield University, 2009.

[58] European Commission. *European battery cell workshop - Final report*. Tech. rep. 2018.

[59] RH Lenssen. "Series Hybrid Electric Aircraft: Comparing the Well-to-Propeller Efficiency with a Conventional Propeller Aircraft". In: (2016).

[60] Andrew B Lambe and Joaquim RRA Martins. "Extensions to the design structure matrix for the description of multidisciplinary design, analysis, and optimization processes". In: *Structural and Multidisciplinary Optimization* 46.2 (2012), pp. 273–284.

[61] Cristophe David et al. "From FAST to FAST-OAD: An open source framework for rapid Overall Aircraft Design". In: European Aeronautics Science Network, 2020.

[62] Daniel Raymer. *Aircraft design: a conceptual approach*. American Institute of Aeronautics and Astronautics, Inc., 2012.

[63] Jan Roskam. *Airplane design*. DARcorporation, 1985.

[64] P Dupont and C Colongo. "Preliminary Design of a Commercial Transport Aircraft, class notes, ISAE-Supaero&Airbus". In: *English edition* (2014).

[65] Cristophe David and Scott Delbecq. *FAST-OAD: Future Aircraft Sizing Tool - Overall Aircraft Design*. https://fast-oad.readthedocs.io/. Accessed: 2020-06-15. 2020.

[66] Alessandro Sgueglia. "Methodology for sizing and optimising a Blended Wing-Body with distributed electric ducted fans". PhD thesis. ISAE-Institut Supérieur de l'Aéronautique et de l'Espace, 2019.

[67] Joaquim RRA Martins and Andrew B Lambe. "Multidisciplinary design optimization: a survey of architectures". In: *AIAA journal* 51.9 (2013), pp. 2049–2075.

[68] Justin Gray, Kenneth Moore, and Bret Naylor. "OpenMDAO: An open source framework for multidisciplinary analysis and optimization". In: *13th AIAA/ISSMO Multidisciplinary Analysis Optimization Conference*. 2010, p. 9101.

[69] John T Hwang and Joaquim Martins. "Parallel allocation-mission optimization of a 128-route network". In: *16th AIAA/ISSMO Multidisciplinary Analysis and Optimization Conference*. 2015, p. 2321.

[70] Athanasios K Barlas et al. "Aeroelastic optimization of a 10 MW wind turbine blade with active trailing edge flaps". In: *34th Wind Energy Symposium*. 2016, p. 1262.

[71] John P Jasa, John T Hwang, and Joaquim RRA Martins. "Open-source coupled aerostructural optimization using Python". In: *Structural and Multidisciplinary Optimization* 57.4 (2018), pp. 1815–1827.

[72] Justin S Gray et al. "Modeling boundary layer ingestion using a coupled aeropropulsive analysis". In: *Journal of Aircraft* 55.3 (2018), pp. 1191–1199.

[73] John T Hwang et al. "Large-scale multidisciplinary optimization of a small satelliteâ€™s design and operation". In: *Journal of Spacecraft and Rockets* 51.5 (2014), pp. 1648–1663.

[74] John T Hwang and Joaquim RRA Martins. "A computational architecture for coupling heterogeneous numerical models and computing coupled derivatives". In: *ACM Transactions on Mathematical Software (TOMS)* 44.4 (2018), pp. 1–39.

[75] Donald R Jones, Matthias Schonlau, and William J Welch. "Efficient global optimization of expensive black-box functions". In: *Journal of Global optimization* 13.4 (1998), pp. 455–492.

[76] M.J. Sasena. "Flexibility and efficiency enhancements for constrained global design optimization with Kriging approximations". PhD thesis. University of Michigan, 2002.

[77] Mohamed Amine Bouhlel et al. "Improving kriging surrogates of high-dimensional design models by Partial Least Squares dimension reduction". In: *Structural and Multidisciplinary Optimization* 53.5 (2016), pp. 935–952. ISSN: 1615-1488. DOI: 10.1007/s00158-015-1395-9. URL: http://dx.doi.org/10.1007/s00158-015-1395-9.

[78] Dimitri Bettebghor et al. "Surrogate modeling approximation using a mixture of experts based on EM joint estimation". In: *Structural and multidisciplinary optimization* 43.2 (2011), pp. 243–259.

[79] Alan G Watson and Randal J Barnes. "Infill sampling criteria to locate extremes". In: *Mathematical Geology* 27.5 (1995), pp. 589–608.

[80] Michael JD Powell. "A direct search optimization method that models the objective and constraint functions by linear interpolation". In: *Advances in optimization and numerical analysis*. Springer, 1994, pp. 51–67.

[81] Dieter Kraft. *A software package for sequential quadratic programming*. DFVLR Obersfaffeuhofen, Germany. 1988.

[82] Philip E Gill, Walter Murray, and Michael A Saunders. "SNOPT: An SQP algorithm for large-scale constrained optimization". In: *SIAM review* 47.1 (2005), pp. 99–131.

[83] Nathalie Bartoli et al. "Adaptive modeling strategy for constrained global optimization with application to aerodynamic wing design". In: *Aerospace Science and Technology* 90 (2019), pp. 85–102. DOI: https://doi.org/10.1016/j.ast.2019.03.041.

[84] Remy Priem et al. "An efficient application of Bayesian optimization to an industrial MDO framework for aircraft design." In: *AIAA AVIATION 2020 FORUM*. 2020, p. 3152.

[85] Nathalie Bartoli et al. "Robust Nacelle Optimization Design investigated in the AGILE European project". In: *19th AIAA/ISSMO Multidisciplinary Analysis and Optimization Conference*. Atlanta, United States, 2018. DOI: 10.2514/6.2018-3250.

[86] Paul Saves et al. "Constrained Bayesian optimization over mixed categorical variables, with application to aircraft design". In: *Proceedings of the International Conference on Multidisciplinary Design Optimization of Aerospace Systems (AEROBEST 2021)*. 2021, pp. 1–758.

[87] Robin Grapin et al. "Constrained Multi-Objective Bayesian Optimization with Application to Aircraft Design". In: *AIAA AVIATION 2022 Forum*. 2022, p. 4053.

[88] Jessie Birman. "Uncertainty quantification and propagation in Conceptual Aircraft Design: from deterministic optimization to chance constrained optimization". PhD thesis. PhD thesis, University of Toulouse III–Paul Sabatier, 2013.

[89] C Leotardi et al. "A framework for efficient simulation-based multidisciplinary robust design optimization with application to a keel fin of a racing sailboat". In: *An International Conference on Engineering and Applied Sciences optimization (OPTI2014), edited by Papadrakakis M. and Karlaftis MG and Lagaros ND*. 2014.

[90] Patrick N Koch et al. "Facilitating probabilistic multidisciplinary design optimization using kriging approximation models". In: *9th AIAA/ISSMO Symposium on Multidisciplinary Analysis and Optimization*. 2002, pp. 1–11.

[91] David R Oakley, Robert H Sues, and Graham S Rhodes. "Performance optimization of multidisciplinary mechanical systems subject to uncertainties". In: *Probabilistic Engineering Mechanics* 13.1 (1998), pp. 15–26.

[92] Imon Chakraborty and Dimitri N Mavris. "Assessing impact of epistemic and technological uncertainty on aircraft subsystem architectures". In: *Journal of Aircraft* 54.4 (2017), pp. 1388–1406.

[93] G Gary Wang and Songqing Shan. "Review of metamodeling techniques in support of engineering design optimization". In: (2007).

[94] S Dubreuil et al. "Propagation of modeling uncertainty by polynomial chaos expansion in multidisciplinary analysis". In: *Journal of Mechanical Design* 138.11 (2016), p. 111411.

[95] Miguel Walter. "A stochastic expansion-based approach for design under uncertainty". PhD thesis. Georgia Institute of Technology, 2013.

[96] Bruno Sudret. "Global sensitivity analysis using polynomial chaos expansions". In: *Reliability engineering & system safety* 93.7 (2008), pp. 964–979.

[97] D Scholz and S Ciornei. "Mach number, relative thickness, sweep and lift coefficient of the wing–an empirical investigation of parameters and equations". In: *Hamburg: HAW Hamburg University of Applied Sciences, DLRK. Paper* (2005).

[98] Denis Howe and George Rorie. *Aircraft conceptual design synthesis*. Professional Engineering Publishing London, UK, 2000.

[99] Yorick Teeuwen. "Propeller Design for Conceptual Turboprop Aircraft". MA thesis. Delft University of Technology, 2017.

[100] Luca Piancastelli, Leonardo Frizziero, and Giampiero Donnici. "The Meredith ramjet: An efficient way to recover the heat wasted in piston engine cooling". In: *Asian Research Publishing Network (ARPN). Journal of Engineering and Applied Sciences. ISSN* 6608 (1819), pp. 10–12.

[101] FW Meredith. *Cooling of aircraft engines with special reference to ethylene glycol radiators enclosed in ducts*. Tech. rep. HM Stationery Office, 1935.

[102] Jack D Mattingly. *Elements of gas turbine propulsion*. McGraw-Hill, 1996.

[103] AM Skellett. "National Advisory Committee for Aeronautics, Nineteenth Annual Report". In: ().

[104] Mark D Guynn. *Evaluation of an aircraft concept with over-wing, hydrogen-fueled engines for reduced noise and emissions*. NASA Langley Research Center, 2002.

[105] Steven C Sherwood, Vishal Dixit, and Chryséis Salomez. "The global warming potential of near-surface emitted water vapour". In: *Environmental Research Letters* 13.10 (2018), p. 104006.

[106] Mykhaylo V Lototskyy et al. "The use of metal hydrides in fuel cell applications". In: *Progress in Natural Science: Materials International* 27.1 (2017), pp. 3–20.

[107] Fuel Cells and Hydrogen Joint Undertaking. *INN-BALANCE project*. https://www.innbalance-fch-project.eu/. Accessed: 2020-11. 2018.

[108] SH Teichel et al. "Design considerations for the components of electrically powered active high-lift systems in civil aircraft". In: *CEAS Aeronautical Journal* 6.1 (2015), pp. 49–67.

[109] Fumatech. *Membrane Humidifiers: fumasep High Performance Membrane Humidifiers for Fuel Cells*. https://www.fumatech.com/NR/rdonlyres/0B9A1C7F-5BA6-4409-A003-5C4E79CD61AB/0/FUMATECH_BWT_GmbHMembrane_Humidifiers.pdf. Accessed: 2020-11. 2020.

[110] James Larminie, Andrew Dicks, and Maurice S McDonald. *Fuel cell systems explained*. Vol. 2. J. Wiley Chichester, UK, 2003.

[111] Patrick Christoph Vratny. "Conceptual design methods of electric power architectures for hybrid energy aircraft". PhD thesis. Technische Universität München, 2019.

[112] Christopher Winnefeld et al. "Modelling and designing cryogenic hydrogen tanks for future aircraft applications". In: *Energies* 11.1 (2018), p. 105.

[113] Ronald W Capps. "Selecting the optimum pipe size". In: *Chemical Engineering* 102.7 (1995), p. 128.

[114] MR Islam et al. "The potential of using nanofluids in PEM fuel cell cooling systems: A review". In: *Renewable and Sustainable Energy Reviews* 48 (2015), pp. 523–539.

[115] Oliver Berger. "Thermodynamische Analyse eines Brennstoffzellensystems zum Antrieb von Kraftfahrzeugen". In: *Duisburg/Essen, Technische Universität, Dissertation*. 2009.

[116] AKG-Group. *AKG-Line A Oil-to-Air cooling systems with AC-motor*. https://www.akg-group.com/fileadmin/user_upload/Brochures/AKG-Line/AKG_LineA_en.pdf. Accessed: 2020-11. 2020.

[117] ATR Marketing. "ATR family booklet". In: *http://www.atraircraft.com* ().

[118] CS25 EASA. *Certification specifications for large aeroplanes*. 2009.

[119] FAA. *Pilot Guide to Takeoff Safety*. https://www.faa.gov/other_visit/aviation_industry/airline_operators/training/media/takeoff_safety.pdf. Accessed: 2022-01. 2000.

[120] Maria Cristina Cameretti et al. "Modeling and investigation of a turboprop hybrid electric propulsion system". In: *Aerospace* 5.4 (2018), p. 123.

[121] ETN Global. *Hydrogen gas turbines. The path toward a zero-carbon gas turbine*. https://etn.global/wp-content/uploads/2020/01/ETN-Hydrogen-Gas-Turbines-report.pdf. Accessed: 2022-09. 2020.

[122] James Felder, Hyun Kim, and Gerald Brown. "Turboelectric distributed propulsion engine cycle analysis for hybrid-wing-body aircraft". In: *47th AIAA aerospace sciences meeting including the new horizons forum and aerospace exposition*. 2009, p. 1132.

[123] Michaël Baudin et al. "OpenTURNS: An Industrial Software for Uncertainty Quantification in Simulation". In: *Handbook of Uncertainty Quantification*. Ed. by Roger Ghanem, David Higdon, and Houman Owhadi. Cham: Springer International Publishing, 2016, pp. 1–38. ISBN: 978-3-319-11259-6. DOI: 10.1007/978-3-319-11259-6_64-1. URL: https://doi.org/10.1007/978-3-319-11259-6_64-1.

[124] Géraud Blatman and Bruno Sudret. "Efficient computation of global sensitivity indices using sparse polynomial chaos expansions". In: *Reliability Engineering & System Safety* 95.11 (2010), pp. 1216–1229.

[125] Nora LuÌˆthen, Stefano Marelli, and Bruno Sudret. "Sparse polynomial chaos expansions: Literature survey and benchmark". In: *SIAM/ASA Journal on Uncertainty Quantification* 9.2 (2021), pp. 593–649.

[126] International Energy Agency (IEA). "Recent trends in the OECD: energy and CO2 emissions". In: (2016).

[127] Mehrdad Ehsani et al. *Modern electric, hybrid electric, and fuel cell vehicles*. CRC press, 2018.

[128] PowerCell. *PowerCell S3 datasheet*. https://www.powercell.se/wordpress/wp-content/uploads/2018/12/S3-Produktblad-190430.pdf. Accessed: 2020-11. 2020.

[129] Samuel Simon Araya et al. "A comprehensive review of PBI-based high temperature PEM fuel cells". In: *International Journal of Hydrogen Energy* 41.46 (2016), pp. 21310–21344.

[130] Y Wang et al. "Dynamic modeling of high temperature PEM fuel cell start-up process". In: *International journal of hydrogen energy* 39.33 (2014), pp. 19067–19078.

[131] Gabriele Loreti, Andrea Luigi Facci, and Stefano Ubertini. "High-Efficiency Combined Heat and Power through a High-Temperature Polymer Electrolyte Membrane Fuel Cell and Gas Turbine Hybrid System". In: *Sustainability* 13.22 (2021), p. 12515.

[132] Hypoint. *We Make Zero Emission Air Transport Possible*. https://hypoint.com/. Accessed: 2022-02. 2022.

[133] Rémy Priem et al. "Upper trust bound feasibility criterion for mixed constrained Bayesian optimization with application to aircraft design". In: *Aerospace Science and Technology* 105 (2020), p. 105980.

[134] Giuseppe Pagnano. *Overview of Clean Sky Technical Programme And Achievements to date*. https://www.cleansky.eu/sites/default/files/documents/Giuseppe%20Pagnano%20Presentation%20Aerodays.pdf. Accessed: 2021-06-14. 2015.

[135] O Majeed. "Parametric Specific Fuel Consumption Analysis of the PW120A Turboprop Engine". In: *17th Canadian Aeronautics and Space Institute Propulsion Symposium*. 2009, pp. 5–7.

[136] Gordon C Oates. *Aerothermodynamics of gas turbine and rocket propulsion*. American Institute of Aeronautics and Astronautics, 1997.

Appendices

Appendix A

Gas turbine model

The gas turbine model is a representation of a twin-shaft free turbine architecture. For the sake of clarity, the station numbering and layout of the gas turbine is shown in Fig. A.1. It provides the simulation process with engine performance data such as the fuel flow and gas turbine efficiency for each control point of the mission in order to evaluate the weight of the fuel that needs to be carried on board to perform the entire mission.

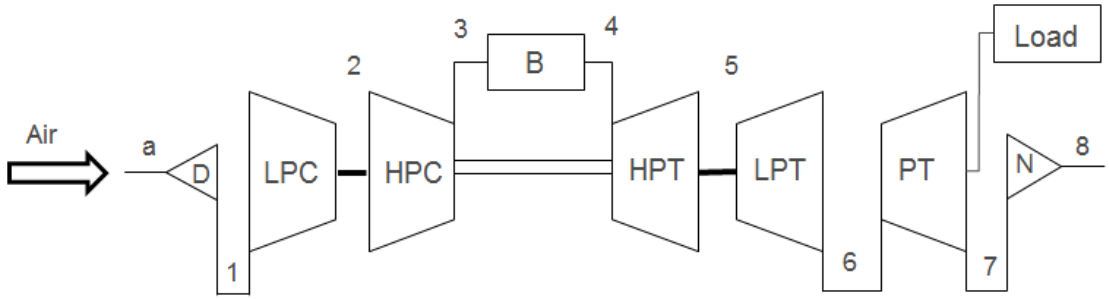

Figure A.1: Gas turbine architecture

This gas turbine model consists of a two-spool air compressor, a combustor, a two-spool gas generator turbine, and a power turbine. For this configuration, the low-pressure compressor (LPC) is driven by the low-pressure turbine (LPT) and the high-pressure compressor (HPC) is driven by the high-pressure turbine (HPT). The air passes through the inlet of the engine before being compressed by the LP and HP compressors. It is later fed into the combustor where the fuel is burnt. The energy produced by the combustion is partially extracted by the gas generator turbine to power the compressor. The remaining energy is extracted by the power turbine and used to drive the propeller to produce thrust. The main cycle parameter data used for the thermodynamic cycle calculations are shown in Table A.1.

The air and the combustion products of the kerosene are modelled as perfect gases, so

Inlet	
Air inlet efficiency, η_d	0.98
Compressors	
HPC Polytropic efficiency, η_{pol}^{hpc}	0.84
HPC Pressure ratio, π_{hpc}	4
HPC bleed airflow*, β_{hpc}	7%
LPC Polytropic efficiency, η_{pol}^{lpc}	0.85
LPC Pressure ratio, π_{lpc}	3
LPC bleed airflow*, β_{lpc}	4%
Combustor	
Turbine Inlet Temperature, TIT	1526 K
Pressure loss	7%
Efficiency, η_b	0.995
Turbines	
HPT Polytropic efficiency, η_{pol}^{hpt}	0.86
HP shaft mechanical efficiency, η_m^{hp}	0.96
LPT Polytropic efficiency, η_{pol}^{lpt}	0.86
LP shaft mechanical efficiency, η_m^{lp}	0.96
PT Polytropic efficiency, η_{pol}^{pt}	0.88
PT shaft mechanical efficiency, η_m^{pt}	0.98
Nozzle	
Nozzle efficiency, η_n	0.98

Table A.1: Cycle parameter data at design condition.

the enthalpy is calculated as the product of pressure specific heat of the gas, C_p, and the temperature T.

$$Pv = RT \tag{A.1}$$

Where:

P = gas pressure (Pa)
v = specific volume (m^3/kg)
R = gas constant ($\frac{J}{kgK}$)
T = gas temperature (K)

The gases, however, are not considered calorically perfect, therefore C_p depends on their temperature. For simplification, only two different values of C_p are considered, before

and after the combustion: $C_{pa} = 1004\frac{J}{kgK}$ and $C_{pg} = 1200\frac{J}{kgK}$, respectively the C_p of the air and the C_p of the exhaust gases.

The relation between the compressor pressure ratio and the temperature pressure ratio is a function of the compressor polytropic efficiency. Eqs. (A.2, A.18) show the calculation of the temperature ratio across the low-pressure compressor and high-pressure compressor.

$$\tau_{lpc} = \pi_{lpc}^{\frac{\gamma-1}{\gamma\eta_{pol}^{lpc}}} \tag{A.2}$$

$$\tau_{hpc} = \pi_{hpc}^{\frac{\gamma-1}{\gamma\eta_{pol}^{hpc}}} \tag{A.3}$$

Where:

$$\begin{aligned} \tau_{hpc} &= \text{HPC stagnation temperature ratio } (T_3/T_2) \\ \tau_{lpc} &= \text{LPC stagnation temperature ratio } (T_2/T_1) \\ \gamma &= \text{heat capacity ratio } (\approx 1.4 \text{ for air}) \end{aligned}$$

The energy balance across the combustor yields the fuel-to-air ratio as follows

$$f = \frac{c_{pg}T_4 - c_{pa}T_3}{\eta_b FHV - c_{pg}T_4} \tag{A.4}$$

Where:

$$\text{FHV= fuel heating value (43.1 MJ/kg)}$$

The mechanical power produced by the gas-generator turbines must equal the power absorbed by the compressor as shown by Eqs. (A.5, A.6.

LP Spool Power Balance

$$m_a(1 - \beta_{hpc} - \beta_{lpc})(1 + f)\eta_m^{lp} c_{pg}(T_5 - T_6) = m_a c_{pa}(T_2 - T_1) \tag{A.5}$$

HP Spool Power Balance

$$m_a(1 - \beta_{hpc} - \beta_{lpc})(1 + f)\eta_m^{hp} c_{pg}(T_4 - T_5) + P_{acc} = m_a(1 - \beta_{lpc})c_{pa}(T_3 - T_2) \tag{A.6}$$

Where:

$$\begin{aligned} P_{acc} &= \text{Accessory drive power requirement} \\ m_a &= \text{reference mass flow at station 1 (kg/s)} \end{aligned}$$

The accessory drive power is extracted to power engine systems such as the fuel pump, alternator, hydraulic pump etc., and it is estimated to be 22.4 kW [135].

The power extracted by the power turbine is:

$$P_{pt} = m_a(1 - \beta_{hpc} - \beta_{lpc})(1 + f)c_{pg}(T_6 - T_7)\eta_m^{pt} \tag{A.7}$$

The residual thrust, $\mathcal{T}_{res}$, produced by the expansion of the gases in the nozzle is calculated by multiplying the mass flow at the power turbine exit station (m_7) times its relative velocity out the exhaust nozzle:

$$\mathcal{T}_{res} = m_7(u_8) - m_a(u_1), m_7 = m_a(1 - \beta_{hpc} - \beta_{lpc})(1 + f) \tag{A.8}$$

The thrust (N) is converted into power (kW) for the calculation of an important engine performance parameter: the equivalent shaft horsepower, ESHP. Eq. (A.10) shows the formula used for the calculation of the ESHP (kW), respectively in cruise and take-off static conditions.

$$P_{shaft} = P_{pt}\eta_{gearbox} \tag{A.9}$$

$$ESHP = P_{shaft} + \frac{T_{nozzle}u_0}{\eta_{propeller}}, ESHP = P_{shaft} + \frac{T_{nozzle}}{k} \tag{A.10}$$

Where:

P_{shaft} = shaft power (kW)
$\eta_{gearbox}$ = gearbox efficiency (=0.95)
$\eta_{propeller}$ = propeller efficiency (=0.88 in cruise)
k = propeller constant at static conditions (=14.92)
u_0= flow speed at the inlet

The off-design analysis is performed following the method described by Mattingly and Oates [136, 102]. The components' efficiencies are assumed to be constant, therefore no scaled performance characteristics are calculated from the original performance maps. The off-design performance is calculated only by considering relations related to the gas generator's turbine and compressor matching and the power turbine and exhaust nozzle matching. For the determination of these relations, some assumptions need to be made. Therefore, it is considered that the pressure ratios across all the turbines is high enough to have chocked flow in the turbine's inlet stations for all the operating conditions during the flight. Moreover, the exit nozzle is considered always unchocked. These assumptions imply constant values of pressure and temperature ratios across the high-pressure turbine (respectively π_{HPT} and τ_{HPT}) and the low-pressure turbine (π_{LPT} and τ_{LPT}). In Table A.2 the cycle performance parameters are classified into independent variables, constant values and dependent variables.

Component	Independent	Constant or known	Dependent
Engine	M_0, T_0, P_0	...	$\dot{m}_0$
Diffuser	...	π_D	...
Compressors	...	η_{HPC}, η_{LPC}	π_{HPC}, τ_{HPC}, π_{LPC}, τ_{LPC}
Combustor	T_4	π_b, η_b	...
Gas-generator Turbines	...	π_{HPT}, τ_{HPT}, π_{LPT}, τ_{LPT}	...
Power turbine	...	η_{PT}	τ_{PT}, π_{PT}
Nozzle	...	π_N	M_8

Table A.2: Performance analysis variables

For this engine, there are four independent variables and eight dependent variables. The determination of the engine-independent variables M_0, T_0, P_0 is directly related to the ambient conditions. Therefore, they are set once the altitude and the aircraft speed are given. The combustor temperature T_4 instead is related to the engine throttle. The design value of T_4 represents its upper limit, but during operation, T_4 is imposed by the power requirement of the specific flight operating point. As already mentioned, the constant and known variables are the design values in Table A.1. Now that the determination of the independent and constant variables is clear, the relations for the calculation of the remaining 8 dependent variables will be shown.

Starting by the engine mass-flow $\dot{m}_0$, the conservation of mass leads to:

$$\dot{m}_2(1+f) = \dot{m}_4 = \frac{P_4 A_4}{\sqrt{T_4}} MFP(M_4) \tag{A.11}$$

Where:

MFP = mass flow parameter

A_4 = throat area at station 4

P, T = stagnation pressure and temperature (partial gas properties are indicated with small letters)

The assumption of chocked flow at the turbine's inlet stations implies $M_4 = 1$, therefore the above equation can be rewritten as:

$$\dot{m}_0 = \frac{P_0 \pi_{HPC} \pi_{LPC} \pi_D \pi_{ram}}{\sqrt{T_4}} (\pi_b A_4 \frac{MFP(M_4)}{1+f}) \tag{A.12}$$

The terms within the brackets under the previous assumption are constant, therefore equating the term to the reference design values (expressed with the subscript "R") gives the following equation for the determination of the engine mass flow:

$$\dot{m}_0 = \dot{m}_{0R} \frac{P_0 \pi_{HPC} \pi_{LPC} \pi_D \pi_{ram}}{(P_0 \pi_{HPC} \pi_{LPC} \pi_D \pi_{ram})_R} \sqrt{\frac{T_{4R}}{T_4}} \tag{A.13}$$

The temperature ratios of the low-pressure and high-pressure compressors are obtained starting from the equations of the LP and HP power balance (Eqs. (A.5, A.6)). Rewriting the equations in terms of temperature ratios, rearranging into constant and variable terms and equating the constant term to the reference design values give:

$$\tau_{LPC} = 1 + \frac{T_4/T_0}{(T_4/T_0)_R} \frac{(\tau_{ram})_R}{\tau_{ram}} (\tau_{LPC} - 1)_R \tag{A.14}$$

$$\tau_{HPC} = 1 + \frac{T_4/T_0}{(T_4/T_0)_R} \frac{(\tau_{ram})_R}{\tau_{ram}} \frac{(\tau_{LPC})_R}{\tau_{LPC}} (\tau_{HPC} - 1)_R \tag{A.15}$$

The pressure ratios of the compressors are derived from the definition of compressor's polytropic efficiency (Eqs. (A.2 and A.18)).

The determination of the power turbine and nozzle-dependent variables is based on the hypothesis of chocked flow at the turbine inlet stations and of unchocked flow at the exit nozzle. These assumptions lead respectively to Eqs. (A.16, A.17).

$$\dot{m}_4 = \frac{P_4 A_4}{\sqrt{T_4}} \sqrt{\frac{\gamma}{R}} \left(\frac{2}{\gamma + 1} \right)^{(\gamma+1)/2(\gamma-1)} \tag{A.16}$$

$$\dot{m}_8 = \frac{P_8 A_8}{\sqrt{T_8}} \sqrt{\frac{\gamma}{R}} M_8 \left(1 + \frac{\gamma - 1}{2} M_8^2 \right)^{-(\gamma+1)/2(\gamma-1)} \tag{A.17}$$

Three equations are needed for the determination of the three variables: τ_{PT}, π_{PT} and M_8.

The first equation is derived from the definition of turbine's polytropic efficiency, expressing the relation between τ_{PT} and π_{PT}:

$$\tau_{PT} = \pi_{PT}^{\frac{(\gamma-1)\eta_{pol}^{pt}}{\gamma}} \tag{A.18}$$

Equating the two equations in accordance with the mass conservation law, rearranging into constant and variable terms, equating the constant term to the reference design values and finally solving for M_8 give:

$$M_8 = M_{8R} \left(\frac{(\tau_{PT})_R}{\tau_{PT}} \right)^{0.5} \frac{\pi_{PT}}{(\pi_{PT})_R} \left(\frac{1 + \frac{\gamma-1}{2} M_8^2}{1 + \frac{\gamma-1}{2} M_{8R}^2} \right)^{(\gamma+1)/2(\gamma-1)} \tag{A.19}$$

Finally the last equation is derived starting from the isoentropic relation:

$$\left(1+\frac{\gamma-1}{2}M_8^2\right)^{\gamma/(\gamma-1)}=\frac{P_8}{p_8}=\frac{P_0}{p_8}\pi_{ram}\pi_D\pi_{LPC}\pi_{HPC}\pi_b\pi_{HPT}\pi_{LPT}\pi_{PT}\pi_N \tag{A.20}$$

And noting that $P_0/p_8 = 1$ because the nozzle is unchocked and solving for π_{PT}:

$$\pi_{PT}=\left(1+\frac{\gamma-1}{2}M_8^2\right)^{\gamma/(\gamma-1)}\frac{1}{\pi_{ram}\pi_D\pi_{LPC}\pi_{HPC}\pi_b\pi_{HPT}\pi_{LPT}\pi_N} \tag{A.21}$$

Eqs.(A, A.19) are easily solved by functional iteration:

1. Initially assume that π_{PT} equals its reference value.
2. Calculate τ_{PT}, using Eq. (A.18).
3. Calculate the M_8, using Eq. (A.19).
4. Calculate the new π_{PT} using Eq. ().
4. Compare the new π_{PT} to the previous value. If the difference is greater than 0.0001, then go to step 2.

Appendix B

Inputs for the baseline aircraft design

Listing B.1: Inputs for turboprop sizing

```
<RHEA>
  <data>
    <TLAR>
      <NPAX >72.0<!--top-level requirement: number of passengers,
          assuming a classic eco/business class repartition--></NPAX>
      <OEI_ceiling units="m" >2900.0</OEI_ceiling>
      <TOD units="m" >1200.0</TOD>
      <TTC units="min" >24.0</TTC>
      <approach_speed units="m/s" >60.0<!--top-level requirement:
          approach speed--></approach_speed>
      <cruise_mach >0.45<!--top-level requirement: cruise Mach number-->
          </cruise_mach>
      <range units="nmi" >750.0<!--top-level requirement: design range--
          ></range>
    </TLAR>
    <geometry>
      <has_T_tail >1.0<!--0=horizontal tail is attached to fuselage / 1=
          horizontal tail is attached to top of vertical tail--></
          has_T_tail>
      <cabin>
        <aisle_width units="m" >0.45<!--width of aisles--></aisle_width>
        <exit_width units="m" >0.75<!--width of exits--></exit_width>
        <crew_count>
          <technical >2.0<!--number of technical crew members--></
              technical>
        </crew_count>
        <seats>
          <economical>
            <count_by_row >4.0<!--number of economical class seats along
                width--></count_by_row>
```

```
23            <length units="m" >0.762<!--length of economical class seats
                  --></length>
24            <width units="m" >0.4572<!--width of economical class seats
                  --></width>
25          </economical>
26        </seats>
27      </cabin>
28      <flap>
29        <chord_ratio >0.3<!--mean value of (flap chord)/(section chord)
              --></chord_ratio>
30        <span_ratio >0.623<!--ratio (width of flaps)/(total span)--></
              span_ratio>
31      </flap>
32      <horizontal_tail>
33        <aspect_ratio >4.555<!--aspect ratio of horizontal tail--></
              aspect_ratio>
34        <sweep_25 units="deg" >6.32<!--sweep angle at 25% chord of
              horizontal tail--></sweep_25>
35        <taper_ratio >0.613<!--taper ratio of horizontal tail--></
              taper_ratio>
36        <thickness_ratio >0.12<!--thickness ratio of horizontal tail--><
              /thickness_ratio>
37      </horizontal_tail>
38      <propulsion>
39        <layout >1.0<!--position of engines (1=under the wing / 2=rear
              fuselage)--></layout>
40        <engine>
41          <count >2.0<!--number of engines--></count>
42          <y_ratio >0.3<!--engine position with respect to total span-->
                </y_ratio>
43        </engine>
44        <propeller>
45          <B >6.0</B>
46        </propeller>
47      </propulsion>
48      <slat>
49        <chord_ratio >0.0<!--mean value of slat chord)/(section chord)--
              ></chord_ratio>
50        <span_ratio >0.0<!--ratio (width of slats)/(total span)--></
              span_ratio>
51      </slat>
52      <vertical_tail>
53        <aspect_ratio >1.6<!--aspect ratio of vertical tail--></
              aspect_ratio>
54        <sweep_25 units="deg" >28.56<!--sweep angle at 25% chord of
              vertical tail--></sweep_25>
55        <taper_ratio >0.6<!--taper ratio of vertical tail--></
              taper_ratio>
```

```
56          <thickness_ratio >0.12<!--thickness ratio of vertical tail--></
                thickness_ratio>
57        </vertical_tail>
58        <wing>
59          <aspect_ratio >11.995<!--wing aspect ratio--></aspect_ratio>
60          <sweep_25 units="deg" >2.3<!--sweep angle at 25% chord of wing--
                ></sweep_25>
61          <taper_ratio >0.618<!--taper ratio of wing--></taper_ratio>
62          <kink>
63            <span_ratio >0.3866<!--ratio (Y-position of kink)/(semi-span)
                  --></span_ratio>
64          </kink>
65          <spar_ratio>
66            <front>
67              <kink >0.15<!--ratio (front spar position)/(chord length) at
                     wing kink--></kink>
68              <root >0.11<!--ratio (front spar position)/(chord length) at
                     wing root--></root>
69              <tip >0.27<!--ratio (front spar position)/(chord length) at
                    wing tip--></tip>
70            </front>
71            <rear>
72              <kink >0.66<!--ratio (rear spar position)/(chord length) at
                    wing kink--></kink>
73              <root >0.57<!--ratio (rear spar position)/(chord length) at
                    wing root--></root>
74              <tip >0.56<!--ratio (rear spar position)/(chord length) at
                    wing tip--></tip>
75            </rear>
76          </spar_ratio>
77        </wing>
78      </geometry>
79      <propulsion>
80        <Power_Offtake units="W" >7500.0</Power_Offtake>
81        <gearbox_eta >0.99</gearbox_eta>
82        <L1_engine>
83          <HP_bleed >1.0</HP_bleed>
84          <LP_bleed >0.97</LP_bleed>
85          <fuel >0.0</fuel>
86          <turbine_inlet_temperature units="degK" >1526.0</
                turbine_inlet_temperature>
87          <combustor>
88            <combustor_eta >0.995</combustor_eta>
89            <combustor_pressure_ratio >0.93</combustor_pressure_ratio>
90          </combustor>
91          <hpc>
92            <hpc_eta_pol >0.84</hpc_eta_pol>
93            <hpc_pressure_ratio >2.6</hpc_pressure_ratio>
```

```
94          </hpc>
95          <hpt>
96            <hpt_eta_mech >0.96</hpt_eta_mech>
97            <hpt_eta_pol >0.86</hpt_eta_pol>
98          </hpt>
99          <inlet>
100           <inlet_eta_pol >0.98</inlet_eta_pol>
101           <inlet_pressure_ratio >1.0</inlet_pressure_ratio>
102         </inlet>
103         <lpc>
104           <lpc_eta_pol >0.85</lpc_eta_pol>
105           <lpc_pressure_ratio >5.65</lpc_pressure_ratio>
106         </lpc>
107         <lpt>
108           <lpt_eta_mech >0.96</lpt_eta_mech>
109           <lpt_eta_pol >0.86</lpt_eta_pol>
110         </lpt>
111         <nozzle>
112           <nozzle_area_ratio >1.33</nozzle_area_ratio>
113           <nozzle_eta_pol >0.98</nozzle_eta_pol>
114           <nozzle_pressure_ratio >1.0</nozzle_pressure_ratio>
115         </nozzle>
116         <pt>
117           <pt_eta_mech >0.98</pt_eta_mech>
118           <pt_eta_pol >0.88</pt_eta_pol>
119         </pt>
120       </L1_engine>
121       <propeller>
122         <disk_loading units="kW/m**2" >184.99</disk_loading>
123       </propeller>
124     </propulsion>
125     <handling_qualities>
126       <static_margin>
127         <target >0.05</target>
128       </static_margin>
129     </handling_qualities>
130     <load_case>
131       <lc1>
132         <U_gust units="m/s" >15.25<!--gust vertical speed for sizing
              load case 1 (gust with minimum aircraft mass)--></U_gust>
133         <Vc_EAS units="m/s" >200.0<!--equivalent air speed for sizing
              load case 1 (gust with minimum aircraft mass)--></Vc_EAS>
134         <altitude units="ft" >20000.0<!--altitude for sizing load case 1
               (gust with minimum aircraft mass)--></altitude>
135       </lc1>
136       <lc2>
137         <U_gust units="m/s" >15.25<!--gust vertical speed for sizing
              load case 2 (gust with maximum aircraft mass)--></U_gust>
```

```
138         <Vc_EAS units="knot" >200.0<!--equivalent air speed for sizing
                load case 2 (gust with maximum aircraft mass)--></Vc_EAS>
139         <altitude units="ft" >20000.0<!--altitude for sizing load case 2
                (gust with maximum aircraft mass)--></altitude>
140       </lc2>
141     </load_case>
142     <mission>
143       <sizing>
144         <climb>
145           <speed units="m/s" >87.5</speed>
146           <thrust_rate >1.0<!--thrust rate (between 0.0 and 1.0) during
                climb phase in sizing mission--></thrust_rate>
147         </climb>
148         <descent>
149           <speed units="m/s" >113.2</speed>
150           <thrust_rate >0.1<!--thrust rate (between 0.0 and 1.0) during
                descent phase in sizing mission--></thrust_rate>
151         </descent>
152         <diversion>
153           <altitude units="ft" >14000.0</altitude>
154           <distance units="m" >185200.0<!--distance to travel during
                diversion in sizing mission--></distance>
155           <mach >0.33</mach>
156         </diversion>
157         <holding>
158           <duration units="s" >1800.0<!--duration of holding phase in
                sizing mission--></duration>
159         </holding>
160         <landing>
161           <fuel units="kg" >20.0<!--mass of consumed fuel during landing
                 phase in sizing mission--></fuel>
162         </landing>
163         <takeoff>
164           <Friction_coefficient_no_brake >0.004</
                Friction_coefficient_no_brake>
165           <V_MCA units="m/s" >50.69</V_MCA>
166           <altitude units="m" >0.0<!--altitude at takeoff in sizing
                mission--></altitude>
167           <flap_angle units="deg" >15.0<!--flap angle during takeoff
                phase in sizing mission--></flap_angle>
168           <fuel units="kg" >10.0<!--mass of consumed fuel during takeoff
                 phase in sizing mission--></fuel>
169           <slat_angle units="deg" >0.0<!--slat angle during takeoff
                phase in sizing mission--></slat_angle>
170           <thrust_rate >1.0</thrust_rate>
171         </takeoff>
172         <taxi_in>
```

```
173           <duration units="s" >60.0<!--duration of taxi-in phase in
                  sizing mission--></duration>
174           <fuel units="kg" >3.0<!--mass of consumed fuel during taxi-in
                  phase in sizing mission--></fuel>
175           <speed units="m/s" >10.0<!--speed during taxi-in phase in
                  sizing mission--></speed>
176           <thrust_rate >0.01<!--thrust rate (between 0.0 and 1.0) during
                   taxi-in phase in sizing mission--></thrust_rate>
177         </taxi_in>
178         <taxi_out>
179           <fuel units="kg" >9.0<!--mass of consumed fuel during taxi-out
                   phase in sizing mission--></fuel>
180         </taxi_out>
181         <main_route>
182           <cruise>
183             <altitude units="m" >6096.0<!--altitude during cruise phase
                    in sizing mission--></altitude>
184           </cruise>
185         </main_route>
186       </sizing>
187     </mission>
188     <weight>
189       <aircraft_empty>
190         <contingency units="kg" >72.0</contingency>
191       </aircraft_empty>
192     </weight>
193     <aerodynamics>
194       <aircraft>
195         <landing>
196           <CL_max >2.8<!--maximum lift coefficient in landing conditions
                  --></CL_max>
197         </landing>
198         <low_speed>
199           <DCD_feather >0.004</DCD_feather>
200         </low_speed>
201       </aircraft>
202     </aerodynamics>
203   </data>
204 </RHEA>
```